

**ÉCOLE DOCTORALE PHYSIQUE ET CHIMIE-PHYSIQUE (182)**

**Institut Charles Sadron (ICS, UPR 22)**

**THÈSE** présentée par :

**Eulalie LAFARGE**

Soutenue le : **18 novembre 2022**

Pour obtenir le grade de : **Docteur de l'université de Strasbourg**

Discipline/ Spécialité : Biophysique et Chimie Physique

**Pore formation in oxidized lipid membranes**

**THÈSE dirigée par :**

**Dr. MARQUES Carlos**

**Dr. SCHRODER André**

Directeur de recherche, ICS, Université de Strasbourg

Chargé de recherche, Université de Lyon

**RAPPORTEURS :**

**Dr. SENGUPTA Khaya**

**Prof. GRÜBMULLER Helmut**

Directeur de recherche, CINaM, Université de Marseille

Professeur, MPIMS, Göttingen

**AUTRES MEMBRES DU JURY :**

**Prof. BECHINGER Burkhard**

**Prof. HEIMBURG Thomas**

Professeur, Université de Strasbourg

Professeur, Université de Copenhague



# Acknowledgements

I first want to acknowledge my supervisors Carlos M., Pierre M. and André S. who substantially helped me during these three years. Despite the geographical distance with Carlos and André, we were often able to discuss results interpretation and science in general. The three of them always took the time to answer my questions with kindness and pedagogy, to review my work and to give me very appreciated advice. I am grateful and conscious of the chance I had to work with them.

I give particular thanks to my team, MCube, which is composed of exceptional members both scientifically but also humanly speaking. I first want to thank all the PhD students I met there (Vaibhav S., Lisa B., Florent F., Swen H., Friedrich W. and Ann G.) who all helped me in many ways. I want to give very special thanks to Othmene B. who welcomed me into the team, taught me so much and became a very good friend. Adrien G., a post-doctoral fellow at my arrival, introduced me to python with a lot of pedagogy, and I am very grateful for that. Marc B. is an ingenious technician who designed several efficient peroxidation devices essential for my PhD. I want to thank Fabrice T. and Tatiana S. who helped me design some experiments and discussed with me about some of the results obtained. I thank Antonio S. and Igor K. who regularly checked on me. Finally, many thanks to an incredible person, Thierry C., who accepted to take part of my mid-thesis presentation jury. Thierry C. always has happiness and jokes to share with us. I believe he is a great teacher caring a lot for his students and it is, in my opinion, the most important aspect when we want to share knowledge. Apart from science, I am grateful for the time spent with the team in the institute but also outside of work. I wish you all the best for the future.

I deeply thank the Institute Charles Sadron which constitutes a very pleasant work environment. Members of the institute are welcoming, easy to talk to, and always ready to help and exchange. To my opinion, the quality of life at work is an essential matter, and this institute offers a very good one, which allows us to achieve good research quality in good conditions.

I want to acknowledge all the institute members that I was lucky to exchange with. The list being too long, I will only give special thanks to the people who influenced me the most and made my time in the institute even more enjoyable. First Jean-Marc C., who is the first person I meet in the Institute and who reflects well the institute atmosphere of kindness. I also want to thank Marie-Celine S.A. who is a ray of sunshine, always sharing happiness and always ready to help everyone. Amparo R.C. is a great person and researcher, she is a good feminine role-model of success to me. I also thank Olivier B. for his help on IT problems and his kindness in the exchange we had. I thank every member of the administration department, and more especially Odile L., Virginie O. and Magali M.. Finally, I give particular thanks to Wiebke D., who gave me the opportunity to work on the institute communication for one year. I learned so much and I really enjoy working with you and Capucine L..

I want to thank all the people who scientifically took part in my project. I first thank Jan B. and Ekaterina Z. for their collaboration. They trained me on electroporation techniques and took part in the discussion of the results. I want to thank Marc S. for the many hours he spent taking good quality cryo-TEM images of my samples and sharing his expertise with me. Mélanie L. helped me so much concerning the  $\mu$ -DSC analysis, she trained me but also answered my questions regarding protocol design and thermogram analysis. I am thankful to Miguel P.P. and Marina K. who gave me the opportunity to collaborate with them on a very interesting project closely linked to my PhD subject. I want to thank Yulia M. for sharing her expertise on phospholipid hydroperoxidation. I thank Emeric W. and Laurence O. for their considerable help in the protocol design in q-NMR. Finally, I thank Alexis B.S with whom, coffee breaks sometimes transformed into my problem-solving, which was always very useful.

I should not forget to thank all master's students who worked with me (Luis R., Amel B., Paul P. and Mathys L.G.), with special thanks to Laure F. and Chloé G. who greatly helped me in the electroporation data analysis and showed a lot of motivation. I am grateful I had the opportunity to supervise all these incredible students, with who I was able to share the knowledge I learned, as well as, gain new human and project management skills. For these opportunities, I want to thank Jerome C. and Loïc J..

Regardless of the work time, I want to thank all PhD students I meet, especially the ones who gave me a warm welcome upon my arrival. We spent such a great time together. I want to give many thanks to the ones who became great friends, especially to Jean M., Javid A., Anaïs d.M., Capucine L., Ricardo A. and Luisiana G. who always share their cheerfulness with their surroundings and try to be positive even in difficult times. To me, these are the best qualities someone can have and share with their loved ones.

I am thankful I was part of the BJC (bureau of young researchers) during these three years. Once again, I met incredible people, and we organized amazing social and scientific events. I know BJC is now in good hands with people who I believe have great qualities to run it.

I finally give my thanks to my family and dear friends. I thank especially my parents who always encouraged me to give the best of me. Many thanks to Anthony C., Carole F., and Timothé A. for the good time we spend at university and now during most of my vacations, it is very relaxing and fun to spend time with you. I also want to thank Gautier L., who always make me laugh, and supported me for a few months during confinement. I thank him for the trip to Corsica that I was waiting for so long. Many thanks to Daniel R., even from far away, it is always a pleasure to talk with you about everything, you are a great person full of kindness and your motivation is inspiring. I want to thank Fedi H. and Emeline T. who were the first persons I met in Strasbourg and with whom I had memorable parties. Many thanks to Vincent B. and Ivana S. who gave me their support, and always followed me for adventure.

I should not forget to thank the jury members, Burkhard Bechinger, Kheya Sen Gupta, Helmut Grubmuller and Thomas Heimburg who took their time to review this work. Finally I thank you for reading my PhD manuscript and making all my work useful for the community.

*Dedicated to my mother...*



# Contents

<b>Preface</b>	<b>xiii</b>
<b>0 Introduction: state of the art</b>	<b>1</b>
0.1 Introduction to biological cell membranes . . . . .	1
0.2 Cell permeability and ion transportation . . . . .	4
0.3 Lipid membrane fluidity . . . . .	7
0.4 Photo-oxidation and its consequences . . . . .	12
0.4.1 Photo-induced oxidation . . . . .	12
0.4.2 Oxidized membrane properties . . . . .	14
0.4.2.1 Peroxidation . . . . .	14
0.4.2.2 Shortened carbon chain . . . . .	17
0.4.3 Photo-therapy . . . . .	17
0.5 Electroporation: promising treatment and analyzing tool . . . . .	18
0.5.1 Introduction to electroporation and its applications . . . . .	18
0.5.2 Pore opening: the underlying mechanism . . . . .	18
0.5.3 Numerical simulations . . . . .	22
0.5.4 Experiments . . . . .	22
0.5.5 Pore characteristics . . . . .	22
0.5.6 Membrane properties and external conditions influence pore formation . . . . .	23
0.6 Objectives . . . . .	23
<b>1 Lipid hydroperoxidation: an efficient photo-reaction</b>	<b>25</b>
1.1 Materials & methods . . . . .	25
1.1.1 Materials . . . . .	25
1.1.2 Nuclear Magnetic Resonance . . . . .	26
1.1.3 UV-Spectroscopy . . . . .	26
1.1.4 Lipid hydroperoxidation . . . . .	26
1.1.5 Purification . . . . .	27
1.1.6 Stability . . . . .	28
1.1.7 Mixture of hydroperoxydized and non-hydroperoxidized lipids	29
1.2 Results & discussion . . . . .	29
1.2.1 Hydroperoxidation reaction optimization . . . . .	32
1.2.2 Hydroperoxidized lipid purification . . . . .	35
1.2.3 POPC-OOH stability . . . . .	36
1.3 Conclusion . . . . .	40
<b>2 Structural analysis of hydroperoxidized lipid membranes</b>	<b>43</b>
2.1 Materials & methods . . . . .	44
2.1.1 Materials . . . . .	44
2.1.2 Preparation of Small Unilamellar Vesicles . . . . .	45
2.1.3 Cryo-Transmission Electron Microscopy . . . . .	45
2.1.4 Image processing . . . . .	46

2.1.5	Large Multilamellar Vesicles preparation . . . . .	48
2.1.6	$\mu$ -Differential Scanning Calorimetry . . . . .	48
2.1.7	Fluorimetry: using Laurdan to test lipid phases . . . . .	50
2.2	Results & discussion . . . . .	51
2.2.1	Hydroperoxidized vesicles imaging . . . . .	51
2.2.1.1	A qualitative structural characterization . . . . .	51
2.2.1.2	Lipid bilayer determination . . . . .	53
2.2.2	Thermal analysis . . . . .	54
2.2.2.1	Thermograms qualitative description . . . . .	54
2.2.2.2	Phase transition temperature . . . . .	56
2.2.2.3	Phase transition enthalpy . . . . .	58
2.3	Conclusion . . . . .	59
<b>3</b>	<b>Electropermeabilization of hydroperoxidized lipid Membranes</b>	<b>63</b>
3.1	Materials & methods . . . . .	64
3.1.1	Materials . . . . .	64
3.1.2	Vesicles Passive permeability . . . . .	64
3.1.3	Electroporation measurement device . . . . .	65
3.1.4	Free standing bilayer preparation . . . . .	66
3.1.5	Conductivity measurements . . . . .	67
3.1.6	Data treatment . . . . .	68
3.1.6.1	Signal pre-treatment . . . . .	69
3.1.6.2	Membrane survival and pore opening probability . . . . .	69
3.1.6.3	Intrinsic electropermeability . . . . .	69
3.1.6.4	Current intensity average . . . . .	70
3.1.6.5	Regimes quantification . . . . .	70
3.1.6.6	Short lifetime pore analysis: a threshold method . . . . .	70
3.1.6.7	Long lifetime pore analysis: square gating method . . . . .	72
3.2	Results & discussion . . . . .	73
3.2.1	Vesicle intrinsic permeability to KCl . . . . .	73
3.2.2	Membrane geometry . . . . .	73
3.2.3	Electric current traces: a qualitative description . . . . .	75
3.2.3.1	Signal baseline: the intrinsic electropermeability . . . . .	77
3.2.3.2	Abrupt intensity jump: pore opening . . . . .	78
3.2.3.3	Complex traces: tentative apprehension . . . . .	78
3.2.4	General membrane behavior under electric stress . . . . .	80
3.2.4.1	Membrane rupture . . . . .	80
3.2.4.2	Membrane intrinsic conductivity . . . . .	81
3.2.4.3	Probability of pore opening . . . . .	83
3.2.4.4	Identifiable pores and other events: a study of different regimes . . . . .	85
3.2.4.5	Membrane average conductivity . . . . .	86
3.2.5	Pore characteristics . . . . .	88
3.2.5.1	Lifetime distribution of identifiable pores . . . . .	88
3.2.5.2	Short lifetime pores . . . . .	88
3.2.5.3	Long lifetime pores . . . . .	91
3.3	Conclusion . . . . .	93

<b>4 Hydroperoxidized membrane: visco-elastic properties</b>	<b>97</b>
4.1 Main results . . . . .	97
4.1.1 Membrane viscosity . . . . .	97
4.1.2 Membrane polarization and hydration . . . . .	99
4.1.3 X-Rays: structural analysis . . . . .	100
4.1.4 Simulations . . . . .	101
4.2 Conclusion . . . . .	102
<b>5 Conclusions and perspectives</b>	<b>103</b>
<b>6 French summary</b>	<b>109</b>
<b>Appendix A Equivalent electric circuit</b>	<b>121</b>
<b>Appendix B Difficulties encountered during electroporation</b>	<b>125</b>
<b>Bibliography</b>	<b>127</b>
<b>List of Abbreviations</b>	<b>141</b>
<b>List of Symbols</b>	<b>143</b>
<b>Physical constants</b>	<b>147</b>
<b>List of Figures</b>	<b>148</b>
<b>List of Tables</b>	<b>157</b>

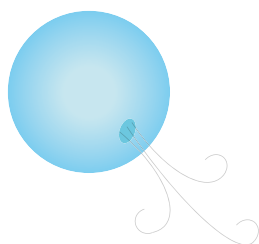


# Preface

Before the PhD, my training mainly focused on polymer properties for industrial applications. I am thus very grateful that I had the opportunity to work on this interdisciplinary project for three years: studying lipids gave me new insight for the future. During this time, I learned a lot about lipid membranes which are fascinating objects with a wide panel of properties and applications. Moreover, being a physical chemist specialized in soft matter, I reinforced my knowledge in physics and coding using Python which were not my prime area of focus.

This thesis was funded by the Franco-German university and work was performed at the Charles Sadron Institute in Strasbourg (France) in collaboration with the Institute of Physiology from the University of Freiburg (Germany). I did my research in the team on the physics of membrane and soft matter (MCube) under the supervision of Carlos Marques, André Schroder, and Pierre Muller.

Biological membranes are essential for the cell welfare. The external plasma membrane defines the limit of the cell, while internal membranes delimit organelles that are involved in many key mechanisms. They are all strong impermeable barriers preventing the unrestrained exchange of most molecules. Disturbance of their permeability leads to uncontrolled flow of molecules from the inside or the outside of the cell, eventually resulting in physiological dysfunction. Many factors are known to perturb the membrane permeability, and one of them -the one we are interested in- is a natural consequence of life under oxygen: the *oxidation*. Oxidation encompasses a multitude of different reactions, all of them changing the chemical structure of targeted molecules.



Phospholipids are abundant amphiphilic molecules composing biological cell membranes and are responsible for the membrane barrier function. Unsaturated (double) bonds present in some phospholipids are the preferential sites for oxidation reactions. Following oxidation, the lipid molecule organization in the membrane is strongly modified. Depending on the reaction type but also on the external conditions, oxidation causes more or less important alterations in the membrane properties. As an example, oxidation can lead to severe membrane damage, causing the opening of reversible holes, called pores. In extreme scenarios, oxidation can even provoke cell death. Oxidation's impact on membrane properties, and more especially on its integrity, is at the center of many studies aiming at understanding the link between lipid oxidation and the development of quite common diseases. Healthcare being an important matter of nowadays society, we believe it is essential to study such membranes, to understand the precise significance of the different oxidation reactions, and more fundamentally to uncover

the pathways involved in membrane permeability and pore formation. This improved knowledge on membrane permeability could be used either to avoid disease by preventing it, or used as an asset to heal or kill defective cells.

Our contribution to this field focus on hydroperoxidation, the first stage of oxidation. Hydroperoxidation is known to induce only "minor" damage to the membrane integrity but has not been yet fully characterized with respect to its impact on membrane permeability. Seeking a deeper understanding of the phenomena, we used model membranes composed of only one mono-unsaturated phospholipid, POPC, abundantly present in mammalian cell membranes. We analyzed POPC membranes containing different fractions (0, 25, 50, 75, and 100 mol %) of POPC-OOH, the hydroperoxidized form of POPC. Membrane permeability being a function of other membrane properties such as its thickness, its polarity, or even its fluidity, it is of prime importance to first characterize the geometrical structure and organization of hydroperoxidized lipids. Finally, we investigated the permeability of a simple hydroperoxidized free-standing membrane. For that, we used a recently developed device that measures electropermeability of the lipid membrane with picoampere and millisecond resolution under physiological conditions.

We believe that our findings will contribute to both the medical and the biological field by providing new membrane structural characterization and new insight on membrane permeability and ion transportation when containing an increasing amount of hydroperoxidized phospholipid. Additionally, in the process of collecting data on the electropermeability of hydroperoxidized membranes, we also gathered a significant amount of data on pore formation in non-oxidized membranes, thus contributing to a field where data is scarce.

## Chapter 0

# Introduction: state of the art

### 0.1 Introduction to biological cell membranes

Thanks to improvements on microscopy devices, during the 17<sup>th</sup> century, scientists were able to observe for the very first time the fundamental unit of life, called a cell. With the rudimental technology of that time, the cell first appeared as an empty capsule surrounded by a membrane. It was only two centuries later, that researchers understood their major importance and studied these complex systems of diverse sizes (0.1 to 100  $\mu\text{m}$ ), shapes, composition, and functions. Cells are able to perform multiple functions and communicate with each other through matter and energy flow. Figure 1 represents an illustration of a cell and its different organelles.



FIGURE 1: Representation of a biological cell with its plasma membrane and different organelles (ex: nucleus, mitochondria). Image taken from [1].

One major aspect of the cell that was ignored up to the early 20<sup>th</sup> century, and on which this work focuses, is its external membrane, a bilayer composed of two leaflets of lipids, responsible for its integrity. Lipids are amphiphilic molecules combining a hydrophilic head with one or several hydrophobic carbon tails conferring them the possibility to self-assemble into a bilayer structure of approximately 5 nm thick in aqueous media [2, 3] as shown in Figure 2.

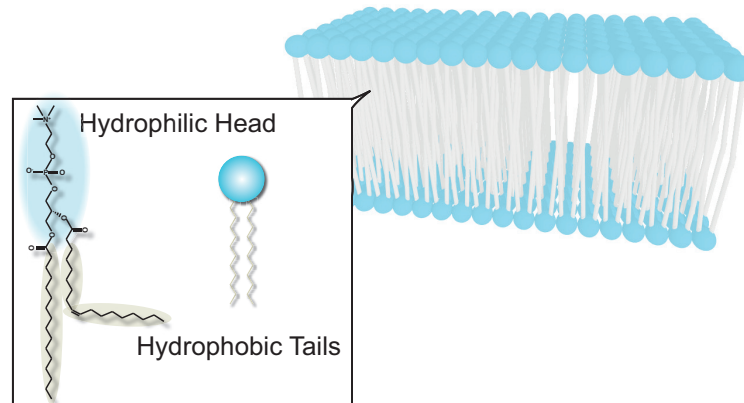


FIGURE 2: Self-assembly of phospholipids into a bilayer with an example of a phospholipid chemical formula and its usual amphiphilic representation.

Many different classes of lipids exist, and cell membranes are a complex mixture of them. Phospholipids, sterol, and sphingolipids are the most common ones in mammalian cell membranes. Among them, phospholipids characterized by their phosphorous-containing head and two hydrophobic tails (Figure 3), are one of the most abundant lipids, with about 50 weight % of the lipid composition in mammalian cell membranes [4]. In the phospholipid subclass, a still wide variety of lipids exists, with different carbon backbone or hydrophilic head groups. Typically, phospholipids of a biological cell membrane are a mixture of 40 % of Phosphatidylcholine (PC), 40 % of Phosphatidylethanolamine (PE), 15 % Phosphatidylserine (PS), and 5 % of other head groups [5]. Regarding the two carbon tails, they can be identical or different, with different carbon lengths (often with an even number between 10 and 26) and different amounts and positions of unsaturated bonds. Another abundant lipid in mammalian cell membranes is cholesterol, from the sterol family. It accounts for roughly 25 weight % of the lipid composition in mammalian cell membranes and is essential for cell viability. Its particular shape makes it interesting to tune the lipid membrane properties, especially the fluidity [6]. The combination of different lipid classes and sub-structures confer specific properties to the membrane (curvature, bending modulus, fluidity, viscosity, hydration, thickness, charge. . .) that biological systems can tune.

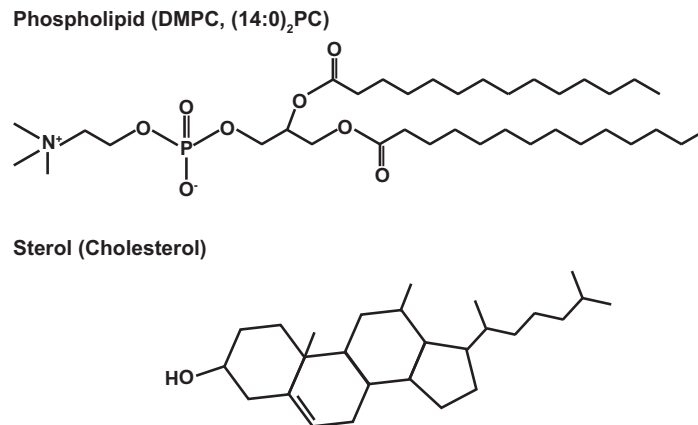


FIGURE 3: Examples of membrane lipids: phospholipid (top) and sterol (bottom) chemical structures, two abundant lipid classes.

The local composition of the membrane can vary in order to tune the local lipid membrane properties. For example, in the outer leaflet, the most abundant class of phospholipids is PC, while the inner leaflet is mostly composed of PE lipids [7]. This asymmetry might be explained by the slightly conical shape of PE, with the tail region wider than the head region giving a higher curvature to the membrane. Biological cell membranes being very complex mixtures, it can be challenging to understand the specific role of each component or to replicate the exact composition for biomimetic trials. Numerous studies thus use model membranes, with simple and controlled mixtures of a limited number of different lipid molecules.

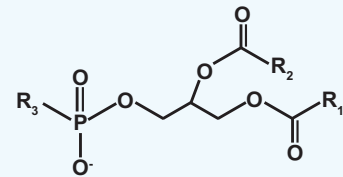
Lipids assemble into fascinating objects and structures depending on the lipid composition, the temperature, the concentration, and the aqueous media. These different structures are important for a variety of industrial applications: food, cosmetics, pharmaceuticals... Vesicles, also called liposomes, are the most common structures. Depending on the targeted application, one can form vesicles of different sizes called small, large, or giant and with different numbers of bilayers, called unilamellar when containing only one bilayer and multilamellar or onion when containing several [8]. For instance, for drug delivery, small multilamellar vesicles are more appropriate to charge a higher amount of hydrophobic drug and move along our body without phagocytosis. On the contrary, for biological cell studies, giant unilamellar vesicles (GUV) are the best biomimetic structures.

### Phospholipid nomenclature

Phospholipid nomenclature relies on the description of the first carbon chain structure ( $R_1$ ), the second chain structure ( $R_2$ ) and the head composition ( $R_3$ ).

$R_1$  and  $R_2$  names depend on the number of carbons and the number of unsaturated bonds, they are often abbreviated either as the first letter of their name (X) or as a sequence of number (a:b), a representing the number of carbons, and b its number of unsaturation.

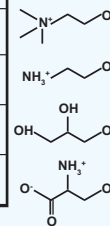
The head name and abbreviation ( $R_3$ ) also depend on  $R_3$  chemical composition.



Some examples are given in the tables below:

Tail name ( $R_{1,2}$ )	Abbreviation (X)	Abbreviation (a:b)
Myristoyl	M	14:0
Palmitoyl	P	16:0
Stearoyl	S	18:0
Myristelaidoyl	-	14:1
Palmitelaidoyl	-	16:1
Oleoyl	O	18:1

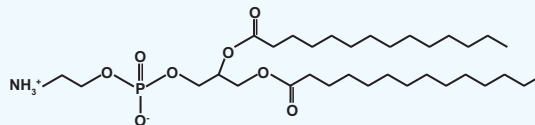
Head name ( $R_3$ )	Abbreviation
Phosphocholines	PC
Phosphoethanolamines	PE
Phosphoserines	PS
Phosphoglycerols	PG



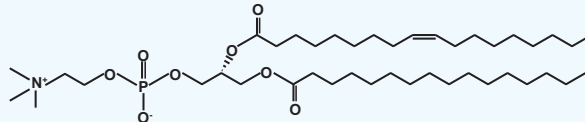
If the phospholipid carbon chains are identical, the name becomes di- $R_1R_3$ , with abbreviation DXPY and (a:b)<sub>2</sub>.

Examples:

1,2-dimyristoyl-glycero-3-phosphoethanolamine  
DMPE  
(14:0)<sub>2</sub> PE



1-palmitoyl-2-oleoyl-glycero-3-phosphocholine  
POPC  
(16:0,18:1) PC



For unsaturated lipids, the position of the unsaturation and its conformation can be given in the abbreviation.

$c\Delta^n$  for a cis unsaturation between the carbons n and n+1

$t\Delta^{n,m}$  for two trans unsaturations between the carbons n and n+1 and m and m+1

## 0.2 Cell permeability and ion transportation

Biological cells exist in a watery environment composed of specific small molecules like sugars, amino acids, and nucleotides able to form macromolecules such as polysaccharides, proteins, and nucleic acid chains (DNA and RNA) respectively [2]. Ions are also one of the most important components found in biological media since they are involved in different essential pathways to exchange energy and information. In this context, molecule or ion translocation across the membrane is strictly regulated by the intermediate of protein carriers inserted inside the lipidic membrane and exerting active transportation [9]. This rigorous control is made possible by the strong barrier properties of the lipid bilayer regarding ions. This is one of the reasons why biological cell membrane integrity is crucial for cell survival.

In absence of assisted transportation channels, the membrane is impermeable to most molecules. The permeability  $P_m^i$  to a given molecule is defined as the ability for that molecule to cross the membrane and is expressed in the same units as velocity ( $\text{m}\cdot\text{s}^{-1}$ ).

The energy barrier for a solute to penetrate inside the membrane hydrophobic core depends on its size, its polarity, and its charge [10]. Small and hydrophobic particles can penetrate easier than big, polar, or ionic molecules [11]. Typically, ion permeability range around  $10^{-14}$  m.s<sup>-1</sup> [12], while big and polar molecules like sugar are around  $10^{-12}$  m.s<sup>-1</sup> [13] and small and non-polar molecules such as CO<sub>2</sub> around  $10^{-2}$  m.s<sup>-1</sup> [14, 15]. A summary of typical membrane permeability values for a few essential compounds is found in Figure 4

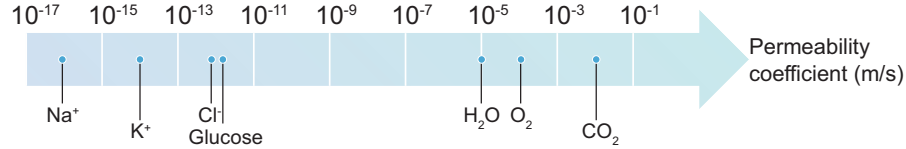


FIGURE 4: Permeability scale of lipidic membranes to some molecules of interest [10, 12–16].

The diffusion of particles from an aqueous phase  $w$  to the membrane interior  $m$  is driven by thermal agitation and by external forces when present. The flow of a particle  $i$  can be induced by a gradient concentration ( $d[i]/dx$ ) between the two aqueous media  $w_1$  and  $w_2$  from each side of the membrane, or by an electric potential gradient ( $dU/dx$ ) in case of charged species. An additional contribution takes into account the fact that the particle goes from the aqueous phase  $w$  to the membrane  $m$  considering their standard chemical potential  $\mu_0^{w,m}$ , thus one obtained:

$$J_i = -D_i^w \left( \frac{d[i]}{dx} + \frac{\mathcal{F}z[i]}{\mathcal{R}T} \frac{dU}{dx} + \frac{[i]}{\mathcal{R}T} \frac{d\mu_0^{w,m}}{dx} \right) \quad (1)$$

where  $J_i$  is the flux density of particle  $i$  able to permeate the membrane (mol.s<sup>-1</sup>.m<sup>-2</sup>),  $D_i^w$  the diffusion coefficient of the particle in the external media  $w$  (m<sup>2</sup>.s<sup>-1</sup>),  $[i]$  the local particle concentration at position  $x$  (mol.m<sup>-3</sup>),  $\mathcal{R}$  the gas constant (J.mol<sup>-1</sup>.K<sup>-1</sup>),  $T$  the temperature (K),  $\mathcal{F}$  the faraday constant (A.s.mol<sup>-1</sup>),  $z$  the particle valence (dimensionless),  $U$  the electrical potential difference (V) and  $\mu_0^{w,m}$  the standard chemical potential between water and the membrane (J.mol<sup>-1</sup>).

The permeability can also be expressed as a function of the partition coefficient  $K^{w,m}$  which corresponds to the concentration ratio between two phases ( $w$  and  $m$ ) at equilibrium, as detailed later in equation 4. The permeability can thus be written:

$$P_m^i = \frac{K_i^{w,m} D_i^w}{d} \quad (2)$$

where  $K_i^{w,m}$  is the dimensionless particle partition coefficient between the lipid membrane  $m$  and the aqueous phase  $w$  and  $d$  is the bilayer thickness (m). As previously stated, the exchange of molecules across the membrane is mostly related to the hydrophobicity and charge of the molecule (both linked to its partition coefficient) and its size (linked to the diffusion coefficient) as detailed below.

The diffusion coefficient of a particle inside a media is a function of the media viscosity and is usually calculated given the Stokes-Einstein equation:

$$D_i^w = \frac{k_b T}{\zeta} = \frac{k_b T}{6\pi\eta_w r_i} \quad (3)$$

where  $k_B$  is the Boltzmann constant (J/K),  $\zeta$  the friction coefficient (Pa.m.s),  $\eta_w$  is the media viscosity (Pa.s) and  $r_i$  the particle radius (m). The bilayer thickness and its viscosity are key parameters in the particle diffusion but are constant for a given membrane composition. Only the size of the particle interfere with its diffusion across a given membrane. As an example, ions, that have a small radius of roughly 1 Å ( $r_{K^+} = 2.43$  Å,  $r_{Cl^-} = 0.79$  Å [17]), have a high diffusion coefficient in water of about  $D_{ion}^{water} \approx 2 \times 10^{-9}$  m<sup>2</sup>/s ( $D_{K^+}^{water} \approx 1.96 \times 10^{-9}$  m<sup>2</sup>/s and  $D_{Cl^-}^{water} \approx 2.03 \times 10^{-9}$  m<sup>2</sup>/s [9]). The size of the particle is thus an important parameter to consider, but particles of similar size and thus diffusion coefficient can exhibit different permeabilities. As a comparison CO<sub>2</sub> possesses a similar diffusion coefficient of  $D_{CO_2}^{water} = 2 \times 10^{-9}$  m<sup>2</sup>/s [10] but membranes are much more permeable to CO<sub>2</sub> than to ions as observed on Figure 4.

This difference is explained by the low partition coefficient of ions. The partition coefficient of a particle between two phases (here water and lipid bilayer), can be seen as the ratio of the equilibrium concentration of the particles in each phase:

$$K_i^{w,m} = \frac{[i]_m}{[i]_w} = \exp\left(-\frac{\Delta E_i^{w,m}}{\mathcal{R}T}\right) \quad (4)$$

with  $\Delta E_i^{w,m}$  the free energy of the system (J), taking into account all energy barriers coming from diverse origins (particle solvation, membrane dipole, surface energy between water and lipid,...). Every molecule dispersed in a solvent forms weak bonds with it, a physical interaction called solvation. In the context of a lipid membrane in water, the energy required for the molecule to break these bonds with water in order to enter the hydrophobic core is called Born energy and is believed to be predominant in the determination of the partition coefficient [10, 18]. The more a compound likes to create bonds with water the more it is soluble in it and the more its translocation is unfavorable. It is known that charged molecules are greatly solvated, which gives a high free energy and thus a low partition coefficient. As a comparison, anionic organic compounds exhibit a partition coefficient between water and hexadecane (hydrophobic carbon chains being similar to bilayer hydrophobic core) between  $10^{-8}$  to  $10^{-28}$  [19] while a neutral compound such as CO<sub>2</sub> has a partition coefficient of 1.5 [20]. Neutral compounds possess a higher partition coefficient than ions, this directly explains the permeability differences of small molecules. Another aspect concerning ions diffusion is the binding of some ions to the membrane. The main effect reported concerns cations binding to the carbonyl region of phospholipids. It has been shown that smaller cation such as  $Na^+$  has a stronger interaction than bigger ones like  $K^+$  explaining their permeability difference [7].

Since passive diffusion for ion transportation is limited, biological cells use a wide variety of self assembling proteins that form tree-dimensional structures and contribute to fundamental functions such as ion transportation as seen in Figure 5. Proteins are polymers formed by the repetition of 20 different amino acid units (usually between 100 to 1000 monomer units) [21]. There is usually the same mass proportion of lipid and protein in cell membrane composition, but the ratio can vary from 0.25 to 4 [22]. Proteins can act as switches and tune their conformation in order to induce or prevent ionic translocation depending on their environments such as the temperature, the voltage, the membrane fluidity, or the ion concentration [23–25]. Fundamentally, they act as sensors to transmit or retain information. Many

studies are interested in their very specific conductivity since proteins assemble to form a stable channel of very specific size [26, 27].

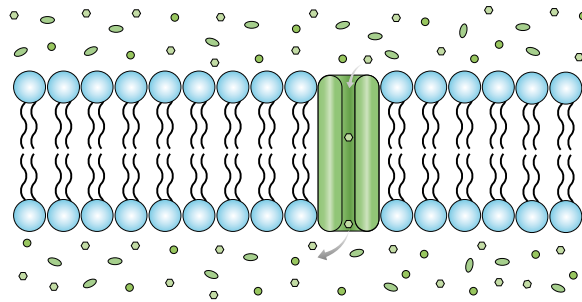


FIGURE 5: Lipidic membrane with inserted transmembrane protein inducing active transportation.

In the biological context, small membrane permeabilities with respect to ions have led to the neglect of passive lipidic membrane permeation in favor of assisted transport by protein ionic channels [28]. Yet, the exact pathways allowing ions and other molecules to cross the hydrophobic membrane core are still a matter of controversy [22]. In particular, it is likely that mechanisms such as phase behavior or lipid oxidation [22, 29] play not only a direct role in passive membrane translocation but also in protein-assisted transport.

### 0.3 Lipid membrane fluidity

Lipids self-assemble in different thermodynamic states, characterized by different degrees of head and tail ordering. Such states, also called phases, depend on the chemical structure, the ambient temperature and other parameters such as pressure, hydration degree, or mechanical stress. Cell lipid bilayers are commonly found in the fluid phase ( $L_\alpha$ ), but some physiological mechanisms require a specific amount of gel phase ( $L_\beta$ ). As illustrated in Figure 6, the fluid phase is a state where lipids are free to move in the membrane with high lateral diffusion coefficients ( $10^{-12} \text{ m}^2 \cdot \text{s}^{-1}$  [30, 31]) and can "jump" from one leaflet to another with a slow time constant (every  $10^5 \text{ s}$  [32]), a phenomenon named flip-flop.

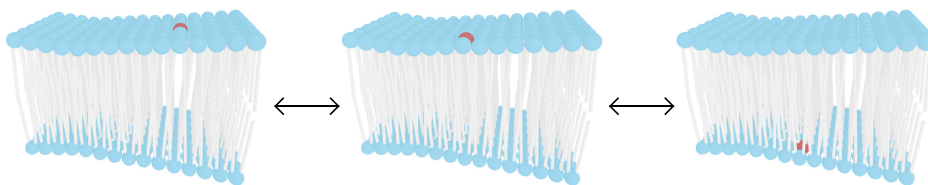


FIGURE 6: In the fluid state the lipids diffuse laterally in the membrane with a high diffusion coefficient ( $\sim \mu^2 \cdot \text{s}^{-1}$ ) and can occasionally ( $\sim$  every day) flip-flop from one leaflet to the other.

In opposition to the fluid phase, in the gel phase, lipids have a lower diffusion coefficient (100 times smaller [31]) linked to a higher order of the heads and of the tails. The tail order parameter defines the orientation of the lipid tail. It is usually small in a fluid phase which is by definition disordered as schematized in Figure 7 and takes an increasing value with the system order. In this phase, lipid tails are stretched, and the membrane exhibits an increase in its thickness [33]. The main

phase transition temperature ( $T_m$ ) of a lipid membrane is defined as the temperature at which the bilayer changes from a gel to a fluid state (or vice versa) as seen in Figure 7.

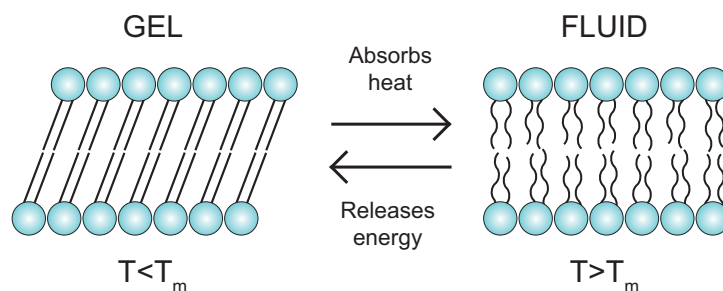


FIGURE 7: Scheme of lipid organization from the gel to the fluid phase.

The phase transition is a non-instantaneous phenomenon since it results from molecular interactions.  $T_m$  can be measured by Differential Scanning Calorimetry (DSC), during which, the sample and its reference are heated or cooled down at a specific speed by precisely controlling the temperature in both cells. When a compound undergoes a phase transition it either takes (endothermic) or releases (exothermic) heat to break or create weak bonds between lipid chains and change conformation. The device adapts its heat flow in order to keep a similar temperature in both cells and measure the differential heat flow between the sample and the reference. The resulting differential heat flow as a function of the temperature exhibits a more or less wide and intense peak near the phase transition temperature depending on the scan rate.  $T_m$  can be extracted from the thermogram using different methods, the most common being to measure the temperature at the intersection of the baseline and the ascending slope of the peak. The area under the peak between the initial temperature  $T_i$  and the final temperature  $T_f$  corresponds to the transition enthalpy  $\Delta H$  (J) as expressed by equation 5:

$$\Delta H = \int_{T_i}^{T_f} \Delta C_p \cdot dT \quad (5)$$

with  $C_p$  the heat capacity in  $\text{J}\cdot\text{K}^{-1}$ . Figure 8 displays an example of a DSC scan, also called thermograms, obtained from DPPC (16:0)<sub>2</sub> with the schematic extraction of  $T_m$ .

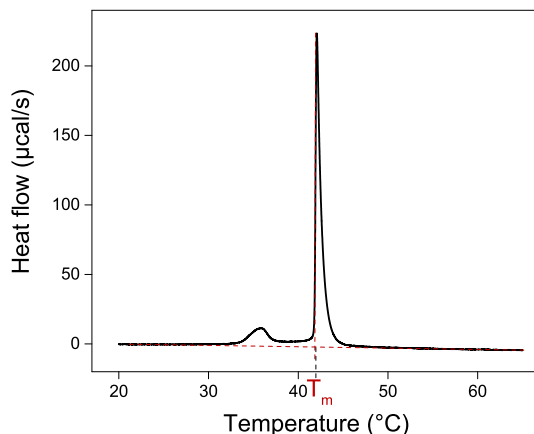


FIGURE 8: DPPC DSC scan obtained at a heating rate of  $0.25\text{ }^{\circ}\text{C}/\text{min}$ . The main transition between the gel and the fluid phase happens around  $T_m=42\text{ }^{\circ}\text{C}$ . DPPC displays also a pre-transition temperature  $T_p$  around  $35\text{ }^{\circ}\text{C}$  from the gel phase to the so-called ripple phase.

Membrane fluidity is correlated to membrane permeability [22]. The main transition of lipid membranes depends on the chemical structure of the lipids and, for membranes assembled from lipid mixtures, on the membrane lipid composition. [3, 34]. As an example, Figure 9 shows that the transition temperature increases with the length of the carbon chain, for identical heads. Longer chains imply a larger number of tail interactions and thus a stronger ordering. For asymmetric lipids, the length of both chains matters and will have a direct impact on the lipid bilayer phase transition temperature. The presence of branched lipid tails containing methyl groups at different positions such as the phytanoyl chains also perturbs the tail order and thus the transition temperature [3].

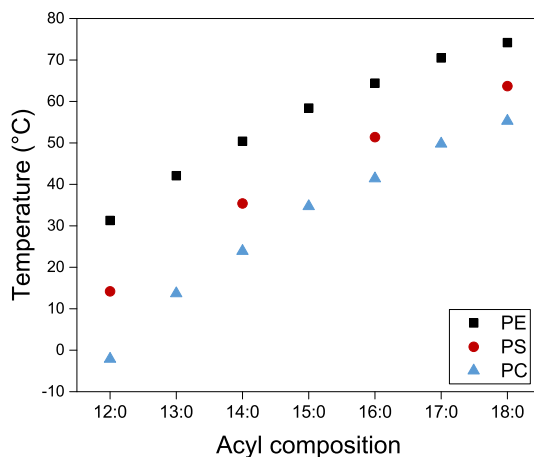


FIGURE 9: Main phase transition temperature of saturated lipids with identical tails as a function of their carbon chain length and their head composition (PS being bound to  $\text{Na}^+$ ). The graph is obtained from  $T_m$  values taken in the Handbook of lipid bilayers [3].

In nature, many lipids possess at least one unsaturation, that perturbs the order and interactions between the chains, resulting in the lowering of the transition temperature. For DOPC  $(18:1)_2$ , for instance, the transition temperature depends on the position of the unsaturation, as shown in Figure 10, the lower transition temperature being obtained for unsaturations located in the middle of the chain. In

addition, most of the unsaturations found in lipids are cis unsaturations, they have a larger impact than trans unsaturations since the lipid tail is slightly tilted [2]. Natural lipids have specific structures that ensure a low enough transition temperature for the lipid membrane to be mainly in the fluid phase at biological temperature.

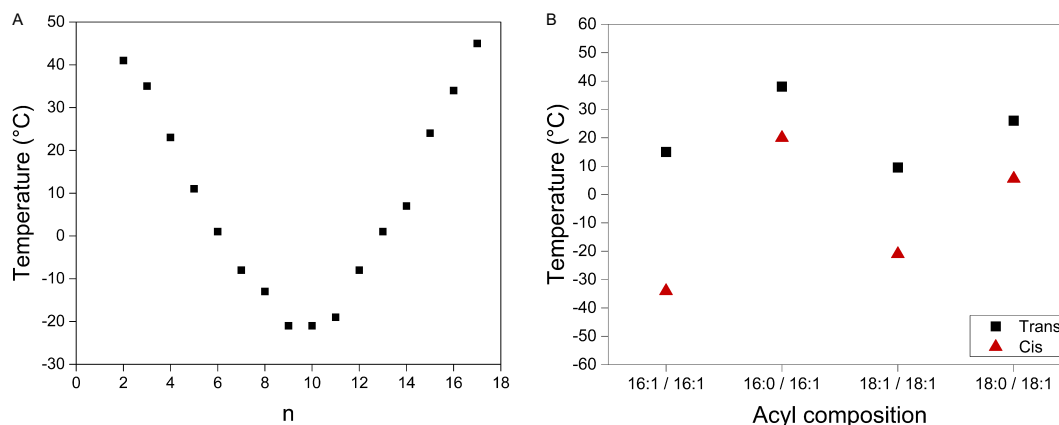


FIGURE 10: (A) Transition temperature between the fluid and gel phase of DOPC ( $18:1c\Delta^n$ )<sub>2</sub> as a function of the cis unsaturation position  $n$  on the carbon chains. Figure reconstructed from Barton et al. (1975) [35] (B) Impact of cis and trans unsaturation on the bilayer phase transition temperature. Values from [3, 35–38].

Bilayer hydration can also impact the transition temperature. As shown in Figure 11, the transition temperature is shifted when adding up to 10 water molecules per lipid that correspond to a fully hydrated bilayer. Under low hydration conditions lipids can order in a highly packed and ordered fluid crystalline phase ( $L_c$ ). For some lipids, bilayer hydration can also induce the presence of another phase, the so-called ripple phase ( $P_\beta$ ) as shown in Figure 8 [40, 41]. The presence of a ripple phase appears as a pre-transition between the gel and the fluid phase showing lateral periodicity.

In a complex lipid mixture containing cholesterol, other phases are observed [2, 42]. The specific shape of cholesterol promotes the alignment of the tails of the surrounding lipids, without however inducing a gel phase. In the presence of cholesterol a new phase is formed called the liquid ordered phase ( $L_o$ ) which differs from the usual disordered fluid phase ( $L_\alpha$ ) also called ( $L_d$ ). Cholesterol induces modifications of the bilayer properties such as an increased thickness, a decreased permeability, and an increased rigidity of the fluid phase. Cholesterol can directly impact the membrane permeability, having different effects depending on its proportion in the membrane [43, 44].

As a response to external conditions such as a change in temperature, biological cell membranes can control their

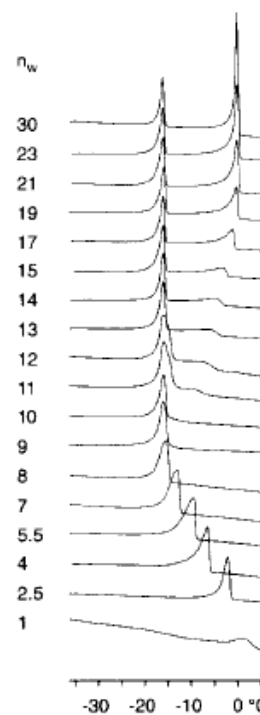


FIGURE 11: Heating DSC scans of DOPC with different water/lipid molecule ratio ( $n_w$ ). Figure taken from Ulrich et al. (1994) [39].

lipid composition to preserve a fluid phase or to allow domain formation when required [45]. The phase transition is a very important feature in biological cells, it is for instance known that some proteins insert and function preferentially in a specific environment [46]. In addition, near the phase transition, in a range of 10 °C, cells can exhibit phase coexistence. Interestingly, it has been shown that under these conditions, lipid membranes are much more permeable to ions as shown in Figure 12. It has been hypothesized that ions probably cross the membrane at the interface between the two different phases [10]. In fact, at the phase coexistence interface, a very disordered phase is present with a lower thickness due to the interdigitation of some lipids as observed in Figure 13. This interface is highly dynamic and appears and disappears in a few nanoseconds [33], this phenomenon being more noticeable for shorter lipid chains [2].

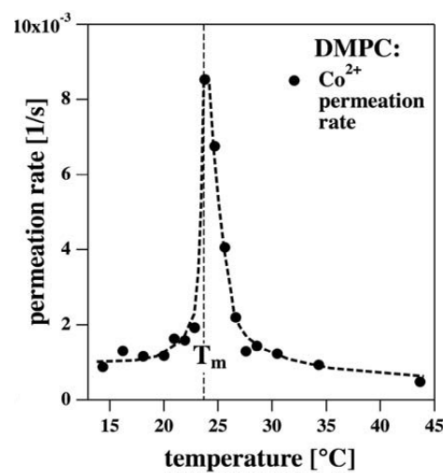


FIGURE 12: Permeability of a DMPC (14:0)<sub>2</sub> membrane regarding  $\text{Co}_2^+$  ions as a function of the temperature. The figure is taken from Heimburg (2010) [22]. Away from the transition temperature of DMPC ( $\sim 24^\circ\text{C}$ ), the membrane is impermeable, however at the neighboring of  $T_m$ , the permeability exhibit a huge increase. Permeation rate represents the time constant for the quenching of a fluorophore inserted inside the bilayer by the  $\text{Co}_2^+$  present in the external media.

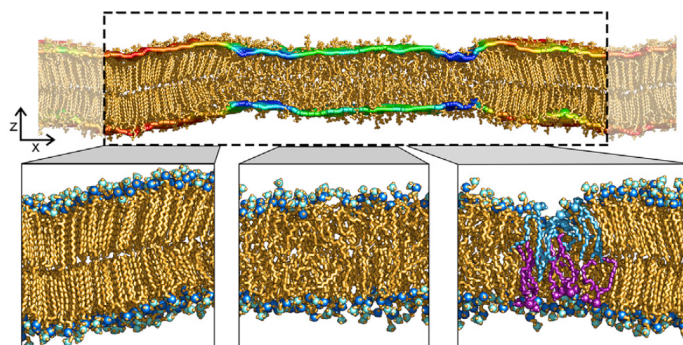


FIGURE 13: Simulation snapshot of phase coexistence during a gel-fluid transition, taken from Kirsch et al. (2019) [33]. Different order coexistence can be observed, with different thicknesses and lipid orientations.

## 0.4 Photo-oxidation and its consequences

Earth's atmosphere being composed of 20 % of oxygen, oxidation is a common and natural process of daily life. In a biological context, essential cell functions require oxidation reactions. As an example, adenosine triphosphate (ATP) synthesis results from glucose and lipid oxidation by mitochondria (an organelle present in some cells). ATP is a key molecule in living organisms able to store energy into chemical bonds and to release it during specific physiological mechanisms such as muscle contraction [21]. Defense mechanisms such as inflammation response, bacteria and viruses phagocytosis, and several other cellular processes also involve oxidation [47]. However, oxidation is also known for its detrimental impact on biological systems [48]. Despite many biological oxidation processes being still unclear, several studies were able to link or hypothesize a link between lipid oxidation and common pathologies such as Parkinson [49], Alzheimer [50, 51], diabetes [52], cancers [53, 54], aging [47], and many others [55, 56]. Human cells are machineries with functionalities of incredible precision. Molecules position themselves and assemble for a precise purpose to work in harmony with surrounding objects or as a response to external stimuli. In this context, uncontrolled chemical lipid oxidation may induce cell physical degeneration and physiological imbalance leading to dysfunctions or illnesses of different degrees of severity.

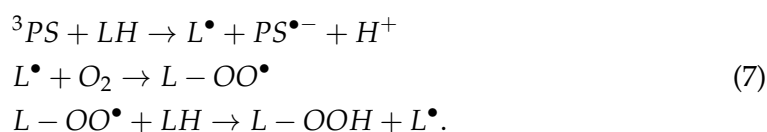
### 0.4.1 Photo-induced oxidation

Hydroperoxidation is one of the main oxidation reactions that occurs in biological media, it is also the first oxidation steps [57]. Despite extensive studies on the subject, the entire reaction pathway is not clearly determined yet. Chemical- or photo-induced peroxidation is believed to be selective to unsaturated lipids and more precisely to cis unsaturations [58, 59]. Lipids containing a high amount of unsaturation can lose an allylic hydrogen bond on the unsaturation and start the peroxidation chain reaction by themselves. For monounsaturated lipids, the reaction must be triggered by an external factor [58, 60].

Photo-induced oxidation is an oxidation reaction that occurs in biological media in presence of light and oxygen. It usually involves enzymatic or radical intermediates [58]. Two reaction pathways are distinguished: type I and type II, their relative abundance depends on the reaction conditions: photosensitizer nature and concentration, illumination power and time, condensed or dispersed lipids,... [57, 61]. Both reactions require the presence of a photosensitizer (PS), a chromatic molecule able to absorb light, rise to a singlet excited state and finally reach a triplet state with a long lifetime. The reaction initiation always starts with the photosensitizer light absorption:



Many photosensitizers exist in physiology media, among them the most involved in biological oxidation are the porphyrins, psoralens, and hypericin [61]. For type I reactions, the photosensitizer in its triplet state ( ${}^3PS$ ) reacts directly with the lipid (LH) by abstraction of one of the two hydrogens involved in the cis unsaturation. The lipid alkyl radical ( $L\bullet$ ) generated can then react with dioxygen ( $O_2$ ) present in the media to form the peroxy radical ( $L-OO\bullet$ ) and finally react with another lipid (LH) producing peroxide lipid ( $L-OOH$ ) and a new lipid radical for an autocatalytic chain reaction following the equation 7 [62]:



The propagation reaction continues until the termination step in which radicals are 'quenched' by antioxidants or by annihilation reactions. The prime product of this reaction is peroxidized lipids, but secondary reactions can follow, leading to the formation of shortened lipid chains [63, 64]. One possible chemical mechanism for the hydroperoxidation propagation is presented in Figure 14 and may explain the shortened chain products obtained in such reaction.

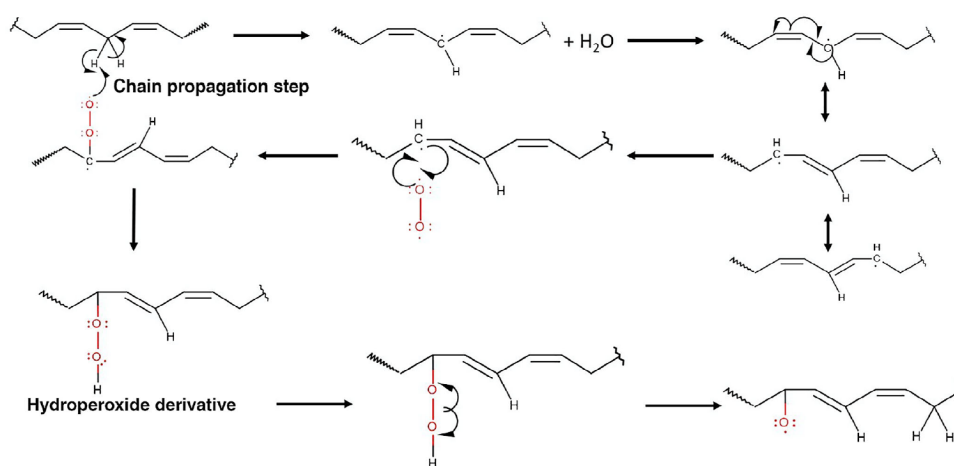
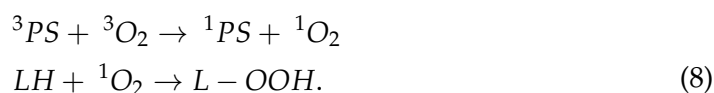


FIGURE 14: Possible reaction propagation between oxidized and non-oxidized lipid chain during type I photo-oxidation. This mechanism explains the possibility of obtaining shortened lipid chain. Figure from Ulmer et al. (2021) [65].

For type II reactions, singlet oxygen  ${}^1O_2$  is believed to be at the center of peroxidation reactions, being the most encountered Reactive Oxygen Species (ROS) [62]. In this reaction, the photosensitizer in its triplet ( ${}^3PS$ ) state can then transfer its energy to a dissolved dioxygen molecule which has a triplet ground state, a rare case in nature (Figure 15). The dioxygen reaches the highly reactive singlet state,  ${}^1O_2$ , having a lifetime of the order of the microsecond in aqueous solutions, while the photosensitizer returns to its ground state. Singlet oxygen reacts then with one of the two equiprobable hydrogen positions of the unsaturated bond to form the peroxidized lipid (LOOH) following the equation [62]:



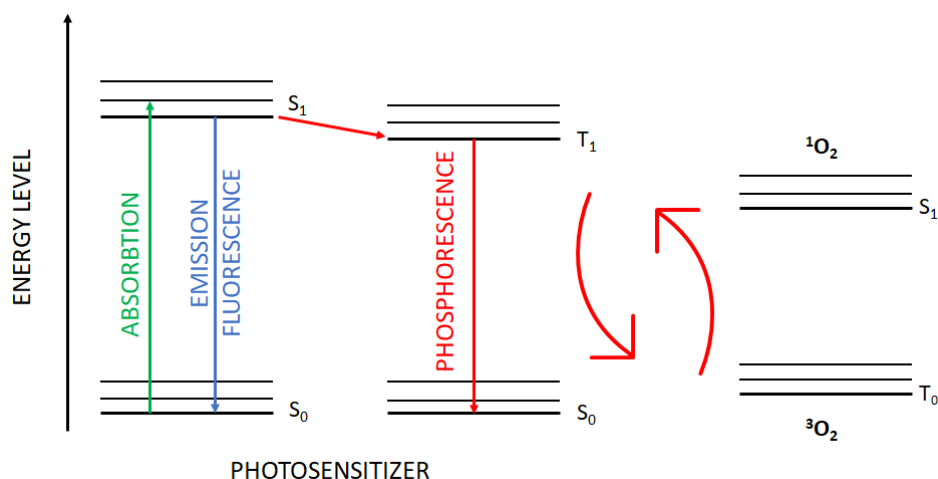


FIGURE 15: Energy level transfer required for type II peroxidation. The photosensitizer in its ground state should first rise its energy to its higher energy singlet state and cross by inter-system crossing its triplet state. The triplet state can then transfer its energy to a dioxygen molecule naturally found in its triplet ground state in order to create a highly reactive singlet oxygen.

For both reaction types on monounsaturated lipids, the peroxidation reaction leads to the formation of two equimolar isomers. In a biological membrane context, for type I reactions to happen, the photosensitizer must be able to permeate inside the hydrophobic lipid core, while for type II reactions this is not required since the dioxygen directly reacts with the lipid since it can permeate inside membranes [16]. Type I reaction using a radical propagation can lead to secondary products such as shortened lipid tails, while type II reaction can be used to oxidize lipids inside a self assembled membrane since  $O_2$  can permeate more easily than some photosensitizers [66]. The presence of transition metals (Iron, Copper,...) in the media can lead to secondary catalysis reactions and result in the shortening of the lipid chain ending with aldehyde, carboxylic, ketone, or alcohol groups [63, 67, 68].

## 0.4.2 Oxidized membrane properties

### 0.4.2.1 Peroxidation

The addition of the polar peroxide group inside the hydrophobic carbon core is known to greatly impact the lipid conformation, indeed, the polar group drives the lipid tail toward the surface where it can interact with lipid heads and water molecules as represented in Figure 16 [69, 70]. Several studies also suggested that above a certain amount of hydroperoxidized lipids, some peroxide groups stay in the hydrophobic core [71]. The induced new lipid conformation leads in turn to modifications of the bilayer properties, as recently shown. The effect of hydroperoxidation on the lipid bilayer properties has been recently reviewed [60, 72], we recall below the major modifications.

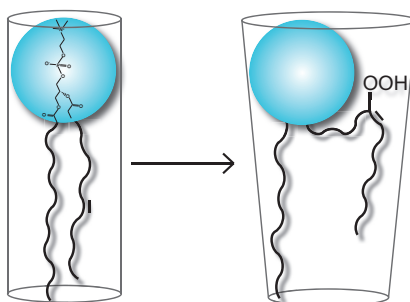


FIGURE 16: Schematic changes of the main conformation of a mono-unsaturated hydroperoxidized lipid in a bilayer.

- As a result of the peroxide addition, and as illustrated in Figure 17, the geometrical aspect of the lipid in bilayers is modified with a lateral expansion. Experiments show an increase in the area per lipid of about 20 % depending on the lipid membrane composition, an increase also seen in numerical simulations [29, 64, 73]. For POPC for instance, typical area per lipid values are usually found around 0.65 - 0.7 nm<sup>2</sup> from both simulations [74] and experiments [75]. The increased area per lipid implies a decrease in the bilayer thickness. Bilayer thickness decrease was evidenced by the reduction of the distance between the two high electron density regions corresponding to the phosphor-containing polar head by X-Ray and simulations [69, 76–78]. Scattering experiments typically find a decrease in the bilayer thickness around 15 % depending on the lipid. One can expect that with the peroxide group looping to the surface, the geometry of the molecule becomes more conical (Figure 16). Another modified geometrical aspect observed in the presence of hydroperoxidized stacked bilayers in excess of water, is the increase in the inter-bilayer distance, indicating the presence of more water in between each bilayer [79].

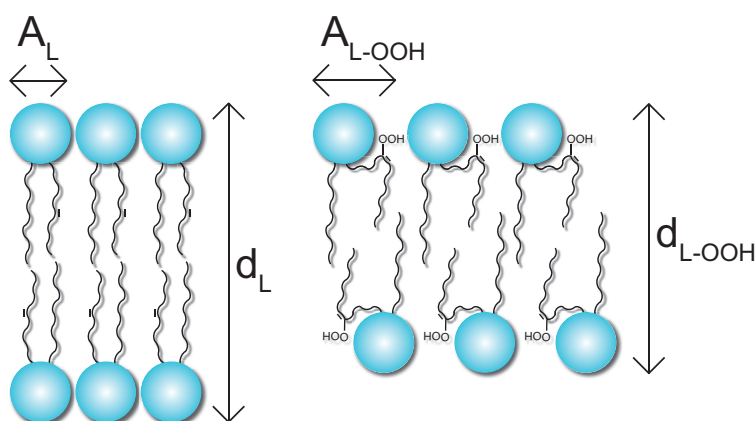


FIGURE 17: Scheme of the increase in the area per lipid from  $A_L$  to  $A_{L-OOH}$  and decrease in the bilayer thickness  $d_L$  to  $d_{L-OOH}$  after hydroperoxidation of mono-unsaturated lipid.

- The elastic properties of the membrane are also impacted by hydroperoxidation. Membranes are often characterized by their elastic modulus, which is composed of the stretching modulus related to the membrane surface tension and the bending modulus linked to the bilayer curvature. Lipid stretching modulus values

are usually around  $200 \text{ mN}\cdot\text{m}^{-1}$ , but when hydroperoxidized the stretching modulus is decreased by a factor of 4 [29]. Concomitantly, the bending modulus is strongly reduced [79], meaning hydroperoxidized membranes are more easily curved and stretched. This might be linked with the hypothesized conical shape of the hydroperoxidized lipid, and its increased lateral expansion.

- In addition, simulations observed a decrease in the order parameter which is consistent with the decrease in elastic modulus [60, 72, 73, 77]. This can probably be explained by the reduced interaction between the lipid tails and correlate with an increased thermal fluctuation linked to the higher inter-membrane distance.

- One may wonder how hydroperoxidation impacts the phase transition temperature. POPC (16:0,18:1) is a phospholipid that is in a fluid phase at ambient temperature ( $T_m = -3 \text{ }^\circ\text{C}$ ) [80]. Studies suggest that hydroperoxidized POPC (POPC-OOH) lipids would be still in the fluid phase at ambient temperature [79]. This is consistent with studies showing an order decrease, suggesting thus a decrease in the transition temperature as proposed by simulations [72]. To the best of our knowledge, no measurement of the transition temperature of hydroperoxidized lipid was made before. But the phase behavior of hydroperoxidized lipids might not be straightforward since, during hydroperoxidation, the cis unsaturation is transformed into a trans unsaturation, creating theoretically more order. However, the polar peroxide group, as suggested previously, looping to the surface, would promote disorder in the carbon area. In addition, the phase state and transition are not trivial matters, for example, phase separation in presence of hydroperoxidized lipids is a matter of controversy. Some evidence evokes the possible presence of phase separation in binary but no concrete proof has been shown yet [81]. However, in ternary mixture the substitution of lipid by their hydroperoxidized form have lead to the observation of phase coexistence [82–85].

- Simulations indicate that the lipid lateral diffusion decreases with hydroperoxidation [86, 87]. In addition, an increase in viscosity is often observed, linked to an increase in membrane rigidity [79, 88, 89]. These findings oppose all the other trends stated above. One might suggest an increased viscosity at the bilayer surface with the creation of a hydrogen bond network formed between head groups, peroxide group, and water molecules, also reducing lipid diffusion, while the hydrophobic cores stay disordered.

Understanding the interaction and organization of hydroperoxidized lipids is certainly not trivial. The increase in viscosity and rigidity accompanied by the decrease in the lateral diffusion would suggest a more organized phase with higher interaction between molecules. However, every other structural parameter such as the elastic modulus, the lateral expansion with the peroxide group loop, or even a higher order found by simulations, seem to indicate less order leading to a more fluid behavior. The question of membrane fluidity is an important matter in our study since it is closely linked to membrane permeability.

- The increase of the membrane dielectric constant due to the addition of the peroxide group may slightly lower the energy barrier for water permeation [90]. Rare water defects are always forming at the interface of lipid membrane assemblies, but their formation is believed to be promoted by the higher dielectric constant, also increasing the bilayer hydration [60, 91]. Experiments show that the hydroperoxidized membrane keeps its low permeability to ions and to larger molecules such as sugars

over minutes or hours [29, 92], but scarce simulations show a slight increase in membrane permeability [93]. An intriguing aspect of oxidized membrane permeability is the momentary loss of impermeability during photo-peroxidation. Two stages are observed during irradiation, first, an increase in the area per lipid that leads to excess area and GUV deformation, second, some buds are expelled from the main GUV so the membrane comes back to a tense configuration sometimes with the formation of local transient pore and loss of membrane integrity [70, 94, 95]. This is likely due to the formation of other species beyond hydroperoxides that we now discuss.

#### 0.4.2.2 Shortened carbon chain

For more severe oxidation effects such as those leading to a truncated lipid chain, the looping of the lipid chain is enhanced [73, 96–98] and it has been shown that the impact on the membrane properties is increased compared to peroxidation [72, 84, 99]. As an example, the permeability of membranes containing such modified lipids has been reported to greatly increase [8, 73]. Even more striking, it has been observed that membranes containing aldehyde lipids can open spontaneous pores [99, 100], compromising membrane integrity, and impacting the viability of cells. Contrary to the decrease of the diffusion coefficient observed for peroxidized lipid probably explained by the formation of a weak bond network at the interface, truncated lipid diffusion is found to increase, likely due to their lower molecular weight [96].

Interestingly, the presence of cholesterol has been shown to reduce hydroperoxidation impact on lipid membrane properties, and especially the permeability, by filling the void in between lipids [101–103]. Indeed, cholesterol is considered to have a conical shape, with a larger tail base, which combines well with the supposed conical shape of oxidized lipids with a larger head region.

#### 0.4.3 Photo-therapy

The damage of cell membrane with photo-oxidation is used to treat diseases and more specifically several cancer forms by photo-therapy which has been proven over the years to be an efficient treatment. It is based on the creation of ROS that can either damage the tumor cell or induce an immune response against it [104]. Nevertheless, irradiating viable cells surrounding can always cause non-deliberated oxidation and might generate strong side effects. Therefore, light irradiation combined with specific chemicals can efficiently target the tumor cells. As an example, one may use the composition asymmetry naturally present in cell membrane leaflets. The outer leaflet being mostly composed of neutral lipids, and the inner one with anionic lipids, photo-oxidation can be used to break this balance and expose anionic lipids such as phosphatidylserine (PS) in the outer leaflet. Drugs that specifically target PS in membrane surfaces can thus be locally delivered, increasing their efficiency [105]. A better understanding of how lipid hydroperoxidation impacts the lipid membrane properties is essential to develop new treatments or drug delivery systems designed to specifically target cells exhibiting specific dysfunctions (diseases). Improved knowledge could lead to the control of membrane permeability to deliver drugs directly inside the cell. In addition, oxidation being linked to disease and aging, research could help to elucidate oxidation pathways related to specific diseases and thus help to find protection methods.

## 0.5 Electroporation: promising treatment and analyzing tool

### 0.5.1 Introduction to electroporation and its applications

Different techniques have been developed to deliver drugs or genes close to or directly inside a cell, and among them, an important technique is *electroporation* (see Figure 18). Electroporation and derived techniques are easy, fast, localized, and non-intrusive medical treatments. It consists in temporally increasing the cell membrane permeability by inducing reversible hole opening thanks to the application of an electric pulse.

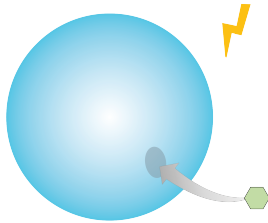


FIGURE 18: Scheme of a pore formed in a cell membrane caused by an electric field and in order to insert a molecule inside.

For medical treatment, short but strong pulses of a few microseconds and ranging from 10 kV/m up to 10 MV/m are used, the strength and length of the pulse depend on the application [106]. However, for too strong or too long electric stress, electroporation can irreversibly rupture the membrane and drive to the cell death. Even if the first sign of damage on biological cells caused by electric field dates back to the middle of the 18<sup>th</sup> century, it's only 30 years ago that electroporation started to be used for medical applications. Originally, electroporation was conceived for gene (part of DNA) transfer by permeating the cell membrane. Using the same principle, it was then also used to load diverse molecules such as drugs, antibodies, or even dyes. Thanks to its versatility, this process can be used for electrochemotherapy, DNA vaccination, inflammation treatment after organ transplantation, and many other treatments [107–110]. One of the main advantages of this modern process is that since the drug is locally delivered inside the cell, its efficiency is much stronger (+50 % efficient) [107] requiring a smaller amount of drug to treat the patient, thus reducing side effects. Apart from the remaining drug side effects, electroporation offers very little discomfort to the patient. Since it is performed under anesthesia, the pain is limited and only bruises or electrode traces may be left on the patient skin, disappearing in a few days [111].

### 0.5.2 Pore opening: the underlying mechanism

Under biological conditions, cells are subjected to an electric potential difference around 70-100 mV due to ion concentration differences across the membrane [9] but this permanent stress is not considered enough to open a large amount of conductive pores. Spontaneous pore opening is a thermally driven process and the energy barrier required can be reduced depending on external conditions (temperature, electric stress...) [112]. If enough energy is brought to the system, lipids can rearrange to stabilize a water channel inside the membrane, also called a transient pore as depicted in Figure 19.C. This water channel allows the exchange of molecules that would usually not be able to cross the hydrophobic core of the membrane.

Pore opening in lipid membranes is a dynamic mechanism which is difficult to observe and characterize with precision. As a consequence, the theory behind electroporation and especially pore opening is still under investigation and many questions remain unsolved despite all the research accomplished on the subject over the past decades. Several hypotheses have been given to describe pore opening mechanisms, but up to now, there is no universal way to determine with certainty the real

process steps. Below is described the main scenario reported in the literature, often referred to as "the standard model of pore formation".

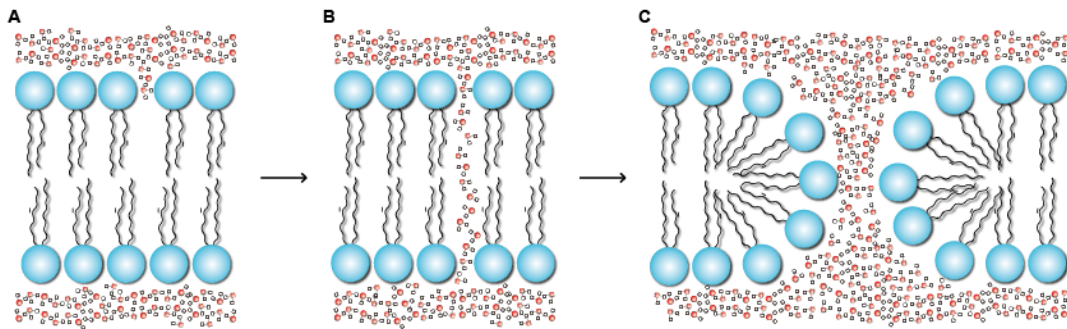


FIGURE 19: Scheme of the growth of a water defect in the membrane and lipid reorganization to form a pore. (A) Water defect starts to enter the membrane (B) grows until forming an entire hydrophobic pore (C) followed by lipid rearrangement to form a stable hydrophilic pore.

- The application of an electric field across a membrane triggers: 1) the polarization of the water molecules and lipid heads [33, 113] that induces molecular orientation (in the picosecond time scale) [114], and 2) accumulation of ions at the membrane interface, increasing the average compression force (electrostriction) and other less discussed effects such as localized electrostatic forces [115, 116]. The potential difference across the membrane leads thus to a thinning of the membrane and an increase in the area per lipid, which create favorable conditions for pore opening since the energy to open a pore is proportional to the membrane lateral compressibility and its thickness [33, 117]. In addition, the polarization and the lower lipid packing likely enhance water defect formation at the interface of the bilayer (Figure 19.A). Simulations show that the polarization is enough to nucleate water defects without any action of ions on the membrane [114]. Interestingly, the perpendicular polarization is found stronger on the anode side, favoring water defect protrusion from this side [113, 118]. This can be explained by the natural hydrogen bonds formed between water and lipids. In absence of an electric field, water molecules are slightly oriented with their hydrogens pointing towards the lipid membrane. When the electric field is turned on, the water molecules weakly bonded to the lipid bilayer in the anode side likely reorient due to the electric field polarization possibly creating some local instabilities.

- The second step of pore opening is the less energetically favorable one. It consists in the increasing presence of water molecules inside the hydrophobic core of the membrane forming a metastable, short-lifetime intermediate state often referred to as *hydrophobic* pore and whose conductive property is unclear. This state has never been observed and clearly characterized, but many theories suggest the requirement of an intermediate state before opening a complete, meta-stable pore [113, 119, 120]. Moreover, simulations showed evidence of water defects growing up to the formation of a full water bridge (also called water finger) connecting both sides of the membrane (Figure 19.B) [114, 121]. The formation of an unstable *hydrophobic* pore can either lead to pore closure or to a more meta-stable structure as explained below in the third step.

• After this intermediate is formed, the third step consists in the reorientation of lipids at the pore interface to minimize energy and stabilize the pore as observed in many simulations [114, 121, 122] and illustrated in Figure 19.C. Tens of lipid head groups, involved in pore opening, are tilting, dragging water molecules with them until forming the so-called *hydrophilic* pore. This gives birth to pores of a few angstroms radius, able either to close or grow up to a few nanometers. Ions and molecules that are usually unable to cross the lipid membrane by permeability can be transported through these lipidic pores, making the membrane briefly permeable. Despite the diversity of pore opening descriptions, all models consider the two types of pores: the *hydrophobic* and the *hydrophilic* pores. Some studies also suggest more complex intermediates with concomitant lipid reorientation and water penetration [113].

At any time during pore opening, lipid molecules can return to their initial conformation of impermeable membrane. After pore closure, it has been evidenced by simulations, that some lipid heads may remain trapped in the hydrophobic core for at least a few nanoseconds [122]. Depending on the time the lipids take to return to their equilibrium position at the interface with the water, these lipids could become part of the nucleation site of another pore. The presence of *pre-pores* that has often been hypothesized [119], can either come from defects induced during pore closing or from the intermediate state between water defect and *hydrophilic* pore. Apart from closing, a *hydrophilic* pore is also able to grow, up to a critical nucleation radius, beyond which, the membrane is believed to rupture.

Despite the scarce experimental evidence on the mechanisms for pore formation, growth, and closing, a commonly accepted phenomenological model has been developed first by Abidor et al. [112], and then widely spread in the literature [120, 123, 124]. This model states the existence of an underlying, one-dimensional energy landscape for pore formation, expressed as a function of the pore radius  $r$ . Such energy landscape  $\Delta E$  (J) considers two contributions. The first one account for the energy cost to create the rim region surrounding the pore, where lipids are in a different configuration from the flat bilayer. It is expressed as a function of the edge line tension  $\gamma$  (J/m) and the pore perimeter. The second expresses the reduction in interfacial energy resulting from the pore opening, and it is expressed as the product of the lateral tension  $\Gamma_0$  (J/m<sup>2</sup>) and the pore area as expressed in equation 9:

$$\Delta E(r) = 2\pi r\gamma - \pi r^2\Gamma_0 \quad (9)$$

the pore perimeter and area being both dependent on its radius  $r$  (m). Different variations of this model exist in the literature, one of them considers the additional stress of the applied electric field that will reduce the energy barrier for pore formation as observed in Figure 20 [124]. *Hydrophobic*  $\Delta E_o$  and *hydrophilic*  $\Delta E_i$  pore opening energy can be given by the equations 10:

$$\begin{aligned} \Delta E_o(r, U) &= 2\pi r d \Gamma_0 \frac{I_1\left(\frac{r}{\lambda_c}\right)}{I_0\left(\frac{r}{\lambda_c}\right)} - \frac{(\epsilon_w - \epsilon_m)\pi r^2}{2d} U^2 \\ \Delta E_i(r, U) &= 2\pi r \gamma(r) - \pi r^2 \Gamma_i - \frac{(\epsilon_w - \epsilon_m)\pi r^2}{2d} U^2 \end{aligned} \quad (10)$$

with:

$$\gamma(r) = \gamma \left( 1 + \frac{C_0}{r^5} \right) \quad (11)$$

where  $I_i(r/\lambda)$  is the modified Bessel function of order  $i$ ,  $\lambda_c$  the characteristic hydrophobic interaction length (m),  $\epsilon$  the permittivity of the electrolyte solution  $w$  and the membrane  $m$  (F/m) and  $C_0$  a constant determined to fit experimental data (m<sup>5</sup>) [125]. Typical values are presented in Table 1 and used to compute Figure 20.

TABLE 1: List of parameters used in equation 10 to compute Figure 20.

Parameter	Value	Reference
Bilayer thickness $d$ (m)	$5 \times 10^{-9}$	[3]
Buffer solution permittivity $\epsilon_w$ (F/m)	$6 \times 10^{-10}$	[126]
Membrane permittivity $\epsilon_m$ (F/m)	$1.86 \times 10^{-11}$	[10]
Hydrophobic surface tension $\Gamma_0$ (J/m <sup>2</sup> )	$5 \times 10^{-2}$	[120]
Hydrophilic surface tension $\Gamma_i$ (J/m <sup>2</sup> )	$1 \times 10^{-3}$	[127]
Edge tension $\gamma$ (J/m)	$2 \times 10^{-11}$	[128]
Characteristic length of hydrophobic interaction $\lambda_c$ (m)	$1 \times 10^{-9}$	[129]
Constant $C_0$ (m <sup>5</sup> )	$1.39 \times 10^{-46}$	[124]
Minimal hydrophilic radius $r_{min}$ (m)	$5 \times 10^{-10}$	[124]

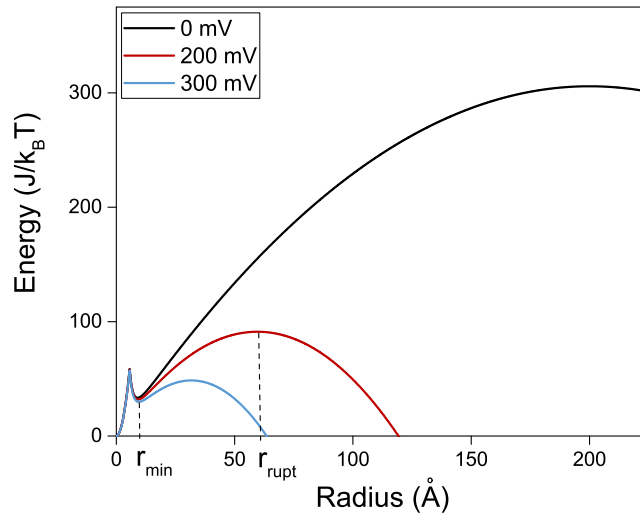


FIGURE 20: Energy landscape for pore formation  $\Delta E$  as a function of the pore opening radius  $r$  for different voltages.

Figure 20 represents the energy landscape underlying the opening of a pore of radius  $r$ . The first part of the curve, while the energy barrier is growing, is related to the formation of the *hydrophobic* intermediate pore. After reaching the barrier top, the pore can either close or stabilize as a *hydrophilic* pores with minimal size  $r_{min}$ . The meta-stable pore can then either close or grow up until inducing the membrane rupture if the critical radius  $r_{rupt}$  is overcome.

Even if this model is widely spread, it was poorly confronted with experimental data and thus never validated. In addition, parameters were fixed with averaged lipid values of edge tension and surface tension in order to fit at best the observations, but this model is not used to predict specific experiments with precisely

measured values. One should have in mind that bilayer thickness, surface tension, edge tension, and the constant  $C_0$  greatly impact the energy landscape obtained from equations 10.

### 0.5.3 Numerical simulations

Pore opening is a fast and small-scale process that cannot be directly observed and measured by microscopy and video recordings. To study pore formation, a combination of theoretical simulations and experiments is required.

Molecular dynamics simulations are a powerful tool able to analyze membrane dynamics at the molecular scale. From the simulation results it is possible to extract pore opening times, frequency, and size and to visualize pore opening steps as discussed before. However, results cannot be trusted blindly since simulation conditions cannot fully mimic real experiments and are limited in space and time [114]. The longest simulation typically lasts no more than a few microseconds, usually around several nanoseconds, and concerns only a few hundred lipids. In addition, the system is not closed, and realistic boundary conditions can be difficult to implement. Even if simulation allows to follow pore opening steps, it is still challenging to extract from simulation results a unique mechanism of water channel formation: how does water first permeate the membrane, what is the pre-pore state structure (if they exist), and are ions involved in the process? [107, 114]

### 0.5.4 Experiments

To complete and validate simulation results, experiments are essential to bring new perspectives. Since pores cannot be directly observed, electropermeability experiments have been established as the reference to indirectly measure pore opening. It usually consists of a setup with electrodes immersed in a saline solution and with either lipid bilayers, vesicles, or biological cells in between [130, 131]. Most of the time, one electrode measures the membrane potential while the other one delivers current to maintain the membrane potential constant (voltage-clamp mode) with a fast system response ( $\gg 1$  MHz). Despite being an indirect measurement and its intrinsic electronic limitations (compromise between the signal/noise ratio and the time and current intensity resolution), electroporation setups have proven to bring new insights into pore formation mechanisms such as pore lifetime, pore opening rates, pore conductivity, and even pore size calculation. Pore opening being a stochastic mechanism governed by statistical thermodynamics, electroporation requires a large set of measurements to provide for reliable average values of the different relevant quantities (pore size, pore life times, etc.)

### 0.5.5 Pore characteristics

Usually, pore radii are reported to be of a few angstroms or nanometers [33, 113, 119, 120, 132–134], implying that only a limited amount of water molecules can penetrate inside the pore. The pore size may depend on the lipid membrane thickness, the thicker is the bilayer, the smaller is the pore [122]

Pore dynamics is characterized by the opening time, the pore lifetime, and finally the closing time. From simulations, it is known that pore opening and closing are very fast processes happening in the nanosecond range [122, 135, 136], the intermediate state occurring even faster, in less than a nanosecond [113]. The opening time is

believed to depend on the lipid species since pore formation requires lipid displacement, for instance, DOPC can rearrange faster than POPC molecules [60, 122]. To our knowledge, no device has been developed, with a time resolution high enough to resolve pore opening or closing. Experiments, however, allow the measurement of the electric response of pores of long lifetime, contrary to simulations that are limited to small lifetimes. On the pore dynamic time scale, both experiments, and simulations are complementary.

### 0.5.6 Membrane properties and external conditions influence pore formation

During electroporation, voltage is reported to act on the lipid membrane phase behavior [116, 137] which is an important feature for experiments, since membrane fluidity is closely linked to membrane permeability. As stated previously in section 0.2, close to the phase transition permeability is increased probably due to phase coexistence, disorder, lateral expansion, and a thinner membrane [22, 33], all of these features also favoring pore nucleation [138–140].

As a consequence of temperature (set close to the  $T_m$  of the membrane), pores can also exhibit stable sizes for higher lifetimes giving conductivity quite similar to protein ionic channels [134, 141]. Other external conditions such as the pH, the presence of drugs or anesthetics, ion concentration, and other thermodynamic variables result also in the opening of stable pores during electroporation [22].

Concerning the relations between membrane properties and pore formation, one may strongly believe that the presence of oxidized lipids in a membrane can enhance pore formation under, or even without an applied electric field. Studies on the effect of lipid oxidation on membrane electroporability and pore formation are however scarce. Experimentally, a single study by Corvalan et al. [81] demonstrates a general increase in membrane conductivity with the increase in hydroperoxidized lipid amount up to 67 %. Numerically, Vernier et al. [142] and Yusupov et al. [143] simulations reveal how local hydroperoxidation slightly facilitates pore formation by decreasing the energy barrier and observe a decrease in the time required for pore opening.

One should note that lipid oxidation and temperature increase can be induced by electroporation and can be considered as an interesting feature to temporarily damage the membrane integrity during patient treatment [107]. However, in complex biological media, other essential molecules such as proteins or DNA may be sensitive to denaturation induced by the strong electric stress. Lipid oxidation is induced by electroporation, likely due to the creation of ROS [144, 145]. It is difficult to quantify, but Rems et al. [93] claimed lipid oxidation not to be significant.

## 0.6 Objectives

The lipid membrane is an essential part of living organism cells, acting as a barrier to prevent unnecessary molecule translocation and keep concentration and potential difference. The perturbation of the lipid membrane properties has a direct impact on its permeability, and so, extreme disturbance can lead to loss of cell integrity and even its death. The modification of the properties of the lipid membrane resulting from oxidation seems to point toward a membrane conductivity enhancement [81, 142, 143, 146]. A deeper analysis of oxidized lipid membrane properties and of the

molecule transportation mechanisms could provide interesting insights into the understanding of disease development linked to the unusual high amount of oxidized lipid.

So far, most published experiments studied only partially oxidized lipid membranes due to experimental limitations or a lack of control of the oxidation reactions. To overcome these issues, simulations have been a powerful tool used to better characterize such membranes, but they have been only scarcely compared to experiments. In addition, the state of the art reveals inconsistency in the hydroperoxidation impact on some of the bilayer properties. As an example, the visco-elastic property of oxidized membranes is not yet fully understood.

Regarding research on membrane conductivity, studies mainly focus on ion active transportation by proteins neglecting the passive membrane permeability but more importantly its ability to form pores, which can be as much conductive as protein channels. During our research, we realized that intensity current signals obtained by electroporation experiments are quite challenging to analyze, explaining the scarcity of experimental studies carefully characterizing pores, and the abundance of numerical simulations.

Our contribution to this field is facilitated by the methods that we developed for control and high yield production of hydroperoxidized phospholipids by photo-oxidation reaction. In the following work, we focus on the study of POPC which is a phospholipid commonly found in cell membranes and that possesses a unique unsaturation allowing single hydroperoxidation. We are also interested in SOPC (18:0,18:1) a lipid with a very similar structure to POPC (only two more carbons on the saturated chain). In Chapter 1, we first report the synthesis of their hydroperoxide forms as nearly pure POPC-OOH and SOPC-OOH.

With Chapter 2, we aim at bringing new insight into the membrane structural properties by measuring mono-unsaturated lipid membrane phase transition temperature and enthalpy when containing different amounts of hydroperoxidized lipid. To the extent of our knowledge, no experimental measurement of hydroperoxidized lipid membrane  $T_m$  has been done yet. We also provide cryo-TEM images of vesicles containing such lipids with a good monolayer resolution in the hope of revealing clues on the geometrical organization of lipids in the membrane and quantify with a rarely used method the decrease in bilayer thickness. Moreover, a collaboration with the team of M. Kuimova at the Imperial College of London is reported in Chapter 4 providing for complementary data on POPC-OOH membrane characterization. The understanding of hydroperoxidized lipid interaction and organization is a matter of interest that may for example resolve the discrepancy in visco-elastic behavior described in the literature.

Afterward, it is essential to characterize pure lipid membrane conductivity to get a full and precise picture of all mechanisms involved in ion transportation in such special membranes. In Chapter 3, after studying the intrinsic permeability of pure lipid membranes, we aim at detecting and characterizing pores using semi-automatized algorithms in order to improve general knowledge of pore opening mechanisms.

## Chapter 1

# Lipid hydroperoxidation: an efficient photo-reaction

Lipid hydroperoxidation is the first oxidation step, involved both in essential biological functions but also in less controlled mechanisms likely leading to disease development. Hydroperoxidation consists in the addition of a polar peroxide group on the targeted unsaturated lipids chain, impacting the properties of the lipid bilayer they compose. Such reactions have been intensely studied, even if the underlying chemical pathways are not determined with certainty yet. Researchers also started to analyze its effect on unsaturated lipid membrane properties (see Chapter 0) using mainly numerical simulations. The scarcity of experiments can be justified by the inaccessibility to hydroperoxidized lipids - or derivatives - due to the lack of a universal, controlled, and fast synthesis method to produce commercial pure hydroperoxidized lipids. Indeed, synthesis found in the literature usually lead to several sub-products requiring further lengthy purification, explaining why hydroperoxidized lipids are not commercialized yet.

In this chapter, an efficient and controlled photo-oxidation reaction to hydroperoxidized POPC (16:0,18:1) and SOPC (18:0,18:1), two mono-unsaturated lipids is described. The technique was originally devised by Y. Moskalenko with input from C. Marques and M. Baptista but did not include a convenient purification method. This Chapter aimed at revisiting the reaction method in order to improve the efficiency and purity of the obtained hydroperoxidized products.

Here, we first describe the optimized experimental technique used to produce hydroperoxidized POPC and SOPC. We then discuss the choice of the experimental conditions and characterize the reaction yield and purity. We finally study the stability of hydroperoxidized lipids under different storage conditions. Results reported in this chapter were essential to unlock the extensive study of membrane properties of pure hydroperoxidized lipids.

## 1.1 Materials & methods

### 1.1.1 Materials

1-palmitoyl-2-oleoyl-glycero-3-phosphocholine (POPC, 16:0-18:1) and 1-stearoyl-2-oleoyl-glycero-3-phosphocholine (SOPC, 18:0-18:1) are purchased in chloroform (25 mg/mL) from Avanti Polar Lipids. They are stored at -20 °C and used without further purification. Chloroform ( $\gg 99\%$ ) is provided by Sigma Aldrich. For NMR analysis, methanol-D<sub>4</sub> (CD<sub>3</sub>OD) with 99.8 % D, acetonitrile-D<sub>3</sub> (CD<sub>3</sub>CN) with 99 % D and chloroform-D (CDCl<sub>3</sub>) with 99.8 % D are purchased from Acros Organics. 1,9-dimethyl-methylene blue (MB) and dimethyl terephthalate (DMTP) with

a purity of 99,98 % are provided as powders from Sigma Aldrich. A 6 mM stock solution of MB in CD<sub>3</sub>OD and a 1.55 mM stock solution of DMTP in CDCl<sub>3</sub> are prepared. Illumination is performed in a homemade box chamber equipped with 48 red LEDs ( $\lambda=656$  nm, delivering 9 Watts each) corresponding to a light power density of 600 W.m<sup>-2</sup> provided by ILS (Intelligent LED Solutions). The illumination chamber is kept under constant ventilation to remove heat excess. Cellulose membrane dialysis tubings ( $\varnothing=0.5$  cm) with a molecular cut-off of 14000 Da are purchased from Sigma Aldrich.

### 1.1.2 Nuclear Magnetic Resonance

Nuclear magnetic resonance (NMR) spectra are recorded on an Avance 400 spectrometer (Bruker, Germany) at 298 K. Chemical shifts ( $\delta$ ) are referenced from residual methanol (3.31 ppm in <sup>1</sup>H NMR) when using methanol-D<sub>4</sub> and residual chloroform (7.26 ppm in <sup>1</sup>H NMR) when using chloroform-D. To perform Quantitative NMR (q-NMR) the sample is left for equilibrium for 5 to 6 min (for temperature and magnetic field equilibration). Parameters are set as follow: the pulse  $\alpha=90^\circ$ , D1=18 s (being 5 times the longest relaxation time T1=3.6 s), acquisition time = 4-5 s, number of scans 64, and dwell time= 62.4  $\mu$ s (dwell time: time between two acquisitions). All NMR spectra are analyzed using MestReNova software.

### 1.1.3 UV-Spectroscopy

UV-spectroscopy analyses are performed using quartz cuvettes and a Perkin-Elmer Lambda 25 spectrometer with a scan speed of 480 nm.min<sup>-1</sup> over 200 to 800 nm. A standard curve is made to relate MB concentration in chloroform to the solution absorbance at 640 nm using solutions of known concentrations of 5, 10, and 15  $\mu$ g/mL.

### 1.1.4 Lipid hydroperoxidation

The two hydroperoxidized isomers of POPC and SOPC (POPC-OOH and SOPC-OOH respectively) shown in Figure 1.1, are synthesized according to a photochemical reaction, using MB as a photosensitizer. In a test tube, 6 mL of 10 mM phospholipid and 50  $\mu$ M MB solution in CD<sub>3</sub>OD is prepared using previously dried phospholipids and the MB stock solution. Before illumination, quick control of the lipid quality is made by NMR. The solution is then exposed to red light illumination ( $\lambda=656$  nm,  $P=600$  W.m<sup>-2</sup>) under constant oxygen flow and magnetic stirring to reach the full conversion in less than 10 min. The conversion rate can be followed by NMR. Figure 1.2 schematizes the synthesis step.

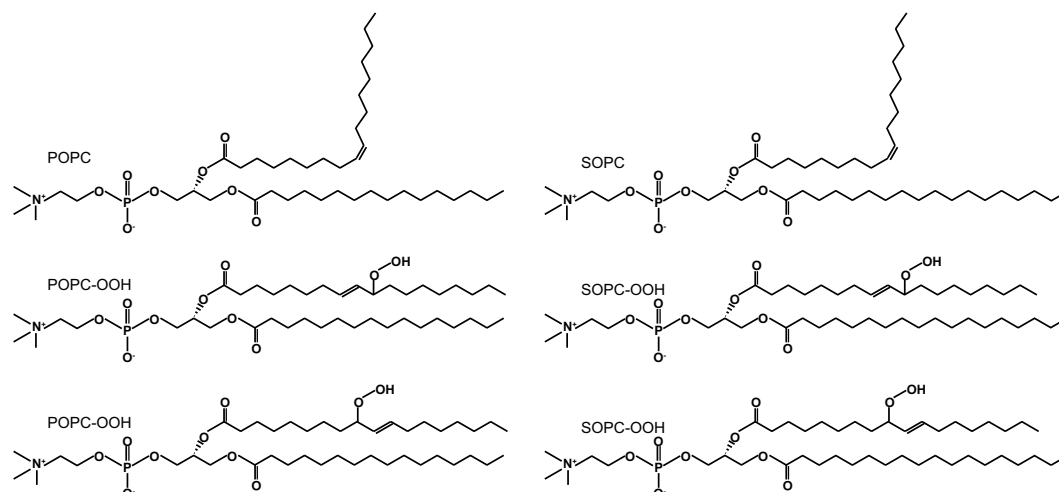


FIGURE 1.1: Chemical formula of POPC and SOPC with their two respective hydroperoxidized isomers.

The same reaction is done by replacing the  $\text{CD}_3\text{OD}$  solvent with mixtures of  $\text{CD}_3\text{CN}/\text{CD}_3\text{OD}$ . The reaction kinetics is monitored by NMR for each solvent. At different time intervals, illumination is stopped and a sample from the solution is taken for NMR analysis to determine the conversion rate.

### 1.1.5 Purification

Only a low quantity of MB photosensitizer is required for the reaction (200 molar times less than phospholipids), and should not perturb further use. However, as a precaution, MB is removed by dialysis. 1 mL of the hydroperoxidized lipid with MB is evaporated and then redispersed in 2 mL of Milli-Q water (to reach a concentration close to 2.5 mg/mL). The obtained solution is placed inside a dialysis tubing of 15 cm length previously washed. The dialysis is performed against 800 mL of Milli-Q water and under stirring at ambient temperatures for 3 h. The obtained lipid in water solution is dried using a rotary evaporator and lipids are redispersed in  $\text{CD}_3\text{OD}$  to perform an NMR control. Hydroperoxidized lipids solutions are kept in  $\text{CD}_3\text{OD}$  at  $-20^\circ\text{C}$  until further use. Lipids can be quantified by the Stewart method [147] using UV-spectroscopy, but in most of the following work, dried lipid quantity is weighted on a precision scale (Mettler Toledo AX205).

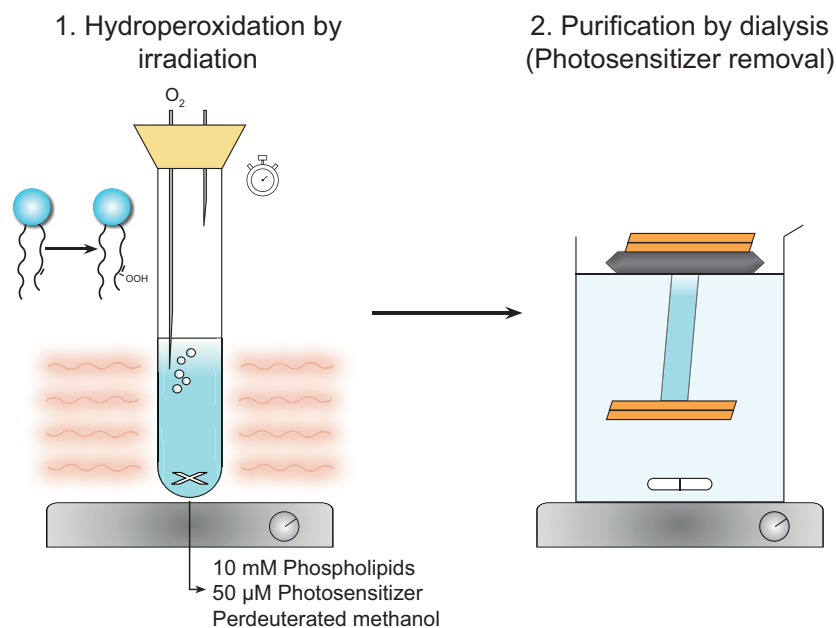


FIGURE 1.2: Sketch of photo-induced lipid hydroperoxidation and purification. After a single reaction step (step 1) the photosensitizer can be easily removed by dialysis (step 2).

A kinetic follow-up using UV-spectroscopy is made to quantify the MB concentration remaining in the hydroperoxidized lipid solution over the dialysis time. Dialyses from the same hydroperoxidized lipid sample are carried out over different duration. The solutions are then dried and redissolved in chloroform for UV-spectroscopy analysis to assess MB concentration. During the dialysis, the whole beaker is protected from light with aluminum foil to prevent photosensitizer activation and photobleaching.

Several purification techniques by chromatography were also tested offering a too long and complex separation method. We used steric exclusion chromatography on polystyrene/divinylbenzene organic column with chloroform, silica column separation using diverse solvents and solvent mixtures first selected with thin layer chromatography, solid phase extraction using PK30 DSC-18 6 mL tubes (Sigma Aldrich) in water/methanol mixtures, and a 500  $\mu$ L centrifugal filters (10K, VWR).

### 1.1.6 Stability

The stability of non-purified POPC-OOH in deuterated chloroform and as a dried film, both stored in a freezer at  $-20\text{ }^{\circ}\text{C}$  is checked by quantitative NMR using DMTP as a standard reference. DMTP is used as a reference to evaluate POPC-OOH NMR integrals evolution. Immediately upon hydroperoxidation, a precisely weighted dried sample of POPC-OOH (around 30 mg) is dissolved in 0.3 mg/mL DMTP in  $\text{CDCl}_3$  stock solution to obtain a molar ratio between POPC-OOH and DMTP of  $\sim 4$ . Typically, we obtain a solution of 6 mM of POPC-OOH and 1.5 mM of DMTP in  $\text{CDCl}_3$ . A 500  $\mu$ L sub-sample is taken for immediate NMR and is conserved at  $-20\text{ }^{\circ}\text{C}$  until further NMR ( $\text{L-CDCl}_3\text{-D}_x$ ). In 6 glass vials of 4 mL, 500  $\mu$ L of the mother solution are dried and kept at  $-20\text{ }^{\circ}\text{C}$  ( $\text{L-Dry}_i\text{-D}_x$ ). Samples are named using  $i$  the number associated with each vial and  $x$  the age of the sample in days.

At different time intervals (first, every day, and then more spaced in time), NMR spectra of L-CDCl<sub>3</sub>-D<sub>x</sub> and one of the L-Dry<sub>i</sub>-D<sub>x</sub> are recorded. The sample L-CDCl<sub>3</sub>-D<sub>x</sub> is analyzed with q-NMR protocol without additional process and stored back at -20 °C as soon as possible to reduce the exposition time outside of the freezer. One chosen L-Dry<sub>i</sub>-D<sub>x</sub> per day is first dissolved in 500 μL CDCl<sub>3</sub>, analyzed by q-NMR protocol, dried from 30 min to 1 h, and stored back in the freezer. The stability of POPC-OOH is also checked on a purified sample conserved in CD<sub>3</sub>OD at -20 °C for 3 months, using standard NMR without DMTP.

### 1.1.7 Mixture of hydroperoxydized and non-hydroperoxidized lipids

In the following chapters, we study the impact of hydroperoxidation on the properties of lipid bilayers. To carry out such analysis, intermediate hydroperoxidation degrees are obtained by mixing POPC (or SOPC) and POPC-OOH (or SOPC-OOH) lipids in CD<sub>3</sub>OD in a precise ratio. The exact hydroperoxidation fraction of the lipids mixture is checked by <sup>1</sup>H NMR, always within ± 5 mol % of the target value.

## 1.2 Results & discussion

Hydroperoxidation reactions carried out using the protocol detailed just above offer a fast and easy procedure to obtain pure hydroperoxidized lipids. The technique works for both POPC and SOPC mono-unsaturated lipids and can be easily extended to other polyunsaturated lipids consisting of different head groups and carbon chain structures such as POPG, DOPC, 18:1 Cardiolipin, and probably many more (unpublished results). The total final weight yield of hydroperoxidized lipid after purification is about 80 weight %, compared to low yield for usual techniques requiring lengthy purification [58]. We are able to considerably reduce both oxidation reaction and purification time by using controlled conditions to avoid the creation of side products.

Lipid structures before and after hydroperoxidation are checked by NMR. Figures 1.3 to 1.6 show NMR spectra of POPC, SOPC, and their hydroperoxidized products with detailed peak attribution corresponding to their chemical structures. Apart from water, chloroform, and methanol, which presence is to be expected, recurrent unexpected solvent traces have been observed in both POPC and SOPC commercial samples. From NMR spectra, ethanol (3.6 ppm and 1.2 ppm) and isopropanol (3.9 ppm and 1.2 ppm) are identified as being already present in SOPC commercial sample, while POPC only contains ethanol traces (shown in POPC NMR spectrum in Figure 1.3). These impurities can be removed by longer solvent evaporation time as seen in Figure 1.4.

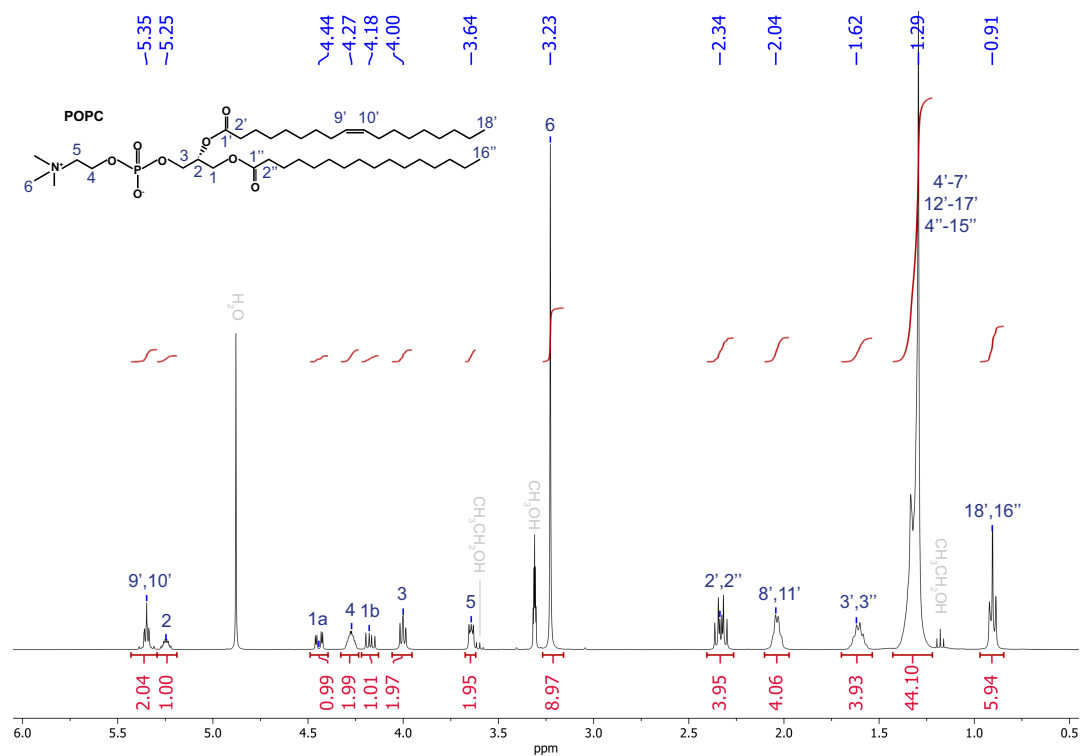


FIGURE 1.3: POPC  $^1\text{H}$  NMR spectrum in  $\text{CD}_3\text{OD}$  with peak attribution related to the molecule. The commercial lipids are dried and redissolved in  $\text{CD}_3\text{OD}$ .

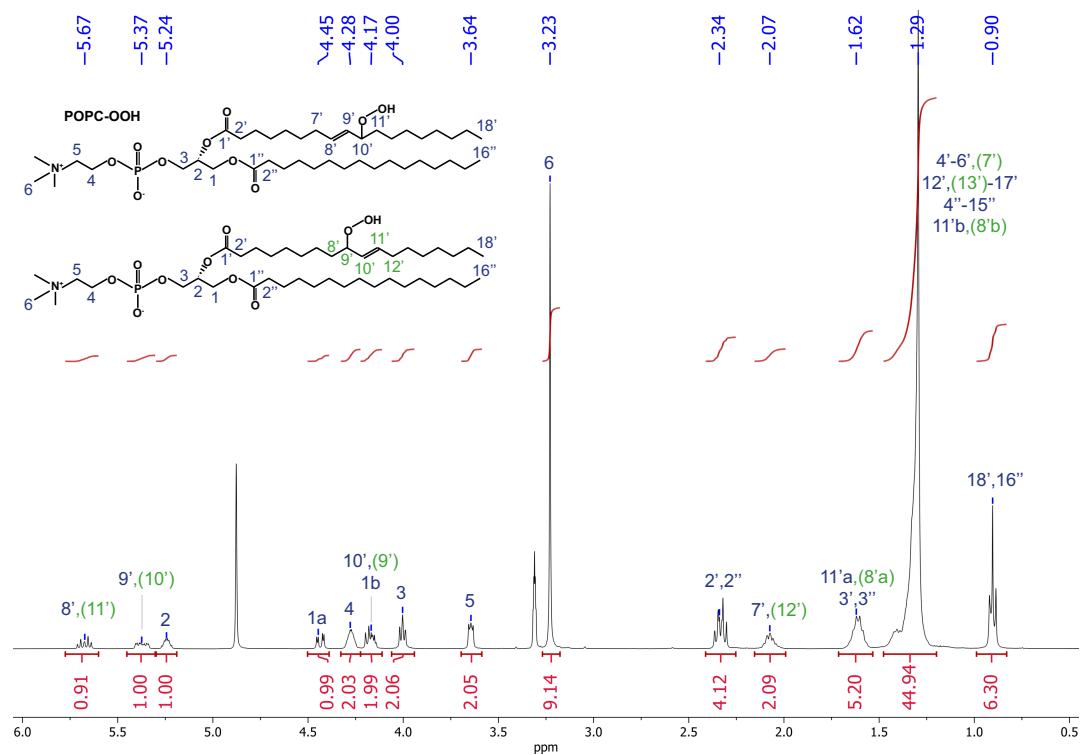


FIGURE 1.4: POPC-OOH isomers  $^1\text{H}$  NMR spectrum in  $\text{CD}_3\text{OD}$  after dialysis with peak attribution related to the molecules. The dialyzed hydroperoxidized lipids are dried and redissolved in  $\text{CD}_3\text{OD}$ .

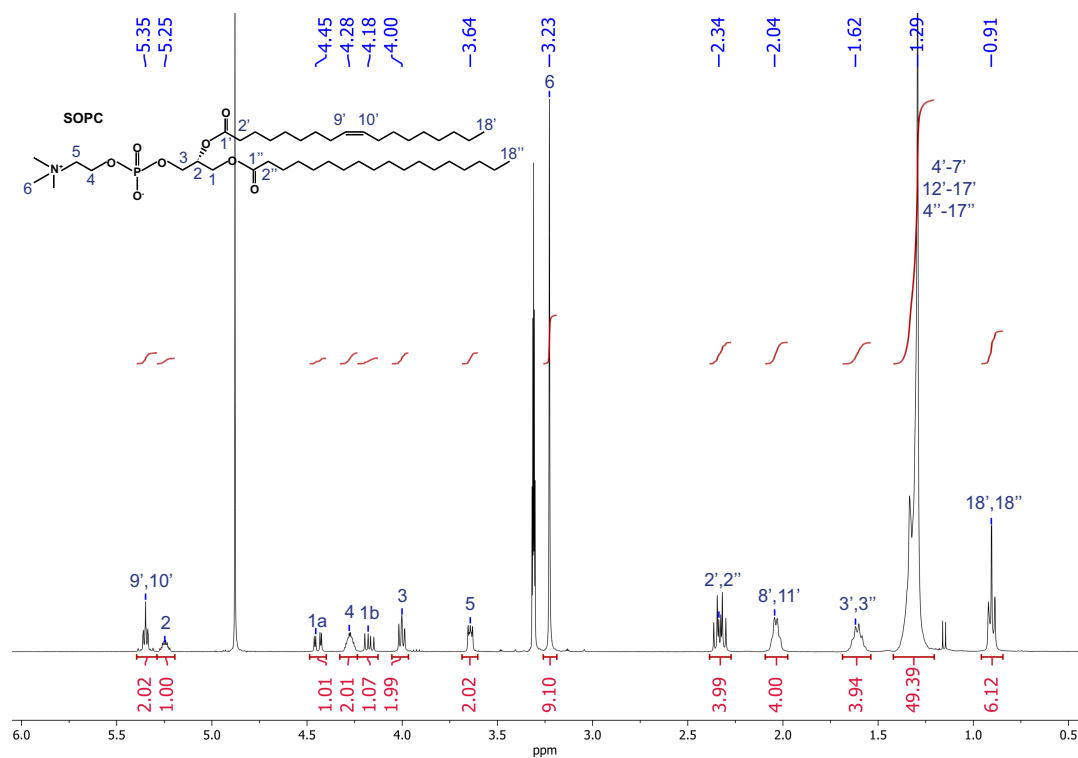


FIGURE 1.5: SOPC  $^1\text{H}$  NMR spectrum in  $\text{CD}_3\text{OD}$  with peak attribution related to the molecule. The commercial lipids are dried and redissolved in  $\text{CD}_3\text{OD}$ .

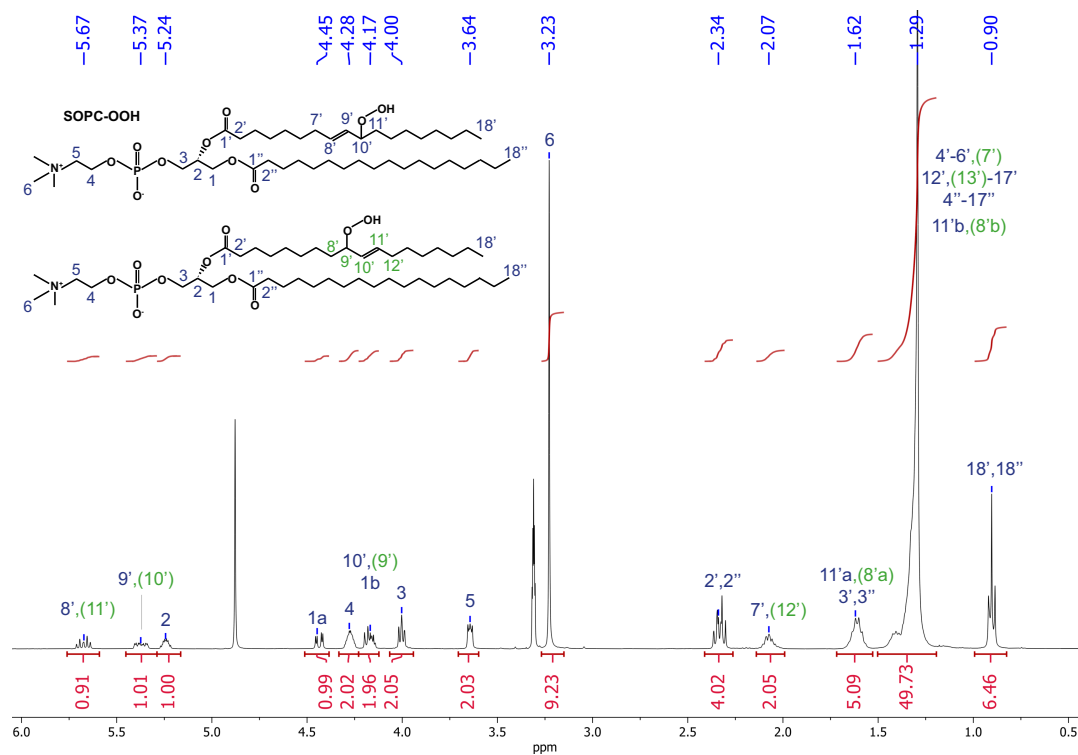


FIGURE 1.6: SOPC-OOH isomers  $^1\text{H}$  NMR spectrum in  $\text{CD}_3\text{OD}$  with peak attribution related to the molecules. The freshly hydroperoxidized lipids are directly analyzed by NMR.

Integrals are normalized by the 5.25 ppm peak corresponding to 1 hydrogen (H) at position 2 indicated on each molecule represented on the NMR spectra above. The hydroperoxidation conversion can be followed by NMR by measuring peak integrals at 5.67 ppm and 5.36 ppm which correspond to the carbons involved in the lipid unsaturation. For a non-oxidized lipid, both unsaturated carbons are equivalent and contribute to the peak at 5.35 ppm for an integral of 2 H. After full conversion, due to the peroxide group addition on one of these two carbons, the chemical displacement of one of the carbons is shifted to higher ppm (5.67 ppm) for integration of 1 H. By measuring the ratio between the 5.67 ppm peak integral and the 5.36 ppm one, it is possible to calculate the hydroperoxidation conversion. Sometimes the sum of both peaks is not precisely equal to 2 as it should be. This could be explained by lipid sub-products formation. Indeed, after hydroperoxidation, peaks at ppm different from the one expected from the lipid molecule can be observed. From their integral, they are usually estimated under less than 1 mol %. NMR spectrum integrals from commercial phospholipid samples are found to vary slightly from one sample to another, leading to what we believe different achievable hydroperoxidation maximal conversion rates. Similar purity variations have been reported in the literature [148, 149]. The typical conversion rate is about  $97 \pm 3$  mol %.

### 1.2.1 Hydroperoxidation reaction optimization

To obtain a high conversion rate in a limited time, experimental conditions are optimized. Here, we use the type II oxidation reaction, meaning the photosensitizer is first reaching its triplet state to transfer its energy to one neighboring dioxygen molecule that will itself react with one of the two carbons of a lipid unsaturation. The reaction speed can then be properly controlled, by acting on illumination power density  $P$  ( $\text{W}\cdot\text{m}^{-2}$ ) and wavelength  $\lambda$  (m), the solvent  $S$ , the photosensitizer  $PS$  (not to be confused with the Phosphatidylserine also abbreviated  $PS$ ) and its concentration  $[PS]$  according to the following equation:

$$[{}^1\text{O}_2] = \tau_{\text{O}_2} Q [PS] \quad (1.1)$$

with  $Q$  the rate of production of  ${}^1\text{O}_2$  from the given photosensitizer under prescribed illumination conditions ( $\text{s}^{-1}$ ), and  $\tau_{\text{O}_2}$  the lifetime of  ${}^1\text{O}_2$  in the chosen solvent (s).  $Q$ , the production rate of  ${}^1\text{O}_2$  can be developed as follows:

$$Q = \varphi H P \lambda (hc)^{-1} \quad (1.2)$$

with  $\varphi$  the dimensionless quantum yield for  ${}^1\text{O}_2$  production from the  $PS$  triplet state,  $H$  the photosensitizer cross-section for light absorption at  $\lambda$  ( $H = 0.0014 \text{ nm}^2$ ),  $P$  the light power density ( $\text{W}\cdot\text{m}^{-2}$ ),  $\lambda$  the light illumination wavelength (656 nm),  $h$  the Planck constant ( $\text{J}\cdot\text{s}$ ) and  $c$  the speed of light ( $\text{m}\cdot\text{s}^{-1}$ ). Since singlet dioxygen is produced from the photosensitizer triplet state, the higher the photosensitizer concentration is, the faster the reaction will be. In addition, a wavelength chosen close to the maximum absorption of the photosensitizer must be used to induce efficient light absorption. The MB maximum absorption in  $\text{CD}_3\text{OD}$  being around 653 nm, the light wavelength is chosen at 656 nm. Moreover, high light power density is used ( $P = 600 \text{ W}\cdot\text{m}^{-2}$ ) to speed up the reaction. The quantum yield,  $\varphi$  is 0.5 [150]. The production rate of  ${}^1\text{O}_2$  takes here the value  $Q = 1.39 \text{ s}^{-1}$ . Finally, the solvent should offer a high singlet oxygen lifetime  $\tau_{\text{O}_2}$  [151]. Values of interest are reported in Table 1.1.

TABLE 1.1: Singlet dioxygen lifetime in different solvent taken from Ross Table [151].

Solvent	$^1\text{O}_2$ lifetime ( $\mu\text{s}$ )	Comments
Methanol	9.5	-
Methanol-D <sub>4</sub>	230	
Acetonitrile	77	Lipid not soluble
Acetonitrile-D <sub>3</sub>	440	
Chloroform	230	Secondary product during oxidation
Chloroform-D	7000	

The solvent choice is also a crucial parameter. As the most abundant molecule in the reaction media, the solvent should be inert (not oxidable nor reactive to other molecules) to avoid secondary reactions and should possess a high  $^1\text{O}_2$  lifetime. Usual solvents such as ethanol and methanol have unfortunately quite a low singlet oxygen lifetime. Other solvents such as chloroform (commonly used to dissolve lipids) and acetonitrile possess both a high singlet dioxygen lifetime. However, oxidation in chloroform leads to secondary products, while pure acetonitrile cannot solubilize lipids. As an alternative, methanol which is also a commonly used solvent for lipids is a good choice, offering an acceptable singlet oxygen lifetime and no side product. Mixtures of methanol and acetonitrile are also a fine option. From Table 1.1 [151], deuterated solvents seem to be an upstanding choice since they offer increased  $^1\text{O}_2$  lifetime and direct NMR. In this study we mostly used  $\text{CD}_3\text{OD}$ . Finally, to design a fast reaction, the photosensitizer concentration should be as high as possible. However, one of the objectives here is to prevent side product formation to facilitate purification. Using too high amount of photosensitizer can lead to secondary reactions with itself, lipids, or solvent [92] as exhibited in Figure 1.7. Too high MB concentration would anyway lead to its aggregation in the solvent. A compromise should then be taken between getting a fast reaction and avoiding the formation of side products.

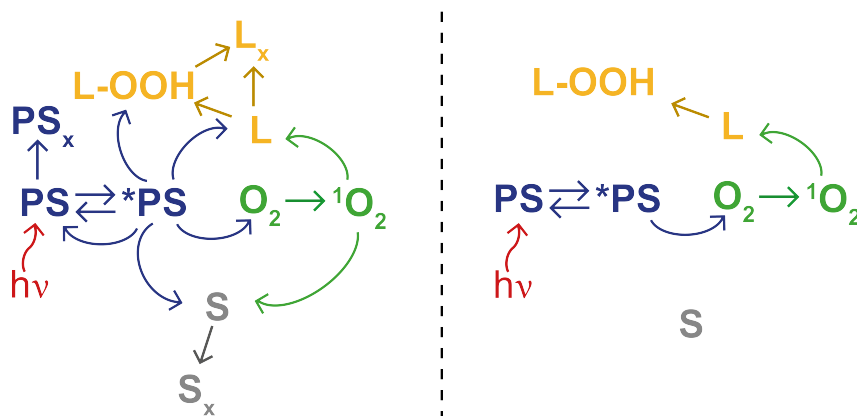


FIGURE 1.7: Typical chemical reaction pathway between compounds involved during lipid (L) photo-oxidation.  $h\nu$  represents the light absorbed by the photosensitizer (PS) to go into its excited state ( $^*PS$ ). In case of uncontrolled reaction (panel left), PS can react with many compounds to induce secondary reactions and many unwanted sub-products ( $PS_x$ ,  $S_x$ ,  $L_x$ ). If both reactants and solvent (S) are carefully chosen and introduced in proper quantities, secondary reactions can be avoided or minimized to obtain hydroperoxidized lipid (L-OOH) with good purity (panel right). Curved arrows represent chemical reactions between the two compounds while straight arrows point to the product obtained.

Under the chosen conditions, using  $CD_3OD$  ( $\tau_{O_2} = 230 \mu s$ ), and  $[MB] = 50 \mu M$  with the previously calculated conversion rate  $Q = 1.39 s^{-1}$ , we obtain an optimized  $^1O_2$  concentration of  $[^1O_2] = 10 nM$  allowing a full conversion of POPC and SOPC into their hydroperoxidized form within a few minutes by avoiding sub-product formation, as confirmed by NMR.

To achieve better reaction time and pushing optimization conditions, inert solvents with a higher singlet oxygen lifetime can be used. For this purpose,  $CD_3CN$  is a good choice offering no side product. However, as stated previously lipids are not soluble in pure  $CD_3CN$  and required a small amount of  $CD_3OD$  to help solubilization. Reaction kinetics are shown in Figure 1.8, comparing mono-unsaturated lipid hydroperoxidation under same experimental conditions, using only different  $CD_3OD/CD_3CN$  volume ratio. When increasing  $CD_3CN$  volume, singlet oxygen lifetime is increased, and reaction time for full conversion is decreased under these conditions from  $\sim 8$  min for a mixture containing 0 % of  $CD_3CN$  to  $\sim 3$  min for 95 %  $CD_3CN$ .

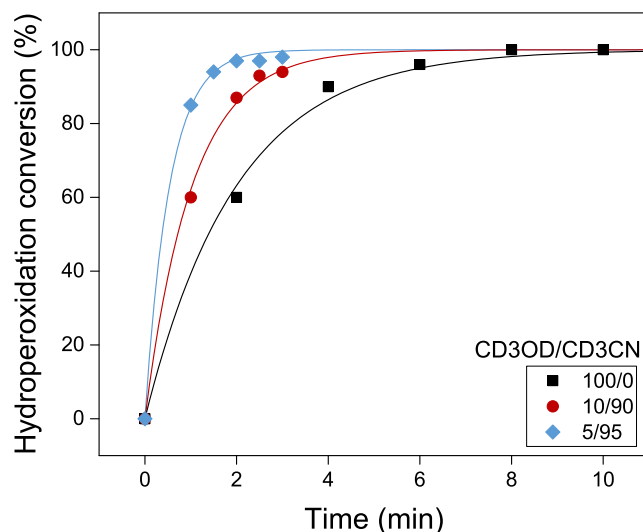


FIGURE 1.8: Hydroperoxidation kinetics using decreasing  $\text{CD}_3\text{OD}/\text{CD}_3\text{CN}$  volume ratios. Hydroperoxidation in pure  $\text{CD}_3\text{OD}$  is made on SOPC while hydroperoxidation in the solvent mixture is done on POPC. Hydroperoxidation percentages are extracted from NMR spectra. Solid lines represent exponential fits.

## 1.2.2 Hydroperoxidized lipid purification

Since no significant side products are detected on NMR spectra, only MB is removed. An easy way of proceeding is to use dialysis in water since MB is a small molecule (416 g/mol) while lipids naturally assemble into bigger objects as GUVs. By using this technique several times, we discovered that cellulose bags absorb MB molecules instead of letting them diffuse across. The quantity of MB removed from the lipidic solution is then proportional to the dialysis bag surface area. This might be explained by the polyphenolic groups in cellulose, that might be able to interact with MB [152]. In the perspective of reducing preparation time, but also minimizing the time lipids are spending out of the freezer, the smallest time required for efficient dialysis is determined by following the decrease of MB concentration in the lipidic solution by UV-spectroscopy over the dialysis time as shown in Figure 1.9. The purification of MB follows an exponential decay with a time constant of roughly 50 min. Using dialysis tubing of 0.5 cm diameters and 15 cm length to purify a lipid-MB solution of respectively 5 mM and 25  $\mu\text{M}$  in 2 mL water,  $\sim 3$  h are required to remove 92 mol % of MB.

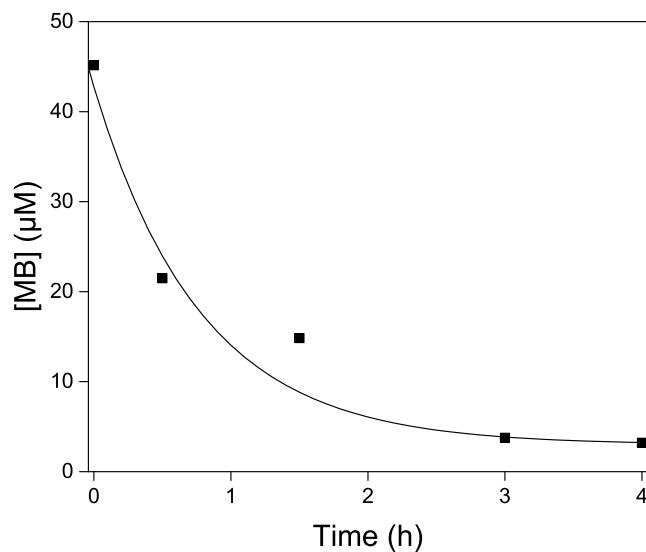


FIGURE 1.9: MB concentration over dialysis time determined by UV-spectroscopy. Full squares are experimental data and the solid line is an exponential fit.

One must keep in mind that a small fraction of MB is photobleached during hydroperoxidation (explaining the value of  $45 \mu\text{M}$  of MB before dialysis). Photobleaching during photo-oxidation is thus quantified to be around 10 mol %, we consider that no further photobleaching occurs during dialysis thanks to the use of aluminum foil. The residual MB concentration after purification is estimated at around  $4 \mu\text{M}$ . Further dialysis on a longer time and higher tubing surface can be designed to reach higher MB removal. NMR analysis in  $\text{CD}_3\text{OD}$  after dialysis is made to verify that purification does not cause any lipid degradation. As seen on the NMR spectrum of the POPC-OOH after dialysis in Figure 1.4, no sub-product can be observed.

### 1.2.3 POPC-OOH stability

Oxidation is the most common degradation process that lipids can suffer from. It can lead to different chemical structures such as the shortened tail phospholipids [65]. In this project hydroperoxidized lipids are studied, thus requiring all secondary oxidation reactions to be avoided. During hydroperoxidation, we show that no significant sub-product is formed, however hydroperoxidized lipid stability over time should be studied and minimized. As an example, one may wonder if hydroperoxidized lipids should be conserved under the same condition as non-oxidized lipids.

Usually, molecules such as antioxidants can be added to prevent lipid oxidation or at least reduce it. If one wants to keep a product as pure as possible and still reduce unwanted oxidation, dioxygen and water should be avoided and lipids should be stored in an organic solvent at low temperature and in absence of light [65]. Dry unsaturated lipids absorb water leading to their hydrolysis. Lyophilization and freeze-thaw cycles have also been reported to degrade lipids. Avanti Polar Lipids, for instance, advises storing lipids in a sealed glass container at  $-20^\circ\text{C}$  in an organic solvent under an inert atmosphere. Studies showed that the lowest temperatures can help lipid storage, however, lower temperatures than  $-20^\circ\text{C}$  are not appropriate when organic solvents are used.

For hydroperoxidized lipid stability, it is often reported that transition metals such as iron or copper should be avoided, else producing unwanted shortened tail

lipids.

In the following, we assess the stability of POPC-OOH over time when stored in different conditions: in  $\text{CDCl}_3$ , in  $\text{CD}_3\text{OD}$ , and as a dry film all at  $-20^\circ\text{C}$  as explained in detail in the materials and methods section (1.1.6).

To perform quantitative NMR (q-NMR) [153], DMTP is chosen as a standard reference for its non-volatility (boiling point at  $288^\circ\text{C}$ ), its non-reactivity to  $\text{CDCl}_3$  [154] and its NMR peak at 8.11 ppm in  $\text{CDCl}_3$  [155] counting for 4 hydrogens (H), that is not overlapping with POPC-OOH NMR signal. We chose to work in  $\text{CDCl}_3$  since DMTP is suspected to react with  $\text{CD}_3\text{OD}$  [154] and being the solvent recommended by Avanti Polar Lipid. We also verify that DMTP is not reacting with POPC-OOH and that the chosen ratio is giving a good enough signal. The typical spectrum of POPC-OOH/DMTP in chloroform is shown in Figure 1.10 corresponding to the Day 0 sample. The targeted molar ratio between DMTP and POPC-OOH of  $\sim 4$  is a good choice to obtain a similar integral between 1H of the POPC-OOH and 4H of the DMTP (with ratio  $\sim 1$ ).

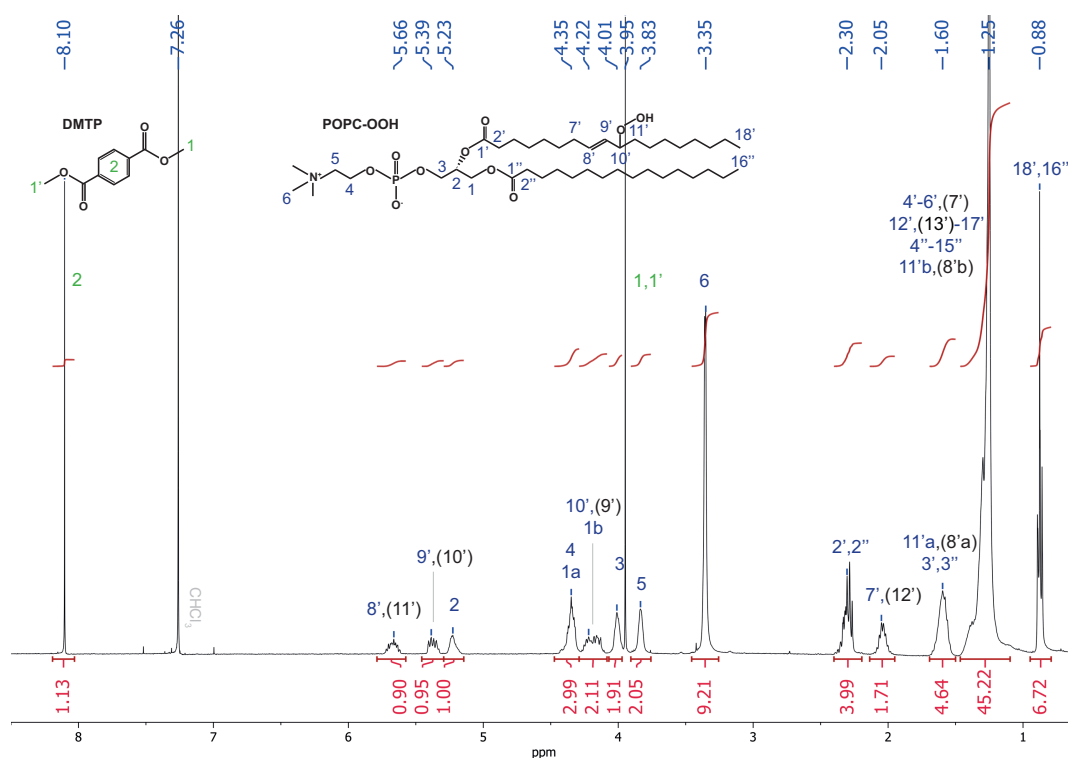


FIGURE 1.10: POPC-OOH isomers with DMTP  $^1\text{H}$  q-NMR spectrum in  $\text{CDCl}_3$  with peak attribution related to the corresponding molecules. Blue and black attribution correspond to each POPC-OOH isomers (only one is represented), and green attribution is for DMTP.

For the dried samples, we analyzed by q-NMR a first sample named L-Dry<sub>1</sub> over three days. Small peaks around 9.7 ppm, 6.7 ppm, 6 ppm, 2.45 ppm, 2.14 ppm, and 0 ppm arise over the age of the sample as observed in Figure 1.11. Their integrals are determined around 0.01, 0.02, 0.10, 0.14, 0.09 and 0.06 respectively for the L-Dry<sub>1</sub>-D<sub>3</sub>. A strong peaks shift in ppm is observed in the 4.5-2.5 ppm range, and a smaller one is visible on other peaks.

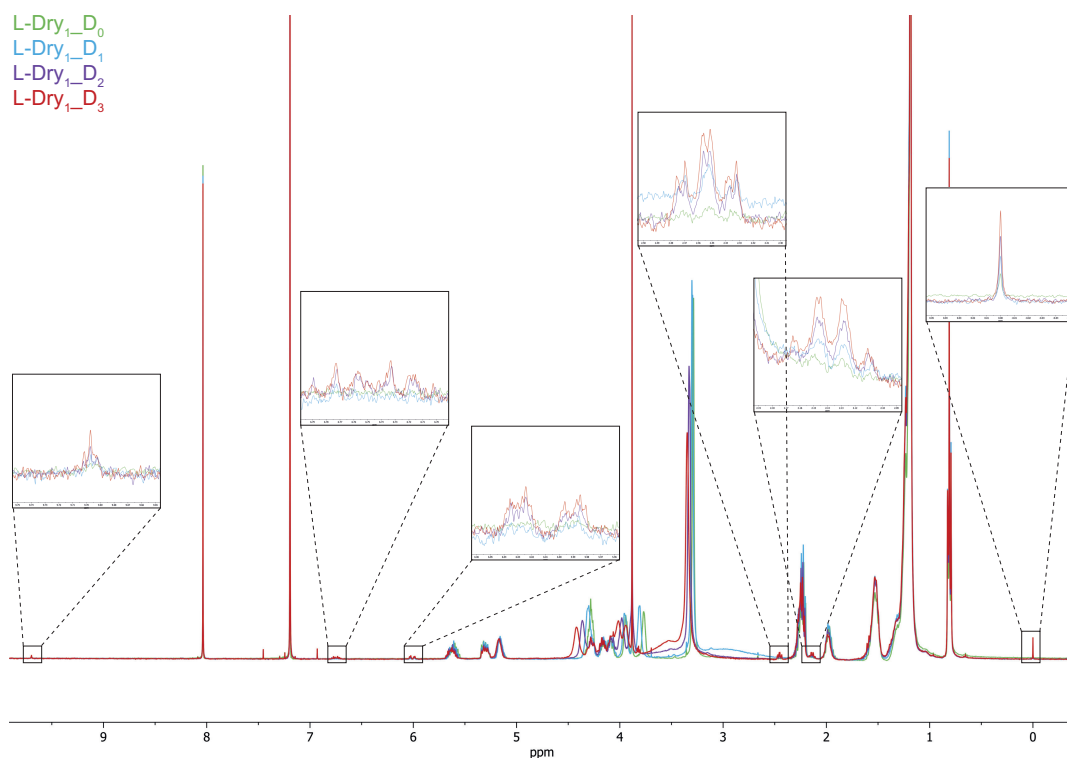


FIGURE 1.11: L-Dry<sub>1</sub> <sup>1</sup>H q-NMR spectra in CDCl<sub>3</sub> recorded at different time (0, 1, 2, 3 days). In black boxes are shown zoom of the impurities growing over drying-redissolving cycles. A shift of typical POPC-OOH peaks is also observed around 2.5-4.5 ppm.

The ratio of peaks corresponding to position 8'(or 11') (5.7 ppm) and 9'(or 10') (5.4 ppm) compared to position 2 of POPC-OOH (5.2 ppm) decreases drastically in a very short amount of time as shown by 5.7 ppm integral decrease of the L-Dry<sub>1</sub> sample in Figure 1.12. All pointing to fast degradation of POPC-OOH and formation of sub-products.

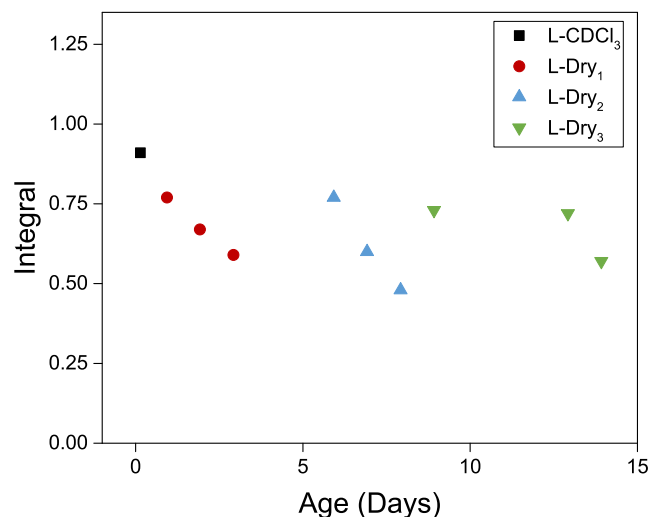


FIGURE 1.12: Integral of 5.7 ppm NMR peaks corresponding to position 8'(11') in POPC-OOH obtained by  $^1\text{H}$  q-NMR of different L-Dry<sub>*i*</sub> samples of different ages. Integrals are normalized with the POPC-OOH position 2 peak integral. Between each data point of the same sample, a drying-redissolving is done.

Surprised by this massive degradation in only a few days, we then decided to study other dried samples, L-Dry<sub>2</sub> and L-Dry<sub>3</sub> as presented in Figure 1.12. The first NMR spectra obtained for both samples are representative of samples not as much deteriorated as the last L-Dry<sub>1</sub> analyzed. The observed fast degradation is thus coming from drying-redissolving cycles and not from storage as exhibited by the different samples in Figure 1.12. We then decided to record one  $^1\text{H}$  q-NMR spectra on each L-Dry<sub>*i*</sub> sample with a longer time gap.

The Figures 1.13.A and B show the evolution of specific peak integrals (always normalized by the integral of the position 2 in POPC-OOH peak) over a month of dried and in CDCl<sub>3</sub> POPC-OOH.

In Figure 1.13.A, one should take into account that the first point corresponds to the freshly hydroperoxydized sample dried only one time after hydroperoxidation (to change solvent), while each other data points correspond to a different daughter sample L-Dry<sub>*i*</sub>, which has been dried only one more time before storage. The ratio between the DMTP peak integral (at position 2, 8.1 ppm) and POPC-OOH head peak integral (at position 2, 5.2 ppm) stays constant in both storages. However both POPC-OOH integrals at 5.7 ppm and 5.4 ppm decrease over time. A difference in slope can be observed in Figure 1.13.B when carefully looking at data separated by day, week, or month time gap. It seems that both 5.4 ppm and 5.7 ppm integrals always lose  $\sim 0.01$  in between q-NMR analyses regardless of the age of the sample. One may suspect that time spent by the sample out of the freezer can be responsible for all observed degradation. We then conclude that POPC-OOH storage as a dried film in a freezer does degrade the lipids over time, while it is likely that storage in CDCl<sub>3</sub> does not degrade them. It raises the question if drying-redissolving cycles are really the cause of lipid degradation, or if it is only due to the extensive time spent out of the freezer.

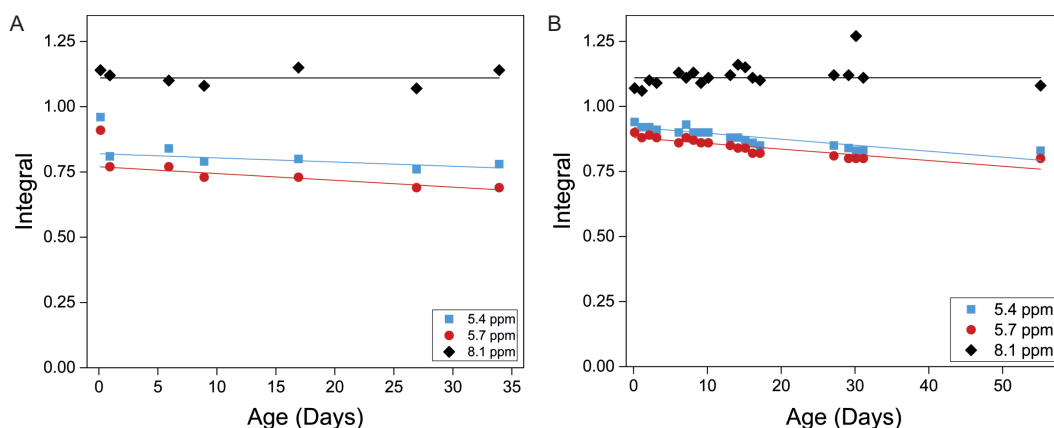


FIGURE 1.13: Integral of NMR peaks corresponding to a different position in POPC-OOH and in DMTP obtained by  $^1\text{H}$  q-NMR of (A) different L-Dry<sub>i</sub> samples and (B) L-CDCl<sub>3</sub> sample over time. Integrals are normalized by the POPC-OOH position 2 peak integral.

For the CDCl<sub>3</sub> sample, lipid degradation induces the emergence of peaks at 9.70 ppm, 9.45 ppm, 6.75 ppm, 6.01 ppm, 3.66 ppm, 3.43 ppm, 2.45 ppm, and 2.14 ppm. By comparison with dry samples (only the one analyzed once), degradation induces the emergence of peaks at 9.70 ppm, 6.75 ppm, 6.01 ppm, 2.45 ppm, and 2.14 ppm. In dry samples peak around 9.45 ppm is not observed as well as peaks around 3.66 ppm and 3.43 ppm both being possibly hidden by the lipid signal due to POPC-OOH peaks shift (as clearly observed in Figure 1.11). For the sample conserved in CDCl<sub>3</sub> no shift of POPC-OOH peaks is observed. They correspond to the same sub-product obtained from drying-redissolving cycles, except for the increase of the peak at 0 ppm which is only observed in repetitively dried samples.

The stability of hydroperoxidized lipids is checked as well in CD<sub>3</sub>OD. A solution of 87 % Hydroperoxidized POPC stored for 3 months in CD<sub>3</sub>OD in the freezer (-20 °C) is analyzed by NMR and compared to the prior NMR spectrum recorded before storage. No side products are formed and integrals are kept almost constant (~ 1 % variation).

Since both CD<sub>3</sub>OD and CDCl<sub>3</sub> organic solvent lead to only limited degradation on lipids when conserved at -20 °C, we decided to store hydroperoxidized lipids in CD<sub>3</sub>OD for convenience and to avoid additional drying required when changing solvent. We tried to avoid the use of water, except when necessary and tried to reduce as much as possible the time spent by the lipid outside the freezer and drying-redissolving cycles.

### 1.3 Conclusion

We developed an efficient method to produce highly pure hydroperoxidized mono-unsaturated lipids, with a good yield of 80 weight %, the matter loss being mainly attributed to the dialysis step. Appropriate choices in experimental conditions (solvent, photosensitizer concentration, light power...) offer a fast reaction with a unique easy step of purification and a conversion rate of  $97 \pm 3$  mol %. The reaction can still be optimized by choosing other solvents or even a more powerful light, but care should always be given to verify that no sub-products are formed since they might

---

greatly impact the membrane properties. Dialysis could also be performed over larger surface dialysis tubing or reduced lipid and MB concentration to be faster and to remove a higher amount of photosensitizer. Despite the purification step performed in water and the following water drying, hydroperoxidized lipids do not seem to degrade contrary to repetitive organic solvent drying-redissolving cycles that lead to the formation of numerous sub-products. We advise to store hydroperoxidized lipids in an organic solvent in a -20 °C freezer and to keep them for only a short amount of time out of the freezer.



## Chapter 2

# Structural analysis of hydroperoxidized lipid membranes

The impact of hydroperoxidation on the structure and fluidity of lipid membranes is a matter of current investigation. Simulations showed an increase in the membrane fluidity with a decreased order [72, 77] which is consistent with the decrease in stretching modulus found by micropipette aspiration and SAXS experiments [29, 79]. However, the use of fluorescent probes and simulations indicate an increased viscosity [79, 88, 89] with a concomitant decrease in the lateral diffusion [86]. These results suggest that the hydroperoxidized lipid membrane cannot be simply understood in reference to standard bilayer behavior.

This chapter aims at better understanding the lipid membrane structure by studying lipid interaction and organization. For that purpose, we analyze Cryo-Transmission Electron Microscopy (TEM) images of POPC and SOPC small unilamellar vesicles containing an increasing amount of hydroperoxidized POPC-OOH and SOPC-OOH respectively. Electron microscopy (EM) is a high resolution microscopy technique consisting in exposing the sample to an electron beam. Electrons are partially transferred across the sample with a part deviated from their initial trajectory depending on the sample chemical composition and density (inducing a phase shift linked to the electrostatic potential). Typically, the larger the density of an atom is, the stronger it deviates electrons, which is the case for the phospholipid head (containing phosphorus) whose phase shift is estimated at  $5 \text{ mrad}/\text{\AA}$  while carbon chains or water shifts are estimated at only  $3.7 \text{ mrad}/\text{\AA}$  [156]. For typical lipid vesicles, cryo-TEM images display a darker contour due to the higher deviation of electrons when travelling closed to the lipid heads as explained in Figure 2.1. The EM image of a 3D object can be in principle predicted by numerically projecting into a plane all the phase shift contributions from the object atoms [157].

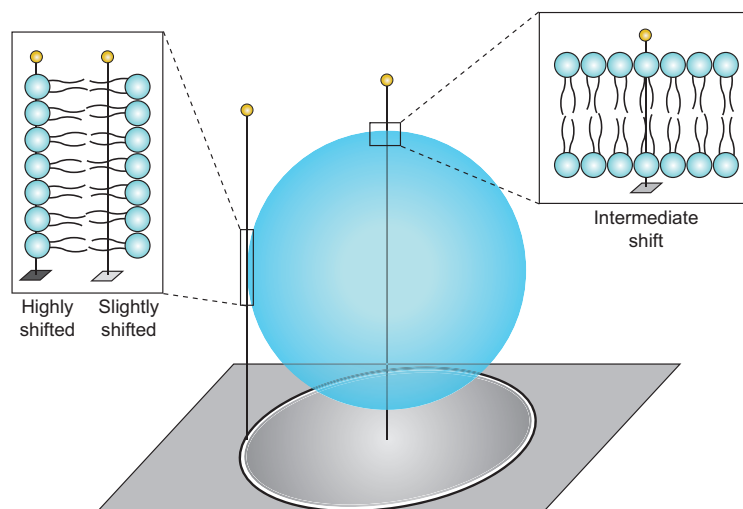


FIGURE 2.1: Cryo-TEM principle. Scheme of a 2D projection obtained from the electron (in yellow) deviation through the 3D vesicles according to atoms phase shift.

Cryo-TEM is characterized by its high resolution. Using this technique might help to resolve variations in membrane structure with lipid peroxidation. In particular, since the images can in our case be resolved to a point where both membrane leaflets are identified, we will measure membrane thickness as a function of hydroperoxidation.

We also study the thermodynamics of the phase transitions for bilayers containing various fractions of hydroperoxidized lipids. To the best of our knowledge, the phase transition temperature  $T_m$  between the gel and the fluid phases has never been measured for hydroperoxidized membranes.  $T_m$  is related to the interaction forces between lipids, as well as to their packing ability. Due to the presence of the lateral -OOH group along the carbon chain, we expect that lipid packing is harder to achieve, and thus we expect that  $T_m$  decreases with hydroperoxydation. We expose here results of  $T_m$  obtained by  $\mu$ -DSC (as described in Chapter 0) on POPC and SOPC large vesicles containing various amounts of their hydroperoxidized forms. From the obtained thermograms, the phase transition enthalpy evolution as a function of hydroperoxidation is also determined. With the intriguing results obtained here, an interpretation is given that enlightens the contradictory results from the literature.

## 2.1 Materials & methods

### 2.1.1 Materials

Mixtures of POPC-OOH/POPC and SOPC-OOH/SOPC are obtained following the method explained in Section 1.1.7. In this chapter, POPC (or SOPC) containing 0, 50 and 100 mol % of POPC-OOH (or SOPC-OOH respectively) are used for cryo-TEM imaging.

Regarding the thermal study, we analyze POPC based membranes containing five different fractions of POPC-OOH (0, 5, 10, 15, 20 mol %) and nine fractions of SOPC-OOH/SOPC membranes (0, 10, 15, 25, 40, 50, 70, 100 mol % of SOPC-OOH),

each composition being produced at least three times always with in  $\pm 3$  mol% of the targeted value. In the following only targeted hydroperoxidation values are indicated for clarity. Three more SOPC based samples are analyzed, one containing 30 mol % and the two others containing 44 mol % of SOPC-OOH.

### 2.1.2 Preparation of Small Unilamellar Vesicles

5 mg of lipids, typically 500  $\mu$ L of a 10 mg/mL in CD<sub>3</sub>OD solution, are placed in a 5 mL round bottom flask and dried by rotary evaporation under reduced pressure. The resulting dry film is hydrated with 1 mL of milli-Q water and stored at 6 °C for 48 h. The sample is then sonicated a first time with a micro-tip (Fisher-brand) (with a signal amplitude corresponding to 1 % of the maximal amplitude, the tip emitting at its resonance frequency) for 2 to 8 min depending on the lipid (see Table 2.1) to form Small Unilamellar Vesicles (SUVs). The sample is afterward extruded through a polycarbonate filter (Whatman Nuclepore) of 0.8  $\mu$ m pore size, using a mini extruder (Avanti Polar Lipids) to break vesicle aggregates. The solution travels 21 times through the polycarbonate filter. Finally, some samples are sonicated a second time (once again depending on the lipid composition) to obtain a good quantity of  $\sim 100$  nm SUVs. SUV solutions are stored at 6 °C before being analyzed by Cryo-TEM.

Dynamic light scattering (DLS) performed on a Zetasizer (Malverne Nano) at 25°C is used to implement the best sonication protocol to form an acceptable number of vesicles smaller than 500 nm for cryo-TEM observation. Results are not detailed here but samples are quite polydisperse, which is not an issue since cryo-TEM segregates vesicles keeping only those small enough to be captured in the thin ice film.

TABLE 2.1: Indicative sonication time to prepare SUVs of each different lipid mixture for cryo-TEM analysis. The first sonication is performed before extrusion and the second sonication (when required) is always performed after extrusion.

Lipid	1 <sup>st</sup> sonication time (min)	2 <sup>nd</sup> sonication time (min)
POPC	2	2
POPC-OOH/POPC (50/50)	2	2
POPC-OOH	3	-
SOPC	8	6
SOPC-OOH/SOPC (50/50)	3	-
SOPC-OOH	2	-

### 2.1.3 Cryo-Transmission Electron Microscopy

Cryo-TEM image acquisition is performed as follows. A 5  $\mu$ L drop of the previously prepared SUV sample is deposited on a lacey carbon film covered 300 mesh Cu grid (Ted Pella) previously rendered hydrophilic using an ELMO glow discharge unit (Cordouan technologies). The excess of sample is removed using a filter paper to obtain a film thinner than 500 nm. The sample is placed inside a homemade chamber held at 22 °C and relative humidity (RH) at 80 % RH. The sample is then rapidly immersed ( $\sim 10\,000$  K/s) into liquid ethane (hold at -190°C using liquid nitrogen to

avoid its evaporation) to obtain a frozen sample preserving the native structure of the vesicles and without forming ice crystals.

The grid is mounted onto a cryo-holder (Gatan 626) and observed under low dose conditions ( $10 \text{ e}^- / \text{\AA}^2$ ) in a Tecnai G2 microscope (FEI) at 200 keV. The sample inside the microscope is let at least 20 min at  $-170^\circ\text{C}$  before image acquisition. Images are acquired using an Eagle slow scan CCD camera (FEI). Under these conditions, we obtain images with a pixel size of 439 pm.

#### 2.1.4 Image processing

Cryo-TEM images are analyzed using a homemade macro on Image J and a python script to extract the lipid bilayer thickness.

Images from TEM are first treated using Image J. Isolated circular SUVs that exhibit an identifiable bilayer, showing both monolayers with a good enough contrast are selected. The oval tool in Image J is used to set by hand the initial SUV perimeter. Afterward, the Image J macro saves a squared sub-image under a name that contains the radius of the circle and the coordinates of the circle center. Each image can then be treated with the script described hereafter.

Figure 2.2 illustrates the script procedure: it first opens the squared picture containing one SUV (Figure 2.2.A) and reads the related information (radius and center coordinate). Figure 2.2.B superimposes (in red) to this picture the SUV perimeter as defined from image J. In the present case, the SUV is positioned close to the TEM carbon grid. The script allows to restrict the region to be analyzed to a fraction of the bilayer, as shown by the red, partial circle in Figure 2.2.B. Cross sections of 60 pixels ( $\simeq 26 \text{ nm}$ ) normal to the lipid bilayers and centered on the perimeter are obtained, and their gray profiles (smoothed using a sliding average function to reduce the noise) are plotted as shown in Figure 2.2.D. Superimposed to the profiles is the average profile: it shows a typical oscillations with a broad peak in the middle. This peak corresponds, on average, to the bilayer position. Due to non-perfectly circular SUV as observed in Figure 2.2.B, the different cross-sections are not perfectly aligned, which creates a poorly representative average of the bilayer gray profile as seen in Figure 2.2.D. To align better all the profiles a correlation is made between each profile and the average in order to minimize their differences by radially sliding the cross section of a few nanometers. The profiles showing the best correlation with the average profile are kept. Figure 2.2.E shows the new series of profiles calculated from the latter correlation procedure, and the corresponding average profile. This average shows now two well defined minimum, corresponding to the two monolayers (dark contours on the original image). Figure 2.2.C shows in red the position of the first minimum (internal monolayer) of each individual profile: it clearly follows what our brain would interpret as the membrane. This correlation procedure can be done several times using the last average as a comparison to obtain a refined profile by eliminating from the image the regions where the image of two monolayers is not well defined. In the final average profile shown in Figure 2.2.F a polynomial fit is done over 10 pixels around the two minimums, from which are extracted the two minimum positions. The bilayer thickness is evaluated as being the distance between these two minimums.

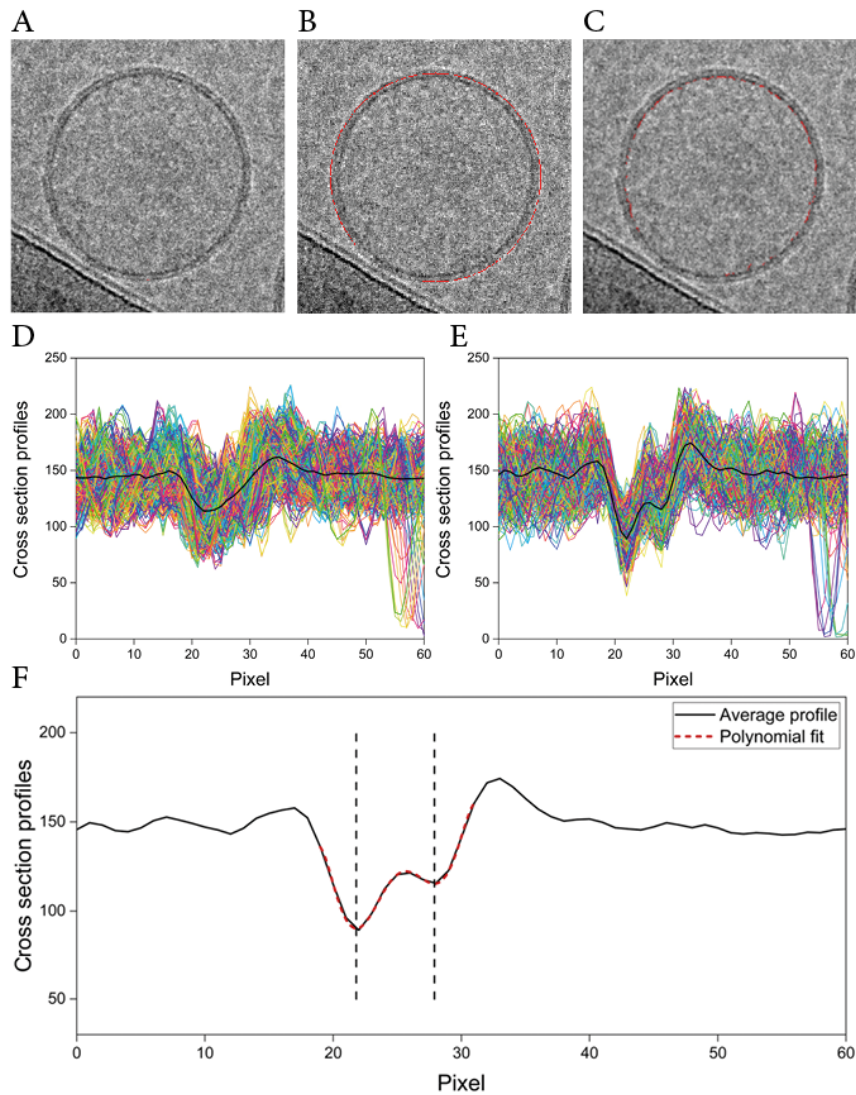


FIGURE 2.2: Steps of the bilayer thickness determination routine. (A) Sub-image centered on a circular SUV with well defined leaflets. (B) Radial selection of the a perfectly circular perimeter determined by hand using Image J. (C) Best determination of the SUV perimeter obtained after cross section alignment by intercorrelation with the average profile. (D) Gray level profiles of the cross-sections centered on the original perimeter circle (red circle in B), and average profile (in black). (E) Set of gray level profiles obtained from the best correlation procedure (see text). Those profiles correspond to the red contour in C. In black is the average profile. (F) Final averaged gray profile with a polynomial fit near the minimum (red dashed line). The bilayer thickness is calculated as the distance between the two minima (vertical dashed lines).

### 2.1.5 Large Multilamellar Vesicles preparation

250  $\mu\text{L}$  of a 10 mg/mL lipid solution in  $\text{CD}_3\text{OD}$  is dried under reduced pressure, and 250  $\mu\text{L}$  of Milli-Q water is added to the precisely weighed dried lipid film. Note that all sample weights ranged in  $2.63 \pm 0.27$  mg. Gentle hydration is applied at room temperature until full dispersion of the lipid film is reached. The obtained solution is vortexed for 1 min (top mix FB15024 Fisher Scientific) and sonicated for 15 min in an ultrasound bath (FB15051 Fisherbrand) to form Large Multilamellar Vesicles (LMVs) of various sizes and degrees of lamellarity.

### 2.1.6 $\mu$ -Differential Scanning Calorimetry

Differential Scanning Calorimetry (DSC) is performed using a  $\mu$ -DSC (MC DSC, TA Instruments) calibrated with pure sapphire. In addition to the reference cell, this device can contain and analyze up to three samples simultaneously. Each run is performed with three samples of the same hydroperoxidation content. The reference cell is filled with Milli-Q water, and each measurement cell is filled with 250  $\mu\text{L}$  of GMV solutions prepared as explained above. Cell masses are equilibrated by adding water, reaching a final concentration of  $\sim 7$  mg/mL. All calorimetric scans and standardizations are carried out with a first set of cooling/heating (C/H) cycles ranging from 20  $^\circ\text{C}$  to -20  $^\circ\text{C}$ , followed by a second set of cycles ranging from 20  $^\circ\text{C}$  to -12  $^\circ\text{C}$ . Each C/H cycle is performed at three different temperature rates: 1  $^\circ\text{C}/\text{min}$ , 0.5  $^\circ\text{C}/\text{min}$  and 0.25  $^\circ\text{C}/\text{min}$  as detailed in Table 2.2. Prior and after each temperature ramp, the temperature is kept constant (isotherm) for the sample to be equilibrated before doing a new temperature ramp. Prior to experiments, scans with empty cells are performed using the same protocol to generate baselines that are then subtracted from the GMV sample scans.

Since the main transition temperature  $T_m$  of both POPC and SOPC are close to 0  $^\circ\text{C}$ , being negative for the former, problems due to freezing of water are expected. Thanks to the undercooling phenomenon, water freezing takes place for negative temperatures during a cooling scan. Under our conditions, freezing occurs randomly between roughly -12 and -18  $^\circ\text{C}$ . Due to this lower limit, some lipid mixture transitions could not be recorded properly. We thus present for some lipid mixtures truncated transition scans on the lower temperature side. Ethylene glycol, glycerol or salt usually used to decrease the freezing point of water are avoided since it has been reported that the addition of any additive could impact the lipid phase transition [158, 159]. Cooling scans ranging from 20 to -20  $^\circ\text{C}$  enable to explore as far as possible the low temperature part of certain transition peaks; indeed, those scans always exhibit the saturated signal of water freezing, as shown in Figure 2.3. Following heating scans starting from -20  $^\circ\text{C}$  could not be exploited due to the strong water fusion signal hiding the bilayer phase transition. On the contrary, avoiding water freezing, C/H scans in the range of 20 to -12  $^\circ\text{C}$  made it possible to record lipid phase transition in both heating and cooling directions for lipid samples with a high enough transition temperature. It is usually advised to record scans at least from  $\pm 10$   $^\circ\text{C}$  above and below the phase transition to have a proper baseline and not be disturbed by the "bounce" artifacts at the beginning of each scan. Since the phase transitions we are interested in are very close to the freezing water temperature, we cannot reach temperatures well below the phase transition temperature and thus some heating scans suffer from the "bounce" artifacts at lower temperatures. In the literature, heating scans are usually shown and exploited to measure  $T_m$ , in the following, we mainly discuss the cooling scans. It is known that phase

transition being a non-instantaneous and cooperative process, slight differences in the measurement of the phase transition temperature are observed between heating and cooling scans. Our cooling scans offer measurements comparable with the ones found in the literature.

We decided to focus on scans acquired with the smallest speed ( $0.25^{\circ}\text{C}/\text{min}$ ) showing more resolved phase transition peaks, with still a good signal. It is worth mentioning that rare thermograms do exhibit peak artifacts, probably due to water. Fortunately, they do not interfere with the lipid phase transition acquisition. Scans are generated with MCDSC-run software and analyzed with NanoAnalyze (TA instruments). The main phase transition temperature is determined as the intersection of the baseline and the highest peak slope, as seen in Figure 8. Heat capacity is calculated as the area below the peak.

TABLE 2.2: DSC scans protocol.

Scan	Direction	Lower temperature ( $^{\circ}\text{C}$ )	Upper temperature ( $^{\circ}\text{C}$ )	Speed rate ( $^{\circ}\text{C}/\text{min}$ )	Equilibrium time (min)	Isotherm time (min)
Scan 1	Cooling	-20	25	-1	10	30
Scan 2	Heating	-20	20	1	10	30
Scan 3	Cooling	-20	20	-0.5	10	30
Scan 4	Heating	-20	20	1	10	30
Scan 5	Cooling	-20	20	-0.25	10	30
Scan 6	Heating	-20	20	1	10	30
Scan 7	Cooling	-12	20	-1	10	30
Scan 8	Heating	-12	20	1	10	30
Scan 9	Cooling	-12	20	-0.5	10	30
Scan 10	Heating	-12	20	0.5	10	30
Scan 11	Cooling	-12	20	-0.25	10	30
Scan 12	Heating	-12	25	0.25	10	30

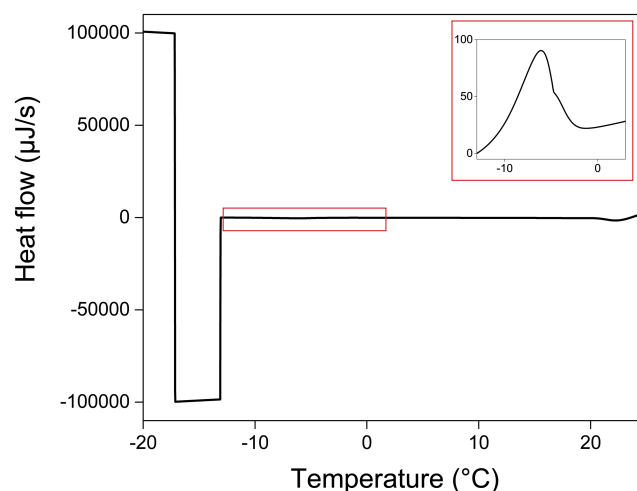


FIGURE 2.3: POPC cooling scan ( $1^{\circ}\text{C}/\text{min}$ ). The saturated heat rate values correspond to water freezing in samples and reference cells. The inset is a zoom on the main phase transition.

### 2.1.7 Fluorimetry: using Laurdan to test lipid phases

Laurdan is a small, amphiphilic molecule, that inserts in bilayers when added to a liposome suspension (see Figure 2.4). When inserted in a hydrophobic medium (including bilayers) Laurdan is fluorescent, with a relatively large emission spectrum ranging from 400 to 550 nm, and an absorption spectrum centered on 350 nm [160]. Laurdan is environment sensitive: its emission spectrum varies strongly with the local polarity of its nearby environment. [161] As a consequence, it has been widely used to study phase transitions in lipid bilayers. Indeed, order parameter, lipid stacking and water content, i.e. membrane hydration are parameters that vary significantly when membrane undergoes a phase transition.

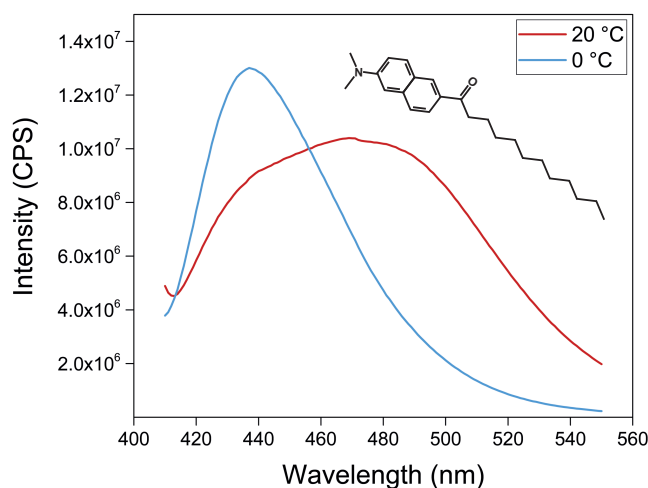


FIGURE 2.4: Laurdan emission spectra when inserted in a SOPC membrane at 0 and 20 °C with its chemical formula.

Characteristic from Laurdan sensitivity is the shape of its emission spectrum with local polarity (see Figure 2.4). Typically, when inserted in a gel phase, Laurdan exhibits a spectrum centered on 440 nm, while when inserted in a fluid bilayer with a non negligible hydration level, Laurdan exhibits a broader emission spectrum with two pics, the first at 440 nm and the second at 490 nm. From Laurdan emission spectra, one can calculate the Generalized Polarization (GP) as an intensity ratio:

$$GP = \frac{I_{440} - I_{490}}{I_{440} + I_{490}}. \quad (2.1)$$

GP is thus expressed as values between 1 and -1. A GP value close to 1 (main contribution at 440 nm) corresponds to low polarity and a gel behavior, while a GP value close to -1 (main contribution at 490 nm) indicates a polar membrane exhibiting a fluid state. We used Laurdan to study gel to fluid phase transition in SOPC. For that purpose we used a spectrofluorimeter (FluoroMax-4, Horiba Jobin Yvon), that enables measuring the Laurdan fluorescent spectra for temperatures down to -2°C.

2  $\mu$ L of a 1 mM Laurdan in ethanol solution ( $\sim$  0.707 mg) are added to 1 mg of SOPC-OOH/SOPC mixtures (SOPC with 0, 25, 50, 75, 100 mol % of SOPC-OOH). The probe/lipid ratio is roughly 1/1000. The solution is dried under nitrogen flux, and the dried film is dispersed in 1 mL of Milli-Q water. The obtained solution is vortexed (top mix FB15024 Fisher Scientific) for 1 min and put in a ultrasound bath (FB15051 Fisherbrand) for 1 min as well. The obtained solution is slightly turbid, a lower lipid concentration is usually used in the literature.

The solution is placed in a quartz cuvette of 2 mL (1 × 0.2 cm) and the Laurdan fluorescence is triggered by an incident light set at 400 nm that cross the sample over the larger side 1 cm. The temperature is decreased from 20 to -2 °C with 1 °C steps. For each temperature, once the temperature instruction is reached the sample is left for equilibration for 15 min. Afterward the emission spectra of the Laurdan is acquired from 410 to 550 nm (with 1 nm step) and perpendicularly to the incident light. We notice a difference between the real temperature of the sample and the instruction gave by the device, the temperature is thus corrected. Water condensation was observed onto the quartz cuvette during measurement, reducing the signal at lower temperature. GP being measured as an intensity ratio the loss of signal does no interfere with its calculation.

## 2.2 Results & discussion

### 2.2.1 Hydroperoxidized vesicles imaging

#### 2.2.1.1 A qualitative structural characterization

We collect more than 50 high resolution images of SUVs composed of the different pure lipids or lipid mixtures as presented in Figure 2.5. We call P0 the pure POPC sample, P50 the mixture of POPC-OOH/POPC 50/50 mol % and P100 the pure POPC-OOH. SOPC based samples are named similarly S0, S50 and S100. Proper optimisation of SUV preparation and expertise in image acquisition, allow the observation of a large enough amount of vesicles with the two phosphorous leaflets easily observable. Only highly spherical and space isolated vesicles are analyzed, we consider between 17 and 41 vesicles for each composition, except for P100 where only 5 vesicles could be analyzed due to the lack of bilayer resolution as detailed bellow.

Most P0 and S0 vesicles show unexpected 2D structures that could perhaps be described as a "golf ball" shape in 3D. Indeed in Figure 2.5, it is visible that P0 and S0 bilayers show non-smooth contours, they exhibit instead a sort of contour "roughness". Similar images have already been observed in the literature for pure POPC vesicles [162] and for saturated lipid vesicles [163]. Tahara et al. [163] believe these specific irregular structures arise from the presence of saturated chains. Thus, POPC and SOPC having one saturated and one unsaturated chain, they might show an intermediate irregular structure. However, this structure is visible only for pure POPC and SOPC samples, and were never seen with 50 % and 100 % -OOH containing samples. Since hydroperoxydation does not modify the saturated chain of POPC, the origin of the irregular structure of POPC and SOPC remains unclear at present, being certainly due to some second order interactions between saturated, unsaturated and/or oxidized chains.

Last but not least, one can remind that crest and tough irregularities can recall structures obtained in the case of the so-called ripple phase [164]. Studies reported that POPC can assemble into this phase under specific conditions (13.5 °C and 75 % RH [165, 166]), but here, SUVs are in excess of water and are always equilibrated in the chamber at 22 °C and 80 % RH before being frozen in their supposed fluid phase. The origin of the roughness in pure POPC or SOPC SUV is thus likely different from the ripple phase.

Apart from the specific POPC and SOPC structure, we could not find any structural hint on a different lipid organization into bilayers caused by the presence of hydroperoxidized lipids.

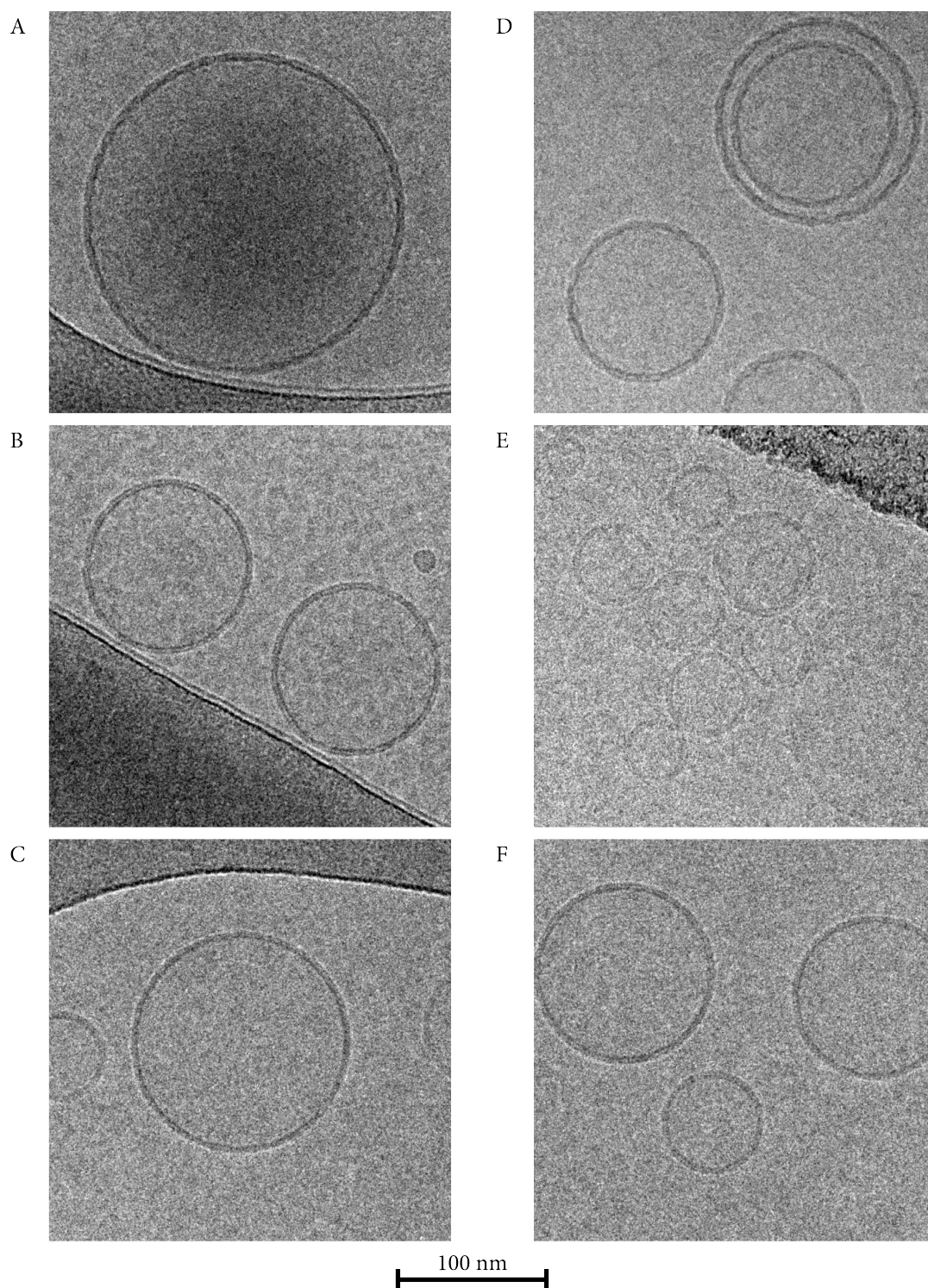


FIGURE 2.5: Examples of images from each sample studied by cryo-TEM: A) P0, B) P50, C) P100, D) S0, E) S50, F) S100.

Another intriguing point is the disappearance of the two well-defined two leaflets in most of P100 vesicles. This result might come from the well-known decrease in the bilayer thickness due to lipid hydroperoxidation, decreasing the space between the two phosphorous regions and so making them less discernible at our EM resolution. This result could also be interpreted as a disordered lipid structure that could lead to a more diffuse phosphorous layer. SOPC having a head-to-head bilayer thickness of  $d_{HH}^{SOPC} = 3.9$  nm [167] slightly higher than POPC ( $d_{HH}^{POPC} = 3.7$  nm) [168], we are able to better identify both leaflet up to fully hydroperoxidized SOPC. This supports the hypothesis that the two phosphorus leaflet disappearance may be due to the decrease in the bilayer thickness more than the disorganization of lipids. In addition, P50 samples do not show specific structural organization. We believe that using an EM with a higher resolution could provide better images of P100 bilayers and may bring new insight into lipid organization.

### 2.2.1.2 Lipid bilayer determination

Cryo-TEM is an emerging technique used to describe lipid bilayer thickness evolution up to a resolution enabling to decipher between  $L_o$  and  $L_d$  phases thicknesses [157, 169]. In this study we simply focus on the measurement of the bilayer thickness. Figure 2.6 shows the average thickness measured on each set of samples using a python script as detailed in the materials and methods section above. One should not forget that the thickness measurements here are done on cryo-TEM images that are 2D projections of 3D objects. Heberle et al. [157] found a good correlation between the measurement of the bilayer thickness between the two gray profile minimums -as measured here- with the actual hydrocarbon thickness  $b$  (m). By considering the two lipids heads (+1 nm [168]), we obtain a decrease of the bilayer thickness of 30 % between POPC and POPC-OOH and 23 % between SOPC and SOPC-OOH. Moreover, our results correlate well with the ones reported in the literature where X-Ray experiments show a decrease of the POPC thickness of roughly 20 % under full hydroperoxidation [69, 77]. The bilayer thickness decrease is well explained by the new conformation taken by the peroxide group carrying carbon chain looping to the bilayer interface. It increases the area per lipid and may allow more lipid interdigitation, all of this leading to a decrease of the thickness. As discussed previously most P100 vesicles do not exhibit very well defined leaflet regions, thus the thickness measurement is less trustworthy.

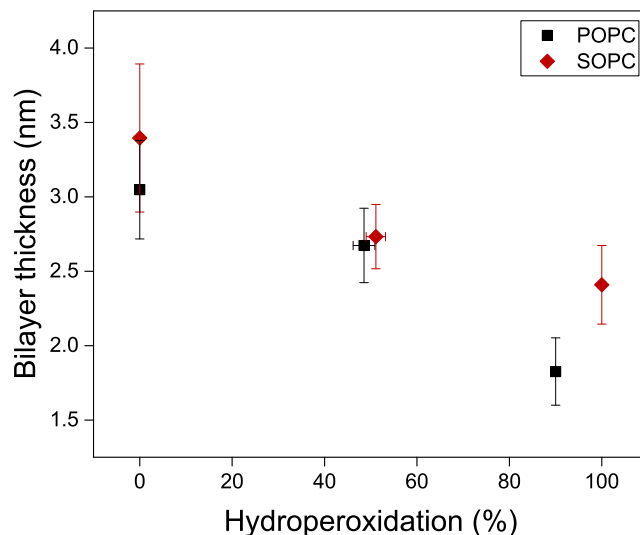


FIGURE 2.6: Average bilayer thickness measured on cryo-TEM images as a function of POPC and SOPC hydroperoxidation degree. Error bars represent the standard deviation.

## 2.2.2 Thermal analysis

### 2.2.2.1 Thermograms qualitative description

Cooling DSC scans of POPC containing an increasing amount of its hydroperoxidized form are displayed in Figure 2.7. All thermograms exhibit an unexpected shoulder on the right slope. This slope is also slightly visible on heating scans from  $-12$  to  $20$  °C, as observed in Figure 2.8.

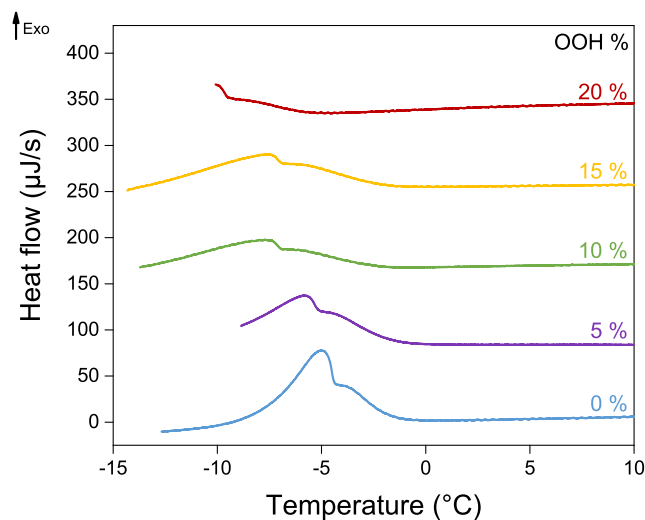


FIGURE 2.7: Cooling scans of POPC containing 0, 5, 10, 15 and 20 mol % of POPC-OOH. Scans are acquired with  $0.25$  °C/min speed and are stopped when the water starts to freeze.

Most DSC studies done on POPC in water do not report such shoulder [170–172], probably because they are most often heating scans performed at higher scan speed ( $2.5$  -  $5$  °C/min). Some of the heating scans from the literature however still exhibit an asymmetry that is perhaps reminiscent of a shoulder [171, 172]. Hernandez et al. [172] explain the phase transition peak asymmetry as being caused by the

presence of the unsaturated chain which decreases the cooperative process of the phase transition. Another noticeable difference between our experiments and the one carried in the references mentioned above is the origin of lipids. In the literature, POPC is either synthesized or bought from Sigma. One study however obtains a similar shoulder in POPC DSC scans [158] by using an extremely low scan speed of  $0.08\text{ }^{\circ}\text{C}/\text{min}$  and using POPC provided by Avanti Polar Lipid (similar supplier as us).

In order to check whether the preparation method of the vesicles could play a role in the shape of the phase transition, we prepare two additional POPC vesicles suspension, one by only vortexing (no ultrasound bath) and the second one by using the micro-tip described in section 2.1.2 for 4 min. DSC scans of these two samples still exhibited the shoulder, indicating that the sample preparation is not the cause of this behavior.

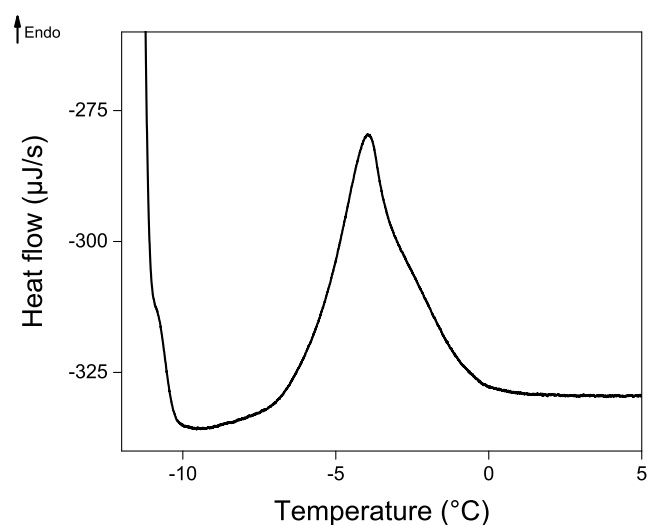


FIGURE 2.8: Heating scan of POPC. The scan is acquired with  $0.25\text{ }^{\circ}\text{C}/\text{min}$  speed. The "bouncing" artifact is visible at the beginning of the scan (at lower temperatures).

Figure 2.9 shows DSC scans of SOPC-OOH/SOPC mixtures up to fully hydroperoxidized SOPC. Pure SOPC samples (or containing a low amount of SOPC-OOH) do not exhibit a shoulder as observed for POPC. By increasing the hydroperoxidation amount, the shape of the thermograms for SOPC containing more than 25 mol % of SOPC-OOH starts to exhibit different features from the pure sample as shown in Figure 2.9. This suggests the possibility of a phase coexistence with the addition of SOPC-OOH.

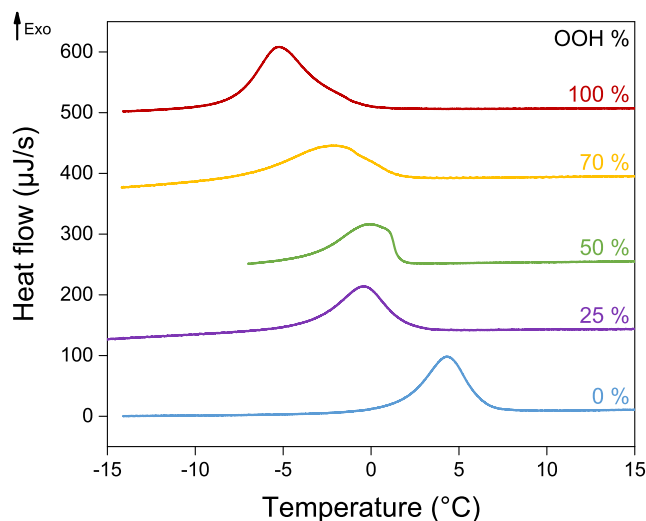


FIGURE 2.9: Cooling scans of SOPC containing 0, 25, 50, 70 and 100 mol % of SOPC-OOH. Scans are acquired with  $0.25^{\circ}\text{C}/\text{min}$  speed and are cut when the water starts to freeze.

We usually obtain very good reproducibility with DSC. However, thermograms obtained for SOPC-OOH/SOPC mixture with compositions between 30 and 50 mol % of SOPC-OOH exhibit strong variation of their transition shape as observed in Figure 2.10. Two samples of very close composition give different phase transition shapes, at a similar temperature. We do not know the origin of such transition modification but it might correlate with the possible phase coexistence and the phase transition temperature plateau presented in the next section in Figure 2.11.

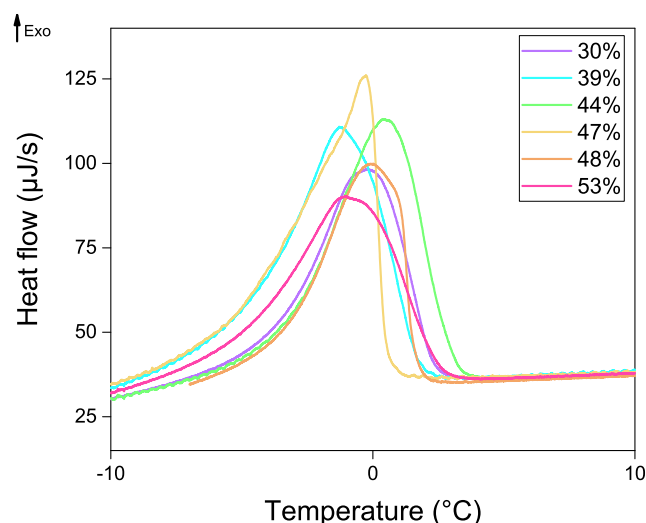


FIGURE 2.10: Cooling scans of SOPC containing 30, 39, 44, 47, 48, and 53 mol % of SOPC-OOH. Scans are acquired with  $0.25^{\circ}\text{C}/\text{min}$  speed and are stopped when the water starts to freeze.

### 2.2.2.2 Phase transition temperature

$T_m$ , the main phase transition is determined as explained before in the Chapter 0 as the intersection between the baseline and the main transition slope. Figure 2.11,

shows the evolution of  $T_m$  for POPC and SOPC based samples containing an increasing amount of their hydroperoxidized forms. Pure POPC and SOPC main phase transitions are measured at  $-3.7^\circ\text{C}$  and  $6.6^\circ\text{C}$  respectively, which are consistent with values found in the literature, despite having been measured on cooling scans [80, 173].

A decrease in the main phase transition temperature is obtained by increasing the amount of hydroperoxidized lipids in the vesicle membranes as already clearly visible in DSC scans (Figures 2.7 and 2.9). SOPC-OOH samples exhibit a phase transition around  $-1.6^\circ\text{C}$ , which represents a difference of  $-8.2^\circ\text{C}$  compared to the pure SOPC. The decrease in  $T_m$  is consistent with the reorientation of a fraction of the peroxide groups towards the interface, increasing the area per lipid and creating more space in the hydrophobic region, giving rise to a less ordered hydrophobic core. Similar phase transition temperature decrease is observed in DMPC/oxPC bilayers (oxPC being aldehyde or carboxyl cutted chain PC) concomitantly with a decreased enthalpy and the emergence of a phase pre-transition [174].

Unfortunately, we are not able to measure the phase transition temperature of POPC membranes containing more than 20 mol % of POPC-OOH. A similar trend as for SOPC based mixtures can be observed over the same molecular ratio (0-20 mol %), corresponding to a decrease of roughly  $0.2^\circ\text{C}/X_{\text{OOH}}\%$ . The phase transition temperatures do not exhibit a monotonous decrease. For intermediate composition between 25 and 70 mol % of SOPC-OOH,  $T_m$  becomes constant. In this range of composition the thermograms, as shown in in Figure 2.10, exhibit a small shoulder. The simpler interpretation of the evolution of the thermograms of the SOPC-OOH/SOPC mixtures is to assume the existence of a phase coexistence region. It is difficult to determine the shape of the phase coexistence region based on DSC results only, but maximum distortion of the thermogram is in our case obtained around the middle composition region, a feature also seen in the thermograms for standard fluid-gel coexistence in binary lipid mixtures. If one assumes that POPC-OOH/POPC mixture behave similarly to SOPC-OOH/SOPC over the full composition range, the phase transition temperature of POPC-OOH can be estimated around  $-12^\circ\text{C}$ .

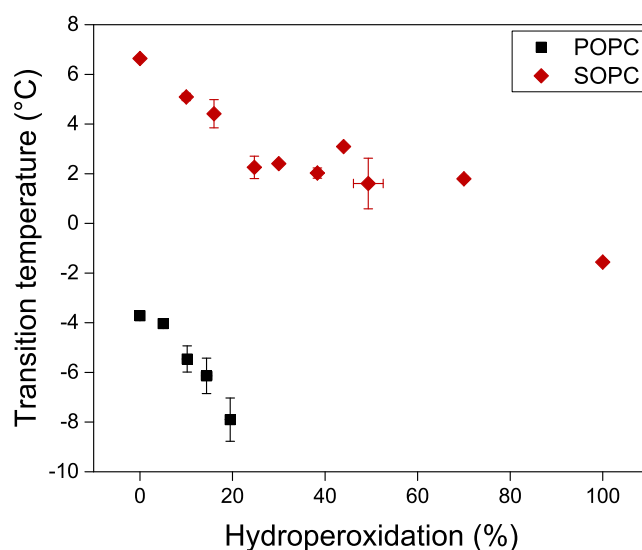


FIGURE 2.11: Evolution of the phase transition temperature of POPC and SOPC containing an increasing amount of their hydroperoxidized forms. Error bars represent the standard deviation.

We also measure the phase transition temperature using Laurdan as a probe inserted in SOPC-OOH/SOPC membranes. From the fluorescent spectra acquired at different temperatures, the GP of the membrane is extracted (equation 2.1) and plotted in Figure 2.12. The plateau obtained at low temperature (visible for 0 and 25 OOH%) is associated with the gel phase, and the linear slope at the highest temperature corresponds to the fluid phase. In the fluid phase, order continues to decrease with increased temperature. The change of slope in between these two phases may correspond to the main phase transition. Temperatures at the slope rupture between the supposed transition and the gel phase correlate quite well with the  $T_m$  obtained by DSC for pure SOPC (6.6 °C) and SOPC containing 25 % of SOPC-OOH (2.3 °C). For pure SOPC-OOH, we cannot observe the gel phase plateau. One can observe that the linear slope at the fluid state decreases with increasing amount of hydroperoxidized lipids, indicating that SOPC membranes are more hydrated than SOPC-OOH ones. These results come in opposition to the usual increased hydration of peroxidized membranes reported in the literature [79]. The measurement performed with Laurdan might be perturbed by the addition of a polar OOH group, potentially able to interact with the probe. These findings however correlate well with the study exposed in Chapter 4, reporting a higher GP and a higher viscosity for POPC-OOH membranes at ambient temperature.

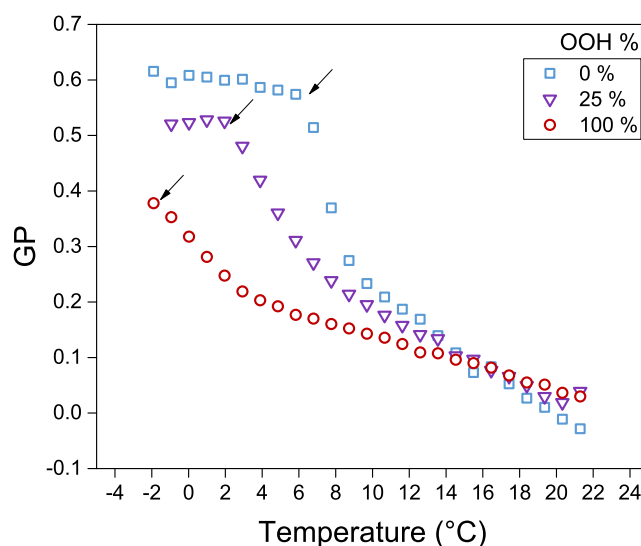


FIGURE 2.12: Evolution of generalized polarization (GP) of SOPC-OOH/SOPC mixtures as a function of the temperature.

### 2.2.2.3 Phase transition enthalpy

The enthalpy  $\Delta H$  measured as the area between the baseline and the phase transition peak (shoulder included) corresponds to the energy required or released by the system to change both the phase organization and interaction. Briefly, in a gel phase, lipids are well ordered and chains interact strongly with each other. Upon an increase of the temperature (that brings more energy to the system) chains decrease their interaction and move more freely. The enthalpy is linked to the heat capacity  $C_p$  (the energy required to increase a sample temperature of 1 °C), see equation 5 in Chapter 0. The enthalpy measurement of most POPC based samples lacks precision

since peaks do not properly reach back to the baseline in most cases, however a reliable measurement can be done for SOPC-based samples.

Figure 2.13 shows the evolution of the transition enthalpy of samples containing an increasing amount of hydroperoxidized lipids. We measured the POPC enthalpy at 19 kJ/mol and at 21 kJ/mol for SOPC consistently with values from the literature [80, 158, 173]. For both POPC and SOPC, containing 0 to 10 or 15 mol % of hydroperoxidized lipid respectively, the enthalpy of the phase transition decreases with the addition of hydroperoxidized lipids ( $-0.94 \text{ kJ}\cdot\text{mol}^{-1}\cdot X_{OOH}^{-1}$  for POPC based samples and  $-0.14 \text{ kJ}\cdot\text{mol}^{-1}\cdot X_{OOH}^{-1}$  for SOPC ones). This decrease could be explained by the addition of a small amount of the peroxide group dispersed in the membrane and creating local disorder. For SOPC, where the full composition range could be studied, the trend is reversed when adding more hydroperoxidized lipids. The final enthalpy for SOPC-OOH is 29.8 kJ/mol. The increased enthalpy can be partially accounted for the change of a cis to a trans unsaturation (+ 14 kJ/mol from cis to trans SOPC [175]). In here, with the snorkeling of the chain to the surface, the effect might be different. One may think that from a certain amount of peroxide group at the bilayer interface, a hydrogen network is created leading to stronger interactions and thus to increased enthalpy.

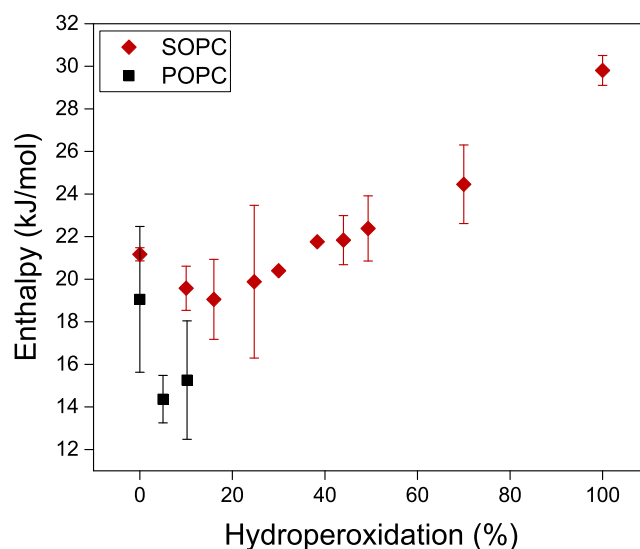


FIGURE 2.13: Evolution of the phase transition enthalpy of POPC and SOPC containing an increasing amount of their hydroperoxidized forms. Error bars represent the standard deviation.

## 2.3 Conclusion

Cryo-TEM images of pure POPC and SOPC vesicles reveal a specific assembly with somewhat rough bilayers already observed in literature on cryo-TEM images of saturated lipids and also on POPC. However, those results were never interpreted. Surprisingly by adding peroxide group on the unsaturated chain this structure disappears. The origin of such an organization remains unexplained, efforts in cryo-TEM or simulations might bring new understanding. It is thus obvious that due to their very different conformation hydroperoxidized lipids reveal a different lipid bilayer

organization

A high image resolution, allows us to measure the lipid bilayer thickness on cryo-TEM images and evidence a decrease in the bilayer of 30 % between POPC and POPC-OOH samples and a decrease of 23 % between SOPC and SOPC-OOH ones, which are consistent with values found in the literature [77]. POPC-OOH images could however benefit from a better microscope resolution to better resolve the two phosphorous leaflets.

Thermal analysis using  $\mu$ -DSC demonstrates a decrease in the phase transition temperature with hydroperoxidation which was anticipated from simulation studies but never measured. [72] We found a decrease in the phase transition temperature of about -8.2 °C between pure SOPC and SOPC-OOH. The enthalpy is also found to decrease over a small amount of hydroperoxidized lipid (below 25 mol % of -OOH) but then increase for a higher amount. The phase transition temperature and enthalpy measured on POPC-OOH/POPC (from 0 to 20 mol % -OOH) exhibit similar trends as the SOPC-OOH/SOPC mixture, thus, similar behavior can be expected for POPC based mixtures.

POPC phase transition is complex, exhibiting a shoulder that might be the overlapping of two phase transitions. This phase transition shape is uncommon for pure lipids (Figure 2.7) that usually show a sharp transition. The origin of such behavior is unknown, the hypothesis that the shoulder is caused by the ripple phase is excluded, and the presence of lipid impurity such as DPPC is unlikely regarding NMR analysis. Microscopy observation of GUV using fluorescent probes sensitive to the lipid bilayer organization such as Laurdan or derivative while decreasing the temperature could help understanding such transition, however due to its negative  $T_m$ , POPC is not a good candidate for such experiments. Significantly, a decrease in  $T_m$  with hydroperoxidation of POPC (up to 20 mol %) is consistent with the increased disorder due to lipid chain looping to the interface as widely reported in the literature [60].

For SOPC samples the phase transition occurs in one single transition as expected for pure compounds. However, the addition of SOPC-OOH above 30 mol % seems to induce the formation of phase coexistence, illustrated by the appearance of a more complex thermograms as seen in Figure 2.9 and 2.10.

The phase transition temperature  $T_m$  and the phase transition enthalpy  $\Delta H$  both decrease when increasing SOPC-OOH amount from 0 to 15 mol %, all indicating an increased disorder and lesser interaction between lipids in both gel and fluid states. This behavior is likely caused by the peroxide group creating local disorder by dragging the hydrophobic chain near the interface. When adding an increasing amount of SOPC-OOH the transition temperature reaches a plateau and all SOPC-OOH/SOPC samples from 25/75 to 70/30 mol % present approximately the same  $T_m$  around 2.2 °C with however very different thermogram shapes and with increasing enthalpy. One may expect SOPC-OOH/SOPC mixtures in this range to organize in different domains coexisting as exhibited by the thermograms shape (Figure 2.9). Since the enthalpy is increasing for this range of composition, one might suspect lipids to be more strongly bonded in each domain. For higher hydroperoxidation amounts, the phase transition temperature decreases, while the enthalpy still increases linearly. Results exposed in the literature (reminded in detail at the beginning of this chapter), show increased fluidity and disorder concomitantly

with increased viscosity. The decreased  $T_m$  associated with the increased enthalpy might reveal an increase in the entropy. Regarding the results obtained here, one may believe that the hydrophobic carbon core is less organized due to the looping of roughly half carbon chains to the interface, thus decreasing the phase transition temperature and increasing the fluidity, and that in parallel the peroxide group at the interface can interact strongly with lipid head and water molecules forming a strong network preventing lipid molecule mobility and increasing the enthalpy as well as the viscosity.

As a summary, the hydroperoxide forms of POPC and SOPC self assemble as bilayers over the full composition range. Hydroperoxidation of POPC and SOPC lowers the transition temperature while, for high enough hydroperoxide content, increases the enthalpy of the transition, thus pointing to a strong increase in the entropy. Such a system could perhaps be described as a strongly cohesive disordered system, cohesion is likely to be provided not only by the trans conformation of the double bond but by interactions between the hydroperoxide groups and the head region of the chains.



## Chapter 3

# Electropermeabilization of hydroperoxidized lipid Membranes

Typical lipid bilayers are greatly impermeable to charged molecules. Studies report negligible permeabilities around  $10^{-12}$  m.s<sup>-1</sup> for Cl<sup>-</sup> and  $10^{-14}$  m.s<sup>-1</sup> for K<sup>+</sup> [176]. As a result, cell membranes are naturally exposed to a potential difference around 70-100 mV, induced by an unbalanced ion concentration between the inside and the outside of the cell [176]. It has nevertheless been observed that membranes under electrical potential can open rare pores, leading to uncontrolled ion flux.

Even though lipid hydroperoxidation induces less pronounced damage than higher oxidation degree - producing shortened carbon chain - [60], the modified properties of such membrane described previously (Chapter 0) still suggest an alteration of their permeability and pore formation ability under electrical stress, whose control is crucial for cell survival in biological media [177].

Given its clear significance, the physical origin of pore opening is intensely debated, and despite intense theoretical and numerical simulation efforts, no unified and quantitative view of the phenomena has yet emerged. The most developed theoretical model for pore opening has never been validated or seriously challenged by experimental data, mainly due to the scarcity of experimental efforts.

The objective of this chapter is to characterize the impact of lipid hydroperoxidation on membrane permeability and membrane behavior under an electric field. In parallel, we aim to improve the understanding of protein-free lipid membrane pore formation mechanisms by providing a new set of experiments with extensive analysis. We believe that numerous life-science related fields would greatly benefit from this study.

We first describe the experimental approach followed to record electric current data and the different methods used for their processing. After a quick evaluation of the POPC and POPC-OOH membrane permeability to KCl ions, the membrane behavior under electric field is qualitatively assessed with the interpretation of the recorded current signals. Then, the response to an electric field of membranes containing increasing hydroperoxidized lipid fractions is determined by studying their conductivity and the voltages at which the membrane ruptures or starts to form pores. Finally, pore lifetime and size are characterized.

Note: in this chapter, we call *membrane rupture* the irreversible breakage of the membrane, whereas, in the literature it sometimes refers to the reversible opening of pores. We also name *intrinsic electropermeability* the transportation of ions across the hydrophobic part of the bilayer, which is a permeability enhanced by an electric

field application. The term *electropemeability* is often used to describe the more generic conductance of the membrane encompassing pore formation.

## 3.1 Materials & methods

### 3.1.1 Materials

Sucrose, chemically cross-linked polyvinyl alcohol (PVA) ( $M_w = 149\,000$  kg/mol), KCl, KOH, and Hepes are provided as powder by Sigma Aldrich. Octane is also bought from Sigma Aldrich. Filling wax (called vitrex in the following) is provided by Vitrex Medical and is used to form wells on microscopy glass slides (thickness of 0.17 mm, Thermo-Scientific). 10  $\mu$ L pipette tips, provided by STARLAB, are used to form free-standing lipid membranes for electroporation. Finally, Meca 4 recording chips of 50  $\mu$ m well diameter are provided by Nanion technology.

In addition to pure POPC and POPC-OOH, we aim to produce POPC containing 25, 50, and 75 mol % of POPC-OOH  $\pm$  5 mol % as described in (Chapter 1). The solvent is then evaporated, and the dried lipids are dissolved in octane to obtain a 10 mg.mL<sup>-1</sup> concentration. Lipids in octane solutions are kept at -20 °C and used within a few weeks, meaning fresh solutions are used for electroporation. Note that old POPC, POPC-OOH or mixtures in octane solutions form white precipitate after some time in the freezer and give viscous solutions at ambient temperature (while DPhPC in octane does not). For each composition, at least three different batches are prepared from three different POPC commercial solutions. Results are grouped by the targeted POPC-OOH amount. Hydroperoxidation percentages used below are the average weighted with the number of membranes used for analysis.

### 3.1.2 Vesicles Passive permeability

POPC and POPC-OOH permeability to KCl is evaluated using phase contrast microscopy as commonly done in the literature [178]. POPC and POPC-OOH GUV are grown using the gel-assisted swelling method developed by the team [179]. Briefly, 100  $\mu$ L of a PVA gel solution - made by dissolving 1.25 g of PVA in 25 mL of water and heating at 90 °C for 3 h - is deposited on a previously cleaned microscopy glass slide. The gel is placed in an oven at 80 °C for at least 30 min to obtain a dry film. 5  $\mu$ L of a 1 mg/mL lipid in organic solvent is slowly added on top of the dried gel and excess of solvent is evaporated under vacuum for 15 min. A well made of vitrex is placed on top of the gel, in a way that lipid deposition is at its center. The well is filled with 150  $\mu$ L of a filtered 100 mM sucrose in water solution (342.3 mg sucrose in 10 mL) to hydrate the lipid dried film and form GUV with similar inside and outside sucrose concentration in 2 h 30. A scheme of the method is presented in Figure 3.1. 75  $\mu$ L of sucrose solution is added to the GUV solution and the resulting GUV solution is kept in an Eppendorf tube in the fridge.

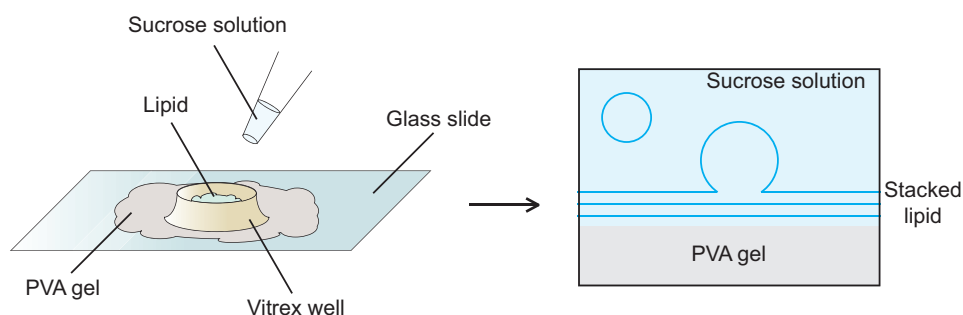


FIGURE 3.1: Scheme of the gel-assisted method used to grow GUVs in sucrose.

GUVs are then observed with a  $\times 10$  objective under phase contrast microscopy (LEICA). GUVs in sucrose are first observed to assess the quality of the sample.  $75 \mu\text{L}$  of a  $100 \text{ mM}$  KCl solution ( $39.68 \text{ mg}$  KCl in  $10 \text{ mL}$  of water) is added to  $75 \mu\text{L}$  of the GUV in sucrose solution. The sample needs a few minutes before GUV sedimentation at the bottom of the well (to the observed focus plan) and for the solution drift to reduce after KCl addition. Numerous images are then taken at different time intervals over  $30 \text{ min}$  of observation. A contrast between the outside (sucrose + KCl) and the inside (sucrose) of the vesicles is visible due to the different refractive indexes of the solutions. If membranes were permeable to KCl, the phase contrast should decrease due to equilibration between inside and outside KCl concentrations.

A unique vesicle is chosen for observation over  $30 \text{ min}$ . Its radial contrast is measured using an Image J plug-in written by Philippe Carl and freely available (<http://questpharma.u-strasbg.fr/html/radial-profile-ext.html>). It averages the gray profiles from pixels equidistant from the center of the GUV on a manually selected radial section. The gray contrast profiles are obtained and analyzed for different images taken over  $30 \text{ min}$ .

### 3.1.3 Electroporation measurement device

Electroporation experiments are carried out on an Orbit Mini workstation (Nanon Technologies, Munich, Germany), with inserted microelectrode cavity array (MECA 4) recording chips (Ionera Technologies, Freiburg, Germany). Chips contain four wells of  $50 \mu\text{m}$  diameter and  $30 \mu\text{m}$  depth, each cavity corresponding to a recording channel. A chloridized silver electrode (Ag/AgCl) is present at the bottom of each well and a unique counter electrode is found at the top of the chip. A 3D representation of one well is shown in Figure 3.2. The Orbit Mini operates in voltage-clamp mode using Elements 4 (e4) channels amplifier (Elements SRL, Cesena, Italy). Voltage can be imposed to only selected channel(s), but with a common value, in the range  $-500 \text{ mV}$  to  $+500 \text{ mV}$ . The current intensity as a function of time - corresponding to ions crossing each well -  $I(t)$  is measured independently, allowing in principle to record the current through four suspended membranes simultaneously. However, the current saturation due to a membrane rupture in one of the channels induces artifact signals in the neighboring channels, we thus chose to work with a unique well at a time.  $I(t)$  is measured with a sampling rate of  $1.2 \text{ kHz}$  and bandwidth  $0.6 \text{ kHz}$ . The Orbit Mini is piloted by elements data reader 3 (EDR 3) software, offering several measurement gauges corresponding to the lower and upper saturation limits of the signal. Capacitance  $C_m$  is determined with a predefined

instrument routine using the  $[-20, 20]$  nA measurement gauge and all current signals are recorded with the smallest gauge of  $[-200, 200]$  pA.

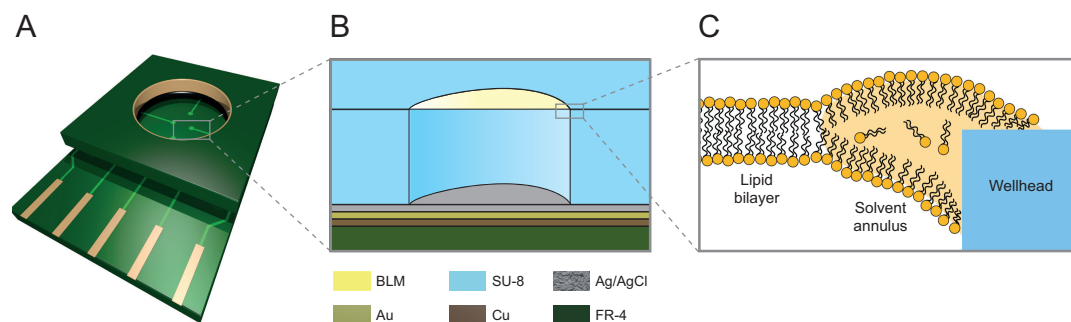


FIGURE 3.2: The free-standing lipid bilayer anchored on a Meca 4 recording chip. (A) is the representation of the Meca 4 chip. (B) shows a vertical cut of one of the wells with a painted bilayer. The lipid bilayer spans a large but not full fraction of the well top, separating a bottom from a top electrolyte solution. In (C) is depicted for illustration purposes the hypothetical geometry of bilayers anchored along the aperture rim.

### 3.1.4 Free standing bilayer preparation

Experiments are conducted at room temperature ( $\sim 20$  °C). The Meca 4 chip is filled with  $150 \mu\text{L}$  of a fresh buffer solution composed of 100 mM KCl and 10 mM HEPES in Milli-Q water, adjusted to pH 7 by addition of 1 M KOH solution, typically  $10 \mu\text{L}$  for a total of 5 mL solution. Special attention is given to the complete air removal from each of the four cavities. A bilayer is painted on the top of the cavity by the air bubble method as schematized in Figure 3.3 and described elsewhere [180]. Briefly, an air bubble is formed directly above the chosen cavity with a  $10 \mu\text{L}$  micropipette tip previously immersed in the lipid-in-octane solution. Afterward, the air aspiration of the bubble leaves attached to the aperture rim a thin octane film stabilized by lipids. The further action of surface tension forces leads to the thinning of this film, up to a stabilized configuration, characterized by a free-standing bilayer of area  $S$  ( $\text{m}^2$ ), surrounded by a thick oil annulus attached to the aperture rim, as schematically depicted in Figure 3.2 and described elsewhere [181]. The presence, stability, and quality of the free-standing bilayer are monitored with EDR 3 software. The absence of any membrane results in a saturated current ( $\pm 200$  pA), while its presence is confirmed with a negligible current in the order of a few picoamperes due to their low permeability to ions. One should note that when 0 mV is entered as a command in EDR 3, the system is actually always under a residual voltage that allows a current measurement. When formed, the membrane is left to equilibrate for at least 1 min while continuously checking the stability of the current signal. In case of an unstable current, the membrane is destroyed and reformed. Afterward, the membrane capacitance  $C_m$  is measured using a specific mode of EDR 3. Capacitance variability is observed, we found that reproducible measurements are obtained for membranes with a stable capacitance ranging from roughly 6 to 13.5 pF, being considered solvent-free bilayers. In presence of imposed voltages smaller than 25 mV, current intensity through the membrane must stay close to a few pA, attesting the membrane to be leakage proof.

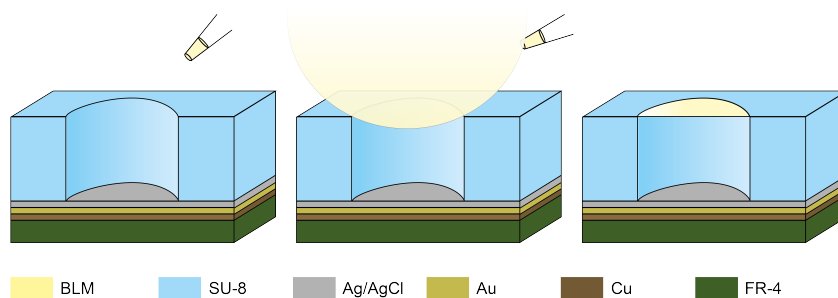


FIGURE 3.3: Scheme of the air bubble technique used to paint free-standing lipid bilayer on top of the Meca 4 well.

### 3.1.5 Conductivity measurements

Once a membrane is formed, EDR 3 software is used to follow and record current intensity traces  $I(t)$  for various imposed voltages  $U$ . The defined protocol with increasing voltages applied to membranes is shown in Figure 3.4. Voltages are increased from 0 mV to 500 mV with 25 mV steps. For each step negative and positive voltages are kept constant for 6 seconds, each applied voltage being separated by a resting time of 6 seconds at 0 mV. A small fraction of the recordings are first acquired by manually implementing the change of voltage in EDR 3 which lead to slight protocol irregularities. The acquisition protocol is then fully automatized with a home-written macro (Pulover's Macro Creator). The protocol is manually stopped at membrane rupture, corresponding to sudden irreversible current saturation (applying a high electric field to an open cavity -without membranes- can lead to chip damage).

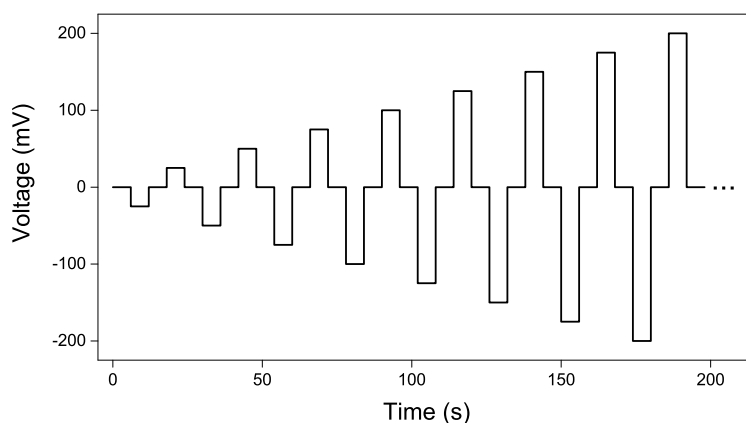


FIGURE 3.4: Voltage protocol  $U(t)$  used for current intensity recordings. Voltages are increased by steps of 25 mV and kept constant for 6 seconds. For each step, negative and positive voltages are applied, all separated by intermediate steps at 0 mV.

In absence of a membrane, even at the imposed 0 mV, the current rise well above the saturation conditions, here  $\pm 200$  pA. An example is given in Figure 3.5, where the current intensity saturates after  $\sim 4.5$  s of  $-325$  mV voltage application, which could either be interpreted as the creation of a "big" pore (with diameter  $D_p \gg 1.3$  nm) or by the membrane rupture. The membrane rupture is confirmed by changing the voltage to 0 mV, if the current still saturates, the membrane is considered definitively broken.

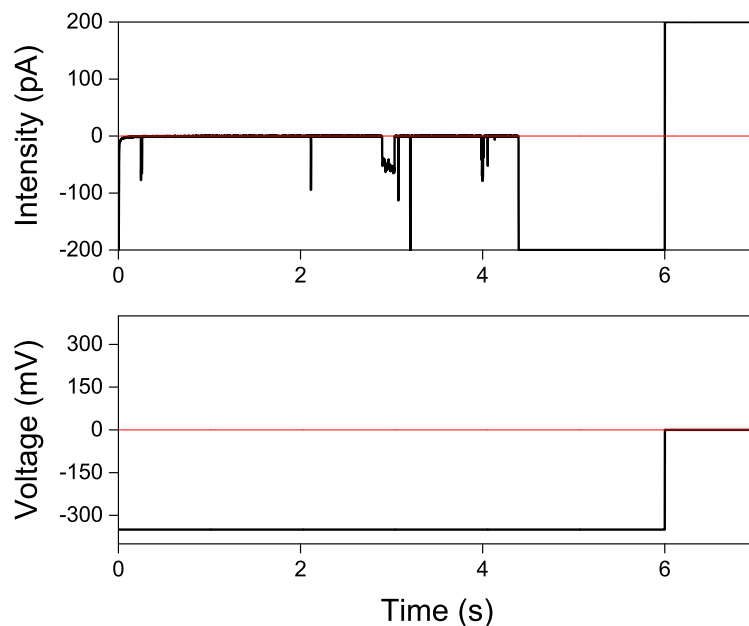


FIGURE 3.5: Intensity  $I(t)$  (top) and concomitant voltage  $U(t)$  (bottom) recording as a function of time evidencing (a POPC) membrane rupture.

If a membrane resists up to the highest voltage being possibly applied by the device ( $U = 500$  mV), it is not considered as a solvent free bilayer, and the experiment is discarded.

More than 50 membranes of each targeted lipid composition are studied: 95 membranes for POPC containing 0 % of POPC-OOH, 94 for 25 %, 53 for 50 %, 76 for 75 %, and 55 for 100 %. Despite the consequent amount of data collected with electroporation, it is important to be aware of the experimental difficulties one could face using this technique, for that one can consult the Annex B.

### 3.1.6 Data treatment

The generic behavior of a phospholipid bilayer submitted to an electric field can be qualitatively described. It is important to note that, under the same conditions, each current signal is unique, conduction events having a stochastic nature. In this study more than 50 membranes of each binary composition are studied, enabling to build a precise enough statistical picture of electric response for the various studied POPC-OOH/POPC compositions. We noted that, apart from the statistical dispersion, the measurements highlighted some slight differences between different batches of lipid mixtures.

Statistical analysis of our data required the development of homemade python scripts implemented on Visual Studio as presented below. Given typical values for the membrane capacitance in picofarad, the response time  $\tau_{RC}$  of the circuit is a few microseconds. However, one should have in mind that all relaxation phenomena observed in the recorded  $I(t)$  traces (during increase or decrease of the current) are on the order of a few milliseconds ( $\tau \simeq 2.8$  ms) due to signal Bessel filtering (bandwidth 0.6 KHz). Thus, we do not use the model of an equivalent electric circuit to study pore opening or closing (the model is presented in annex A), we instead consider  $\tau \simeq$  ms to estimate the size of short lifetime pores.

### 3.1.6.1 Signal pre-treatment

Electroporation data are stored in .abf format, often used in electrophysiology to obtain compressed files. They correspond to time, intensity, and voltage lists that are opened, in our case, using the open access *pyabf* library in python [182]. Each recorded  $I(t,U)$  signal is decomposed in sub-signals  $I_U(t)$  of 6 s during which the voltage is maintained constant. When a new value of voltage is applied, the current first raises almost instantaneously to a peak value and then follows an exponential decay with the time constant  $\tau$  already mentioned above (see Figure A.2). This peak is called *capacitance peak*. Under our conditions, we have  $\tau \sim 2.8$  ms, determined as being the time required to decrease from a factor  $1/e^1$  from the maximum value reached by this peak. For simplicity, this initial current peak related to the charging of the membrane by ion condensation, is suppressed from the traces for further data analysis by removing the 200 first data points ( $\sim 160$  ms) of the sub-signals. In most routines, for a matter of convenience, intensities recorded during negative voltages are inverted and used as positive values.

The different routines described below are used to determine different features of the  $I(t)$  signals and are always applied to a set of .abf experiments grouping the same targeted POPC-OOH/POPC membrane composition.

### 3.1.6.2 Membrane survival and pore opening probability

At the beginning of this specific routine, the time over which the signal is analyzed can be chosen ( $< 6$  s). It can be used to study both membrane rupture and pore opening as a function of the applied voltage time.

The rupture voltage for each membrane of the same hydroperoxidation degree is determined.  $I_U(t)$  signals for each applied voltage are studied in the time appearance order. For a given voltage, when a  $I_U(t)$  signal ends with a saturated intensity and that the next  $I_0(t)$  average absolute intensity is above 25 pA, the membrane is considered broken. At each applied voltage, the number of membranes still present is counted to determine the probability of membrane survival.

For each  $I_U(t)$ , the average of current below 20 pA  $\bar{I}_{<20}$  is calculated to establish a baseline when possible. If the maximum current intensity is above  $\bar{I}_{<20} + I_T$ ,  $I_T$  being a threshold arbitrary set at 7 pA (way above the noise), the membrane is considered to form at least one pore in the time interval set at the beginning of the routine. The time of the first pore opening is recorded. Similarly, the percentage of membrane opening at least one pore for the chosen time is counted to obtain the probability of pore opening. We are conscious of the limitation of such a routine based on arbitrary thresholds (being a compromise between noise and pore intensity) but it allows us to make a good comparison between the membrane of different compositions.

### 3.1.6.3 Intrinsic electropermeability

The measurement of the membrane intrinsic electropermeability intensity  $I_c$  is done on carefully chosen constant baselines where conductive events are avoided (requiring human action). This is easily realized for low or intermediate values of voltage, for which the frequency of intensity jump is limited, however, increasing care must be taken to select the adequate, current jump-free, fragments of the  $I_U(t)$  traces when increasing the voltage.  $I_c$  is calculated as the average intensity on the selected section. The current density  $i_c = I_c/S$  is obtained by normalizing the intensity with the

surface  $S$  occupied by each membrane (see section 3.2.2). An averaged  $i_c$  is calculated for each voltage and each membrane composition. Membranes showing too high  $i_c(U)$  are discarded, being suspected of current leakage or long lifetime pore openings.

#### 3.1.6.4 Current intensity average

From each  $I_U(t)$ , the average of intensities below 195 pA (to remove saturation) is calculated. Obtained values are averaged for each voltage and lipid composition to obtain  $\bar{I}(U)$ .

#### 3.1.6.5 Regimes quantification

Signals are described by three different regimes that will be defined in section 3.2.3: short lifetime pore, long lifetime pore, and complex regime. Here, each  $I(t)$  trace is categorized as exhibiting either no pore or at least one of the regimes stated above. The probability for the membrane to display each one of the regimes independently of the others is obtained by counting the number of membranes showing each regime at each specific voltage.

#### 3.1.6.6 Short lifetime pore analysis: a threshold method

Pore detection algorithms can be found in literature, but are mostly developed for conductivity recordings of ion channels, *i.e.* characterized by well-defined intensity plateaus. Those algorithms cannot be transposed for the analysis of our current signals, that exhibit a large variety of peaks, with complex duration and intensity patterns [183]. Besides, various models exist, to filter current intensity signals, but again, rare are the ones relevant for analyzing our complex traces [184].

To properly detect pores in our  $I(t)$  traces, we developed a first algorithm, called *threshold method*, devoted to the analysis of time isolated pore events. It is worth mentioning that this algorithm requires human action, indeed, one should wisely select appropriate sub-signal sections where pores do not overlap in time. In addition, the algorithm requires as an input parameter the cut-off threshold intensity  $I_T$ . In practice, for each  $I_U(t)$  we evaluate the spontaneous signal fluctuations (noise) around the average baseline  $I_c$  and set the threshold value  $I_T$  well above fluctuations (dashed red line in Figure 3.6) and below any - out of noise - intensity jump maxima. The signal noise can vary from one experiment to the other, and one needs to adjust the detection threshold accordingly to detect pores with the smallest intensity as possible.  $I_T$  threshold is the most often used around 3 pA.

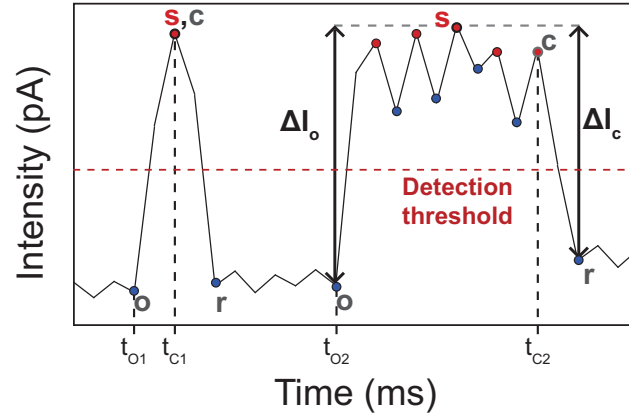


FIGURE 3.6: Scheme of the *threshold* detection method to detect opening time ( $t_o$ ), closing time ( $t_c$ ), and intensity  $I_p$  for two isolated pores. Only pores above the detection threshold are considered.  $s$  represent the maximal intensity of a pore, and  $r$  the first point after pore closure.

The algorithm scans  $I_U(t)$  trace to determine every local maximum (red circles) above the threshold associated with their two local minimums (before and after, blue circles) as shown in Figure 3.6 for two successive pores. Data are scanned in time order up to its first local maximum above the threshold  $I_T$ . The pore opening is set (points  $o$ ) and the temporary opening intensity  $\Delta I_o$  is calculated as being the difference between the first maximum and the minimum tagged as the pore opening  $I(o)$ . Scanning continues, with the identification of every local maximum (with their minimum) until the closing of the pore. If scanned maximums between pore opening and closing, have a higher intensity value than the previous one (points  $s$  as an example), this new maximum is selected and  $\Delta I_o$  is recalculated accordingly ( $I(s)-I(o)$ ). Pore closing is detected when the closing intensity  $\Delta I_c$  (calculated as the difference between the last calculated maximum and the last scanned minimum ( $I(s)-I(r)$ )) is at least bigger than  $\Delta I_o \times 0.5$ . The pore closing (points  $c$ ) is tagged as the last local maximum before point  $r$ .

The pore lifetime  $\tau_p$  is calculated as the difference between closing  $t(c)$  and opening  $t(o)$  times. The maximal intensity of the pore signal is calculated as the maximum between  $\Delta I_o$  and  $\Delta I_c$ . For pores having a long enough lifetime  $\tau_p \gg \tau$ ,  $I_p$  is directly obtained. For pores opening for  $\tau_p \ll \tau$ ,  $I_p$  can be calculated from the  $I(\tau_p)$  measurement considering the device filtering with the time constant  $\tau$ .

Please note that noise in the baseline signal can induce an error in the definitions of both  $o$  and  $s$ , which is at maximum equal to two time intervals (here 1.6 ms). Note also that the algorithm overestimates pore current by a value comparable to the amplitude of open pore fluctuations plus the baseline fluctuation since for simplicity the maximum of the current (point  $s$ ) and minimum before pore opening are chosen for its calculation (Figure 3.6).

The *threshold method* is first used to build the time isolated pore lifetime distribution in section 3.2.5.1 and then to analyze data restricted to pores with a lifetime smaller than 10 ms in section 3.2.5.2. An example of the *threshold method* detection is shown in Figure 3.7.

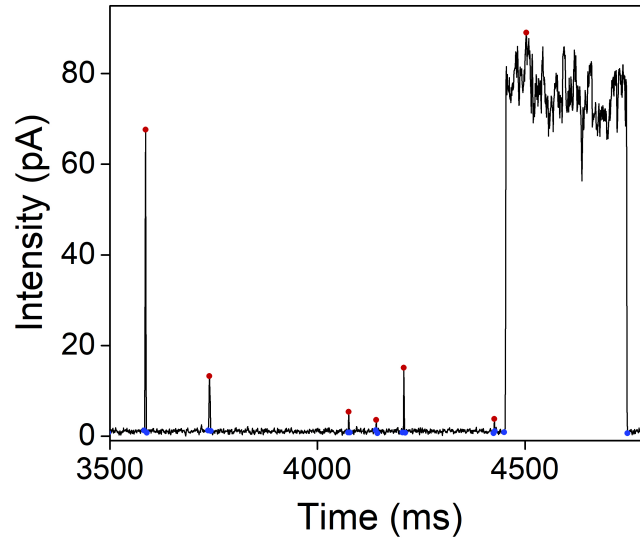


FIGURE 3.7: Example of detection of time isolated pores using the *threshold method* showing 6 short lifetime pores and one long lifetime pore.

### 3.1.6.7 Long lifetime pore analysis: square gating method

A second algorithm, the *square gating method*, is developed to determine intensity plateaus in complex current traces. Similarly to the previous routine, it also requires human action to tune filtering parameters ( $N_0$  and  $G_{\text{noise}}$ ) depending on the noise of each  $I_U$  signal. The filtering ignores intensity jumps of duration smaller than 20 ms, and averages intensities when fluctuations are smaller than the local noise  $N_{\text{loc}}$ , rendering a free of noise filtered signal with only well defined intensity plateaus.

To take into account the fact that the signal exhibits heterogeneous noise - increasing noise with intensity -, the algorithm re-calculates a local acceptable fluctuation  $N_{\text{loc}}(I)$  for each intensity  $I$  using a linear law  $N_{\text{loc}}(I) = N_0(1 + I \cdot G_{\text{noise}})$ . If intensities are out of the  $N_{\text{loc}}$  boundary for more than 20 ms, a new plateau is considered. The initial values are set at  $N_0=5$  pA and  $G_{\text{noise}}=0.02$  but were adapted when necessary. Figure 3.8 shows an example of signal filtering according to this method.

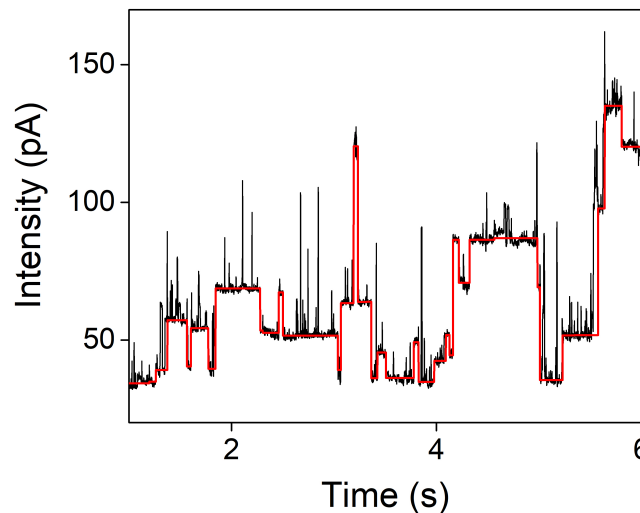


FIGURE 3.8: Example of signal filtering for long lifetime pore detection using the *square gating method*.

## 3.2 Results & discussion

One should note that most previous electroporation studies use 1,2-diphytanoyl-glycero-3-phosphocholine (DPhPC, 4ME 16:0), which form very stable membranes 3.6 nm thick [185], the aim being to only study protein channels conductivity. Here we want to analyze POPC membranes, which is more relevant since present in high amount in mammalian biological cells and which behave very differently and form less stable membranes compared to DPhPC.

### 3.2.1 Vesicle intrinsic permeability to KCl

POPC and POPC-OOH membrane impermeability to KCl salt is assessed by studying GUV with different internal/external media using phase contrast microscopy. Figure 3.9 shows the evolution of the radially averaged gray level of a POPC and a POPC-OOH GUV after the addition of salt in the external media. Time starts when the observed vesicle is sedimented, always less than 5 min after KCl addition. Similarly to POPC, POPC-OOH GUVs do not show significant contrast loss, indicating a relatively impermeable membrane to salt for 30 min -time above the one over which electroporation experiments are carried out-. The phase contrast curves can differ slightly from each other due to the quite high vesicle concentration used here and the drift of non sedimented vesicles that cross above the observed GUVs.

Permeability of oxidized lipid vesicles has already been studied previously [186, 187], however, in these studies they assessed the permeability during vesicle oxidation, which is greatly suspected to cause only transient pore opening, inducing a loss of contrast. Here we show that after oxidation membranes do not open spontaneous pores.

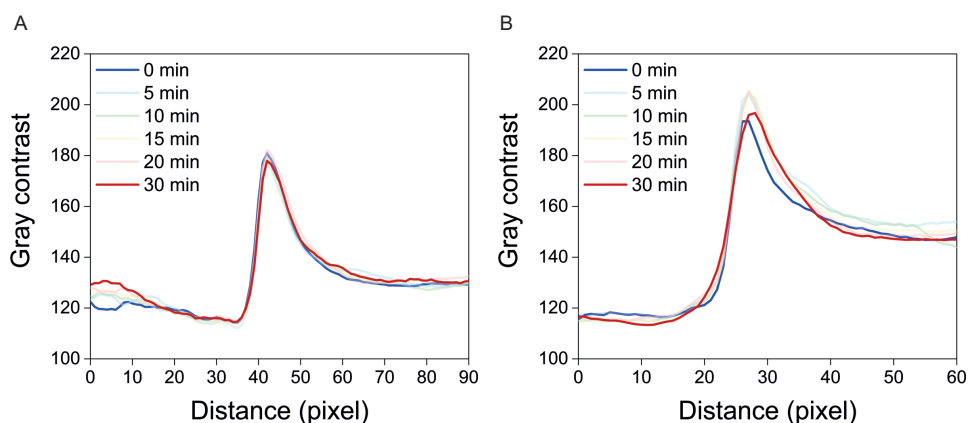


FIGURE 3.9: (A) POPC and (B) POPC-OOH GUV radially averaged gray level evolution over 30 min after KCl addition in the outer media.

### 3.2.2 Membrane geometry

Before analyzing the  $I(t)$  traces, one may be interested in the membrane geometry. As described previously, the membrane can be characterized by its capacitance  $C_m$ , which is related to the effective surface  $S$  that the bilayer occupies as described by the equation 3.1:

$$S = \frac{C_m b}{\varepsilon_0 \varepsilon_m^0} \quad (3.1)$$

with  $b \sim 2.7$  nm [168] the hydrophobic thickness,  $\varepsilon_0$  the vacuum permittivity ( $\text{F}\cdot\text{m}^{-1}$ ) and  $\varepsilon_m^0 \sim 2-5$  [136] the membrane relative permittivity (dimensionless).

Figure 3.10 presents the values of the capacitance  $C_m$  of all the studied membranes. Most membrane capacitances are found in the 6 to 13.5 pF range. Lower capacitances can be measured, but the associated membrane often exhibits unusually stable behavior. Higher capacitances have also been measured, we believe they correspond to defective leaky membranes with maybe improper anchoring.

The largest capacitance measured for decent membranes is about 13.5 pF. If one hypothesizes this value to correspond to an oil-free membrane of maximum possible surface  $S_{\text{max}} = 1963 \mu\text{m}^2$ , one should consider  $\varepsilon_m^0 = 2.1$  which is the typical value used in the literature [136]. The specific capacitance  $c_m$  is then given by  $c_m = C_m/S = \varepsilon_0 \cdot \varepsilon_m^0 / b = 6.9 \text{ mF}\cdot\text{m}^{-2}$ . Measurements by the droplet interface bilayer [188], where, similarly to our system, the bilayer is also exposed to an oil reservoir give  $c_m = 6.8 \text{ mF}\cdot\text{m}^{-2}$  for POPE, a lipid with the same tail architecture as POPC but with a different headgroup. This certainly reinforces our choice of  $\varepsilon_m^0 = 2.1$  and  $c_m = 6.9 \text{ mF}\cdot\text{m}^{-2}$ .

Unexpectedly, hydroperoxidation has no statistically significant impact on the bilayer capacitance. The average is always  $\sim 9$  pF corresponding to a membrane of 42  $\mu\text{m}$  diameter and a membrane surface  $S = \pi(D_m/2)^2 = 1385 \mu\text{m}^2$  with a solvent annulus 4  $\mu\text{m}$  wide.

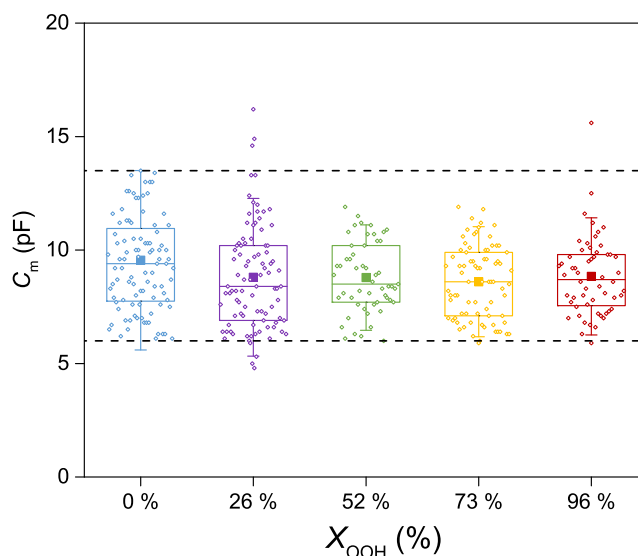


FIGURE 3.10: Capacitance values  $C_m$  of the investigated bilayers depending on the hydroperoxidation amount in membranes ( $X_{\text{OOH}}$ ). The box plot represents the distribution of membrane capacitance based on the first quartile, the median, the mean (filled square symbol), the third quartile, and with whiskers showing standard deviation. The dashed lines correspond to 6 and 13.5 pF, the usual range of membrane capacitance.

In general, organic solvent trapped inside the lipid bilayer is known to lower its specific capacitance [189]. However, thermodynamic arguments suggest that if some finite fraction of oil is present in the bilayer, it should be constant throughout all layers of the same lipid composition. In the following, we will thus interpret

capacitance variations as resulting only from variations in the surface  $S$  of the free-standing bilayer and use the measurement of  $C_m$  as a surface measurement.

In our experiments, the ratio between roughly the larger and the smaller measured acceptable values of the capacitance  $C_m$  is  $13.5/6=2.25$ . Despite having a well-defined average, capacitances span thus a rather large range of values. Reasons for such variations are hypothesized as being related to the manual painting of the lipid membrane which brings each time a different amount of lipid and solvent, impacting the solvent annulus size. It is worth mentioning that with stable DPhPC membranes, the amount of lipid and solvent brought to form the free-standing bilayer, and thus the capacitance, can be easily modified using air bubbles. However, POPC and POPC-OOH membranes being less stable it is more difficult to control.

The aperture rim surface as shown in Figure 3.11, an optical microscopy image of one of the wells used for our experiments, shows geometrical irregularities that certainly play a role in the anchoring of the lipid film. Moreover, other heterogeneities can also be present such as spatial variations in the chemical nature of the SU-8 surface. Variability of traces should come as no surprise, given the heterogeneity of the formed film geometry that adds up to the intrinsic stochasticity of the ion transport processes analyzed here.

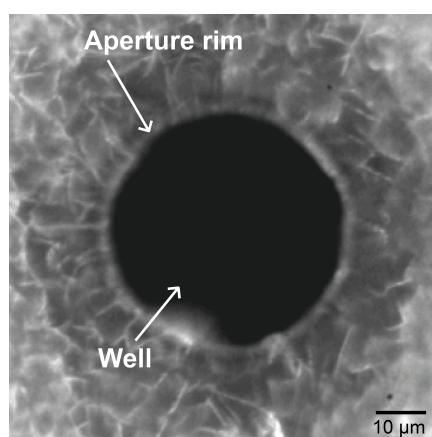


FIGURE 3.11: Microscopy image of a Meca 4 chip cavity on which lipid bilayers are formed. As the image shows, the aperture edge displays small irregularities, which are different from well to well, contributing to the variations in the quality of the anchored bilayers and corresponding signals.

### 3.2.3 Electric current traces: a qualitative description

Current intensity crossing free-standing bilayers of different hydroperoxidation degrees as a function of time and applied voltage are recorded during electroporation experiments. As for any statistical phenomena, the visual aspect of the traces varies strongly from experiment to experiment even under the same conditions. Examples of traces from our system are shown in Figure 3.12 for three different fractions of oxidized lipids (0 %, 50 %, and 100 %) and for six different applied voltages ( $\pm 50$  mV,  $\pm 100$  mV, and  $\pm 150$  mV). Traces for pure POPC (0 % of POPC-OOH) and 50 % mixtures compare well with results from [81] who did not report results for 100 % POPC-OOH. A general trend is observed that corresponds to an increase of the charge transport both with independently the increase of lipid hydroperoxidation and with the electric field applied.

An asymmetry that favors charge transport for negative electric potential can be observed. It occurs when it drives  $K^+$  ions from the large volume ( $\sim 150 \mu\text{L}$ ) above the membrane into the 60 pL well below the membrane, and correspondingly drives  $Cl^-$  ions in the opposite direction. The cause of such asymmetry is not known yet, but one may believe it results from one or a combination of the several intrinsic asymmetries of the Meca 4 chip: different volumes above or below the membrane, membrane anchoring at the edges of the well, electrochemistry events at the electrode in the well. Nevertheless, it has only a limited impact on our observations and it does not perturb the precise quantitative analysis of the results.

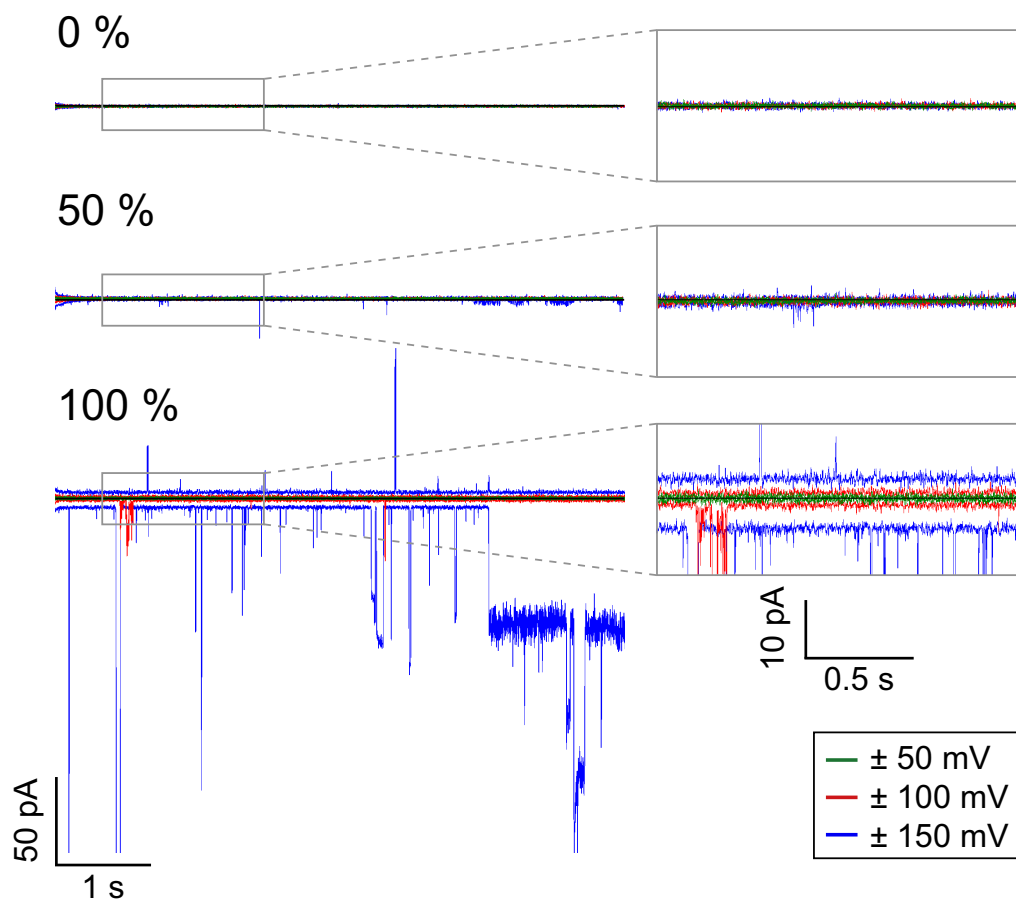


FIGURE 3.12: Examples of current traces obtained under voltage-clamp conditions for POPC membranes containing 0 %, 50 %, or 100 % of POPC-OOH under applied voltages of  $\pm 50$  mV,  $\pm 100$  mV and  $\pm 150$  mV. Expanded traces are shown in the right panels.

To rationalize the observed signals, it is useful to establish a correspondence between the shape of the traces and the membrane phenomena which they likely arise from. Figure 3.13 proposes such correspondence for the basic conduction events that can be identified. Four typical fragments of experimental data are displayed with their corresponding schematic electric signal and the likely membrane configurations that lead to such signals. Detailed explanations of each signal fraction are given in the following sections.

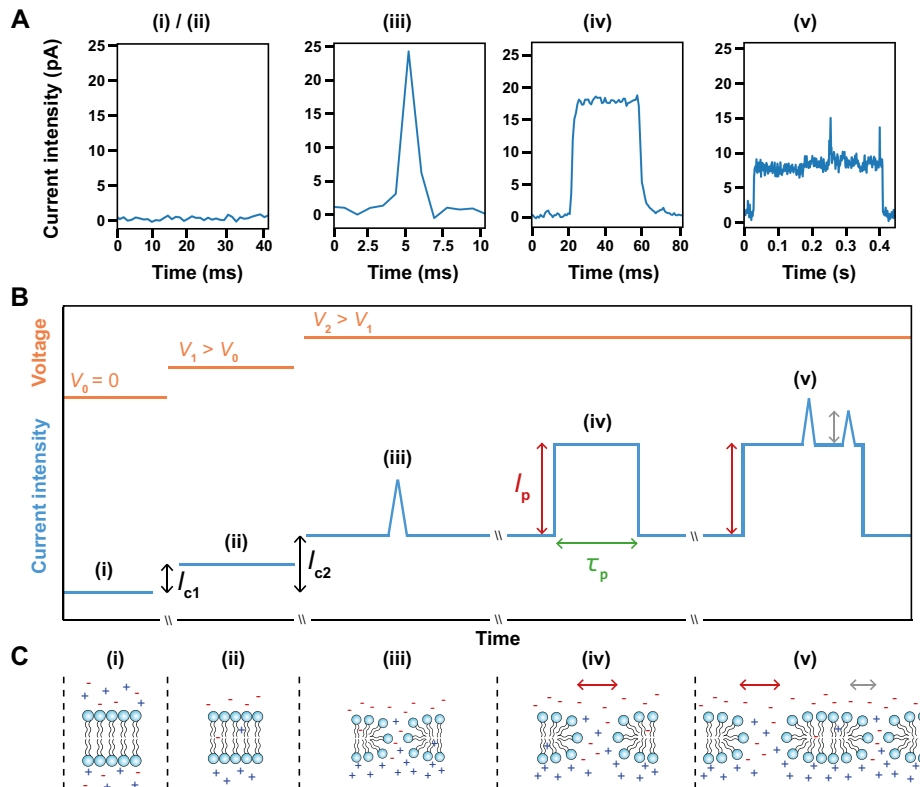


FIGURE 3.13: Current traces and associated membrane geometry. (A) Identifiable sections of the current intensity traces  $I(t)$  along with (B) their schematic representation and (C) their presumed membrane conformation. Under no (i) or small (ii) applied voltages, the current fluctuates smoothly about a small ( $\sim$  pA) average current. Charge accumulation on both sides of the membrane acts as a capacitor, and a small number of ions cross the membrane. Under larger applied voltages, the opening of short lifetime pores (iii) and long lifetime pores (iv) can be detected by the sudden rise of the current corresponding to angstrom-size pores. Pores can accommodate lipid heads along the pore rim, in a conformation referred to as hydrophilic pores. When a small amount of pores is opened they can still be individually detected in the current traces (v).

### 3.2.3.1 Signal baseline: the intrinsic electropermeability

Every abrupt conductive event rests on a base current averaged  $I_c$  with typical noise of  $\sim 2$  pA, present in all traces. In the absence of an applied voltage ( $U=0$  mV), one has  $I_c = 0$ : the membrane simply separates two volumes of the ionic solution. Ion crossing from one side to the other is possible but rare and it does not result in a net current (Figure 3.13.i). When a voltage  $U$  is applied, a finite value of  $I_c$  is observed of the order of a few picoamperes (Figure 3.13.A). It corresponds to the transport of individual charges across the entire membrane, and as further described below its value is directly related to the membrane intrinsic permeability with respect to the electrolyte, here KCl. Charges accumulated on both sides of the membrane act as a capacitor of a few picofarads, and a small number of ions cross the membrane. Charge accumulation at the membrane interface under the electric field is represented in Figure 3.13.C. Under 100 mV we estimated roughly one charge condensed per 350 lipids.

### 3.2.3.2 Abrupt intensity jump: pore opening

Additionally to this average current, several other conductive events can be detected, of variable amplitude and duration. Upon increasing voltage the traces can display, sudden changes in the conductance levels as shown in sections (iii)-(v) of Figure 3.13, that either reach a maximum and immediately - (iii) - or some time later - (iv) - decreases towards the baseline. The sudden increase in the amount of charge transported across the membrane is interpreted as the consequence of the creation of a new spatially localized aqueous pathway through which ions can freely move. Such pathways are generally designated as pores, and the number of charges conveyed through the pore is a function of the applied voltage, the ion concentration, and importantly for the interpretation of the results, the pore size. Pore opening and closing follow their own statistical dynamics, thus pore diameter is given by a time dependent function  $D_p(t)$ . Since pore opening is found to happen in a few nanoseconds by simulations, under our experimental condition (dynamic variations being limited by  $\tau \sim 2.8$  ms) one may approximate pore opening dynamic as a square gate functions with two limiting situations:  $D_p$  while the pore is open and 0 otherwise as seen in Figure 3.13.

Section (iii) shows a signal, that we arbitrarily name short-lived pore, that corresponds to the opening and closing of pores with a lifetime  $\tau_p < 10$  ms. Section (iv) shows the opposite example of a long-lived pore where  $\tau_p > 20$  ms  $\gg \tau$  and thus a stationary intensity value can be reached before the pore closes.

Phospholipids involved in the formation of hydrophilic pores reorganize in such a way that all the inside pore surface is carpeted by phospholipid heads as shown in sections (iii) to (v) of Figure 3.13.C. It should be stressed that such traces correspond to the formation of a time isolated *single* pore in the whole membrane, and thus, that only a vanishing fraction of the membrane lipids is directly involved in pore formation, estimated as less than one part per billion for a 1 nm pore radius in a membrane of 40  $\mu\text{m}$  diameter.

### 3.2.3.3 Complex traces: tentative apprehension

When more than one pore at a time is present in the membrane, the complexity of the traces increases, often to a point where the correspondence between the intensity and the state of the membrane cannot be made. Section (v) of Figure 3.13 shows a more complex signal where this connection is still possible, with the opening of a long-lived pore followed twice by the opening and closing of short-lived pores and eventually by the closing of the long-lived pore. Note that the signal does not provide any information about the relative localization of any of the pores, one could for instance have the second short-lived pore opening at the same place as the first one, or in a far located position.

Examples of recurrent traces of larger complexity, and with no straightforward interpretation are displayed in Figure 3.14. We describe in the following our hypothetical interpretation of these traces.

Pore formation being a statistical mechanism, one may expect a Poisson distribution for pore opening over time. However, it is quite common to observe in the  $I(t)$  traces cluster of conductive events as displayed in Figure 3.14.A. This phenomenon can be interpreted as the alternation of a unique pore between an open and a closed state. It could also be caused by the formation of interconnected pore

networks, formed by pores opening and closing near each other. The development of microscopy observation of the membrane under electroporation experiments would be very useful to clarify what really happens when such conductive events are recorded.

Long lifetime pores are quite interesting, easy to study when isolated in time, but much harder when overlapped. Figure 3.14.B shows what we believe to be a pore size relaxation with characteristic time in the second range, much larger than the pore opening and filtering time constant. In panel C, an example of a long-lived pores signal shows a recurrent intensity around 20 pA. This constant value, despite opening and closing, could be interpreted as one (or several) pore(s) opening with a specific size. The idea of a pore being able to open and close alternatively gives, in our opinion, clue to the existence of the pre-pore state already mention by previous studies [119].

Pein et al. [183] enumerate diverse mechanisms that can interfere with electroporation signal interpretation. One of them is the *heterogeneous noise* which is the increase of noise fluctuation during a conduction event. Basically, the noise increases with the current intensity recorded. We identify the same mechanism in our signals as observed in the first part of the signal in Figure 3.14.D, however, sometimes the fluctuation is not always proportional to the current intensity as seen in the second part of the signal, where noise is different for pores of similar intensities. This increased fluctuation is not understood up to now, the membrane may enter in a different unknown fluctuating conductive state, or it could be artifacts from the electronic device.

Figure 3.14.E exhibits what we could call typical complex signals, with high intensity fluctuation very close in time, and without going back to the baseline in between. The membrane can enter in this complex regime and come back to a fully closed state afterward. We are not able to give interpretation to such signals.

Baseline fluctuation artifacts are observed in our data, they may be caused by membrane anchoring or heterogeneity in the bilayer. As an example, we observed in some of the recorded signals periodic oscillations with very different shapes and periods (see Figure 3.14.F), we were not able to find the source causing such signals by trying to isolate as much as possible the Orbit mini device or analyze the external condition when such oscillation where observed. Another rare baseline artifact seen is the linear increase in the baseline intensity over time - not shown here-. Artifacts impacting electroporation data analysis were already reported previously [183].

Since the interpretation of electroporation signals is challenging, we focus on easily identifiable pores and did not study these complex signals as thoroughly as isolated *single* pores and long-lived pores. The complexity of electroporation traces of pure lipid membranes can explain the rare efforts made to interpret them.

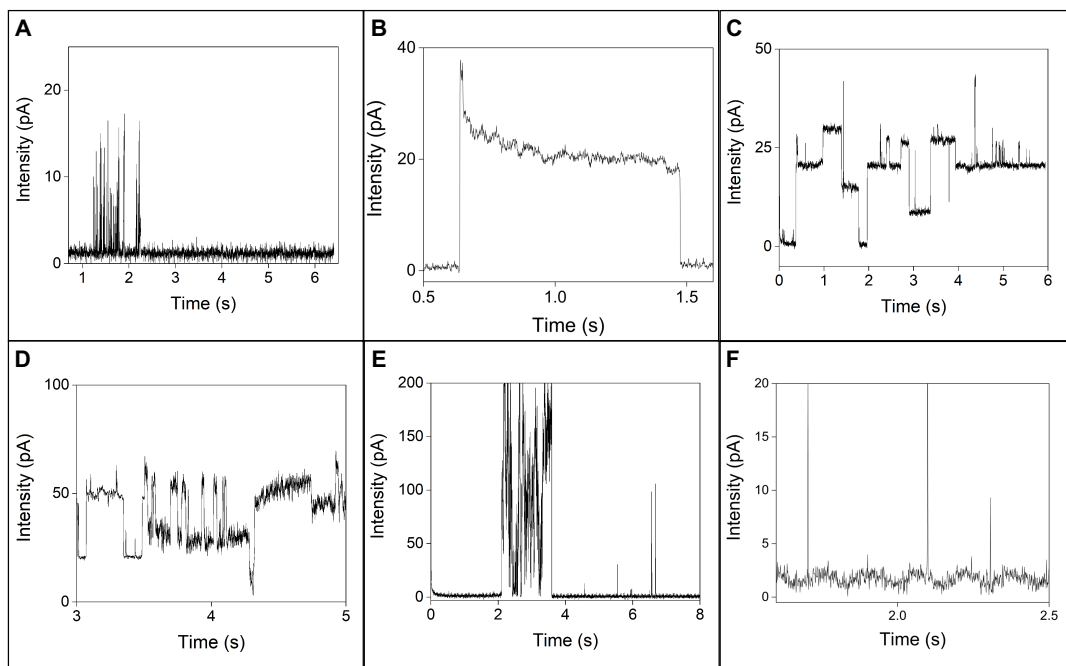


FIGURE 3.14: Typical  $I(t)$  traces observed during electroporation, all intensities are presented as positive. (A) shows the clustering of pore formations in time (POPC under  $-225$  mV). (B) shows the intensity - size - relaxation of a long lifetime pore (POPC under  $-225$  mV). (C) shows the opening of long lifetime pores of specific sizes (POPC containing 70 mol % of POPC-OOH under 100 mV). (D) Example of two types of heterogeneous noise (POPC containing 70 mol % of POPC-OOH under 125 mV). (E) shows complex signals eventually going back to a more stable state (POPC under  $-300$  mV). (F) Example of a periodic baseline oscillation (POPC containing 70 mol % of POPC-OOH under  $-150$  mV).

### 3.2.4 General membrane behavior under electric stress

#### 3.2.4.1 Membrane rupture

When a membrane is subjected to a too high electric field, it irreversibly ruptures. Many hypothetical scenarios can be behind this phenomenon: a very large pore, a localized large tear, or complete instability.

In any case, since the membrane rupture is caused by the application of a too high electric stress, it sets the voltage boundary over which membranes can be studied  $[-U_{rupture}, U_{rupture}]$ . Being of a statistical nature, we map here the probability for membrane survival as a function of voltage and hydroperoxidation degree (see Section 3.1.6.2). The membrane survival probability, *i.e.* the complementary to one of rupture probability, is shown in Figure 3.15 as a function of voltage for the different membrane compositions. The disparity of membrane rupture voltage among membranes of the same composition is shown in the slope of the curves.

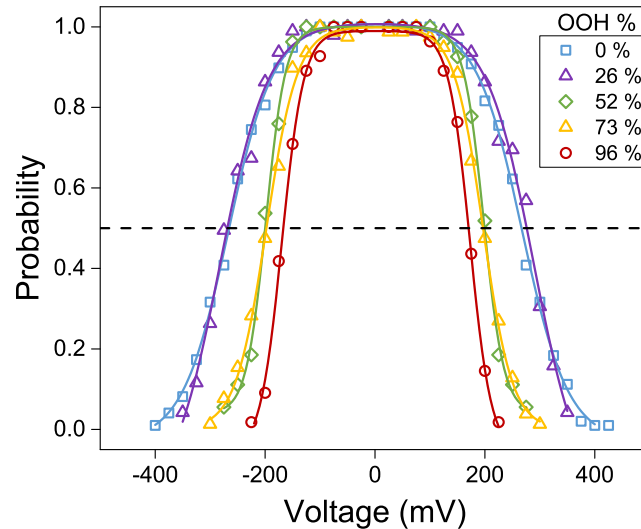


FIGURE 3.15: Probability of the membrane survival as a function of the applied voltage (during 6 seconds) and hydroperoxidation degree of POPC membranes. Symbols represent the calculated probability from at least 50 membranes. Solid lines are a visual guide to the eyes.

As stated before, the voltage increases membrane rupture probability. In addition, we show here that hydroperoxidized membranes are less resistant to voltage and often rupture for lower electric stress. As the figure shows, while pure POPC membranes (0 % -OOH) have a 50 % probability of breaking at 300 mV, for nearly full hydroperoxidized membranes (96 % -OOH), the 50 % rupture probability is reached at only 175 mV. As we will see below for all investigated phenomena, hydroperoxidation renders the membranes always more responsive to electric fields.

Such rupture events often occur soon after a new value of the applied voltage (visible in the traces and confirmed with the constant membrane rupture probability as a function of the voltage application time -not shown-). The membrane breakage recorded manifests with a characteristic time similar to  $\tau$  letting us believe the rupture occurs in less than a few milliseconds. This would discard the hypothesis of the pore size relaxation to a critical radius since it is believed to occur in a few seconds as discussed just before.

#### 3.2.4.2 Membrane intrinsic conductivity

If one pictures the lipid membrane as a barrier restricting ionic mobility, the standard formulations by Goldman, Hodgkin, Katz, and others [10, 176, 190–192] can be used to predict the ion current density  $i_c = I_c/S$ , as a simple square-shape potential that depends only on the barrier height  $\Delta E_m$  and on a barrier thickness  $d$ . This leads to a linear relationship between the current  $I$  and the applied potential  $V$  as illustrated in Figure 3.16.

However, current-voltage relations  $I(U)$  with a supra-linear component can be obtained from the trapezoidal barrier functions with two lengths,  $d$  the total membrane thickness - basis of the barrier - and  $b$  the smaller hydrophobic thickness - top of the barrier at height  $\Delta E_m$  - [193] as schematically represented in Figure 3.16. This and other barrier shapes were developed to better describe the gradual increase of the barrier height as the ions cross the hydrophilic phospholipid head region until they reach the hydrophobic core of the bilayer. Conductivity predictions from the

trapezoidal barrier are often written as a cubic expansion of the applied potential (equation 3.2):

$$i_c = e C_{ion} P_m u \left( 1 + \left( 1 - \frac{b^2}{d^2} \right) \frac{u^2}{24} \right) \quad (3.2)$$

with  $u = eU/(k_B T)$  (dimensionless),  $e$  the elementary charge (C) and  $C_{ion}$  the ion concentration ( $\text{mol.m}^{-3}$ ). With the trapezoidal model,  $i_c$  is for small applied voltages a linear function of  $U$  but acquires a supra-linear character as the voltage increases. In the linear regime, the intrinsic barrier that the ions need to cross is only weakly modified by the electric field and the height of the barrier related to the permeability  $P_m$  dominates the ion displacement across the bilayer. As the applied voltage increases, the barrier is distorted by the field.

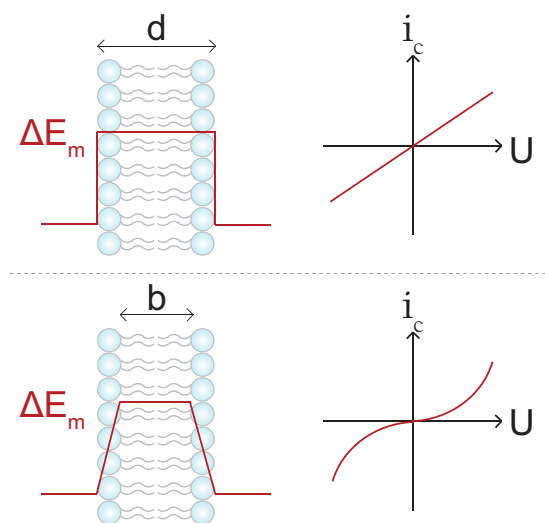


FIGURE 3.16: Shape of the  $i_c(U)$  curves depending on the membrane potential shape.  $\Delta E_m$  is the membrane potential barrier,  $b$  the hydrophobic thickness of the bilayer and  $d$  the total thickness.

Figure 3.17.A presents  $i_c(U)$  data and fitted curves for all the hydroperoxidation degrees. Data are extracted from measurements as explained in materials & methods by carefully excluding all the events that can be identified as pores so that only the intrinsic electropemeability is reported. For better comparison with results from the literature, we plot in the Y-axis both the measured current density  $i_c$  (left) and the corresponding current  $I_c$  crossing a membrane of  $42 \mu\text{m}$  diameter, the average diameter of membranes as inferred above from capacity measurements.

Solid lines Equation 3.2 fit well the data over a voltage range that depends on the hydroperoxidation degree. The dashed lines indicate the continuation of the solid line fit but they do not have a good correspondence to data anymore. Nevertheless, it is still possible with these fits to determine the two fitting parameters: the permeability  $P_m$  from the linear term and the ratio  $b/d$  from the cubic one.  $P_m$  of a specific POPC-OOH/POPC composition, is first obtained with a linear fit on each membrane  $i_c(U)$  over a restrained range of voltage  $[-100,100]$  mV, and then averaged for membranes of a same composition. The obtained values are plotted in Figure 3.17.B. The ratio  $b/d$  is then determined by fitting the average  $i_c$  with the cubic model (equation 3.2) by fixing the linear part with the previously found averaged  $P_m$ . For high voltage, the  $i_c(U)$  curves are not properly fitted by the equation 3.2, cubic fits are

then applied on different ranges of voltage  $[-U, U]$ , to determine the best range giving a coherent cubic coefficient and a good fit quality ( $R^2$ ). Fits with an exponential function do not bring a better agreement between predicted and observed values.

$P_m$  for pure POPC is measured at  $2.8 \times 10^{-12} \text{ m.s}^{-1}$ , consistent with reported permeability values for the anion  $\text{Cl}^-$ . We believe  $\text{Cl}^-$  dominates charge transport across the lipid membrane since water molecule polarization at the bilayer interface is found to facilitate anions transport over cations [10, 12].  $P_m$  values increase steadily with the peroxidation level, up to  $11 \times 10^{-12} \text{ m.s}^{-1}$  for the fully hydroperoxidized bilayer, an increase of roughly a factor 4, as shown in Figure 3.17.B. Fittings return an almost constant value for the ratio  $b/d = 0.87 \pm 0.05$ , typical for values reported in the literature for lipid membranes [194].

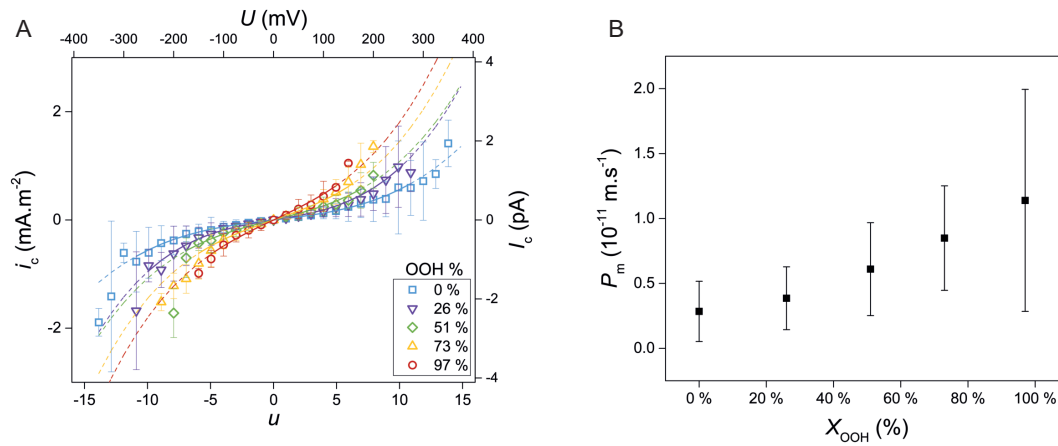


FIGURE 3.17: Intrinsic membrane electropermeability. (A)  $i_c(u)$  is the average current flowing through a pore-free membrane. The left axis measures current density  $i_c$  while the scale on the right axis expresses current  $I_c$  across a patch of  $42 \mu\text{m}$  diameter. The bottom axis displays normalized voltage units  $u = eU/(k_B T)$  while applied voltage  $U$  is shown at the top horizontal axis. The solid line represents the cubic fit of the data, dashed lines show when the fit starts to be less relevant. (B) Permeability  $P_m$  of POPC membranes as a function of  $X_{\text{OOH}}$ , the molar fraction of hydroperoxidized lipids. For both panels, error bars represent the standard deviation.

### 3.2.4.3 Probability of pore opening

For large enough applied voltages  $U$ , the intensity traces show the emergence of ionic transport across the membrane through pores, as depicted above in sections (iii), (iv), and (v) of Figure 3.13. Electroporation is a mechanism that requires a minimum applied potential called  $U_{\text{threshold}}$ , from which pores start to open. We evaluate for each membrane composition the probability for a membrane to remain free of pores during the six seconds when a constant voltage is applied. Figure 3.18 shows this probability for each membrane composition. Increasing the POPC-OOH amount in membranes results, at any imposed voltage, in an increase of the probability of opening at least one pore per membrane and in a decrease of  $U_{\text{threshold}}$ . For instance, hardly any pore can be detected for pure POPC membranes at applied voltages lower than 50 mV, while for the same voltage in half of the pure POPC-OOH membranes, at least one pore is observed in the 6 s of voltage application. The shape of the probability curves is indicative of significant heterogeneity in membrane behavior

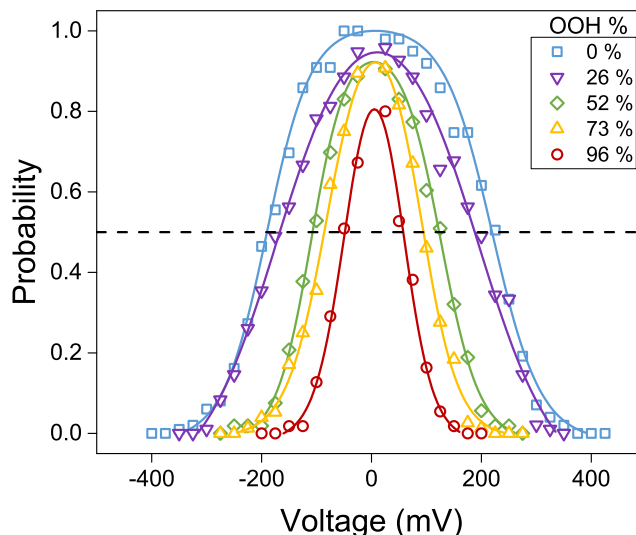


FIGURE 3.18: Probability for membranes to be free of pores during 6 seconds as a function of the voltage and the hydroperoxidation degree of POPC membranes. Symbols represent the calculated probability, solid lines are visual guides to the eyes. The dashed line represents the half probability of pore opening.

As pore opening requires an important rearrangement of the lipid, at least locally in the neighborhood of the pore, one might wonder if some lipid reorganizations can impact the  $I_c(U)$  curves, and thus attempt to correlate some of the features to the probability of pore formation. As reported in section 3.2.4.2, the supra-linear behavior of  $I_c(U)$  cannot be accurately described by equation 3.2 above a given voltage  $U_{\text{cubic}}$ , which depends on  $X_{\text{OOH}}$  as the limit between the continuous and dashed lines (Figure 6.8).  $U_{\text{cubic}}$  correlates with voltages at which pore opening probability reaches values close to 0.9, defined as  $U_{90}$  and being determined in Figure 3.18. Figure 3.19 shows the correlation between  $U_{\text{cubic}}$  and  $U_{90}$ . Thus, the trapezoidal model behind equation 3.2 stops to be valid when the electric fields are high enough to bring the membrane into a high probability of pore opening conditions.

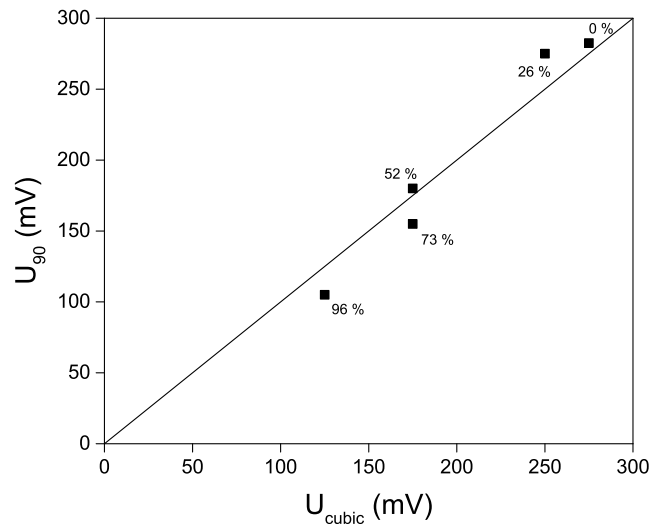


FIGURE 3.19: The validity range of the trapezoidal representation of the membrane potential  $U_{cubic}$  correlates to a high enough voltage that corresponds to the probability of opening at least one pore in 6 s close to 0.9,  $U_{90}$ .  $X_{OOH}$  values are given for each corresponding data point.

#### 3.2.4.4 Identifiable pores and other events: a study of different regimes

To provide a finer description of the pores opened by the membranes, we classified pores into three different categories a) *short lifetime pore* when it closes in a time  $\tau_p$  smaller than 10 ms, b) *long lifetime pore* if  $\tau_p > 20$  ms and c) *complex behavior* corresponding to all other types of conduction events, where the correspondence between the trace and the state of the membrane cannot be established. The probability for a membrane to open a pore of each of these three categories (regardless of the other categories) has been determined for every applied voltage and membrane peroxidation degree and displayed in Figure 3.20.

As the figure shows, the opening probability increases with voltage for all classes of pores. Due to membrane rupture, the curves reach a maximum before declining to zero, explained by the incapacity of observing any pore opening. In addition, membrane behavior is heterogeneous and sometimes depend on the membrane stability, as we saw that more stable membranes were the one forming fewer pores but surviving to higher voltages.

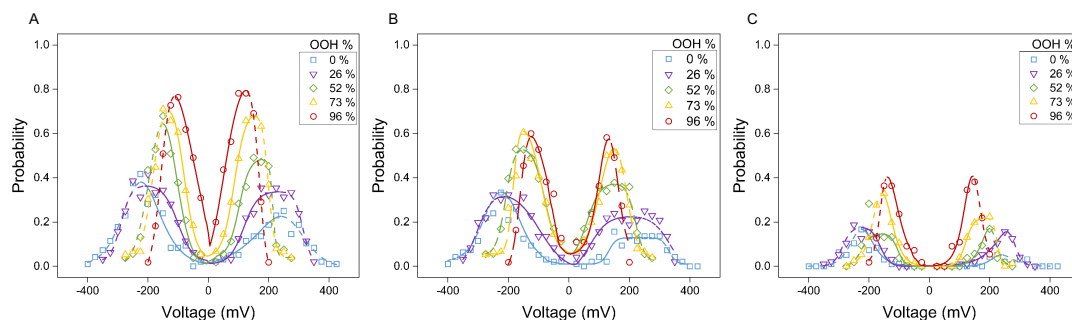


FIGURE 3.20: Membrane probability to open (A) short, (B) long lifetime pore or (C) exhibiting complex behavior at different voltages and lipid hydroperoxidation degree. Symbols are the experimental probabilities, solid lines are visual guides for relevant probabilities and dashed lines are visual guides for biased data due to membrane rupture.

For any given membrane composition, short lifetime pores are predominant in membrane traces -nearly seen in every membrane-, hydroperoxidation however increases their frequency. Long lifetime pores appeared unevenly distributed among the traces of different bilayers -regardless of the POPC-OOH amount-, for some bilayers, long pores rarely open, while others systematically display long pores over the full sequence of applied voltages. This heterogeneity in the membrane behavior may be explained by the presence of impurities in some membranes, initiating stable pore openings. Long-lived pores observed in pure lipid membranes are usually reported to occur at temperatures close to the lipid phase transitions, ions being suspected to cross more easily at the thin interface between two phases [134]. In our conditions we are way above the transition temperature for the full range of POPC-OOH/POPC composition (see Chapter 2, section 2.2.2.2). Melikov et al. [119] explain that if impurities are triggering pore formation and pre-pores, these impurities must also exist in biological membranes.

Clearly, short lifetime and long lifetime pores open over the same voltage range. Membranes of each composition were able to open pores of every category, with a net increase of the pore opening frequency with hydroperoxidation degree. More complex signals are triggered by slightly higher voltages but do form for all membrane compositions.

### 3.2.4.5 Membrane average conductivity

As the probability of pore formation increases with both voltage and hydroperoxidation, their contribution to the total ionic current across the membrane eventually dominates the signal. A measure of this current is provided by the value of  $\bar{I}$ , the current averaged over the full duration of the measurement. Although the total average current cannot discriminate between different modes of charge transport, it provides a benchmark value and it is, as such, a quantity often reported within the context of Black Lipid Membrane (BLM) electrical measurements.

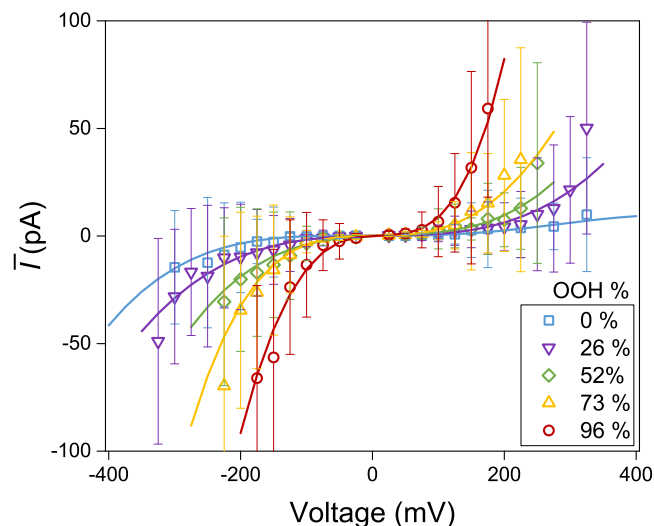


FIGURE 3.21: Mean current intensity  $\bar{I}$  as a function of the applied voltage for the different lipid membrane compositions. Solid lines represent visual guide to the eyes and error bars the standard deviation.

Figure 3.21 displays  $\bar{I}(U)$  curves for POPC membranes containing an increasing amount of POPC-OOH. Comparable results are reported in Corvalan et al. [81] for a more restricted range of POPC-OOH/POPC mixtures. As for the intrinsic intensity  $I_c$ , the average total current  $\bar{I}$  increases non linearly with the voltage and the hydroperoxidation degree of the bilayer, however with a much higher contribution to the conductivity of the membranes as seen in Figure 3.22 for membranes under 150 mV. Intrinsic electropermeability is thus much less conductive than pore opening event, which is even more pronounced for high hydroperoxidation degree.

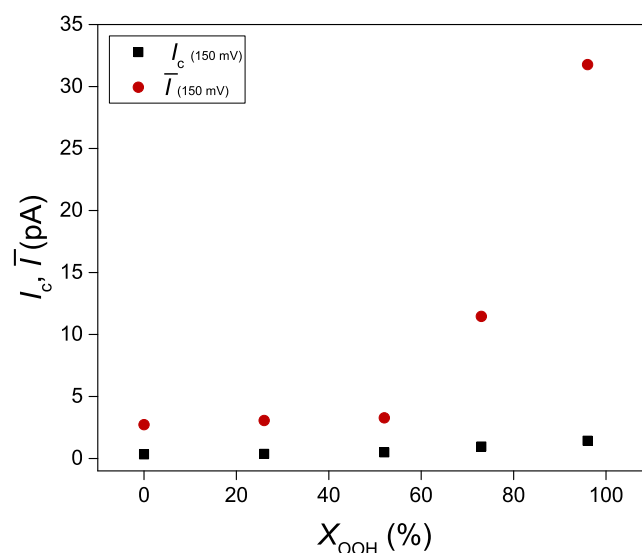


FIGURE 3.22: Comparison between the pore-free intrinsic current  $I_c$  and the total average current  $\bar{I}$  taken at +150 mV, as a function of hydroperoxydation.

### 3.2.5 Pore characteristics

#### 3.2.5.1 Lifetime distribution of identifiable pores

Using the *threshold method* (see section 3.1.6.6), we detect identifiable pores with a well defined opening and closing current jump (without lifetime discrimination).

Results from this pore-detection routine allow to built the pore lifetime distribution displayed in Figure 3.23 with 0.8 ms time bins. It is worth stressing that since no variation of pore lifetimes is observed with applied voltage, histograms are computed by grouping all pores counted for a given POPC-OOH composition irrespective of voltage.

As the figure shows, there is no noticeable trend difference in the distributions according to peroxidation degree. If one excludes the first point that is at the limit of resolution, the combined distribution follows a decay with a maximum distribution around 2.5 ms. Our findings are in line with those reported by other groups [119], which also find a mean pore lifetime of a few milliseconds independently of the applied voltage using DPhPC BLM geometry in 100 mM KCl and recording with 1 ms time resolution. Once again, the predominant frequency of short-lived pore opening is well represented compared to the long-lived ones.

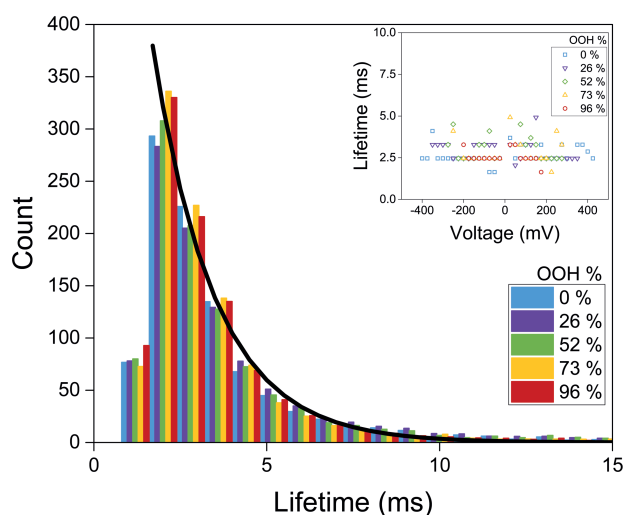


FIGURE 3.23: Pore lifetime distribution (bins=0.8 ms) normalized for 1000 pores. The solid line represents a guide for the eyes of the distribution decay. The figure in caption shows the independence of the pore lifetime median evolution with the applied voltage, justifying to group all lifetimes regardless of the voltage.

In the following, we discriminate between short and long-lived pores using the *threshold method* and *square gating method* respectively, to better determine each pore category's characteristics and abundance.

#### 3.2.5.2 Short lifetime pores

Given the average lifetime of short-lived pores  $\bar{\tau}_p = 1.8$  ms obtained by the *threshold method*, most of the pores detected in this category cannot reach a stationary conductive state which requires  $\tau_p \gg \tau_{RC}$  (Figure A.2). Proper measurement of  $I_p$  the current that flows across the pore of diameter  $D_p$  cannot be directly measured. It is nevertheless possible to extract pore intensity values  $I_p$  from the current traces using the pore maximum intensity  $I(\tau_p)$  and the device filtering time constant  $\tau$ .

Theoretical  $I_p$  values obtained can be associated to pores sizes  $D_p$  [195] using the equation 3.3:

$$D_p = 2\sqrt{\frac{b}{\pi\sigma} \frac{I_p}{U}} \quad (3.3)$$

with  $\sigma=1.29 \text{ S.m}^{-1}$ , the solution conductivity for a 100 mM KCl solution [196]. From the linear  $I_p(U)$ , we obtained an average diameter  $\bar{D}_p = 6.7 \pm 2.0 \text{ \AA}$  independently of hydroperoxidation degree as shown in Figure 3.24, comparable to the lower range of radii reported in the literature [33, 113, 119, 120, 132, 133]. This small value of the radius can be explained by our choice of recording current intensity with the smallest [-200,200] pA gauge to reduce the signal to noise ratio but at the same time does not allow us to characterize bigger pores than  $45 \text{ \AA}$  under 25 mV down to  $11 \text{ \AA}$  under 400 mV due to current saturation. No link has been reported between the pore size and the voltage [119], indeed for a specific voltage, membranes can open pores of different conductance and size but always with a similar average regardless of the voltage.

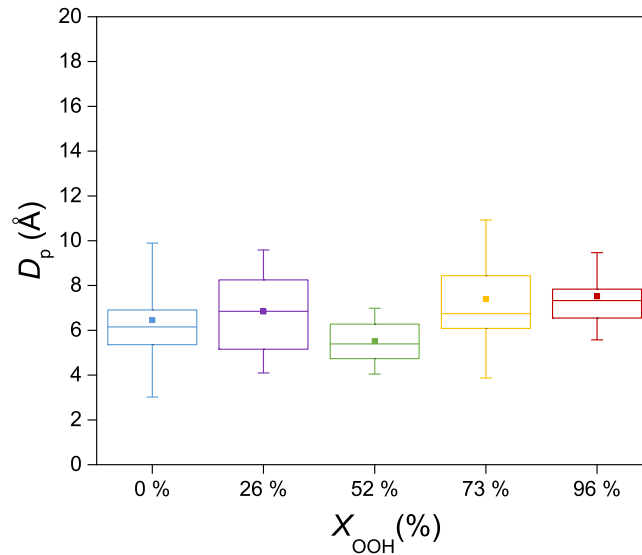


FIGURE 3.24: Average pore diameter  $D_p$  of short lifetime pores for different hydroperoxidation degrees  $X_{OOH}$ . The filled square represents the average, the middle line the median, the edges of the box the first and third quartile, and the whiskers the standard deviation.

We measure the frequency of short lifetime pores opening using the *threshold method* on only pores having lifetime  $\tau_p < 10 \text{ ms}$ . Figure 3.25.A shows the pore opening frequency  $N_s$  of short lifetime pores expressed as the average number of pore opening in one second for a given applied voltage. As the figure shows, the frequency increases with both voltage and POPC-OOH fraction in the bilayer.

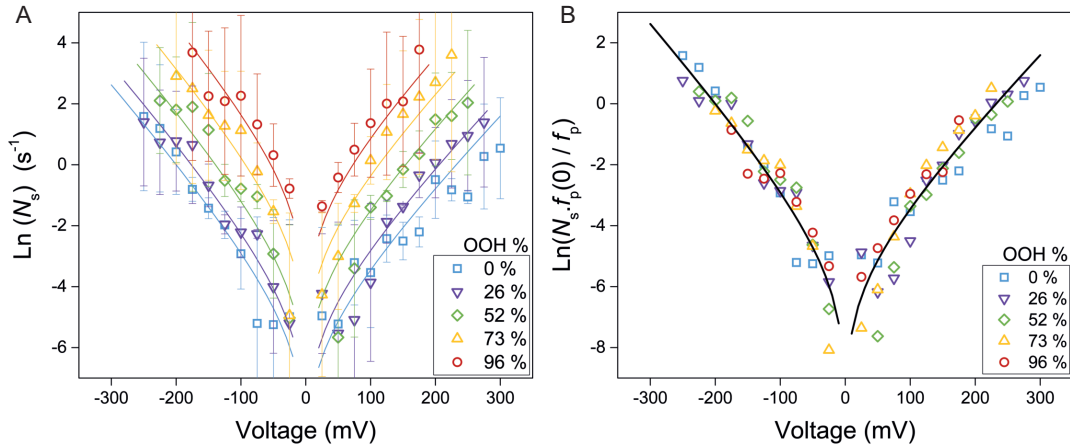


FIGURE 3.25: (A) Average number of short lifetime pores opening per second  $N_s$  as a function of the voltage for the different hydroperoxidation degrees in POPC membranes. Error bars represent standard deviation. Solid lines represent exponential fit. (B) The master curve is obtained by normalizing  $N_s$  over  $f_p(X_{\text{OOH}})/f_p(0)$ .

The semi-logarithmic representation of Figure 3.25.A reveals a nearly linear dependence of  $\ln N_s$  with applied voltage for all the samples, with an almost identical slope for all POPC-OOH fractions. This suggests that under our conditions, the frequency of pore opening  $N_s$  follows the empirical relation:

$$N_s = f_p u \exp(\alpha u) \quad (3.4)$$

with  $f_p$  the pore opening attempt rate ( $\text{s}^{-1}$ ) and  $\alpha$  a dimensionless experimental constant. All the information on the POPC-OOH fraction  $X_{\text{OOH}}$  is carried by the pore opening attempt rate  $f_p$  alone. The master curve in Figure 3.25.B is obtained by finding  $f_p(X_{\text{OOH}})/f_p(0)$  values that minimize vertical distance in the semi-logarithmic representation of all curves with respect to  $X_{\text{OOH}} = 0$ . Fits of this master plot give the pair of values ( $\alpha^+ = 0.50$ ,  $f_p^+ = 1.1 \times 10^{-3} \text{ s}^{-1}$ ) and ( $\alpha^- = -0.56$ ,  $f_p^- = 1.5 \times 10^{-3} \text{ s}^{-1}$ ) for respectively the positive and the negative branches. Figure 3.26 displays the influence of POPC-OOH fraction  $X_{\text{OOH}}$  on the normalized attempt rate  $f_p/f_p(0)$ . As the figure shows both the positive and negative branches are well described by the linear function  $\ln(f_p(X_{\text{OOH}})/f_p(0)) = 0.045X_{\text{OOH}} - 0.26$ .

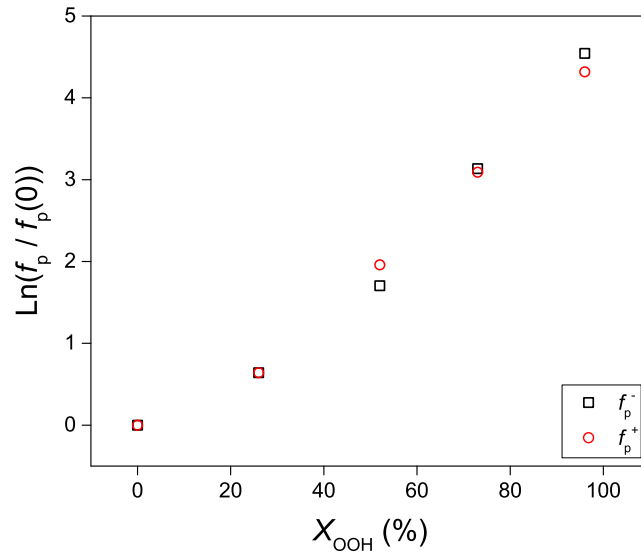


FIGURE 3.26: Pore opening attempt rate for positive  $f_p^+$  and negative  $f_p^-$  voltages for the different hydroperoxydation degree of membranes  $X_{OOH}$  (normalized by  $f_p^+(0)$  and  $f_p^-(0)$  respectively).

### 3.2.5.3 Long lifetime pores

Pores with lifetimes much larger than the intrinsic equivalent electric circuit time  $\tau_p \gg \tau_{RC}$ , reach a stationary current value despite the fluctuations. They exhibit similar current traces to the ones reported by T. Heimburg for bilayers near their main transition temperature [22]. These gating signals can as well evoke the signature of currents carried by ionic protein channels, which correspond in general to rather long-lived pores of a well defined size [28]. This study aims to determine if, similarly to proteins, lipidic membranes can open pores of a specific size -and thus conductivity-.

In practice, we developed the *square gating method* -see section 3.1.6.7- to filter the signal  $I(t)$  and obtain a signal only composed of constant currents of long lifetime. Each intensity level is linked to a long lifetime pore, even when overlapping each other. We then were able to collect information on pore size and lifetime similarly to the *threshold technique* used before. One should recall that as already stated, and seen in Figure 3.23 long-lived pores are much more rare than short-lived pores, and thus we have a larger statistical uncertainty when determining the characteristics of these pores. The average number of pore opening per second is determined similarly as for short-lived pores, however, data being quite noisy, no proper fitting of the curves could be done (not shown). One can still distinguish despite the noise, a general increase in the pore frequency with voltage and hydroperoxidation.

For these long-lived pores the intensity of each pore can be directly measured from the stationary value  $I_p$  reached by the current.  $I_p$  distribution does not give any statistical support for asserting that pores open with a fixed size -and thus conduct a fixed current- for membranes of a given composition. There is rather a broad distribution of currents, from which an average value can nevertheless be extracted. Significantly, the average current values do follow a linear relation with applied voltage, thus enabling to compute an average pore conductance corresponding to an average pore size of  $\bar{D}_p = 7.4 \pm 2.8 \text{ \AA}$ , a value close to the one found for short lifetime pores. We did not find any statistically significant variation in average currents with degrees of membrane oxidation as observed in Figure 3.27.

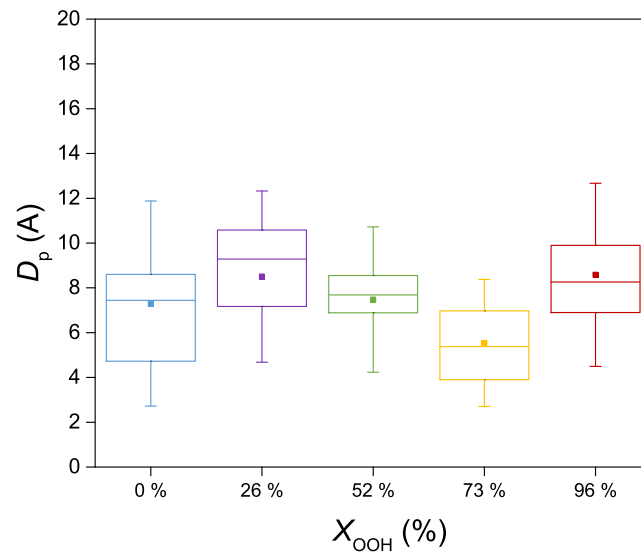


FIGURE 3.27: Average pore diameter  $D_p$  of long lifetime pores over the different voltages for different hydroperoxidation degree  $X_{OOH}$ . The filled squares represent the average, the middle line the median, the edges of the box the first and third quartile and the whiskers the standard deviation.

The lifetime distribution of pores lasting more than 20 ms shows, similarly to short lifetime pore distribution, indicating a decaying probability for pore having increasing lifetimes, see Figure 3.28.

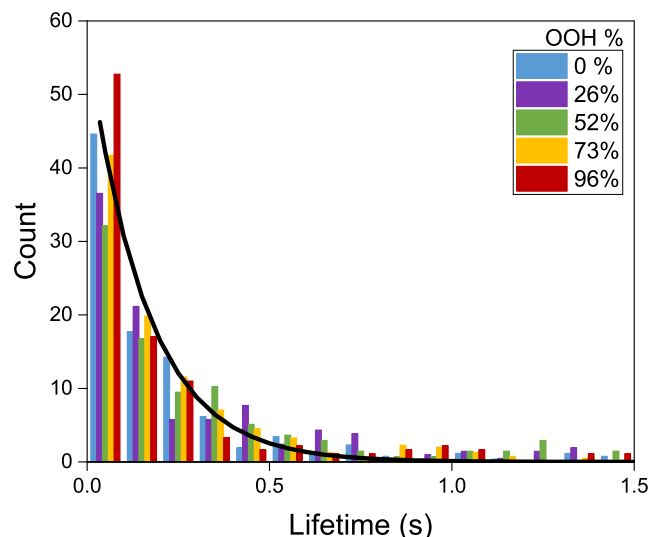


FIGURE 3.28: Pore lifetime distribution (bins = 100 ms) for long lifetime pores detected with the squared signal idealization technique (Normalized to 100 pores). The solid line correspond to visual guide for the eyes.

### 3.3 Conclusion

By measuring ionic current intensity across  $50\ \mu\text{m}$  BLM diameter, we are able to give a precise picture of hydroperoxidized membrane conductivity under electric field. It should be stressed that we can paint POPC lipid bilayers up to fully hydroperoxidized ones. This is likely due to the good control of hydroperoxidation that we can achieve, the use of only freshly hydroperoxidized lipids, and the small size of our wells that allows us to form more stable membranes.

As described in the Chapter 0, lipid hydroperoxidation is known to induce severe membrane modifications, but unexpectedly, the capacitance does not vary with the hydroperoxidation degree of the membrane. Given the smaller thicknesses of the oxidized membranes and the expected larger dielectric permittivity of their hydrophobic core, one would expect an increase in capacitance with lipid hydroperoxidation. The changes in the structure of the membrane are however complex: an important fraction of the tails bearing the peroxide groups adopt a snorkeling configuration, thus changing not only the hydrophobic core in a non-trivial manner but changing also the structure of the head region where the peroxide groups are added to the interface [29, 71, 79, 86]. The hypothetical balance of these effects to keep a constant specific capacitance with increasing hydroperoxidation poses an interesting question, to which all-atom simulations might provide some insight.

Optimal data acquisition in membrane electroporation studies requires not only to paint stable membranes but also to be able to increase the applied potential and collect data without premature membrane breakage. The quantitative evaluation of membrane survival probability under an electric field shown in Figure 3.15 provides a useful guide for experiment planning, especially regarding the lower survival probability at increasing voltages for hydroperoxidized lipid containing membranes.

The applied potential  $U_{rupture}^{half}$  measured at half membrane survival probability

(dashed lines in Figure 3.15) decreases irregularly with  $X_{OOH}$ . It is likely that membrane survival depends not only on the intrinsic membrane features but also more likely on other factors such as the heterogeneity of membrane anchoring discussed in section 3.2.2.

Another interesting aspect is that hydroperoxidized membranes usually exhibit numerous conduction events before breaking ( $N_s = 25$  pores per second for POPC-OOH under -175 mV), showing progressive signs of damage, while pure POPC membranes (or only weakly hydroperoxidized ones) rupture without any pre-rupture hint in most of the cases ( $N_s = 5$  pores per second for POPC at -400 mV). It gives the intuition that POPC membranes rupture suddenly, while hydroperoxidized membranes show a kind of *resilience* associated with the ability to release stress instead of irreversibly rupturing.

Conductivity measurements performed in free of pore membranes revealed an increase of factor 4 of the permeability  $P_m$  from a non hydroperoxidized membrane to a fully hydroperoxidized one. Such changes cannot be only explained by the small decrease ( $\sim 20\%$ ) of membrane thickness [69]. The observed increase is better interpreted as due to a lowering of the membrane barrier potential  $\Delta E_m = -\ln(4)k_B T$ , at least with respect to anion  $Cl^-$  that dominates transport here, consistently with the known increase of polarity of the inner membrane region [71].

The validity of equation (3.2) with  $P_m(X_{OOH})$  and a constant  $b/d$  ratio over a limited range of voltages shows that membranes can be accurately represented in that range by the same trapezoidal barrier potential shape with only a hydroperoxidation-dependent barrier height  $\Delta E_m$ . The range of validity coinciding up to the voltage range where the membrane has a high probability of opening at least one pore suggests that a distortion of the membrane structure might be required for the emergence of pore openings.

As the voltage is ramped up, an increasing number of diverse conduction events associated with the opening of pores is detected. Despite complex  $I(t)$  traces, a large number of events are easily identifiable with characterizable size and lifetime. Among these identifiable pores, the large majority has lifetimes of a couple of milliseconds, as shown in Figure 3.23 independently of the lipid hydroperoxydation and the voltage. As similar values have been already reported with other membrane composition [119], it is likely that pore lifetime only depends on parameters extrinsic to the membrane. The survival of such small pores over milliseconds or more suggests that they correspond to the so-called conductive hydrophilic pores: lipid head re-organization is expected to occur in tens of nanoseconds only after a (likely) non conductive water channel nucleates inside the membrane [135].

The identifiable pores that we detect, for both short and long-lived, open with a small average diameter of 0.7 nm, independent of voltage and hydroperoxidation state. Regardless of hydroperoxidation, pores that we detect have a similar average diameter and similar lifetime distribution independently of voltage, indicating that pore characteristics do not depend on membrane composition.

The number of short lifetime pores that we detect is a function of applied voltage and hydroperoxidation degree, the voltage effect on the pore formation frequency being independent of the hydroperoxidation degree since  $\alpha$  in equation 3.4 is a constant. Figure 3.26 shows that a fully hydroperoxidized POPC bilayer sees its activation barrier for pore formation lowered by about  $5 k_B T$ , with a roughly linear

dependence on  $X_{\text{OOH}}$  (see Figure 3.26). Thus, full hydroperoxidation lowers the barrier for pore formation by as much as an electric field of  $\sim 200$  mV, a rule of thumb that would be interesting to correlate with the molecular transformations induced by the insertion of the -OOH group in the POPC unsaturated chain [60, 73, 197, 198].

The voltage dependence that we observe does not follow the predictions of the standard model for pore formation in lipid bilayers, and its many variants [112, 120, 123, 124]. The dependence of pore creation rate is based on the *square* of the applied potential  $U^2$ , justified by the symmetry of the pore formation to negative or positive voltage, as well as the  $U^2$  dependence of the membrane tension involved in the Maxwell stress. However, the symmetry of the system is experimentally uncertain with a slightly higher response to negative voltages, moreover, the lipid head group and water molecule polarization are known to play an important role in the pore formation process but are not taken into account in this model. We do not know if this arguments could be enough to justify another kind of dependence to the voltage but their highlight some weak spots of the theory. In addition, to the best of our knowledge, this dependence has never been experimentally confirmed. Scarce data exists [119] that has been interpreted as proof of such quadratic variation [136], however, at the first glance data do not look more linear, thus a strong confirmation of this theory has not been reported yet. Our empirical data, following equation 3.4, suggests rather a direct dependence with the pore opening attempt rate  $f_p$  and the activation energy that is lowered proportionally to the voltage. Such linear dependence has also been reported in a paper combining experiments and numerical simulations, where they qualitatively discuss the action of the field on the dipolar state of the lipids [113]. Our results rule out the much discussed  $U^2$  reduction of the barrier for pore nucleation. Under our experimental conditions, we observe instead an  $\exp(\alpha U)$  increase in the number of pores formed during a given period. We anticipate many fruitful developments along the pore opening rate to better decipher the molecular forces and membrane properties that control pore opening.

Considering the constant pore characteristics (size and lifetime), the average conductivity  $\bar{I}$  increase can be fully attributed to the increased pore formation rate. By calculating each pore type (short-lived pores, long-lived pores, or complex signals) contribution to the actual membrane conductivity  $\bar{I}$ , we find that short-lived pores despite their predominant appearance frequency do not contribute consequently to the membrane conductivity ( $< 1$  pA for POPC-OOH membranes at 150 mV). Long-lived pores contribute mainly to the membrane conductivity ( $\sim 24$  pA at 150 mV for POPC-OOH membranes), meaning that complex regimes contribute only modestly to it ( $\sim 8$  pA at 150 mV for POPC-OOH membranes, considering a total intensity at 32 pA extracted from Figure 3.21).

Complex signals contribution is then not negligible, however, the complexity of the current intensity signals as described previously makes their analysis extremely challenging, explaining the scarcity of their precise description in the literature. The conduction mechanism underlying complex traces is still unclear, it is unknown if it comes from the membrane itself, its anchoring or from another process.

With this study analyzing many thousands of conduction events, we contribute to the discussion about pore formation in lipid membranes with a new set of statistically relevant data that challenges current views and brings fresh insight to the field. Our results reinforce the picture that has been unraveling over the last decade to describe fully hydroperoxidized lipid membranes: despite the strong molecular modifications that induce a larger area per lipid, a smaller thickness, and a weaker elastic

modulus, we find that these membranes retain their integrity and their barrier property to ions as observed by the GUV experiment and confirmed by the calculation of fully hydroperoxidized lipid membrane permeability around  $P_m = 11 \times 10^{-12} \text{ m.s}^{-1}$ . The work in this paper further shows that hydroperoxidized bilayers behave in a quantitatively different manner yet qualitatively standard one with respect to membrane intrinsic electropermeation and pore formation. They display a four-fold larger permeability with respect to the anion  $\text{Cl}^-$ , and open pores with a larger frequency at weaker electric fields but with the same slope ( $\alpha$ ). Our results provide not only a clear picture of the effects of oxidation on membrane electropermeability but contribute also to the understanding of the role of applied electric fields in pore opening in lipid membranes.

## Chapter 4

# Hydroperoxidized membrane: visco-elastic properties

Our structural and thermodynamic studies of the hydroperoxidized POPC and SOPC point to several non-standard features of these membranes, as discussed in Chapter 2. Briefly, lipid disorder is observed to increase without a concomitant decrease in self-assembly cohesion. This enlightens another unusual feature that had been reported by Prof. M. Kuimova group at Imperial College London, after in-situ oxidation of lipid bilayers: the increase of membrane viscosity [199]. Since in-situ oxidation produces other oxidized species beyond hydroperoxides, we joined our efforts with the Imperial College team to thoroughly investigate the viscosity of membranes containing several fractions of hydroperoxidized POPC. This was mainly the PhD work of M. Paez-Perez, I contributed by providing hydroperoxidized lipids and by participating in the meetings of the collaboration to discuss and plan experimental work, and to interpret results.

The pre-print of the paper "*Directly imaging emergence of phase separation in peroxidized lipid membranes*", currently under review, reports M. Paez-Perez work. Here, I summarize the main findings of that study.

## 4.1 Main results

### 4.1.1 Membrane viscosity

To assess the membrane viscosity, we use BODIPY based fluorescent probes (also called molecular rotors) BC10 and BC6++, which are sensitive to the viscosity of their environment. BC10 localizes more in the hydrophobic core, while the BC6++ probes the bilayer interface. These molecular rotors in a viscous environment see their intramolecular motion reduced, inducing a larger decay time of the fluorescence emission. It is then possible by using Fluorescence Lifetime Imaging Microscopy (FLIM) to measure the emitted photon lifetime  $\tau_{ph}$  (extracted from the fluorescence emission exponential decay) and thus calculate their environment viscosity  $\eta$ . The relation between the lifetime and the viscosity is usually established by doing a calibration curve measuring both parameters in solutions of easily measurable viscosity (such as methanol-glycerol mixtures) [200, 201]. In equations 4.1 and 4.2 are exposed these relations for both BC10 and BC6++:

$$BC10 : \log_{10}(\tau_{ph}) = 0.4569 \log_{10}(\eta) - 0.75614 \quad (4.1)$$

$$BC6++ : \ln(\tau_{ph}) = 0.5 \ln(\eta) - 1.9. \quad (4.2)$$

We first study vesicles made of POPC-OOH/POPC controlled mixtures using FLIM with BC10 and BC6++ probes. As seen in Figure 4.1.A, we obtain a linear increase in viscosity from  $159 \pm 21$  cP for pure POPC to  $241 \pm 16$  cP for POPC-OOH using the BC10 in LUVs. A very similar increase from  $144 \pm 6$  cP to  $239 \pm 16$  cP using BC6++ in GUVs is shown in Figure 4.1.B. These two measurements are very consistent with each other, however, they show higher viscosities compared to Scanavachi et al. [79] who observed a slight increase from roughly 35 cP to 40 cP. Moreover, the viscosity evolution is measured using BC10 probes during in-situ type II photohydroperoxidation with Tetraphenylporphyrin (TPP) as a hydrophobic photosensitizer ( $\lambda = 420$  nm) -whose degree of oxidation cannot be controlled properly-. We observed an increased viscosity from  $121 \pm 11$  cP to  $298 \pm 14$  cP.

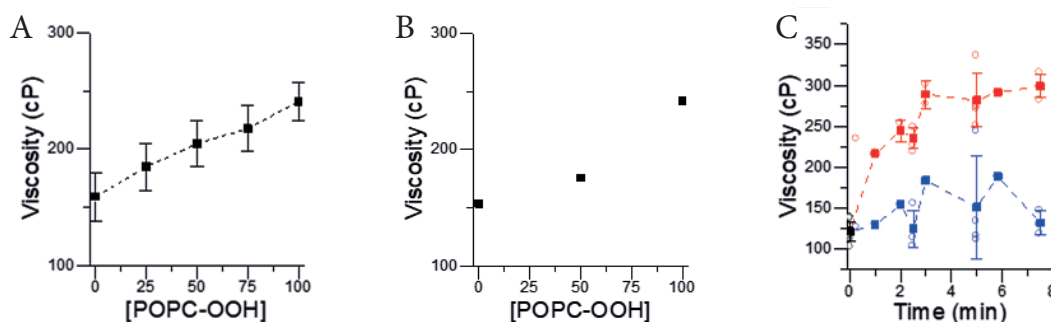


FIGURE 4.1: Evolution of the viscosity as a function of POPC hydroperoxidation, (A) using the BC10 probe in pre-made mixtures, (B) using BC6++ in pre-made mixtures and (C) using BC10 in in-situ hydroperoxidation (red curve) and no oxidation (blue curve). Error bars represent the standard deviation.

From all viscosity measurements above, POPC viscosity is compatible with a viscosity of a fluid disorder phase while POPC-OOH viscosity corresponds better to the typical viscosity of fluid ordered domains [202].

One can notice that the distribution of viscosity is much wider when increasing the amount of hydroperoxidation for both probes used in pre-mixed compositions as observed in Figure 4.2. Images exhibit very localized lifetime differences, evoking the possibility of phase coexistence.

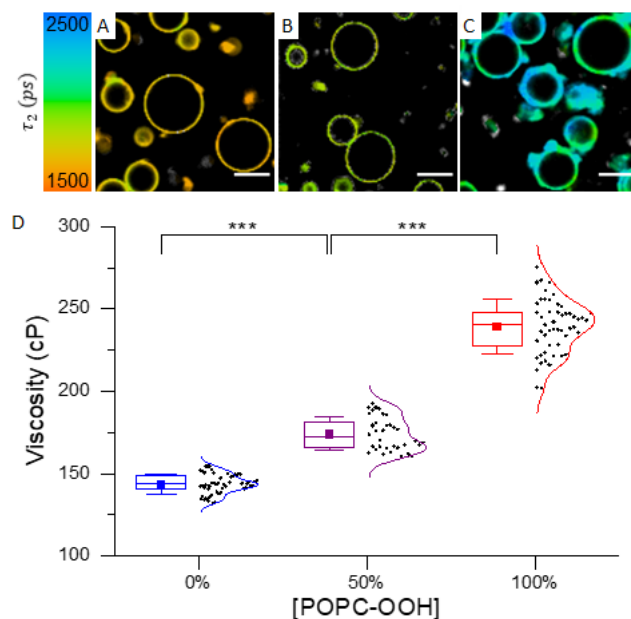


FIGURE 4.2: (A to C) FLIM images of POPC-OOH/POPC (0/100, 50/50 and 100/0) GUVs stained with BC6++ (scale bar: 20  $\mu\text{m}$ ) with (D) the associated viscosity distribution for the three different compositions.

#### 4.1.2 Membrane polarization and hydration

Here we use Laurdan (see section 2.1.7 from Chapter 2) to assess POPC-OOH/POPC bilayer polarity and hydration. We record by fluorimetry the Laurdan emission spectra in POPC-OOH/POPC controlled mixtures, the GP is calculated and plotted as exhibited in Figure 4.3.

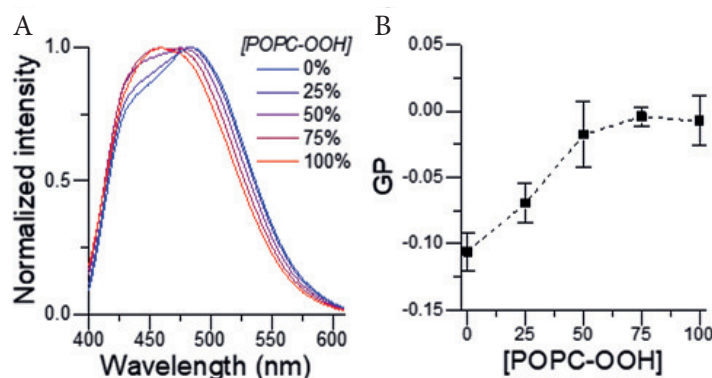


FIGURE 4.3: (A) Laurdan fluorescent spectra depending on the lipid membrane composition (at 22.5  $^{\circ}\text{C}$ ). (B) GP evolution calculated from (A) as a function of the amount of POPC-OOH using equation 2.1.

An evolution of GP from  $-0.11 \pm 0.01$  cP to  $-0.01 \pm 0.02$  cP is observed for vesicles composed of POPC to fully hydroperoxidized POPC. This result can be interpreted as a decrease in polarity and hydration, which can be associated with an increase in lipid packing and viscosity with the increasing fraction of hydroperoxidized lipid. Similar GP evolution is found in Scanavachi et al. [79], however they detailed that polarity is actually believed to increase with the addition of the peroxide group. Moreover from literature, hydration (water penetration) is also known to increase

with hydroperoxidation [60, 72]. The counter-intuitive increase in the GP may be explained by the contribution of an additional band at 460 nm which is not taken into account in the GP calculation.

The evolution of the GP as a function of the temperature is shown in Figure 4.4 for POPC containing different fractions of POPC-OOH. These curves are consistent with the one plotted for SOPC in Figure 2.12, with a slight decrease of the slope in the fluid phase when increasing the amount of hydroperoxidized lipids. These curves also point to a less fluid behavior of the hydroperoxidized membranes.

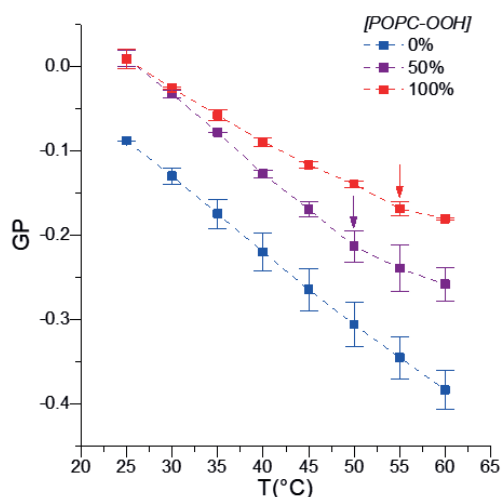


FIGURE 4.4: Evolution of the GP as a function of the temperature for vesicles made of POPC containing 0, 50 and 100 mol % of POPC-OOH. Error bars represent the standard deviation.

### 4.1.3 X-Rays: structural analysis

By using Small Angle X-ray Scattering (SAXS) and Wide Angle X-ray Scattering (WAXS), we evaluate the bilayer structural properties. With SAXS peaks (Figure 4.5.A), we observe two diffraction peaks related to the bilayer thickness and the inter bilayer distance. By increasing the hydroperoxidation amount in the membrane the first peak shift to lower  $q$  and both peaks become broader being the proof of a more heterogeneous sample and higher inter-bilayer spacing.

By fitting the data with Caillé theory [203] one can obtain the bending modulus. We find here that hydroperoxidation decreases the bending modulus, consistent with literature [79] and with a more conical shape.

WAXS analysis presented in Figure 4.5.B is more indicative of smaller distances. In the case of lipid bilayer, scattering can be related to the lateral space between lipids. With the increase in hydroperoxidation, the peak becomes much broader, being linked to the formation of lateral heterogeneities. This can be explained by the peroxide group positioning at the interface as well as the emergence of domains.

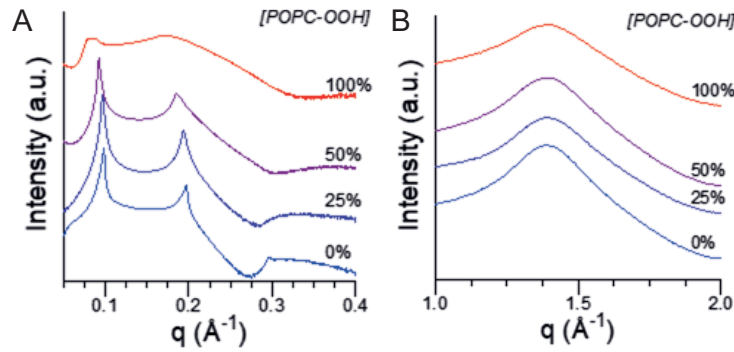


FIGURE 4.5: X-Ray scattering intensity profiles for POPC-OOH/POPC mixtures. (A) SAXS profiles and (B) WAXS profiles.

#### 4.1.4 Simulations

To confirm experimental results, additional simulations are carried out. We first show a decrease in the lipid diffusion coefficient of 20 % with hydroperoxidation, consistent with the decrease already reported in the literature [86, 87]. This is also consistent with the increase in viscosity reported above.

Moreover, we reveal a non trivial chain organization. Fully saturated chains (16:0) are found to be less ordered with the hydroperoxidation increase, consistent with the increased fluidity reported in the literature as well as the decrease in the phase transition temperature found previously in Chapter 2. However, the order present in the second lipid chain (18:1) seems to greatly depend on the position of the carbon under study. The ones close to the unsaturation (i.e. to the peroxide group and the interface) possess an order parameter higher than the other ones as exhibited in Figure 4.6. This increased order corresponds to the carbons close to the interface, consistent with the hypothesis that near the lipid head group a structured hydrogen network is formed, potentially explaining the increased viscosity while the hydrophobic core possesses an increased fluidity.

Finally, simulations suggest that POPC-OOH clusters preferentially with itself while POPC does not have preferential clustering, and pure POPC-OOH membrane possesses a heterogeneous lateral structure with diverse area per lipid and thickness, consistent with phase coexistence (see the paper attached).

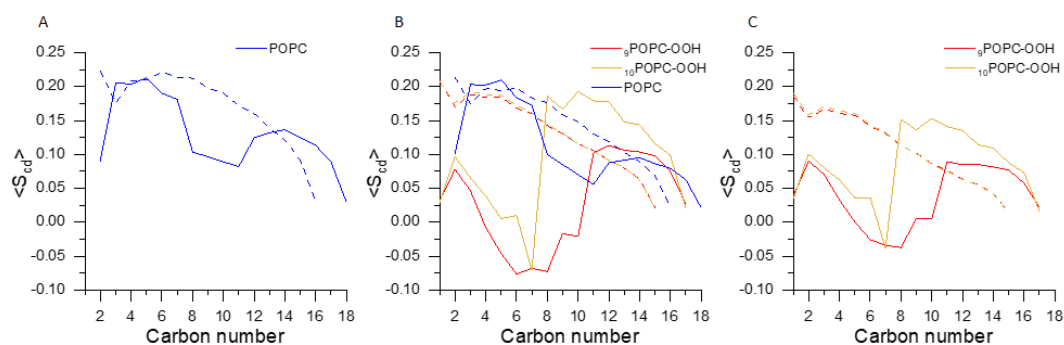


FIGURE 4.6: Average lipid order parameter  $S_{cd}$  as a function of the carbon position for (A) POPC, (B) a mixed POPC-OOH/POPC 50/50 mol % and (C) the two POPC-OOH isomers. Dashed lines correspond to the saturated chain (16:0) while solid lines to the (18:1) chain. POPC-OOH<sub>n</sub> correspond to POPC-OOH with the peroxide group on the  $n^{\text{th}}$  carbon.

## 4.2 Conclusion

The viscosity of POPC membranes containing an increasing amount of POPC-OOH increases from roughly 150 cP to 240 cP comparable with typical viscosities of the  $L_d$  and  $L_o$  phases respectively. Viscosity increase upon hydroperoxidation is a counter-intuitive result given the reduction of elastic modulus and chain order, but consistent with our findings of a larger membrane cohesion. It could also be related to the presence of composition heterogeneities.

Indeed, the image heterogeneities observed in FLIM (Figure 4.2) and the broadening of X-ray peaks with hydroperoxidation, all suggest the formation of lateral heterogeneities of various order with the addition of hydroperoxidized lipids. Simulations support the clustering of hydroperoxidized lipids, as well as the formation of domains of different structures and orders.

In addition, heterogeneity of behavior as a function of the depth of the bilayer can be suspected as well. Despite the decreased order in the hydrophobic core (Figure 4.6), the higher order present near the interface could lead to the increased viscosity and to the decrease in the lateral diffusion coefficient. Clearly, these results correlate well with the increased enthalpy of the main transition that we have measured for SOPC-OOH.

## Chapter 5

# Conclusions and perspectives

Lipid membrane permeability is a matter of interest for the study of biological function but also for applications in drug delivery and other fields. Due to their hydrophobic core, lipid bilayers are known to be quite impermeable to large or hydrophilic molecules, and especially to ions. Their principal role is to maintain compartmentalization, while translocation of molecules is controlled by protein assemblies.

Hydroperoxidation and other types of oxidation, often linked to the disruption of membrane properties and to cell dysfunction, lead to the appearance of very common diseases. Oxidation is known to decrease the bilayer thickness, increase the area per lipid, increase the membrane polarity and modify the fluidity, the elastic modulus and the dynamics of the membrane. All changes caused by oxidation seem to point out to an increase in membrane permeability that can in some cases damage the cell integrity and lead to its death. This process is even used in photo-therapy to induce cell apoptosis. Even if the consequences of oxidation on bilayer properties has gained interest over the time, the lack of availability of such lipids prevents a comprehensive understanding of changes induced by oxidation on the membrane structure and on membrane behavior.

Membrane permeability being often linked to other membrane properties such as its polarity, its thickness, and even its viscosity, it is thus necessary to study the membrane as a whole. The objectives of this thesis were 1) to offer a fast, easy and controlled method to obtain pure hydroperoxidized lipids in order to unlock further experimental studies of hydroperoxidized bilayers, 2) to better characterize intrinsic hydroperoxidized lipid membrane properties by focusing on their structural aspects: membrane thickness, lipid organisation and interaction, membrane viscoelasticity, and more importantly ionic membrane intrinsic permeability, 3) to characterize membrane behavior under an electric field as a function of its hydroperoxylation degree and 4) to provide new insight on pore formation in pure lipid membranes which is often neglected in favor of proteins ionic channels. For that purpose, POPC and SOPC membranes containing increasing amounts of POPC-OOH and SOPC-OOH respectively were studied. Hydroperoxidized lipids were obtained by photo-oxidation and characterized by cryo-TEM, DSC and electroporation. Moreover, we joined an effort at the Imperial College of London, for the characterization of hydroperoxidized lipid membranes by FLIM, fluorimetry, X-rays and numerical simulations.

We first improved a photo-oxidation method to obtain pure hydroperoxidized lipids in roughly 10 min by using high illumination power, an appropriate solvent and appropriate quantities of photosensitizer. This method offers a high yield of

80 weight % after photosensitizer removal and reach in average  $97 \pm 3$  mol % conversion. Hydroperoxidized lipids are found to be stable over several months when stored in an organic solvent at  $-20$  °C, however repetitive drying-solvating cycles leads to degradation.

Cryo-TEM shows the first images of vesicles assembled from hydroperoxidized lipids, thus confirming at the molecular level the formation of bilayers from these lipids. They further evidence a specific shape (crest and trough) of pure POPC and SOPC vesicles that disappear with the addition of the peroxide groups. It is thus clear that hydroperoxidized lipids induce different lipid organization. Even if such roughness in lipid SUV was already observed by cryo-TEM, their origin is unknown [163]. The resolution in the bilayer leaflet imaging allowed to measure the bilayer thickness. The addition of hydroperoxidized decreased the thickness of POPC bilayers up to 30 % and SOPC bilayers up to 23 % consistently with values reported in the literature [77].

As proposed by simulations [72] but never experimentally measured, the temperature of the gel to fluid phase transition of hydroperoxidized lipid membrane is believed to decrease with respect to its non-hydroperoxidized form. This would be induced by the increased disorder obtained from the specific conformation adopted by the carbon chains bearing the peroxide groups. We confirmed this hypothesis by DSC, and found a decrease of roughly 8 °C from pure SOPC to pure SOPC-OOH. The enthalpy of phase transition, related to the interaction between lipids, is found to decrease for SOPC containing between 0 and 20 mol % of SOPC-OOH, the addition of some peroxide group might create defects and decrease interaction between the carbon chains. Above 25 mol % of SOPC-OOH, the enthalpy linearly increases with the hydroperoxidation amount. One can assume the peroxide group to form weak bonds with lipid head groups and water molecules. The increased phase transition enthalpy with the decreased phase transition temperature points to a higher entropy. Hydroperoxidized membranes may thus be described as cohesive but disordered membranes. Moreover, between 25 to 70 mol % of SOPC-OOH, the phase transition temperature is constant, but the shape of the phase transition in thermograms varies with the appearance of a small shoulder that could be interpreted as a phase coexistence. Finally, POPC and POPC-OOH/POPC mixtures thermograms have been recorded only up to 20 mol % of POPC-OOH due to the low phase transition temperature and water freezing. The trends of POPC based sample phase transition temperature and enthalpy seem to follow the same ones as SOPC samples with increasing hydroperoxidized lipids. All POPC based samples exhibit phase transition with a shoulder which can be explained for mixtures but which is surprising for a pure compound.

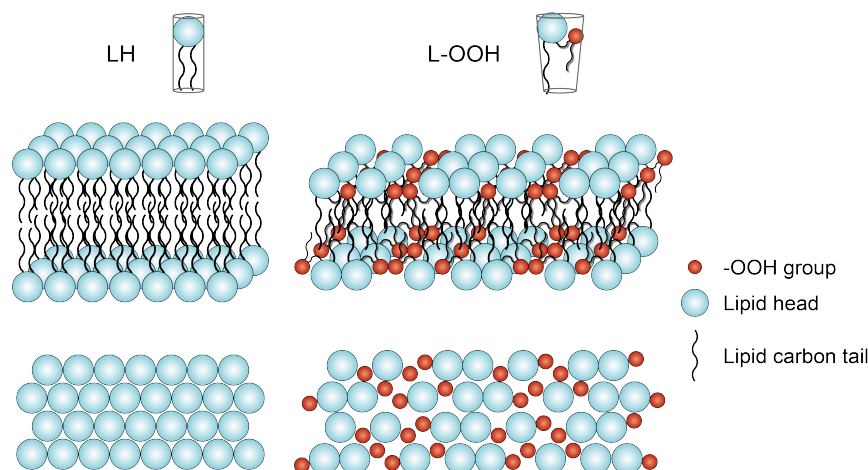


FIGURE 5.1: Hydroperoxidation effect on structural organization of lipid membranes. Hydroperoxydation increases the area per lipid and creates interactions between water and the peroxide group that facilitate water defects in the hydrophobic core. In addition, the conical shape of hydroperoxidized lipid facilitates the hydrophilic pore stabilisation.

The visco-elastic properties of POPC-OOH/POPC membranes have been characterized by our collaborators at the Imperial College of London. An increase of the viscosity from 150 cP to 240 cP is found which is consistent with the literature [79] but in contradiction with the increased fluidity and decreased order. X-rays scattering in combination with simulations showed a decrease in the bending modulus, an increase in the inter-bilayer distance, an increase in the area per lipid and a global decrease of the bilayer order which are all expected from the literature [72, 79]. Overall, results from our paper "*Directly imaging emergence of phase separation in peroxidized lipid membranes*" point to lateral and normal heterogeneities, and preliminary hints at phase coexistence. An interesting result obtained by simulation is that order depends on the depth within the bilayer, it exhibits increasing disorder deep in the membrane but increased order at the lipid head interface when POPC is hydroperoxidized. This supports the previous assumption that hydroperoxidized lipids possess increased disorder in the hydrophobic core which increases membrane fluidity due to the carbon tail looping to the interface, while at the same time, the peroxide group at the interface is strongly suspected to interact with lipid head group and water molecules creating a strong hydrogen network, increasing the viscosity and the phase transition enthalpy.

Results from electroporation experiments on POPC-OOH/POPC mixtures exhibit a constant capacitance despite the well-known decrease of the bilayer thickness and suspected permittivity increase. We showed that hydroperoxydation can decrease the POPC intrinsic permeability to ions by a factor of 4 which is consistent with the bilayer thickness decrease and the increased polarity usually reported in the literature, yet, pure POPC-OOH membranes keep their impermeability as confirmed by the GUV observation using phase contrast microscope and expected from the calculation of their small permeability to ions around  $11 \times 10^{-12} \text{ m.s}^{-1}$ . Hydroperoxidized POPC membranes are more fragile and break at much weaker voltages. Under an electric field, they do form a higher number of pore under lower voltages and the energy barrier of pore formation is found to decrease linearly with

hydroperoxidation by  $5 k_B T$  for fully hydroperoxidized membranes. Hydroperoxidation seems to facilitate pore formation, which can be qualitatively explained by the more numerous water defects observed in such membranes due to increased interaction and area per lipid, and the more conical shape of hydroperoxidized lipid that may stabilize more efficiently the conductive hydrophilic pores. Under biological conditions ( $\sim 100$  mV [9]) POPC membranes conduct less than 10 pS while POPC-OOH conduct roughly 100 pS which correspond to more than  $60 \times 10^6$  ions per second. The linear dependence of the energy barrier for the pore opening as a function of the voltage, disagrees with the theoretical standard model predicting a square dependence. Experimental data are scarce but another study points to the same linear relation [113] supporting our results. The mechanism of pore formation being still unknown it is difficult to assess the reasons why experiments deviate from the theoretical model. Finally pore lifetime (a few milliseconds) and size ( $\sim 7$  Å) are in average similar for all POPC-OOH/POPC compositions. Pore characteristics are likely independent on the membrane composition and intrinsic properties, as an example similar lifetime have been observed for pores in DPhPC supported bilayer [119].

As stated above, our findings that the activation energy for pore formation is linearly reduced by the voltage does not support the standard theoretical model for pore formation that predicts a quadratic function of the voltage. These important results challenge the current understanding of pore formation under an electric field and require thus further exploration and confirmation. The linear variation with the electric potential suggests that the coupling of the system dipoles, such as the lipid and interfacial water dipoles play a major role in pore opening. One could thus use lipids with different head groups or reduce the amount of interfacial water molecules by adding small sugars known to also position at the membrane interface competing with water. A better assessment of the importance of the dipolar coupling effects could also be indirectly tested by changing the lipid tail geometry and interactions using saturated or poly-unsaturated lipids. For example thinner membranes are believed to enhance pore formation but the effect of the electric field on the activation energy for pore formation has never been measured. Other properties such as the membrane elasticity, the space between lipids, or in the case of oxidation the polarity of the membrane are suspected to act on pore formation and thus their impact should be precisely studied. Ions are believed not to interfere in pore formation, the use of different ionic species interacting differently with the membrane might be helpful to verify this hypothesis. Experimental developments along these lines could bring fruitful insights to the mechanism of pore formation and could lead to new theoretical understanding.

The system we use showed slight asymmetry in pore formation. We are conscious that the small aperture rim used in our study ( $50 \mu\text{m}$ ) might bias results, one could for example use bigger aperture sizes of 100 or 150  $\mu\text{m}$  diameter to verify its importance on membrane anchoring and pore formation rate. Electroporation is an indirect measurement of pore formation since pore opening is deduced from the observation of current intensity signals and not from direct pore opening observation. As presented in the Chapter 3 it is still a suitable technique from which important information can be extracted. However, the development of a direct microscopic observation combined with electroporation would be a powerful tool to fully interpret the current signals recorded. This technique would confirm the pore lifetime and size already measured here, but more importantly would allow to characterize the

more complex traces, discarded in our study. Observation of pore opening location could also give clues to the so-called pre-pore existence, the connection of different pore opening, and finally give an explanation to the membrane rupture.

In biological systems most ion transportation is controlled by protein ionic channels. The insertion of such channels in lipid bilayer depends greatly on the bilayer properties (thickness, fluidity,...). Since hydroperoxydation acts on the membrane properties, one can wonder which impact it can have on the protein ionic channels insertion and function. Now that hydroperoxidized lipid membrane conductivity has been carefully characterized, it can be interesting to study protein ionic channel conductivity in such membranes. Preliminary results using  $\alpha$ -Hemolysin showed a good insertion in POPC membranes containing 0, 50 and 100 mol % of POPC-OOH. The bilayer thickness and fluidity modification are thus small enough not to perturb the channel insertion. The conductivities measured in the different membranes (POPC, POPC-OOH and mixture 50/50 mol %) do exhibit an asymmetry between positive and negative electric field which depend on the side of protein insertion. At first glance, the conductive properties of such channel do not seem perturbed by the hydroperoxydation but a more careful analysis must be performed. It is known that ionic channels are able to switch to a closed conformation in order to prevent ion translocation. In our preliminary experiments this is observed only in rare cases and does not seem to depend on the membrane composition. Finally, the  $\alpha$ -Hemolysin is known to lead to the cell death by inducing membrane rupture, we did not observe premature rupture in presence of such ionic channels and found back the exact same rupture probability as a function of the voltage as for protein-free POPC-OOH/POPC membranes.

The efficient lipid hydroperoxydation method developed here will unlock hydroperoxidized lipid availability and thus promote research on hydroperoxidized lipid membrane properties. The technique could still be optimized to hopefully lead to hydroperoxidized lipid commercialization.

As raised in Chapter 2 and Chapter 4 the visco-elastic properties of the membranes are not fully elucidated yet, more research by probing the viscosity of the membranes should be carried on using different techniques. Since heterogeneities of behavior within the membranes are suspected, using different fluorescent probes located at different depth could enlighten on lipid organization and cohesion. Also, the use of rotor probes for measuring membrane viscosity reports values at the molecular level. Measuring membrane viscosity at larger scales (in giant vesicles) could provide for a better assessment of viscosity modifications.

DSC results point to a more cohesive, and yet, more disordered membrane when hydroperoxydation increases. It would be interesting to lead the same study by tuning the unsaturation position along the carbon chain and observe its influence on the membrane state. We would expect a lower impact of hydroperoxydation for lipids containing their unsaturated bond closer to the head, the looping impacting less the hydrophobic carbon chain order. However, the interaction between the head and the peroxide group might still bring more cohesion in the membrane.

Along our intensive efforts to understand how lipid hydroperoxydation impacts the membrane visco-elastic properties, we encountered remarkable and quite unexpected behavior. One of them is the shape of POPC phase transition, which shows an unusual shoulder for a pure compound. This phenomenon aroused our curiosity,

however we could not understand its origin. We wonder if imaging POPC membranes around their  $T_m$  by cryo-TEM might reveal interesting structures.

Another interesting noticeable organisation is the one revealed by cryo-TEM images on POPC and SOPC SUVs, showing irregular shape. The use of X-ray might help to characterize and understand this structure. In addition the imaging of other lipids with different carbon tail or head might help to find the structural origin of such organization.

As a take-home message, one should always consider the importance of controlling the lipid hydroperoxidation amount in biological cells, since it greatly impacts the membrane properties and may affect different biological mechanisms. Especially the barrier effect of the membrane is slightly compromised by hydroperoxidation. Hence, we believe deeper knowledge on hydroperoxidized lipid membrane properties can unravel the understanding of some biological pathways. New insight may also have a more general impact on treatment of oxidized-lipid-related disease and help for new therapy implementation. It could be interesting to use photo-therapy as a localized pre-treatment to lower the field required for the electroporation step.

## Chapter 6

# French summary

### Introduction

Les membranes des cellules biologiques sont composées de lipides, des molécules amphiphiles qui s'assemblent en bicouche dans les milieux aqueux. Cette organisation permet aux membranes d'avoir un cœur hydrophobe (qui n'aime pas l'eau), les rendant imperméables aux molécules chargées et hydrophiles (qui aiment l'eau). Cette fonction est essentielle pour réguler le trafic des ions et autres molécules qui se fait alors majoritairement par l'intermédiaire de canaux formés par des protéines contrôlant précisément leur passage. L'imperméabilité des membranes lipidiques est cependant un désavantage lorsqu'il s'agit d'insérer volontairement un principe actif, un gène ou toute autre molécule dans une cellule.

La santé étant au coeur de notre société, de nombreux travaux sont réalisés afin d'inventer de nouveaux objets transportant des principes actifs au plus proche de la zone ciblée sans forcément réussir à passer la membrane cellulaire. Pour une meilleure efficacité de ces systèmes et pour réduire les effets secondaires lors de l'usage de grandes quantités de principe actif, une technique appelée électroporation a été développée. Elle permet, par l'application d'une forte impulsion électrique sur une zone ciblée, de perméabiliser les membranes sur une très courte durée afin d'y faire pénétrer les molécules préalablement injectées dans son voisinage. En effet, sous l'influence d'un champ électrique, les membranes lipidiques sont capables d'ouvrir des nanopores éphémères capables de laisser passer toutes sortes de molécules. Les conditions de durée de pulse et d'intensité doivent être très précisément contrôlées afin de seulement perméabiliser la membrane temporairement et de ne pas détruire la bicouche de façon permanente, ce qui entraînerait la mort de la cellule. Pour optimiser les conditions d'électroporation, il est important de bien connaître les propriétés des membranes, comme leur épaisseur, leur fluidité et leurs propriétés mécaniques et structurales, qui dépendent à l'évidence de la structure chimique des lipides (polarité), de leur conformation (longueur de molécule, courbure, packing) et de leur mobilité.

Il est établi que l'oxydation de lipides insaturés intervient dans un certain nombre de processus assurant le bon fonctionnement des cellules [21]. Ces mêmes réactions d'oxydation sont également connues pour être néfastes -lorsqu'elles ne sont pas maîtrisées- et sont reliées à l'apparition de nombreuses maladies assez répandues comme le diabète, Alzheimer, Parkinson, des cancers et bien d'autres encore [47, 50, 53]. L'électroporation s'utilisant dans un contexte de thérapie, sur des cellules malades et donc, dans certains cas, oxydées, il semble important de bien caractériser les propriétés de ces membranes. Notamment, il a été montré que l'oxydation des lipides, dépendant de son ampleur, peut grandement affecter l'épaisseur des bicouches [73], leur fluidité [77], leur élasticité [29], l'organisation et la forme des lipides [69] et donc potentiellement impacter la perméabilité des membranes et leur

capacité à former des pores. Pour des stades d'oxydation avancés, il a même été observé la formation de pores en l'absence de stress électrique [99].

Une grande partie des études discutant des propriétés des membranes composées de lipides oxydés sont des simulations. Les expériences sont malheureusement peu nombreuses et le degré d'oxydation n'y est pas toujours bien contrôlé - n'allant pas jusqu'à étudier des membranes entièrement oxydées -. De plus, certaines propriétés n'ont jamais été précisément étudiées jusqu'alors, même si des tendances sont suspectées. Ce manque de données peut être lié à la faible disponibilité de ce genre de lipides. Les lipides hydroperoxydés (produit résultant du premier stade d'oxydation), ne sont, par exemple, pas commercialisés. De plus, les membranes oxydées montrent des comportements qui rentrent en compétition, comme par exemple une plus grande fluidité accompagné d'une plus grande viscosité, ce qui semble assez contre-intuitif aux premiers abords. Les modifications des propriétés des lipides sont souvent liées à la conformation adoptée par les lipides hydroperoxydés très différente des lipides d'origine puisque le groupe peroxyde (qui est polaire) est fortement suspecté de se positionner à l'interface afin d'interagir avec les têtes polaires comme le schématise la Figure 6.1.

Notre équipe ayant développé une technique rapide et contrôlée pour entièrement hydroperoxyder les lipides insaturés, nous pouvons facilement étudier les membranes contenant différentes quantités de ces lipides afin de combler certaines lacunes de la littérature. Notamment, nous souhaitons étudier d'une part certaines propriétés structurales (température de transition, organisation de la membrane, fluidité, perméabilité) des bicouches contenant différentes quantités de lipides hydroperoxydés, et d'autre part analyser précisément la réponse de ces membranes sous champ électrique afin de mieux comprendre les mécanismes de formation de pore impliqués lors de l'électroporation. L'enjeu ici est de mieux caractériser les propriétés, notamment de perméabilité, des membranes hydroperoxydées avec et sans stress électrique afin par exemple d'apporter un meilleur contrôle lors du traitement de certaines maladie par électroporation. Il est également intéressant et pertinent pour notre étude de mieux comprendre les modifications -non triviales- impliquées par l'ajout du groupement peroxyde sur les propriétés des lipides.

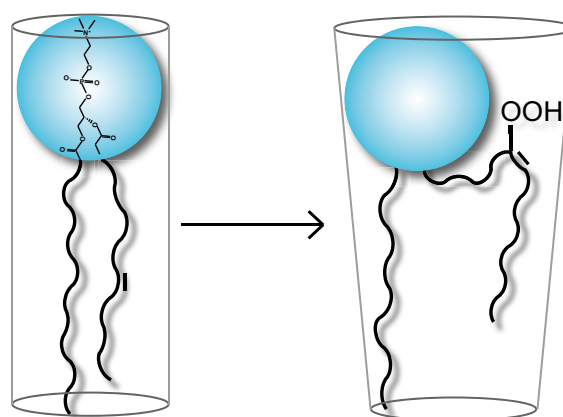


FIGURE 6.1: Hydroperoxydation d'un lipide monoinsaturé. Repositionnement du groupe peroxyde à la surface de la bicouche pour interagir avec la tête polaire et les molécules d'eau dans le cas d'un assemblage en bicouche.

## Résultats

### Hydroperoxydation des lipides mono-insaturés

Pour faciliter l'interprétation des analyses et étudier l'effet d'une seule réaction d'hydroperoxydation par lipide, des membranes modèles composées d'un seul lipide monoinsaturé (et de sa version hydroperoxydée) sont utilisées. Ici, nous nous attardons sur le 1-palmitoyl-2-oleoyl-glycero-3-phosphocholine (POPC, 16:0-18:1) habituellement présent en grande quantité dans les cellules biologiques, et le 1-stearoyl-2-oleoyl-sn-glycero-3-phosphocholine (SOPC, 18:0-18:1) ayant une structure chimique similaire au POPC tout en possédant une température de transition de phase légèrement plus élevée (dus à ses deux carbones supplémentaires sur la chaîne saturée).

L'hydroperoxydation se fait par photo-oxydation grâce à l'intermédiaire d'un photosensibilisateur. La réaction est dans un premier temps optimisée en utilisant une puissance lumineuse plus forte, un solvant adapté et des quantités de réactifs appropriées dans le but d'obtenir des lipides hydroperoxydés en seulement quelques minutes et sans produits secondaires. Les lipides sont ensuite purifiés en enlevant le photosensibilisateur par dialyse en 3 heures. Le rendement total de la méthode est de 80 % massique après dialyse, ce qui offre une technique d'hydroperoxydation très efficace comparées à ce qui est généralement proposé dans la littérature. De plus, nous atteignons des degrés d'oxydation de  $97 \pm 3$  mol % molaires déterminés par RMN.

Après avoir optimisé les conditions d'hydroperoxydation du POPC et SOPC pour produire leur forme hydroperoxydées (POPC-OOH et SOPC-OOH respectivement), des mélanges entre lipides LH et leur version hydroperoxydées L-OOH sont ensuite réalisés pour cibler des compositions spécifiques LH/L-OOH.

### Impact de l'hydroperoxydation sur les propriétés des membranes

#### Épaisseur des bicouches

Dans un premier temps, les propriétés structurales des membranes formées à partir de lipides hydroperoxydés sont étudiées. Pour cela, des petites vésicules (SUV) de POPC et SOPC contenant 0, 50 et 100 % molaire de leur forme hydroperoxydée sont imagées par Cryo-Microscopie Electronique à Transmission (Cryo-TEM). La résolution de la Cryo-TEM permet de visualiser relativement bien les deux feuillettes hydrophiles de la bicouche (zone plus sombre due aux phosphores présents dans les têtes).

Les vésicules composées de POPC ou SOPC présentent une structure alvéolée (voir Figure 6.2), déjà observée dans la littérature sur des lipides saturés et sur certaines images de POPC, mais à notre connaissance, dont l'origine est encore inconnue [162]. Cette structure disparaît avec l'addition de POPC-OOH ou SOPC-OOH à 50 et 100 % molaire, indiquant que la nouvelle conformation prise par ces lipides leur permet de s'assembler de façons différentes.

Les images de cryo-TEM ont également révélé une moins bonne visualisation des deux feuillettes dans les vésicules de POPC-OOH. Cela peut être expliqué par une épaisseur de bicouche trop faible atteignant les limites de résolution de notre microscope.

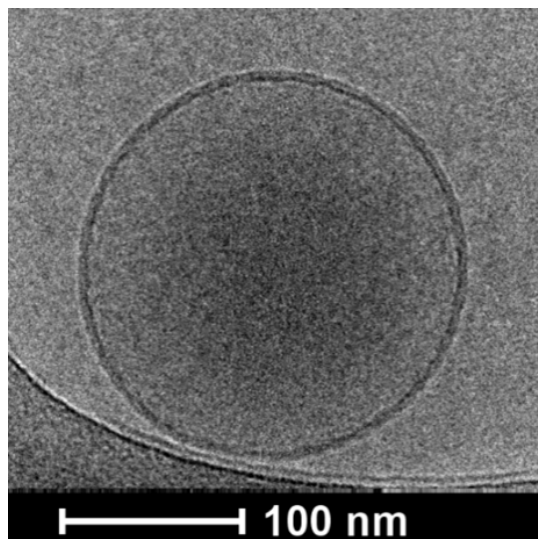


FIGURE 6.2: Images de cryo-TEM de SUV de POPC. Des structures bosselées sont visibles sur les bicouches de POPC.

A partir des images de Cryo-TEM obtenues, l'épaisseur des bicouches est mesurée. Il est à noter que les images sont des projections 2D des électrons traversant des objets 3D, ce qui peut distordre les dimensions. Il a été cependant montré que l'épaisseur de bicouche mesurée sur les images (distance entre les deux feuillet de phosphore) correspond bien avec l'épaisseur hydrophobe des bicouches [157]. Une diminution de 30 % de l'épaisseur entre le POPC et le POPC-OOH, et 23 % entre le SOPC et le SOPC-OOH (Figure 6.3) est obtenue, ce qui est cohérent avec les diminutions d'épaisseur déjà décrites dans la littérature provenant de simulations ou rayon-X [73, 76].

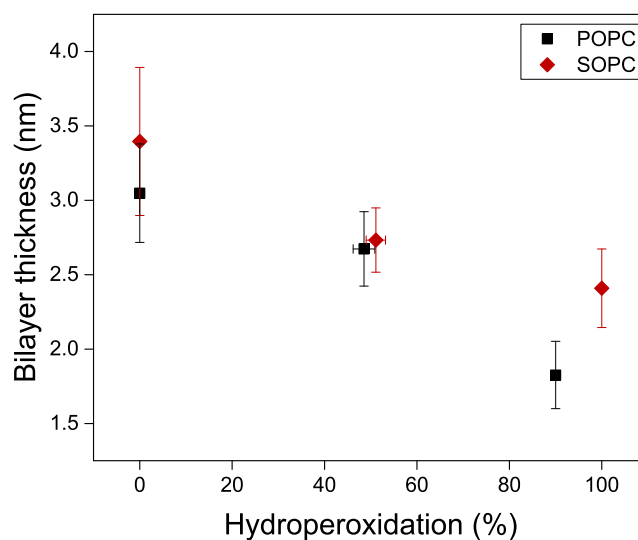


FIGURE 6.3: Variation de l'épaisseur de bicouches de POPC et SOPC en fonction de leur degré d'hydroperoxydation (en % molaire). Note : l'épaisseur réelle n'est pas mesurée ici, mais une projection des bicouches de vésicules 3D sur un plan 2D.

### Fluidité et température de transition

La fluidité des membranes étant un paramètre clé dans leur perméabilisation, l'évolution de la température de transition de membranes hydroperoxydées est étudiée par calorimétrie différentielle à balayage (DSC) sur des solutions contenant des vésicules de POPC ou SOPC contenant différentes quantités de lipides hydroperoxydés. Le POPC possède une température de transition aux alentours de  $-4\text{ }^{\circ}\text{C}$ . En augmentant le degré d'hydroperoxydation dans les membranes de POPC, une diminution de la température de transition a été observée. La mesure étant faite dans l'eau pure il est malheureusement difficile d'accéder à des températures trop basses car l'eau congèle. Il n'est donc pas possible de mesurer la température de transition du POPC-OOH. Cependant la température de transition de membranes de POPC contenant jusqu'à 20 % de POPC-OOH est tout de même obtenue aux alentours de  $-7,5\text{ }^{\circ}\text{C}$ .

Afin de mesurer l'impact d'une hydroperoxydation totale, le SOPC qui possède une température de transition aux alentours de  $6,5\text{ }^{\circ}\text{C}$  est utilisé. Lorsque les vésicules sont totalement hydroperoxydées la température de transition chute à environ  $-1,5\text{ }^{\circ}\text{C}$  comme l'indique la Figure 6.4.A. La diminution de la température de transition entre les phases gel et fluide des membranes de POPC et SOPC avec l'augmentation de leur homologue hydroperoxydé peut être interprétée comme une plus grande désorganisation dans les membranes causée par l'ajout du groupement peroxyde au milieu de la chaîne hydrophobe. Ce groupe polaire, supposé remonter vers la surface, peut en effet grandement casser l'ordre et les interactions au sein du cœur hydrophobe des membranes et apporter une plus grande fluidité.

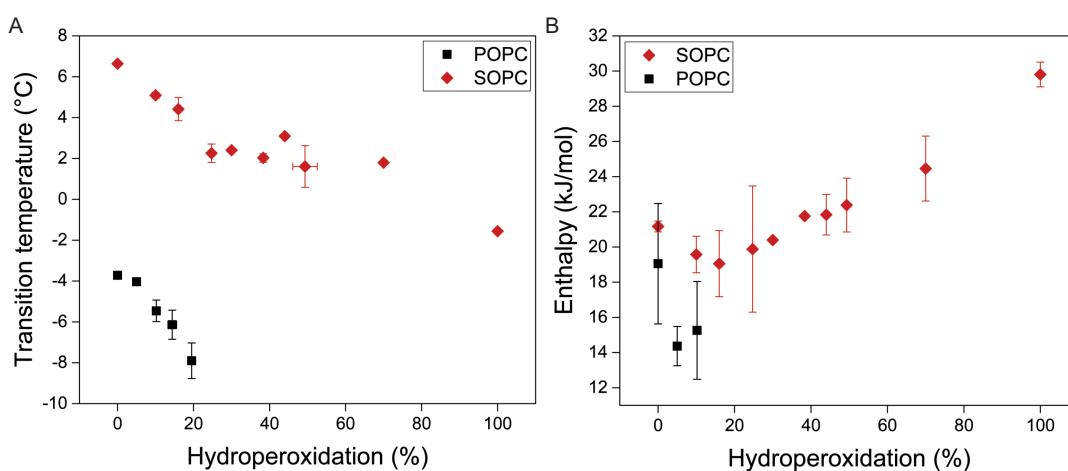


FIGURE 6.4: (A) Température de transition entre la phase gel et fluide de vésicules de POPC et SOPC contenant différentes proportions de leur version hydroperoxydée (B) Enthalpie de transition entre la phase gel et fluide de vésicules de POPC et SOPC contenant différentes proportions de leur version hydroperoxydée.

L'enthalpie de la transition de phase est également mesurée pour des mélanges de POPC-OOH/POPC et SOPC-OOH/SOPC. Elle traduit les interactions à former ou casser afin de passer d'une phase à une autre. La Figure 6.4.B montre tout d'abord une diminution de l'enthalpie avec l'ajout de petites quantités de lipides hydroperoxydés (<20 % molaire), ce qui semble cohérent avec la remontée à la surface des groupes peroxydes, entraînant avec eux une chaîne carbonée et diminuant ainsi leurs interactions avec les autres. Au delà de 20 % molaire de SOPC-OOH, l'enthalpie augmente linéairement avec la quantité de SOPC-OOH, indiquant de

plus fortes interactions. Il est alors possible d'imaginer qu'un fort réseau de liaisons hydrogènes se forme à l'interface entre les têtes, les groupes peroxydes et les molécules d'eau créant ainsi de fortes interactions.

### Viscosité des membranes

L'effet de l'hydroperoxydation sur l'ordre, le packing et la fluidité des membranes n'est pas encore précisément établi puisque les résultats trouvés dans la littérature semblent parfois assez contradictoires. En collaboration avec le département de chimie de l'*Imperial College* de Londres, les propriétés viscoélastiques des membranes de POPC après hydroperoxydation sont étudiées en utilisant l'imagerie des temps de vie de fluorescence (FLIM) des sondes BC10 et BC6++ s'insérant dans les membranes composées de POPC et contenant différentes fractions de POPC-OOH. En étudiant le temps de vie de fluorescence des sondes il est possible de remonter à la viscosité des membranes des vésicules. Une augmentation de la viscosité de 160 à 240 cP est obtenue pour des membranes de POPC contenant 0 à 100 mol % de POPC-OOH (Figure 6.5) cohérente avec une étude récemment menée [79] mais surprenante aux vues des autres modifications de la bicouche induites par l'hydroperoxydation reportées jusqu'ici. Les bicouches hydroperoxydées sont en effet connues pour avoir un paramètre d'ordre plus faible et une plus grande fluidité [72].

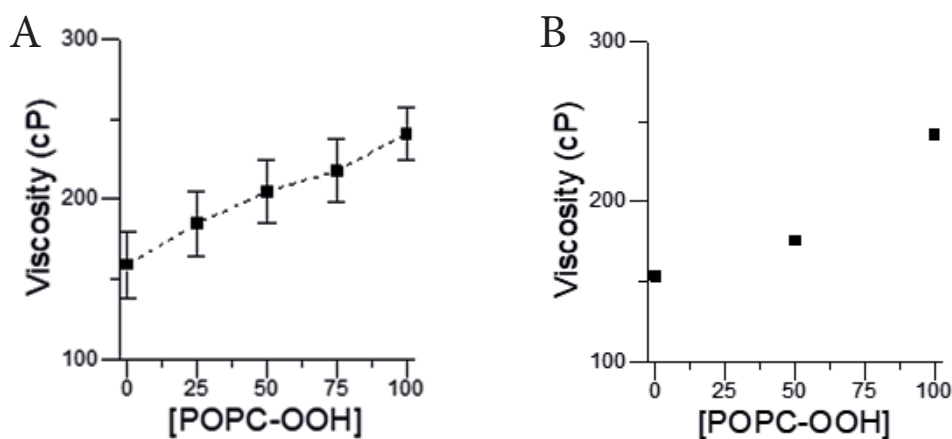


FIGURE 6.5: Augmentation de la viscosité dans les membranes de POPC contenant une quantité de POPC-OOH croissante obtenues à partir des temps de vie du fluorophore (A) BC10 et (B) BC6++

### Hétérogénéités générées par l'oxydation

Toujours dans le cadre de la collaboration avec *Imperial College*, une diminution du module de courbure est mise en lumière en ajustant les pics de diffractions obtenus par Rayons-X (SAXS) sur des bicouches superposées. (Figure 6.6.B) Cette diminution est cohérente avec d'autres études précédemment menées [29, 72]. La diminution du module de courbure est assez facilement concevable du fait qu'un lipide hydroperoxydé semble adopter une forme plus conique due au positionnement du groupe peroxyde à la surface de la membrane alors que les phospholipides non oxydés sont usuellement schématisés par des cylindres (Figure 6.1).

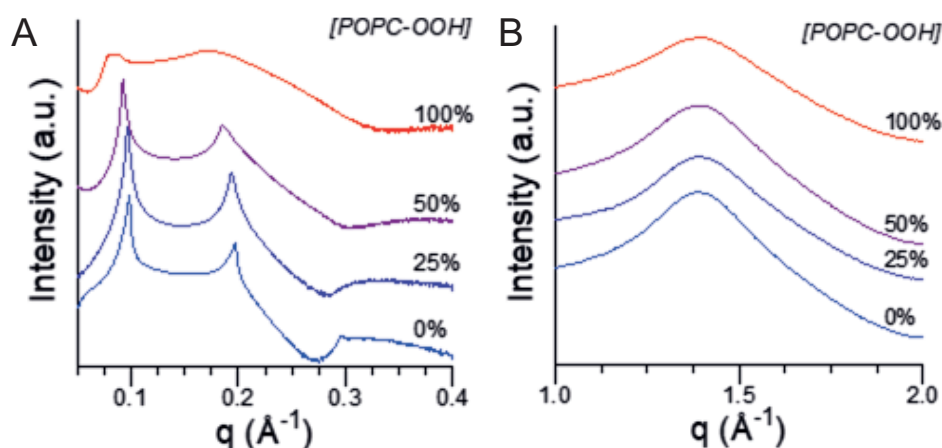


FIGURE 6.6: (A) SAXS et (B) WAXS montrant un élargissement des pics de diffraction obtenus avec l'augmentation du degré d'hydroperoxydation dans les membranes.

L'élargissement des pics de diffraction de SAXS et WAXS (Figure 6.6) suggère une augmentation des hétérogénéités latérales (aire par lipide) et orthogonales à la membrane (épaisseur). En associant ces élargissements de pics avec d'autres résultats détaillés dans le Chapitre 4 ou dans la publication "*Directly imaging emergence of phase separation in peroxidized lipid membranes*", il est suggéré que la présence de lipides hydroperoxydés induit la formation de domaines de différents ordre, viscosité et épaisseur. Ces résultats sont supportés par les simulations également faites dans le cadre de cette étude.

La Figure 6.7 illustre bien les hétérogénéités orthogonales à la bicouche qui montre une augmentation du désordre au sein du coeur hydrophobe et une région plus ordonnée pour les carbones proches de l'interface.

Les résultats obtenus dans le cadre de ma thèse mis en relation avec la littérature, indiquent la possibilité d'une organisation complexe au sein de la membrane, ce qui supporte l'hypothèse d'un réseau ordonné à l'interface accompagné d'un coeur hydrophobe plus désordonné. En effet, l'augmentation de la viscosité et la diminution du coefficient de diffusion peuvent être expliqués par la formation d'un réseau hydrogène entre les têtes, l'eau et les groupements peroxydes, simultanément avec une plus grande fluidité et un plus grand désordre dû à la conformation prise par la chaîne insaturée qui remonte à la surface, réduisant ainsi les interactions dans le coeur hydrophobe.

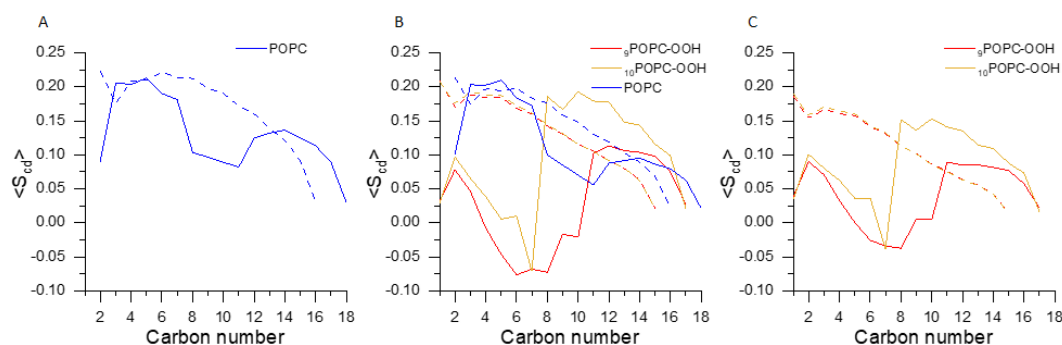


FIGURE 6.7: Paramètre d'ordre de chaque carbone des chaînes lipidiques saturées et insaturées du (A) POPC, (B) POPC-OOH/POPC 50/50 %mol et (C) POPC-OOH.

## Réponses des membranes lipidiques pures à un stress électrique

Après avoir mieux caractérisé les propriétés des membranes hydroperoxydées, la perméabilité aux ions  $K^+$ ,  $Cl^-$  de bicouches suspendues de POPC contenant 0, 25, 50, 75 et 100 % molaire de POPC-OOH est caractérisée sous une différence de potentiel de quelques millivolts et maintenue pendant plusieurs secondes. Une solution tampon de pH 7 contenant 100 mM de KCl est utilisée pour être dans des conditions semblables aux conditions biologiques. Le courant traversant la membrane est étudié et interprété soit comme une perméabilité soit comme la formation de pores.

Pour des voltages inférieurs au voltage seuil d'électroporation, la perméabilité des membranes selon le voltage mais également selon leur degré d'hydroperoxydation augmente (Figure 6.8.A). De ce fait la perméabilité intrinsèque des membranes en absence de champ électrique est calculée et une augmentation d'un facteur 4 entre les membranes de POPC et les membranes de POPC-OOH est obtenue (Figure 6.8.B). L'hydroperoxydation du POPC peut donc abaisser le potentiel de la membrane de  $\Delta E = -\ln(4)K_bT$ . Sur cette gamme de voltage, ou les pores se font rares, la géométrie de la membrane est conservée, et l'hydroperoxydation n'affecte pas le ratio  $b/d$ ,  $b$  étant l'épaisseur du coeur hydrophobe et  $d$  l'épaisseur totale.

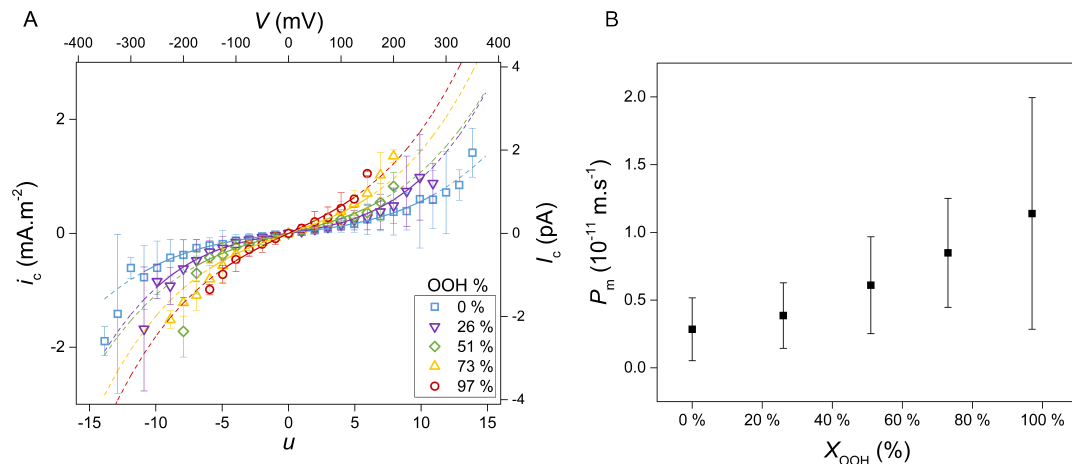


FIGURE 6.8: (A) Intensité de la ligne de base (correspondant aux ions passant sans former de pores) normalisée par la surface des membranes en fonction du voltage appliqué et du degré d'hydroperoxydation des membranes de POPC. (B) Perméabilité calculée des membranes de POPC par rapport aux ions  $K^+$ ,  $Cl^-$  en fonction du degré d'hydroperoxydation.

Au delà du seuil d'électroporation, il est possible de mesurer des événements de conduction de différent temps de vie, intensité de courant et complexité pouvant être associés à l'ouverture de pores. Dans cette étude nous nous concentrons sur l'étude des sauts uniques de conduction bien définis et isolés dans le temps, les signaux plus complexes étant difficiles à caractériser et interpréter. En étudiant les signaux d'intensité selon le degré d'hydroperoxydation des membranes, il a été observé que les membranes contenant une plus grande quantité de POPC-OOH sont plus sensibles au voltage et forment un nombre de pores beaucoup plus important, mais surtout à de plus faibles voltages (Figure 6.9). Contrairement au modèle théorique répandu [112] décrivant la formation de pore comme proportionnel à une barrière d'énergie dépendant du carré du voltage, nos données expérimentales indiquent plutôt dépendance linéaire, ce qui est également retrouvé dans les données publiées par Bockmann et al. [113]. L'ouverture des pores peut être expliqué par l'orientation

des lipides selon leur moment dipolaire sous l'influence du champ électrique, plutôt que seulement par les caractéristiques viscoélastiques de la membrane. La barrière d'énergie pour ouvrir un pore est abaissée de  $5k_bT$  lorsqu'une membrane de POPC est totalement oxydée. Les membranes hydroperoxydées sont également plus fragiles et rompent à des voltages plus bas (375 mV pour le POPC contre 175 mV pour le POPC-OOH).

Il nous a été possible de caractériser les pores par leur taille et leur temps de vie. Le temps de vie des pores suit une unique distribution quel que soit le degré d'hydroperoxydation des membranes avec une plus grande représentation des pores ouvert pendant 2-3 ms. Enfin, le diamètre moyen des pores est calculé autour de 7 Å indépendamment du degré d'hydroperoxydation introduit dans la membrane.

Les membranes hydroperoxydées sont donc beaucoup plus sensibles au stress électrique conduisant les ions de façon plus efficace et à de plus faibles voltages, résultats faisant écho à une étude similaire [81]. Cependant étant plus sensibles, elles sont également plus fragiles et rompent sous des contraintes plus faibles.

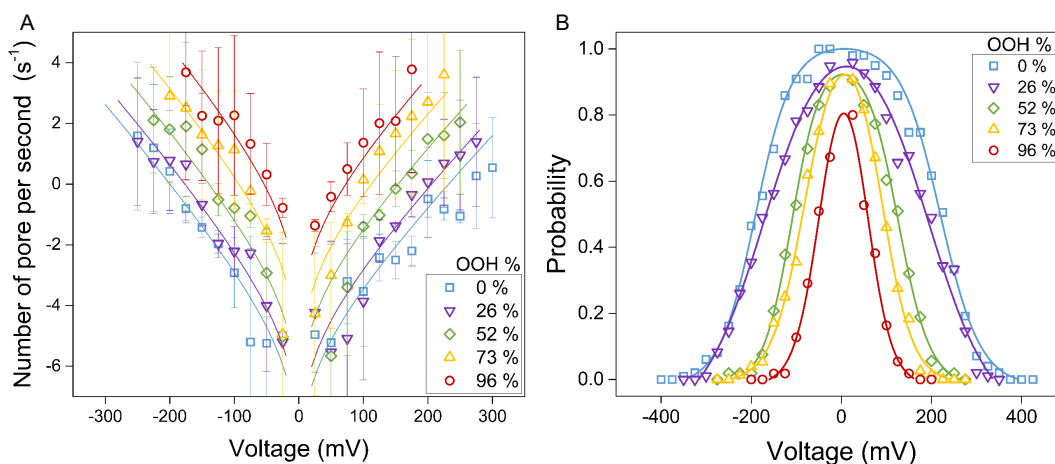


FIGURE 6.9: (A) Nombre de pores ouverts par seconde en fonction du voltage et du degré d'hydroperoxydation des membranes de POPC. (B) Probabilité de former au moins un pore pour chaque application de voltage (6 s) pour différentes membranes de POPC contenant différents degrés d'hydroperoxydation.

## Conclusion

L'établissement d'un protocole fiable d'hydroperoxydation de lipides monoinsaturés comme le POPC et le SOPC a facilité l'étude des propriétés structurales, mécaniques et dynamiques de ces membranes. La littérature a souvent montré que les lipides hydroperoxydés possèdent une épaisseur plus faible ainsi qu'une aire par lipide plus grande. Grâce à l'imagerie des vésicules par cryo-TEM nous avons confirmé une diminution de l'épaisseur, mais n'avons pas observé la formation de structures spécifiques lors de l'ajout de lipides hydroperoxydés. Les lipides oxydés ont également un module de courbure plus faible et donc une forme plus conique facilitant la courbure des membranes (voir Figure 6.10). Dans cette étude nous avons également montré une diminution de la température de transition de phase et de

l'ordre dans le coeur hydrophobe des membranes. Ces changements structuraux résultant de l'hydroperoxydation peuvent alors être expliqués par l'ajout de groupements peroxyde au milieu des chaînes hydrophobes changeant énormément la conformation des molécules de lipide au sein de la bicouche. En contre partie la viscosité des membranes et l'enthalpie de transition de phase augmente, indiquant de plus fortes interactions entre les lipides. Ces modifications sont compatibles avec une diminution du coefficient de diffusion des lipides hydroperoxydés. Il est alors possible d'imaginer que le groupement peroxyde créé un réseau d'interaction hydrogènes avec les têtes et les molécules d'eau, réduisant ainsi leur mouvement.

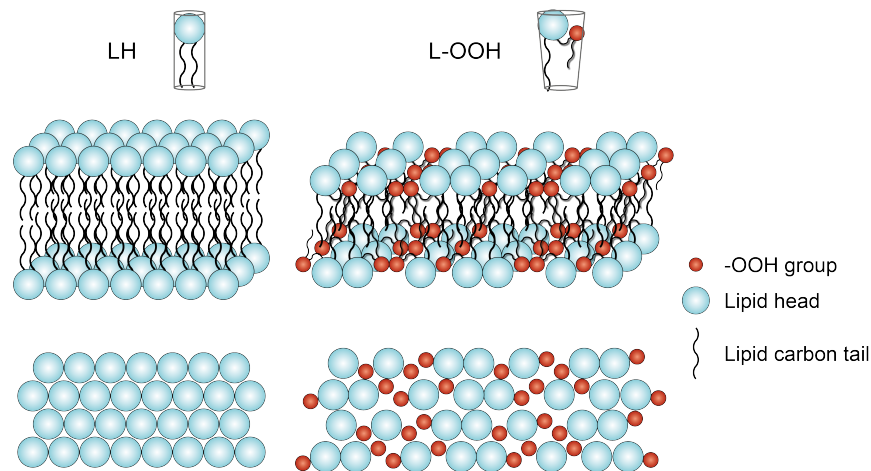


FIGURE 6.10: Effet de l'hydroperoxydation sur l'organisation structurale des membranes. Les membranes hydroperoxydées ont une plus grande aire par lipide et peuvent plus facilement accueillir des molécules d'eau de part l'espace entre les lipides et d'autre part par les interactions du groupe peroxyde avec l'eau. La forme plus conique des lipides hydroperoxydés apporte une plus grande courbure au membrane, facilitant la stabilisation des pores.

Une fois les membranes hydroperoxydées mieux caractérisées, il est intéressant de caractériser leur perméabilité par électroporation. Les membranes lipidiques peuvent laisser passer des molécules par perméabilité ou par la formation de pores. Pour des stress électriques faibles (ou même nuls), la perméabilité des membranes hydroperoxydées augmente de façon cohérente avec la diminution de l'épaisseur de la bicouche et l'augmentation de la polarité des membranes. De plus, pour des voltages plus élevés les membranes hydroperoxydées peuvent former plus de pores conduisant ainsi les ions. Les pores se forment à des voltages beaucoup plus faibles en présence de lipides hydroperoxydés. Cela peut s'expliquer par l'augmentation de l'aire par lipide, la diminution de l'épaisseur des bicouches et les interactions du groupement peroxyde avec les molécules d'eau qui peuvent donner lieu à une pénétration de défauts d'eau facilité au sein de la bicouche, étant l'étape initiale de nucléation de pores. De plus, la forme conique des lipides peut faciliter leur réorganisation lors de la stabilisation du pore (Figure 6.10).

A des différences de potentiel proches de ceux trouvés dans les cellules biologiques, les membranes de POPC ne forment que de rares pores, gardant ainsi leur intégrité, alors que les membranes de POPC-OOH forment quand à eux un nombre de pores non négligeable induisant le passage de nombreux ions. Bien que l'hydroperoxydation impacte grandement les propriétés conductives des membranes, elle n'a pas d'influence sur la taille et le temps de vie des pores.

L'électroporation sur des cellules contenant des lipides hydroperoxydés est donc facilitée. Des pulses électriques de plus faible intensité peuvent suffire à perméabiliser les membranes afin d'y introduire des molécules. De plus, une attention particulière doit être donnée à la fragilité accrue de telles membranes il est donc nécessaire ne pas appliquer de stress électriques trop importants pouvant mener à la mort des cellules.



## Appendix A

# Equivalent electric circuit

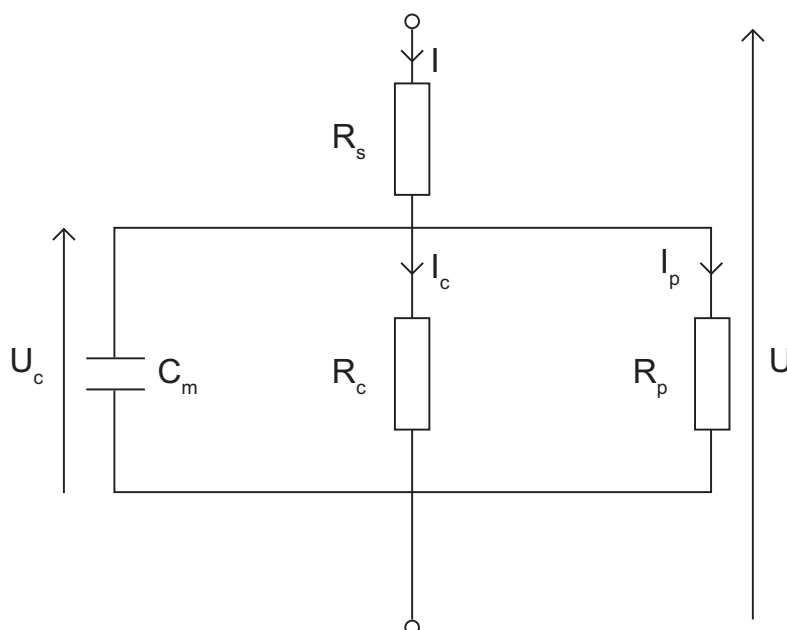


FIGURE A.1: Equivalent electric circuit of a free-standing bilayer.  $R_s$  is the instrument resistance, which also includes the electrolyte,  $C_m$  is the membrane capacitance, and  $R_c$  is the intrinsic membrane resistance in absence of pores through which flows a current  $I_c$ . When a pore opens, an added current  $I_p$  flows through the pore resistance  $R_p$ . The instrument works in a voltage clamp mode where the potential difference  $U$  is always kept constant.

The minimal representation of the equivalent electric circuit of our measurement platform [112, 136, 204] is depicted in Figure A.1, where membrane is modeled as a parallel capacitor  $C_m$  and resistance  $R_m = R_c R_p(t) / (R_c + R_p(t))$ , with  $R_c$  the membrane resistance in absence of pore, and  $R_p(t)$  the pore resistance being a function of time. In the simplest pore models where the pore stays open at a constant diameter  $D_p$  for a duration  $\tau_p$  one has  $R_p(t) = R_p$  while the pore is open and  $R_p(t) = \infty$  otherwise. The resistance of the set-up is represented with a general resistance  $R_s$  estimated in the megaohm range ( $10^6 \Omega$ ).

Typical value of the diverse resistance present in the circuit are:  $R_s \sim 10^6$ ,  $R_c \sim 10^{11}$ , and  $R_p \sim 10^8 \Omega$  ( $R_c > R_p > R_s$ ). Under the application of a new potential difference  $U$ , ions accumulate at the membrane interface and charge it with a time constant  $\tau_{RC}$ :

$$\frac{1}{\tau_{RC}} = \frac{1}{C_m} \left( \frac{1}{R_s} + \frac{1}{R_m} \right) \quad (\text{A.1})$$

with  $\tau_{RC}$  response time of the circuit (s),  $C_m$  the system capacitance (F),  $R_s$  the system resistance ( $\Omega$ ) and  $R_m$  the membrane resistance ( $\Omega$ ). In absence of pore, one obtain  $\tau_{RC} \simeq C_m R_s$ . In the following,  $\tau_{RC}$  will be used in absence of pores and  $\tau_d$  when a pore is open.

Under an applied voltage  $U$ , the potential difference  $U_c(t)$  across the membrane follows the differential equation:

$$C_m \frac{dU_c(t)}{dt} = -U_c(t) \left( \frac{1}{R_s} + \frac{1}{R_c} + \frac{1}{R_p(t)} \right) + \frac{U(t)}{R_s}. \quad (\text{A.2})$$

Integration of equation A.2 provides a solution for  $U_c(t)$ , and for the current measured by the instrument  $I(t) = [U(t) - U_c(t)]/R_s$ . When a pore open (at  $t_o$ ), and for a time  $\tau_p$  (eventually long enough to reach the stationary membrane discharged when  $\tau_p \gg \tau_d$ ) the intensity increases following:

$$I(t) = \frac{U}{R_s} \left[ 1 - \frac{R_c}{R_s + R_c} \exp\left(-\frac{t - t_o}{\tau_d}\right) - \frac{R_m}{R_s + R_m} \left( 1 - \exp\left(-\frac{t - t_o}{\tau_d}\right) \right) \right] \quad (\text{A.3})$$

with  $t_o < t < t_o + \tau_p$ .

After the pore closes at a time  $t_c (=t_o + \tau_p)$ , the intensity decays towards its initial stationary value, following:

$$I(t) = \frac{U}{R_s} \left[ 1 - \frac{R_m}{R_s + R_m} \exp\left(-\frac{t - t_c}{\tau_{RC}}\right) - \frac{R_c}{R_s + R_c} \left( 1 - \left( 1 - \exp\left(-\frac{\tau_p}{\tau_d}\right) \right) \exp\left(-\frac{t - t_c}{\tau_{RC}}\right) \right) \right]. \quad (\text{A.4})$$

If the pore stays open for enough time compared to the filtering characteristic time ( $\tau_p \gg \tau$ , see Figure A.2), the current first rises from its stationary value  $I_c = U/(R_s + R_c) \simeq U/R_c$  to a higher stationary value  $I_c + I_p = U/(R_s + R_m) \simeq U/R_p$  while the potential at the capacitor decreases from the stationary value  $UR_c/(R_s + R_c)$  to a slightly smaller stationary value  $UR_m/(R_s + R_m)$ . If the pore is short-lived ( $\tau_p \ll \tau$ ) one cannot directly evaluate the pore resistance  $R_p$  from the  $I_p$  stationary value.  $I_p$  can still be evaluated by measuring the current  $I_c + I(\tau_p)$ , the maximum intensity reached at  $t_c$  by numerically solving the equation A.3.

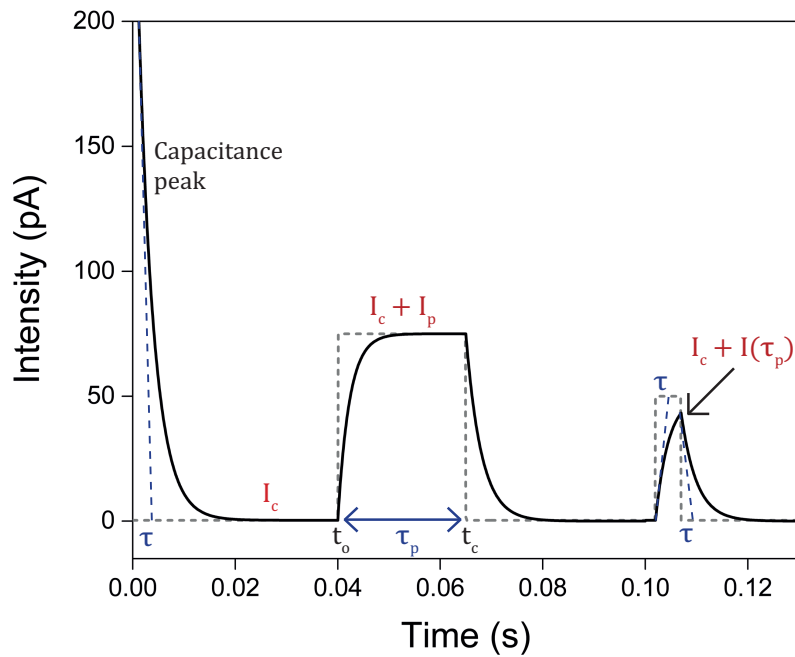


FIGURE A.2: Capacitance peak followed by completely and partially developed pore signals. The black solid line corresponds to ideal intensity measurements using our filtering conditions (bandwidth 0.6 kHz,  $\tau \sim 2.8$  ms), while the gray dash line shows the current that instantaneously ( $\sim$  nanosecond [135]) flow across the pore. The capacitance peak corresponds to ions charging the membranes, other current fluctuations correspond to pore opening or closing. When pores are closed, the current crossing the membrane is called  $I_c$ , when a pore opens ( $t_o$ ) the intensity value increases by  $I(\tau_p)$ . The intensity value can increase up to a stationary intensity  $I_p$  if the pore is long-lived enough ( $\tau_p > \tau$ ). After pore closure ( $t_c$ ) the current goes back to its initial  $I_c$  value.



## Appendix B

# Difficulties encountered during electroporation

I want to point out the difficulties encountered during electroporation measurement and current intensity analysis. First, it can be difficult to form POPC stable membranes (regardless of the hydroperoxidation), indeed, along experiments, we notice that a combination of using a fresh lipid solution in octane, a fresh buffer solution and a carefully chosen Meca 4 well is necessary to obtain stable and non-leaky membranes. We believe our lipids solution in octane may not be stable over long times, forming sometimes white precipitate, contrary to the commonly used DPhPC that stay perfectly soluble over time. We also noticed that membranes are more stable when using fresh buffer solution (< 1 week), whereas usually it can be conserved for several months. I personally strongly believe that the SU-8 surface and maybe well-head heterogeneities of the Meca 4 chips are determinant factors in membrane formation (at least for POPC membranes that are less stable than DPhPC) since for our experiments some chips are preferentially chosen to paint stable membrane, while it is impossible on others.

Despite experimental aspects that can be easily solved by using proper conditions, the data analysis can also be challenging. As in every measurement, data are collected with noise. Regarding the small intensity of some events observed here, a part of the information may be hidden by the noise. The choice of the smallest measurement gauge (200 pA) reduces the noise to only  $\sim 2$  pA, but prevents the observation of current above the gauge limit. Moreover, due to the presence of artifacts observed in our signals but also reported in Pein et al.[183] (discussed in section 3.2.3.3), some current intensity interpretation are not reliable, the noise enhancement sometimes way above the expected behavior is a good example. Finally, electroporation current intensity interpretation do not give any information on the pore localisation.



# Bibliography

1. Cell Biology Flipped Course. <https://www.ibiology.org/> (2020).
2. Mouritsen, O. G. *Life-as a matter of fat* (Springer, 2005).
3. Marsh, D. *Handbook of lipid bilayers* (CRC press, 2013).
4. Andreoli, T. E., Fanestil, D. D., Hoffman, J. F. & Schultz, S. G. *Physiology of membrane disorders* (Springer Science & Business Media, 2013).
5. Yeagle, P. L. *The membranes of cells* (Academic Press, 2016).
6. Ohvo-Rekilä, H., Ramstedt, B., Leppimäki, P. & Slotte, J. P. Cholesterol interactions with phospholipids in membranes. *Progress in lipid research* **41**, 66–97 (2002).
7. Gurtovenko, A. A. & Vattulainen, I. Effect of NaCl and KCl on phosphatidylcholine and phosphatidylethanolamine lipid membranes: insight from atomic-scale simulations for understanding salt-induced effects in the plasma membrane. *The Journal of Physical Chemistry B* **112**, 1953–1962 (2008).
8. Chatterjee, S. & Agarwal, S. Liposomes as membrane model for study of lipid peroxidation. *Free radical biology and medicine* **4**, 51–72 (1988).
9. Stein, W. D. & Litman, T. *Channels, carriers, and pumps: an introduction to membrane transport* (Elsevier, 2014).
10. Hanneschlaeger, C., Horner, A. & Pohl, P. Intrinsic membrane permeability to small molecules. *Chemical reviews* **119**, 5922–5953 (2019).
11. Nishimura, K. *et al.* Identification of giant unilamellar vesicles with permeability to small charged molecules. *RSC advances* **4**, 35224–35232 (2014).
12. Hauser, H., Oldani, D. & Phillips, M. Mechanism of ion escape from phosphatidylcholine and phosphatidylserine single bilayer vesicles. *Biochemistry* **12**, 4507–4517 (1973).
13. Wood, R., Wirth Jr, F. & Morgan, H. Glucose permeability of lipid bilayer membranes. *Biochimica et Biophysica Acta (BBA)-Biomembranes* **163**, 171–178 (1968).
14. Missner, A. *et al.* Carbon dioxide transport through membranes. *Journal of Biological Chemistry* **283**, 25340–25347 (2008).
15. Olbrich, K., Rawicz, W., Needham, D. & Evans, E. Water permeability and mechanical strength of polyunsaturated lipid bilayers. *Biophysical journal* **79**, 321–327 (2000).
16. Ivanov, I. I., Fedorov, G. E., Gus'kova, R. A., Ivanov, K. I. & Rubin, A. B. Permeability of lipid membranes to dioxygen. *Biochemical and biophysical research communications* **322**, 746–750 (2004).
17. Clementi, E., Raimondi, D. & Reinhardt, W. P. Atomic screening constants from SCF functions. II. Atoms with 37 to 86 electrons. *The Journal of chemical physics* **47**, 1300–1307 (1967).

18. Benos, D. J., Deamer, D. W., Kleinzeller, A. & Fambrough, D. M. *Membrane permeability: 100 years since Ernest Overton* (Academic Press, 1999).
19. Ebert, A., Hanneschlaeger, C., Goss, K.-U. & Pohl, P. Passive permeability of planar lipid bilayers to organic anions. *Biophysical journal* **115**, 1931–1941 (2018).
20. Walter, A. & Gutknecht, J. Permeability of small nonelectrolytes through lipid bilayer membranes. *The Journal of membrane biology* **90**, 207–217 (1986).
21. Lodish, H. *et al.* *Molecular Cell Biology*. (WH Freeman and Company, 2003).
22. Heimburg, T. Lipid ion channels. *Biophysical chemistry* **150**, 2–22 (2010).
23. DeCoursey, T. E. Voltage and pH sensing by the voltage-gated proton channel, HV1. *Journal of The Royal Society Interface* **15**, 20180108 (2018).
24. Schmidt, D., Jiang, Q.-X. & MacKinnon, R. Phospholipids and the origin of cationic gating charges in voltage sensors. *Nature* **444**, 775–779 (2006).
25. Tomita, T., Watanabe, M. & Yasuda, T. Influence of membrane fluidity on the assembly of Staphylococcus aureus alpha-toxin, a channel-forming protein, in liposome membrane. *Journal of Biological Chemistry* **267**, 13391–13397 (1992).
26. Song, L. *et al.* Structure of staphylococcal  $\alpha$ -hemolysin, a heptameric trans-membrane pore. *Science* **274**, 1859–1865 (1996).
27. Marracino, P. *et al.* Transprotein-electropore characterization: a molecular dynamics investigation on human AQP4. *ACS omega* **3**, 15361–15369 (2018).
28. Mosgaard, L. D. & Heimburg, T. Lipid ion channels and the role of proteins. *Accounts of chemical research* **46**, 2966–2976 (2013).
29. Weber, G. *et al.* Lipid oxidation induces structural changes in biomimetic membranes. *Soft matter* **10**, 4241–4247 (2014).
30. Tamm, L. K. & McConnell, H. M. Supported phospholipid bilayers. *Biophysical journal* **47**, 105–113 (1985).
31. Wu, E., Jacobson, K. & Papahadjopoulos, D. Lateral diffusion in phospholipid multibilayers measured by fluorescence recovery after photobleaching. *Biochemistry* **16**, 3936–3941 (1977).
32. McConnell, H. M. & Kornberg, R. D. Inside-outside transitions of phospholipids in vesicle membranes. *Biochemistry* **10**, 1111–1120 (1971).
33. Kirsch, S. A. & Böckmann, R. A. Coupling of membrane nanodomain formation and enhanced electroporation near phase transition. *Biophysical journal* **116**, 2131–2148 (2019).
34. Ipsen, J. H. & Mouritsen, O. G. Modelling the phase equilibria in two-component membranes of phospholipids with different acyl-chain lengths. *Biochimica et Biophysica Acta (BBA)-Biomembranes* **944**, 121–134 (1988).
35. Barton, P. G. & Gunstone, F. Hydrocarbon chain packing and molecular motion in phospholipid bilayers formed from unsaturated lecithins. Synthesis and properties of sixteen positional isomers of 1, 2-dioctadecenoyl-sn-glycero-3-phosphorylcholine. *Journal of Biological Chemistry* **250**, 4470–4476 (1975).
36. Okuyama, H., Okajima, N., Sasaki, S., Higashi, S. & Murata, N. The cis/trans isomerization of the double bond of a fatty acid as a strategy for adaptation to changes in ambient temperature in the psychrophilic bacterium, *Vibrio* sp. strain ABE-1. *Biochimica et Biophysica Acta (BBA)-Lipids and Lipid Metabolism* **1084**, 13–20 (1991).

37. Van Dijk, P., De Kruijff, B., Van Deenen, L., De Gier, J. & Demel, R. The preference of cholesterol for phosphatidylcholine in mixed phosphatidylcholine-phosphatidylethanolamine bilayers. *Biochimica et Biophysica Acta (BBA)-Biomembranes* **455**, 576–587 (1976).
38. Wang, Z.-q., Lin, H.-n., Li, S. & Huang, C.-h. Phase Transition Behavior and Molecular Structures of Monounsaturated Phosphatidylcholines: CALORIMETRIC STUDIES AND MOLECULAR MECHANICS SIMULATIONS. *Journal of Biological Chemistry* **270**, 2014–2023 (1995).
39. Ulrich, A. S., Sami, M. & Watts, A. Hydration of DOPC bilayers by differential scanning calorimetry. *Biochimica et Biophysica Acta (BBA)-Biomembranes* **1191**, 225–230 (1994).
40. Pluhackova, K. *et al.* A critical comparison of biomembrane force fields: structure and dynamics of model DMPC, POPC, and POPE bilayers. *The Journal of Physical Chemistry B* **120**, 3888–3903 (2016).
41. Akabori, K. & Nagle, J. F. Structure of the DMPC lipid bilayer ripple phase. *Soft matter* **11**, 918–926 (2015).
42. McMullen, T. P., Lewis, R. N. & McElhaney, R. N. Cholesterol–phospholipid interactions, the liquid-ordered phase and lipid rafts in model and biological membranes. *Current opinion in colloid & interface science* **8**, 459–468 (2004).
43. Raffy, S. & Teissie, J. Control of lipid membrane stability by cholesterol content. *Biophysical journal* **76**, 2072–2080 (1999).
44. Mouritsen, O. G. & Zuckermann, M. J. What’s so special about cholesterol? *Lipids* **39**, 1101–1113 (2004).
45. Pernet, F., Gauthier-Clerc, S. & Mayrand, É. Change in lipid composition in eastern oyster (*Crassostrea virginica* Gmelin) exposed to constant or fluctuating temperature regimes. *Comparative Biochemistry and Physiology Part B: Biochemistry and Molecular Biology* **147**, 557–565 (2007).
46. Simons, K. & Toomre, D. Lipid rafts and signal transduction. *Nature reviews Molecular cell biology* **1**, 31–39 (2000).
47. Ames, B. N., Shigenaga, M. K. & Hagen, T. M. Oxidants, antioxidants, and the degenerative diseases of aging. *Proceedings of the National Academy of Sciences* **90**, 7915–7922 (1993).
48. Logani, M. & Davies, R. Lipid oxidation: biologic effects and antioxidants—a review. *Lipids* **15**, 485–495 (1980).
49. Ruipérez, V., Darios, F. & Davletov, B. Alpha-synuclein, lipids and Parkinson’s disease. *Progress in lipid research* **49**, 420–428 (2010).
50. Butterfield, D. A. & Lauderback, C. M. Lipid peroxidation and protein oxidation in Alzheimer’s disease brain: potential causes and consequences involving amyloid  $\beta$ -peptide-associated free radical oxidative stress. *Free Radical Biology and Medicine* **32**, 1050–1060 (2002).
51. Mitomo, H., Chen, W.-H. & Regen, S. L. Oxysterol-induced rearrangement of the liquid-ordered phase: a possible link to Alzheimer’s disease? *Journal of the American Chemical Society* **131**, 12354–12357 (2009).
52. Nagashima, T. *et al.* Increase of serum phosphatidylcholine hydroperoxide dependent on glycemic control in type 2 diabetic patients. *Diabetes research and clinical practice* **56**, 19–25 (2002).

53. Cejas, P. *et al.* Implications of oxidative stress and cell membrane lipid peroxidation in human cancer (Spain). *Cancer Causes & Control* **15**, 707–719 (2004).
54. Cai, F., Dupertuis, Y. M. & Pichard, C. Role of polyunsaturated fatty acids and lipid peroxidation on colorectal cancer risk and treatments. *Current Opinion in Clinical Nutrition & Metabolic Care* **15**, 99–106 (2012).
55. Upston, J. M. *et al.* Disease stage-dependent accumulation of lipid and protein oxidation products in human atherosclerosis. *The American journal of pathology* **160**, 701–710 (2002).
56. Reed, T. T. Lipid peroxidation and neurodegenerative disease. *Free Radical Biology and Medicine* **51**, 1302–1319 (2011).
57. Girotti, A. W. Photodynamic lipid peroxidation in biological systems. *Photochemistry and photobiology* **51**, 497–509 (1990).
58. Girotti, A. W. Mechanisms of lipid peroxidation. *Journal of free radicals in biology & medicine* **1**, 87–95 (1985).
59. Aitken, R. J., Wingate, J. K., De Iulius, G. N., Koppers, A. J. & McLaughlin, E. A. Cis-unsaturated fatty acids stimulate reactive oxygen species generation and lipid peroxidation in human spermatozoa. *The Journal of Clinical Endocrinology & Metabolism* **91**, 4154–4163 (2006).
60. Siani, P., de Souza, R., Dias, L., Itri, R. & Khandelia, H. An overview of molecular dynamics simulations of oxidized lipid systems, with a comparison of ELBA and MARTINI force fields for coarse grained lipid simulations. *Biochimica et Biophysica Acta (BBA)-Biomembranes* **1858**, 2498–2511 (2016).
61. Grossweiner, L. I., Grossweiner, J. B. & Rogers, B. G. *The science of phototherapy: an introduction* (Springer, 2005).
62. Stratton, S. P. & Liebler, D. C. Determination of singlet oxygen-specific versus radical-mediated lipid peroxidation in photosensitized oxidation of lipid bilayers: effect of  $\beta$ -carotene and  $\alpha$ -tocopherol. *Biochemistry* **36**, 12911–12920 (1997).
63. Reis, A. & Spickett, C. M. Chemistry of phospholipid oxidation. *Biochimica et Biophysica Acta (BBA)-Biomembranes* **1818**, 2374–2387 (2012).
64. Itri, R., Junqueira, H. C., Mertins, O. & Baptista, M. S. Membrane changes under oxidative stress: the impact of oxidized lipids. *Biophysical reviews* **6**, 47–61 (2014).
65. Ulmer, C. Z. *et al.* A review of efforts to improve lipid stability during sample preparation and standardization efforts to ensure accuracy in the reporting of lipid measurements. *Lipids* **56**, 3–16 (2021).
66. Boccalini, G. *et al.* Methylene blue-containing liposomes as new photodynamic anti-bacterial agents. *Journal of Materials Chemistry B* **5**, 2788–2797 (2017).
67. Fruhwirth, G. O., Loidl, A. & Hermetter, A. Oxidized phospholipids: from molecular properties to disease. *Biochimica et Biophysica Acta (BBA)-Molecular Basis of Disease* **1772**, 718–736 (2007).
68. Reis, A., Domingues, M., Amado, F. M., Ferrer-Correia, A. & Domingues, P. Separation of peroxidation products of diacyl-phosphatidylcholines by reversed-phase liquid chromatography–mass spectrometry. *Biomedical Chromatography* **19**, 129–137 (2005).

69. De Rosa, R., Spinozzi, F. & Itri, R. Hydroperoxide and carboxyl groups preferential location in oxidized biomembranes experimentally determined by small angle X-ray scattering: Implications in membrane structure. *Biochimica et Biophysica Acta (BBA)-Biomembranes* **1860**, 2299–2307 (2018).
70. Riske, K. A. *et al.* Giant vesicles under oxidative stress induced by a membrane-anchored photosensitizer. *Biophysical journal* **97**, 1362–1370 (2009).
71. Junqueira, H. *et al.* Molecular organization in hydroperoxidized POPC bilayers. *Biochimica et Biophysica Acta (BBA)-Biomembranes* **1863**, 183659 (2021).
72. Jurkiewicz, P. *et al.* Biophysics of lipid bilayers containing oxidatively modified phospholipids: insights from fluorescence and EPR experiments and from MD simulations. *Biochimica et Biophysica Acta (BBA)-Biomembranes* **1818**, 2388–2402 (2012).
73. Wong-Ekkabut, J. *et al.* Effect of lipid peroxidation on the properties of lipid bilayers: a molecular dynamics study. *Biophysical journal* **93**, 4225–4236 (2007).
74. Sapay, N., Bennett, W. D. & Tieleman, D. P. Thermodynamics of flip-flop and desorption for a systematic series of phosphatidylcholine lipids. *Soft Matter* **5**, 3295–3302 (2009).
75. Petrache, H. I., Dodd, S. W. & Brown, M. F. Area per lipid and acyl length distributions in fluid phosphatidylcholines determined by <sup>2</sup>H NMR spectroscopy. *Biophysical journal* **79**, 3172–3192 (2000).
76. Mason, R. P., Walter, M. F. & Mason, P. E. Effect of oxidative stress on membrane structure: small-angle X-ray diffraction analysis. *Free Radical Biology and Medicine* **23**, 419–425 (1997).
77. Van der Paal, J., Neyts, E. C., Verlackt, C. C. & Bogaerts, A. Effect of lipid peroxidation on membrane permeability of cancer and normal cells subjected to oxidative stress. *Chemical science* **7**, 489–498 (2016).
78. Chng, C.-P., Sadvovsky, Y., Hsia, K. J. & Huang, C. Site-specific peroxidation modulates lipid bilayer mechanics. *Extreme Mechanics Letters* **42**, 101148 (2021).
79. Scanavachi, G. *et al.* Lipid hydroperoxide compromises the membrane structure organization and softens bending rigidity. *Langmuir* **37**, 9952–9963 (2021).
80. Davis, P., Coolbear, K. & Keough, K. Differential scanning calorimetric studies of the thermotropic phase behaviour of membranes composed of dipalmitoyllecithin and mixed-acid unsaturated lecithins. *Canadian Journal of Biochemistry* **58**, 851–858 (1980).
81. Corvalán, N. A., Caviglia, A. F., Felsztyna, I., Itri, R. & Lascano, R. Lipid hydroperoxidation effect on the dynamical evolution of the conductance process in bilayer lipid membranes: a condition toward criticality. *Langmuir* **36**, 8883–8893 (2020).
82. Megli, F. M., Russo, L. & Sabatini, K. Oxidized phospholipids induce phase separation in lipid vesicles. *FEBS letters* **579**, 4577–4584 (2005).
83. Jacob, R. F. & Mason, R. P. Lipid peroxidation induces cholesterol domain formation in model membranes. *Journal of Biological Chemistry* **280**, 39380–39387 (2005).
84. Tsubone, T. M., Junqueira, H. C., Baptista, M. S. & Itri, R. Contrasting roles of oxidized lipids in modulating membrane microdomains. *Biochimica et Biophysica Acta (BBA)-Biomembranes* **1861**, 660–669 (2019).

85. Haluska, C. K. *et al.* Photo-activated phase separation in giant vesicles made from different lipid mixtures. *Biochimica et Biophysica Acta (BBA)-Biomembranes* **1818**, 666–672 (2012).
86. Guo, Y., Baulin, V. A. & Thalmann, F. Peroxidised phospholipid bilayers: insight from coarse-grained molecular dynamics simulations. *Soft matter* **12**, 263–271 (2016).
87. Borst, J. W., Visser, N. V., Kouptsova, O. & Visser, A. J. Oxidation of unsaturated phospholipids in membrane bilayer mixtures is accompanied by membrane fluidity changes. *Biochimica et Biophysica Acta (BBA)-Molecular and Cell Biology of Lipids* **1487**, 61–73 (2000).
88. Dobretsov, G., Borschevskaya, T., Petrov, V. & Vladimirov, Y. A. The increase of phospholipid bilayer rigidity after lipid peroxidation. *FEBS letters* **84**, 125–128 (1977).
89. Choe, M., Jackson, C. & Yu, B. P. Lipid peroxidation contributes to age-related membrane rigidity. *Free Radical Biology and Medicine* **18**, 977–984 (1995).
90. Stark, G. The effect of ionizing radiation on lipid membranes. *Biochimica et Biophysica Acta (BBA)-Reviews on Biomembranes* **1071**, 103–122 (1991).
91. Conte, E., Megli, F. M., Khandelia, H., Jeschke, G. & Bordignon, E. Lipid peroxidation and water penetration in lipid bilayers: a W-band EPR study. *Biochimica et Biophysica Acta (BBA)-Biomembranes* **1828**, 510–517 (2013).
92. Bacellar, I. O. *et al.* Photosensitized membrane permeabilization requires contact-dependent reactions between photosensitizer and lipids. *Journal of the American Chemical Society* **140**, 9606–9615 (2018).
93. Rems, L., Viano, M., Kasimova, M. A., Miklavčič, D. & Tarek, M. The contribution of lipid peroxidation to membrane permeability in electroporation: A molecular dynamics study. *Bioelectrochemistry* **125**, 46–57 (2019).
94. Sankhagowit, S. *et al.* The dynamics of giant unilamellar vesicle oxidation probed by morphological transitions. *Biochimica et Biophysica Acta (BBA)-Biomembranes* **1838**, 2615–2624 (2014).
95. Mertins, O. *et al.* Physical damage on giant vesicles membrane as a result of methylene blue photoirradiation. *Biophysical journal* **106**, 162–171 (2014).
96. Beranova, L., Cwiklik, L., Jurkiewicz, P., Hof, M. & Jungwirth, P. Oxidation changes physical properties of phospholipid bilayers: fluorescence spectroscopy and molecular simulations. *Langmuir* **26**, 6140–6144 (2010).
97. Klauda, J. B. *et al.* Update of the CHARMM all-atom additive force field for lipids: validation on six lipid types. *The journal of physical chemistry B* **114**, 7830–7843 (2010).
98. Huang, J. & MacKerell Jr, A. D. CHARMM36 all-atom additive protein force field: Validation based on comparison to NMR data. *Journal of computational chemistry* **34**, 2135–2145 (2013).
99. Boonnoy, P., Jarerattanachai, V., Karttunen, M. & Wong-Ekkabut, J. Bilayer deformation, pores, and micellation induced by oxidized lipids. *The journal of physical chemistry letters* **6**, 4884–4888 (2015).
100. Boonnoy, P., Karttunen, M. & Wong-Ekkabut, J. Alpha-tocopherol inhibits pore formation in oxidized bilayers. *Physical Chemistry Chemical Physics* **19**, 5699–5704 (2017).

101. Štefl, M. *et al.* Comprehensive portrait of cholesterol containing oxidized membrane. *Biochimica et Biophysica Acta (BBA)-Biomembranes* **1838**, 1769–1776 (2014).
102. Khandelia, H., Loubet, B., Olżyńska, A., Jurkiewicz, P. & Hof, M. Pairing of cholesterol with oxidized phospholipid species in lipid bilayers. *Soft Matter* **10**, 639–647 (2014).
103. Kerdous, R., Heuvingh, J. & Bonneau, S. Photo-dynamic induction of oxidative stress within cholesterol-containing membranes: shape transitions and permeabilization. *Biochimica et Biophysica Acta (BBA)-Biomembranes* **1808**, 2965–2972 (2011).
104. Dolmans, D. E., Fukumura, D. & Jain, R. K. Photodynamic therapy for cancer. *Nature reviews cancer* **3**, 380–387 (2003).
105. Davis, H. W. *et al.* Enhanced phosphatidylserine-selective cancer therapy with irradiation and SapC-DOPS nanovesicles. *Oncotarget* **10**, 856 (2019).
106. Weaver, J. C., Smith, K. C., Esser, A. T., Son, R. S. & Gowrishankar, T. A brief overview of electroporation pulse strength–duration space: A region where additional intracellular effects are expected. *Bioelectrochemistry* **87**, 236–243 (2012).
107. Yarmush, M. L., Golberg, A., Serša, G., Kotnik, T. & Miklavčič, D. Electroporation-based technologies for medicine: principles, applications, and challenges. *Annu Rev Biomed Eng* **16**, 295–320 (2014).
108. Belehradek, M. *et al.* Electrochemotherapy, a new antitumor treatment. First clinical phase I-II trial. *Cancer* **72**, 3694–3700 (1993).
109. Gehl, J. Electroporation: theory and methods, perspectives for drug delivery, gene therapy and research. *Acta Physiologica Scandinavica* **177**, 437–447 (2003).
110. Neumann, E., Schaefer-Ridder, M., Wang, Y. & Hofschneider, P. Gene transfer into mouse lymphoma cells by electroporation in high electric fields. *The EMBO journal* **1**, 841–845 (1982).
111. Mir, L. *et al.* Effective treatment of cutaneous and subcutaneous malignant tumours by electrochemotherapy. *British journal of cancer* **77**, 2336–2342 (1998).
112. Abidor, I. *et al.* Electric breakdown of bilayer lipid membranes: I. The main experimental facts and their qualitative discussion. *Journal of electroanalytical chemistry and interfacial electrochemistry* **104**, 37–52 (1979).
113. Böckmann, R. A., De Groot, B. L., Kakorin, S., Neumann, E. & Grubmüller, H. Kinetics, statistics, and energetics of lipid membrane electroporation studied by molecular dynamics simulations. *Biophysical journal* **95**, 1837–1850 (2008).
114. Casciola, M. & Tarek, M. A molecular insight into the electro-transfer of small molecules through electropores driven by electric fields. *Biochimica et Biophysica Acta (BBA)-Biomembranes* **1858**, 2278–2289 (2016).
115. Lewis, T. J. A model for bilayer membrane electroporation based on resultant electromechanical stress. *IEEE transactions on dielectrics and electrical insulation* **10**, 769–777 (2003).
116. Heimburg, T. The capacitance and electromechanical coupling of lipid membranes close to transitions: the effect of electrostriction. *Biophysical journal* **103**, 918–929 (2012).
117. Nagle, J. & Scott Jr, H. Lateral compressibility of lipid mono- and bilayers. Theory of membrane permeability. *Biochimica et Biophysica Acta (BBA)-Biomembranes* **513**, 236–243 (1978).

118. Tekle, E., Astumian, R., Friauf, W. & Chock, P. Asymmetric pore distribution and loss of membrane lipid in electroporated DOPC vesicles. *Biophysical journal* **81**, 960–968 (2001).
119. Melikov, K. C. *et al.* Voltage-induced nonconductive pre-pores and metastable single pores in unmodified planar lipid bilayer. *Biophysical journal* **80**, 1829–1836 (2001).
120. Glaser, R. W., Leikin, S. L., Chernomordik, L. V., Pastushenko, V. F. & Sokirko, A. I. Reversible electrical breakdown of lipid bilayers: formation and evolution of pores. *Biochimica et Biophysica Acta (BBA)-Biomembranes* **940**, 275–287 (1988).
121. Tieleman, D. P., Leontiadou, H., Mark, A. E. & Marrink, S.-J. Simulation of pore formation in lipid bilayers by mechanical stress and electric fields. *Journal of the American Chemical Society* **125**, 6382–6383 (2003).
122. Bennett, W. D., Sapay, N. & Tieleman, D. P. Atomistic simulations of pore formation and closure in lipid bilayers. *Biophysical journal* **106**, 210–219 (2014).
123. Powell, K. T. & Weaver, J. C. Transient aqueous pores in bilayer membranes: a statistical theory. *Bioelectrochemistry and Bioenergetics* **15**, 211–227 (1986).
124. Kotnik, T., Rems, L., Tarek, M. & Miklavčič, D. Membrane electroporation and electropermeabilization: mechanisms and models. *Annual review of biophysics* **48**, 63–91 (2019).
125. Neu, J. C. & Krassowska, W. Asymptotic model of electroporation. *Physical review E* **59**, 3471 (1999).
126. Chandra, A. Static dielectric constant of aqueous electrolyte solutions: Is there any dynamic contribution? *The Journal of Chemical Physics* **113**, 903–905 (2000).
127. Weaver, J. C. & Chizmadzhev, Y. A. Theory of electroporation: a review. *Bioelectrochemistry and bioenergetics* **41**, 135–160 (1996).
128. Freeman, S. A., Wang, M. A. & Weaver, J. C. Theory of electroporation of planar bilayer membranes: predictions of the aqueous area, change in capacitance, and pore-pore separation. *Biophysical journal* **67**, 42–56 (1994).
129. Israelachvili, J. & Pashley, R. Measurement of the hydrophobic interaction between two hydrophobic surfaces in aqueous electrolyte solutions. *Journal of colloid and interface science* **98**, 500–514 (1984).
130. Kramar, P., Miklavcic, D. & Lebar, A. M. A system for the determination of planar lipid bilayer breakdown voltage and its applications. *IEEE Transactions on Nanobioscience* **8**, 132–138 (2009).
131. Weaver, J. C. Electroporation of cells and tissues. *IEEE transactions on plasma science* **28**, 24–33 (2000).
132. Sengel, J. T. & Wallace, M. I. Imaging the dynamics of individual electropores. *Proceedings of the National Academy of Sciences* **113**, 5281–5286 (2016).
133. Son, R. S., Smith, K. C., Gowrishankar, T. R., Vernier, P. T. & Weaver, J. C. Basic features of a cell electroporation model: illustrative behavior for two very different pulses. *The Journal of membrane biology* **247**, 1209–1228 (2014).
134. Antonov, V. F., Anosov, A. A., Norik, V. P. & Smirnova, E. Y. Soft perforation of planar bilayer lipid membranes of dipalmitoylphosphatidylcholine at the temperature of the phase transition from the liquid crystalline to the gel state. *European Biophysics Journal* **34**, 155–162 (2005).

135. Levine, Z. A. & Vernier, P. T. Life cycle of an electropore: field-dependent and field-independent steps in pore creation and annihilation. *The Journal of membrane biology* **236**, 27–36 (2010).
136. Vasilkoski, Z., Esser, A. T., Gowrishankar, T. & Weaver, J. C. Membrane electroporation: The absolute rate equation and nanosecond time scale pore creation. *Physical review E* **74**, 021904 (2006).
137. Antonov, V., Smirnova, E. Y. & Shevchenko, E. Electric field increases the phase transition temperature in the bilayer membrane of phosphatidic acid. *Chemistry and physics of lipids* **52**, 251–257 (1990).
138. Papahadjopoulos, D., Jacobson, K., Nir, S. & Isac, I. Phase transitions in phospholipid vesicles fluorescence polarization and permeability measurements concerning the effect of temperature and cholesterol. *Biochimica et Biophysica Acta (BBA)-Biomembranes* **311**, 330–348 (1973).
139. Cruzeiro-Hansson, L. & Mouritsen, O. G. Passive ion permeability of lipid membranes modelled via lipid-domain interfacial area. *Biochimica et Biophysica Acta (BBA)-Biomembranes* **944**, 63–72 (1988).
140. Corvera, E., Mouritsen, O., Singer, M. & Zuckermann, M. The permeability and the effect of acyl-chain length for phospholipid bilayers containing cholesterol: theory and experiment. *Biochimica et Biophysica Acta (BBA)-Biomembranes* **1107**, 261–270 (1992).
141. Blicher, A., Wodzinska, K., Fidorra, M., Winterhalter, M. & Heimburg, T. The temperature dependence of lipid membrane permeability, its quantized nature, and the influence of anesthetics. *Biophysical journal* **96**, 4581–4591 (2009).
142. Vernier, P. T. *et al.* Electroporating fields target oxidatively damaged areas in the cell membrane. *PloS one* **4**, e7966 (2009).
143. Yusupov, M., Van der Paal, J., Neyts, E. C. & Bogaerts, A. Synergistic effect of electric field and lipid oxidation on the permeability of cell membranes. *Biochimica et Biophysica Acta (BBA)-General Subjects* **1861**, 839–847 (2017).
144. Benov, L., Antonov, P. & Ribarov, S. Oxidative damage of the membrane lipids after electroporation. *General physiology and biophysics* **13**, 85–85 (1994).
145. Gabriel, B. & Teissie, J. Generation of reactive-oxygen species induced by electropermeabilization of Chinese hamster ovary cells and their consequence on cell viability. *European Journal of Biochemistry* **223**, 25–33 (1994).
146. Maccarrone, M., Bladergroen, M. R., Rosato, N. & Agro, A. F. Role of lipid peroxidation in electroporation-induced cell permeability. *Biochemical and Biophysical Research Communications* **209**, 417–425 (1995).
147. Stewart, J. C. M. Colorimetric determination of phospholipids with ammonium ferrothiocyanate. *Analytical biochemistry* **104**, 10–14 (1980).
148. Grabielle-Madelmont, C. & Perron, R. Calorimetric studies on phospholipid—water systems: I. dl-Dipalmitoylphosphatidylcholine (DPPC)—water system. *Journal of colloid and interface science* **95**, 471–482 (1983).
149. Pfeiffer, H., Klose, G. & Heremans, K. Reorientation of hydration water during the thermotropic main phase transition of 1-palmitoyl-2-oleoyl-sn-glycero-3-phosphocholine (POPC) bilayers at low degrees of hydration. *Chemical Physics Letters* **572**, 120–124 (2013).
150. Montalti, M., Credi, A., Prodi, L. & Gandolfi, M. T. *Handbook of photochemistry* (CRC press, 2006).

151. Wilkinson, F., Helman, W. P. & Ross, A. B. Rate constants for the decay and reactions of the lowest electronically excited singlet state of molecular oxygen in solution. An expanded and revised compilation. *Journal of Physical and Chemical Reference Data* **24**, 663–677 (1995).
152. Rafatullah, M., Sulaiman, O., Hashim, R. & Ahmad, A. Adsorption of methylene blue on low-cost adsorbents: a review. *Journal of hazardous materials* **177**, 70–80 (2010).
153. Bharti, S. K. & Roy, R. Quantitative <sup>1</sup>H NMR spectroscopy. *TrAC Trends in Analytical Chemistry* **35**, 5–26 (2012).
154. Westwood, S. *et al.* Development and validation of a suite of standards for the purity assignment of organic compounds by quantitative NMR spectroscopy. *Metrologia* **56**, 064001 (2019).
155. Rundlöf, T. *et al.* Survey and qualification of internal standards for quantification by <sup>1</sup>H NMR spectroscopy. *Journal of pharmaceutical and biomedical analysis* **52**, 645–651 (2010).
156. Wang, L., Bose, P. S. & Sigworth, F. J. Using cryo-EM to measure the dipole potential of a lipid membrane. *Proceedings of the National Academy of Sciences* **103**, 18528–18533 (2006).
157. Heberle, F. A. *et al.* Direct label-free imaging of nanodomains in biomimetic and biological membranes by cryogenic electron microscopy. *Proceedings of the National Academy of Sciences* **117**, 19943–19952 (2020).
158. Böckmann, R. A., Hac, A., Heimburg, T. & Grubmüller, H. Effect of sodium chloride on a lipid bilayer. *Biophysical journal* **85**, 1647–1655 (2003).
159. Van Echteld, C., De Kruijff, B. & De Gier, J. Differential miscibility properties of various phosphatidylcholine/lysophosphatidylcholine mixtures. *Biochimica et Biophysica Acta (BBA)-Biomembranes* **595**, 71–81 (1980).
160. Osella, S. & Knippenberg, S. Laurdan as a molecular rotor in biological environments. *ACS Applied Bio Materials* **2**, 5769–5778 (2019).
161. Sánchez, S. A., Tricerri, M., Gunther, G., Gratton, E., *et al.* Laurdan generalized polarization: from cuvette to microscope. *Modern research and educational topics in microscopy* **2**, 1007–1014 (2007).
162. Tonggu, L. & Wang, L. Cryo-EM sample preparation method for extremely low concentration liposomes. *Ultramicroscopy* **208**, 112849 (2020).
163. Tahara, Y. & Fujiyoshi, Y. A new method to measure bilayer thickness: cryo-electron microscopy of frozen hydrated liposomes and image simulation. *Micron* **25**, 141–149 (1994).
164. Majewska, M., Mrdenovic, D., Pieta, I. S., Nowakowski, R. & Pieta, P. Nanomechanical characterization of single phospholipid bilayer in ripple phase with PF-QNM AFM. *Biochimica et Biophysica Acta (BBA)-Biomembranes* **1862**, 183347 (2020).
165. Sengupta, K., Raghunathan, V. & Katsaras, J. Novel structural features of the ripple phase of phospholipids. *EPL (Europhysics Letters)* **49**, 722 (2000).
166. Sengupta, K., Raghunathan, V. & Katsaras, J. Structure of the ripple phase of phospholipid multibilayers. *Physical Review E* **68**, 031710 (2003).
167. Greenwood, A. I. *et al.* CRAC motif peptide of the HIV-1 gp41 protein thins SOPC membranes and interacts with cholesterol. *Biochimica et Biophysica Acta (BBA)-Biomembranes* **1778**, 1120–1130 (2008).

168. Kučerka, N., Tristram-Nagle, S. & Nagle, J. F. Structure of fully hydrated fluid phase lipid bilayers with monounsaturated chains. *The Journal of membrane biology* **208**, 193–202 (2006).
169. Cornell, C. E., Mileant, A., Thakkar, N., Lee, K. K. & Keller, S. L. Direct imaging of liquid domains in membranes by cryo-electron tomography. *Proceedings of the National Academy of Sciences* **117**, 19713–19719 (2020).
170. Curatolo, W., Sears, B. & Neuringer, L. J. A calorimetry and deuterium NMR study of mixed model membranes of 1-palmitoyl-2-oleylphosphatidylcholine and saturated phosphatidylcholines. *Biochimica et Biophysica Acta (BBA)-Biomembranes* **817**, 261–270 (1985).
171. Davis, P., Fleming, B., Coolbear, K. & Keough, K. Gel to liquid-crystalline transition temperatures of water dispersions of two pairs of positional isomers of unsaturated mixed-acid phosphatidylcholines. *Biochemistry* **20**, 3633–3636 (1981).
172. Hernandez-Borrell, J. & Keough, K. Heteroacid phosphatidylcholines with different amounts of unsaturation respond differently to cholesterol. *Biochimica et Biophysica Acta (BBA)-Biomembranes* **1153**, 277–282 (1993).
173. Tada, K. *et al.* Barotropic and thermotropic bilayer phase behavior of positional isomers of unsaturated mixed-chain phosphatidylcholines. *Biochimica et Biophysica Acta (BBA)-Biomembranes* **1788**, 1056–1063 (2009).
174. Wallgren, M. *et al.* Impact of oxidized phospholipids on the structural and dynamic organization of phospholipid membranes: a combined DSC and solid state NMR study. *Faraday Discussions* **161**, 499–513 (2013).
175. Ladbroke, B. & Chapman, D. Thermal analysis of lipids, proteins and biological membranes a review and summary of some recent studies. *Chemistry and physics of lipids* **3**, 304–356 (1969).
176. Hille, B. *Ionic channels in excitable membranes* 3rd (Sinauer Associates, 2001).
177. Smolen, J. E. & Shohet, S. B. Permeability changes induced by peroxidation in liposomes prepared from human erythrocyte lipids. *Journal of lipid research* **15**, 273–280 (1974).
178. Peterlin, P., Jaklič, G. & Pisanski, T. Determining membrane permeability of giant phospholipid vesicles from a series of videomicroscopy images. *Measurement Science and Technology* **20**, 055801 (2009).
179. Weinberger, A. *et al.* Gel-assisted formation of giant unilamellar vesicles. *Biophysical journal* **105**, 154–164 (2013).
180. Zaitseva, E. *et al.* in *Patch Clamp Electrophysiology* 67–92 (Springer, 2021).
181. White, S. H. Analysis of the torus surrounding planar lipid bilayer membranes. *Biophysical journal* **12**, 432–445 (1972).
182. Harden, S. pyABF 2.3.5. [Online]. Available at <https://swharden.com/pyabf/> or <https://pypi.org/project/pyabf/> (2022).
183. Pein, F., Bartsch, A., Steinem, C. & Munk, A. Heterogeneous Idealization of Ion Channel Recordings—Open Channel Noise. *IEEE Transactions on NanoBioscience* **20**, 57–78 (2020).
184. VanDongen, A. A new algorithm for idealizing single ion channel data containing multiple unknown conductance levels. *Biophysical Journal* **70**, 1303–1315 (1996).

185. Hung, W., Chen, F. & Huang, H. W. Order–disorder transition in bilayers of di-phytanoyl phosphatidylcholine. *Biochimica et Biophysica Acta (BBA)-Biomembranes* **1467**, 198–206 (2000).
186. Bacellar, I. O. *et al.* Permeability of DOPC bilayers under photoinduced oxidation: Sensitivity to photosensitizer. *Biochimica et Biophysica Acta (BBA)-Biomembranes* **1860**, 2366–2373 (2018).
187. Heuvingh, J. & Bonneau, S. Asymmetric oxidation of giant vesicles triggers curvature-associated shape transition and permeabilization. *Biophysical journal* **97**, 2904–2912 (2009).
188. Gross, L. C., Heron, A. J., Baca, S. C. & Wallace, M. I. Determining membrane capacitance by dynamic control of droplet interface bilayer area. *Langmuir* **27**, 14335–14342 (2011).
189. Ardham, V. R., Zoni, V., Adamowicz, S., Campomanes, P. & Vanni, S. Accurate estimation of membrane capacitance from atomistic molecular dynamics simulations of zwitterionic lipid bilayers. *The Journal of Physical Chemistry B* **124**, 8278–8286 (2020).
190. Goldman, D. E. Potential, impedance, and rectification in membranes. *The Journal of general physiology* **27**, 37–60 (1943).
191. Hodgkin, A. L. & Katz, B. The effect of sodium ions on the electrical activity of the giant axon of the squid. *The Journal of physiology* **108**, 37 (1949).
192. Frankenhaeuser, B. Sodium permeability in toad nerve and in squid nerve. *The Journal of physiology* **152**, 159 (1960).
193. Hall, J. E., Mead, C. & Szabo, G. A barrier model for current flow in lipid bilayer membranes. *The Journal of Membrane Biology* **11**, 75–97 (1973).
194. Fuks, B. & Homble, F. Permeability and electrical properties of planar lipid membranes from thylakoid lipids. *Biophysical journal* **66**, 1404–1414 (1994).
195. Kowalczyk, S. W., Grosberg, A. Y., Rabin, Y. & Dekker, C. Modeling the conductance and DNA blockade of solid-state nanopores. *Nanotechnology* **22**, 315101 (2011).
196. Haynes, W. M., Lide, D. R. & Bruno, T. J. *CRC handbook of chemistry and physics* (CRC press, 2016).
197. Buettner, G. R. The pecking order of free radicals and antioxidants: lipid peroxidation,  $\alpha$ -tocopherol, and ascorbate. *Archives of biochemistry and biophysics* **300**, 535–543 (1993).
198. Ginkel, G., ávan't Veld, A. A., ávan Zandvoort, M. A., LouáWratten, M., *et al.* Impact of oxidized lipids and antioxidants, such as vitamin E and lazaroids, on the structure and dynamics of unsaturated membranes. *Journal of the Chemical Society, Faraday Transactions* **88**, 1901–1912 (1992).
199. Vyšniauskas, A., Qurashi, M. & Kuimova, M. K. A molecular rotor that measures dynamic changes of lipid bilayer viscosity caused by oxidative stress. *Chemistry—A European Journal* **22**, 13210–13217 (2016).
200. Hosny, N. A. *et al.* Mapping microbubble viscosity using fluorescence lifetime imaging of molecular rotors. *Proceedings of the National Academy of Sciences* **110**, 9225–9230 (2013).
201. López-Duarte, I., Vu, T. T., Izquierdo, M. A., Bull, J. A. & Kuimova, M. K. A molecular rotor for measuring viscosity in plasma membranes of live cells. *Chemical Communications* **50**, 5282–5284 (2014).

202. Dent, M. R. *et al.* Imaging phase separation in model lipid membranes through the use of BODIPY based molecular rotors. *Physical Chemistry Chemical Physics* **17**, 18393–18402 (2015).
203. Zhang, R. *et al.* Small-angle x-ray scattering from lipid bilayers is well described by modified Caillé theory but not by paracrystalline theory. *Biophysical journal* **70**, 349–357 (1996).
204. Barnett, A. & Weaver, J. C. Electroporation: a unified, quantitative theory of reversible electrical breakdown and mechanical rupture in artificial planar bilayer membranes. *Bioelectrochemistry and bioenergetics* **25**, 163–182 (1991).



# List of Abbreviations

## Lipids

DMPC	1,2-dimyristoyl-glycero-3-phosphocholine
DMPE	1,2-dimyristoyl-glycero-3-phosphoethanolamine
DOPC	1,2-dioleoyl-glycero-3-phosphocholine
DPhPC	1,2-diphytanoyl-glycero-3-phosphocholine
DPPC	1,2-dipalmitoyl-glycero-3-phosphocholine
oxPC	cutted chain oxidized lipid
POPC	1-palmitoyl-2-oleoyl-glycero-3-phosphocholine
POPC-OOH	Hydroperoxidized POPC
POPE	1-palmitoyl-2-oleoyl-glycero-3-phosphoethanolamine
POPG	1-palmitoyl-2-oleoyl-glycero-3-phosphoglycerol
SOPC	1-stearoyl-2-oleoyl-glycero-3-phosphocholine
SOPC-OOH	Hydroperoxidized SOPC

## Measurement techniques

DLS	Dynamic Light Scattering
DSC	Differential Scanning Calorimetry
EM	Electron Microscopy
FLIM	Fluorescence Lifetime Imaging Microscopy
NMR	Nuclear Magnetic Resonance
q-NMR	Quantitative NMR
SAXS	Small Angle X-Ray Scattering
TEM	Transmission Electron Microscopy
WAXS	Wide Angle X-Ray Scattering

## Other abbreviations

2D	2 Dimention
3D	3 Dimention
ATP	Adenosine TriPhosphate
BLM	Black Lipid Membrane
CCD	Charge Coupled Device
CD <sub>3</sub> CN	Deuterated acetonitril
CD <sub>3</sub> OD	Deuterated methanol
CDCl <sub>3</sub>	Deuterated chloroform
CPS	Count per second
C/H	Cooling/Heating
DMTP	DiMethyl TerePhtalate
DNA	DeoxyriboNucleic Acid
EDR	Elements Data Reader

<b>GP</b>	<b>Generalized Polarization</b>
<b>GUV</b>	<b>Giant Unilamellar Vesicle</b>
<b>ICS</b>	<b>Institute Charles Sadron</b>
<b>LED</b>	<b>Light Emitting Diode</b>
<b>LMV</b>	<b>Large Multilamellar Vesicle</b>
<b>LUV</b>	<b>Large Unilamellar Vesicle</b>
<b>MB</b>	<b>1,9-dimethyl Methylene Blue</b>
<b>MCube</b>	<b>Membrane et Matière Moles</b>
<b>PC</b>	<b>PhosphatidylCholine</b>
<b>PE</b>	<b>PhosphatidylEthanolamine</b>
<b>pH</b>	<b>Potentiel Hydrogen</b>
<b>PhD</b>	<b>Doctor of Philosophy</b>
<b>PS</b>	<b>PhosphatidylSerine (Chapter 0)</b>
<b>PS</b>	<b>PhotoSensitizer (Chapter 1)</b>
<b>PVA</b>	<b>PolyVinyl Alcohol</b>
<b>RH</b>	<b>Relative Humidity</b>
<b>RNA</b>	<b>RiboNucleic Acid</b>
<b>ROS</b>	<b>Reactive Oxygen Species</b>
<b>SUV</b>	<b>Small Unilamellar Vesicle</b>
<b>TPP</b>	<b>TetraPhenylPorphyrin</b>
<b>UV</b>	<b>Ultra-Violet</b>
<b>-OOH</b>	<b>Peroxide group</b>

## Notations

<b>c</b>	<b>Closing (or intrinsic to membrane)</b>
$D_i$	<b>Day i</b>
$L_\alpha$	<b>Fluid phase</b>
$L_\beta$	<b>Gel phase</b>
$L_c$	<b>Liquid crystalline phase</b>
$L_d$	<b>Disordered fluid phase</b>
<b>LH</b>	<b>Lipid</b>
$L_o$	<b>Ordered fluid phase</b>
<b>L-OOH</b>	<b>Hydroperoxidized lipid</b>
<b>m</b>	<b>Membrane</b>
<b>o</b>	<b>Opening</b>
$P_\beta$	<b>Ripple phase</b>
<b>P0</b>	<b>POPC</b>
<b>P50</b>	<b>POPC-OOH/POPC mixture 50/50 mol %</b>
<b>P100</b>	<b>POPC-OOH</b>
<b>p</b>	<b>Pore</b>
<b>S</b>	<b>Solvent</b>
<b>S0</b>	<b>SOPC</b>
<b>S50</b>	<b>SOPC-OOH/SOPC mixture 50/50 mol %</b>
<b>S100</b>	<b>SOPC-OOH</b>
$S_i$	<b>Singlet state of energy level i</b>
$T_i$	<b>Triplet state of energy level i</b>
<b>w</b>	<b>Aqueous phase</b>

# List of Symbols

$[i]$	Concentration of i	$mol.m^{-3}$
$A_i$	Area per lipid i	$m^2$
$b$	bilayer hydrophobic thickness	$m$
$C_0$	Experimental constant	$J.m^{-4}$
$C_{ion}$	Ion concentration	$mol.m^{-3}$
$C_m$	Capacitance	$F$
$C_p$	Heat capacity	$J.K^{-1}$
$c_m$	Specific capacitance	$F.m^{-2}$
$D1$	Relaxation time	$s$
$D_i^j$	Diffusion of i in the medium j	$m^2.s^{-1}$
$D_p$	Pore diameter	$m$
$\overline{D}_p$	Average pore diameter	$m$
$d$	Total bilayer thickness	$m$
$d_{HH}^i$	Head to head thickness of i bilayer	$m$
$f_p$	Pore opening attempt rate	$s^{-1}$
$G_{noise}$	Noise gain	-
$H$	Light absorption cross section	$m^2$
$I$	Current intensity	$A$
$\overline{I}$	Average current intensity	$A$
$I_c$	Intrinsic current intensity through the membrane	$A$
$I_i$	Modified Bessel function of order i	-
$I_p$	Current intensity through pores of a specific size	$A$
$I_U$	Current intensity measured at voltage U	$A$
$I_T$	Current intensity threshold	$A$
$I_\lambda$	Laurdan emission spectra intensity at $\lambda$	-
$\overline{I}_{<20}$	Average of intensity below 20 pA	$A$
$i_c$	Membrane intrinsic current density	$A.m^{-2}$
$J_i$	Flux density of i	$mol.s^{-1}.m^{-2}$
$K^{i,j}$	Partition coefficient between i and j	-
$M_w$	Molecular weight	$kg/mol^{-1}$
$N_0$	Initial noise threshold	$A$
$N_{loc}$	Calculated local noise threshold	$A$
$N_s$	Number of pore per second (pore opening frequency)	$s^{-1}$
$n_w$	Water/lipid molecule ratio	-
$P$	Power light density	$W.m^{-2}$
$P_m^i$	Permeability of the membrane in regard to i	$m.s^{-1}$
$Q$	$^1O_2$ production rate	$s^{-1}$
$q$	Wave (or scattering) vector	$m^{-1}$
$R^2$	Fit quality	-
$R_c$	Intrinsic membrane resistance without pore	$\Omega$
$R_m$	Membrane resistance	$\Omega$
$R_p$	Pore resistance	$\Omega$

$R_s$	Instrument resistance	$\Omega$
$r_i$	Radius of i	m
$r_{\min}$	Minimum hydrophilic pore radius	m
$r_{\text{rupt}}$	Maximum pore radius before rupture	m
S	Membrane surface	$\text{m}^2$
$S_{cd}$	Order parameter	-
$S_{\max}$	Membrane maximal surface	$\text{m}^2$
T	Temperature	K
$T_1$	Longest relaxation time	s
$T_m$	Phase transition temperature	K
$T_p$	Pre-transition temperature	K
t	Time	s
$t_c$	Time of the pore closing	s
$t_o$	Time of the pore opening	s
$t^*$	Path time	s
U	Potential difference, Voltage	V
$U_{90}$	Voltage where 90 % of the membrane open at least one pore	V
$U_c$	Membrane potential	V
$U_{\text{cubic}}$	Voltage where the cubic fit stop properly fitting the data	V
$U_{\text{pore}}^{\text{half}}$	Voltage for half membrane to open at least one pore	V
$U_{\text{rupture}}$	Membrane rupture potential	V
$U_{\text{rupture}}^{\text{half}}$	Voltage for half membrane to rupture	V
$U_{\text{threshold}}$	Electroporation voltage threshold	V
u	Normalized voltage	-
$X_{\text{OOH}}$	Molar fraction of hydroperoxidized lipid	mol %
x	Position (or distance)	m
z	Valence	-
z $\gamma$	NMR pulse angle	rad
$\alpha$	Emperical constante (pore formation)	-
$\Gamma$	Surface tension	$\text{J.m}^{-2}$
$\gamma$	Edge line tension	J/m
$\Delta E$	Energy	J
$\Delta H$	Enthalpy	J
$\Delta I_c$	Pore closing intensity	A
$\Delta I_o$	Pore opening intensity	A
$\delta$	Chemical shift	ppm
$\epsilon_i$	Permittivity of i	F/m
$\epsilon_i^0$	Relative permittivity of i	-
$\eta_i$	Viscosity of the medium i	Pa.s
$\lambda_c$	Characteristic hydrophobic interaction length	m
$\lambda$	Light wavelength	m
$\mu_0^{i,j}$	Standard chemical potential between i and j	$\text{J.mol}^{-1}$
$\nu$	Photon frequency	Hz
$\zeta$	Friction coefficient	Pa.m.s
$\sigma$	Solution conductivity	$\text{S.m}^{-1}$
$\tau$	Electroporation device time constant	s
$\tau_d$	Time to charge the membrane in presence of pore	s
$\tau_{RC}$	Time to charge the membrane in absence of pore	s

---

$\tau_p$	Pore lifetime	s
$\tau_{ph}$	Photon lifetime	s
$\tau_{MB}$	MB triplet state lifetime	s
$\tau_{O_2}$	$^1O_2$ triplet lifetime	s
$\bar{\tau}_p$	Average pore lifetime	s
$\varphi$	Quantum yield	-



# Physical constants

Avogadro constant	$N_a$	$6.022\,141 \times 10^{23} \text{ mol}^{-1}$
Boltzmann constant	$k_B$	$1.380\,649 \times 10^{-23} \text{ J K}^{-1}$
Elementary charge	$e$	$1.602\,177 \times 10^{-19} \text{ C}$
Faraday constant	$\mathcal{F}$	$9.648\,533 \times 10^4 \text{ A s mol}^{-1}$
Gas constant	$\mathcal{R}$	$8.314\,463 \text{ J mol}^{-1} \text{ K}^{-1}$
Permittivity of vacuum	$\epsilon_0$	$8.854\,188 \times 10^{-12} \text{ F m}^{-1}$
Planck constant	$h$	$6.626\,070 \times 10^{-34} \text{ J Hz}^{-1}$
Speed of light	$c$	$2.997\,925 \times 10^8 \text{ m s}^{-1}$



# List of Figures

1	Representation of a biological cell with its plasma membrane and different organelles (ex: nucleus, mitochondria). Image taken from [1]. . .	1
2	Self-assembly of phospholipids into a bilayer with an example of a phospholipid chemical formula and its usual amphiphilic representation. . . . .	2
3	Examples of membrane lipids: phospholipid (top) and sterol (bottom) chemical structures, two abundant lipid classes. . . . .	3
4	Permeability scale of lipidic membranes to some molecules of interest [10, 12–16]. . . . .	5
5	Lipidic membrane with inserted transmembrane protein inducing active transportation. . . . .	7
6	In the fluid state the lipids diffuse laterally in the membrane with a high diffusion coefficient ( $\sim \mu^2.s^{-1}$ ) and can occasionally ( $\sim$ every day) flip-flop from one leaflet to the other. . . . .	7
7	Scheme of lipid organization from the gel to the fluid phase. . . . .	8
8	DPPC DSC scan obtained at a heating rate of 0.25 °C/min. The main transition between the gel and the fluid phase happens around $T_m=42$ °C. DPPC displays also a pre-transition temperature $T_p$ around 35 °C from the gel phase to the so-called ripple phase. . . . .	9
9	Main phase transition temperature of saturated lipids with identical tails as a function of their carbon chain length and their head composition (PS being bound to $Na^+$ ). The graph is obtained from $T_m$ values taken in the Handbook of lipid bilayers [3]. . . . .	9
10	(A) Transition temperature between the fluid and gel phase of DOPC (18:1c $\Delta^n$ ) <sub>2</sub> as a function of the cis unsaturation position $n$ on the carbon chains. Figure reconstructed from Barton et al. (1975) [35] (B) Impact of cis and trans unsaturation on the bilayer phase transition temperature. Values from [3, 35–38]. . . . .	10
11	Heating DSC scans of DOPC with different water/lipid molecule ratio ( $n_w$ ). Figure taken from Ulrich et al. (1994) [39]. . . . .	10
12	Permeability of a DMPC (14:0) <sub>2</sub> membrane regarding $Co_2^+$ ions as a function of the temperature. The figure is taken from Heimburg (2010) [22]. Away from the transition temperature of DMPC ( $\sim 24$ °C), the membrane is impermeable, however at the neighboring of $T_m$ , the permeability exhibit a huge increase. Permeation rate represents the time constant for the quenching of a fluorophore inserted inside the bilayer by the $Co_2^+$ present in the external media. . . . .	11
13	Simulation snapshot of phase coexistence during a gel-fluid transition, taken from Kirsch et al. (2019) [33]. Different order coexistence can be observed, with different thicknesses and lipid orientations. . . .	11

14	Possible reaction propagation between oxidized and non-oxidized lipid chain during type I photo-oxidation. This mechanism explains the possibility of obtaining shorted lipid chain. Figure from Ulmer et al. (2021) [65]. . . . .	13
15	Energy level transfer required for type II peroxidation. The photosensitizer in its ground state should first rise its energy to its higher energy singlet state and cross by inter-system crossing its triplet state. The triplet state can then transfer its energy to a dioxygen molecule naturally found in its triplet ground state in order to create a highly reactive singlet oxygen. . . . .	14
16	Schematic changes of the main conformation of a mono-unsaturated hydroperoxidized lipid in a bilayer. . . . .	15
17	Scheme of the increase in the area per lipid from $A_L$ to $A_{L-OOH}$ and decrease in the bilayer thickness $d_L$ to $d_{L-OOH}$ after hydroperoxidation of mono-unsaturated lipid. . . . .	15
18	Scheme of a pore formed in a cell membrane caused by an electric field and in order to insert a molecule inside. . . . .	18
19	Scheme of the growth of a water defect in the membrane and lipid reorganization to form a pore. (A) Water defect starts to enter the membrane (B) grows until forming an entire hydrophobic pore (C) followed by lipid rearrangement to form a stable hydrophilic pore. . .	19
20	Energy landscape for pore formation $\Delta E$ as a function of the pore opening radius $r$ for different voltages. . . . .	21
1.1	Chemical formula of POPC and SOPC with their two respective hydroperoxidized isomers. . . . .	27
1.2	Sketch of photo-induced lipid hydroperoxidation and purification. After a single reaction step (step 1) the photosensitizer can be easily removed by dialysis (step 2). . . . .	28
1.3	POPC $^1\text{H}$ NMR spectrum in $\text{CD}_3\text{OD}$ with peak attribution related to the molecule. The commercial lipids are dried and redissolved in $\text{CD}_3\text{OD}$ . . . . .	30
1.4	POPC-OOH isomers $^1\text{H}$ NMR spectrum in $\text{CD}_3\text{OD}$ after dialysis with peak attribution related to the molecules. The dialyzed hydroperoxidized lipids are dried and redissolved in $\text{CD}_3\text{OD}$ . . . . .	30
1.5	SOPC $^1\text{H}$ NMR spectrum in $\text{CD}_3\text{OD}$ with peak attribution related to the molecule. The commercial lipids are dried and redissolved in $\text{CD}_3\text{OD}$ . . . . .	31
1.6	SOPC-OOH isomers $^1\text{H}$ NMR spectrum in $\text{CD}_3\text{OD}$ with peak attribution related to the molecules. The freshly hydroperoxidized lipids are directly analyzed by NMR. . . . .	31

- 1.7 Typical chemical reaction pathway between compounds involved during lipid (L) photo-oxidation.  $h\nu$  represents the light absorbed by the photosensitizer (PS) to go into its excited state (\*PS). In case of uncontrolled reaction (panel left), PS can react with many compounds to induce secondary reactions and many unwanted sub-products ( $PS_x$ ,  $S_x$ ,  $L_x$ ). If both reactants and solvent (S) are carefully chosen and introduced in proper quantities, secondary reactions can be avoided or minimized to obtain hydroperoxidized lipid (L-OOH) with good purity (panel right). Curved arrows represent chemical reactions between the two compounds while straight arrows point to the product obtained. . . . . 34
- 1.8 Hydroperoxidation kinetics using decreasing  $CD_3OD/CD_3CN$  volume ratios. Hydroperoxidation in pure  $CD_3OD$  is made on SOPC while hydroperoxidation in the solvent mixture is done on POPC. Hydroperoxidation percentages are extracted from NMR spectra. Solid lines represent exponential fits. . . . . 35
- 1.9 MB concentration over dialysis time determined by UV-spectroscopy. Full squares are experimental data and the solid line is an exponential fit. . . . . 36
- 1.10 POPC-OOH isomers with DMTP  $^1H$  q-NMR spectrum in  $CDCl_3$  with peak attribution related to the corresponding molecules. Blue and black attribution correspond to each POPC-OOH isomers (only one is represented), and green attribution is for DMTP. . . . . 37
- 1.11 L-Dry<sub>1</sub>  $^1H$  q-NMR spectra in  $CDCl_3$  recorded at different time (0, 1, 2, 3 days). In black boxes are shown zoom of the impurities growing over drying-redissolving cycles. A shift of typical POPC-OOH peaks is also observed around 2.5-4.5 ppm. . . . . 38
- 1.12 Integral of 5.7 ppm NMR peaks corresponding to position 8'(11') in POPC-OOH obtained by  $^1H$  q-NMR of different L-Dry<sub>i</sub> samples of different ages. Integrals are normalized with the POPC-OOH position 2 peak integral. Between each data point of the same sample, a drying-redissolving is done. . . . . 39
- 1.13 Integral of NMR peaks corresponding to a different position in POPC-OOH and in DMTP obtained by  $^1H$  q-NMR of (A) different L-Dry<sub>i</sub> samples and (B) L- $CDCl_3$  sample over time. Integrals are normalized by the POPC-OOH position 2 peak integral. . . . . 40
- 2.1 Cryo-TEM principle. Scheme of a 2D projection obtained from the electron (in yellow) deviation through the 3D vesicles according to atoms phase shift. . . . . 44

2.2	Steps of the bilayer thickness determination routine. (A) Sub-image centered on a circular SUV with well defined leaflets. (B) Radial selection of the a perfectly circular perimeter determined by hand using Image J. (C) Best determination of the SUV perimeter obtained after cross section alignment by intercorrelation with the average profile. (D) Gray level profiles of the cross-sections centered on the original perimeter circle (red circle in B), and average profile (in black). (E) Set of gray level profiles obtained from the best correlation procedure (see text). Those profiles correspond to the red contour in C. In black is the average profile. (F) Final averaged gray profile with a polynomial fit near the two minimum (red dashed line). The bilayer thickness is calculated as the distance between the two minima (vertical dashed lines). . . . .	47
2.3	POPC cooling scan (1 °C/min). The saturated heat rate values correspond to water freezing in samples and reference cells. The inset is a zoom on the main phase transition. . . . .	49
2.4	Laurdan emission spectra when inserted in a SOPC membrane at 0 and 20 °C with its chemical formula. . . . .	50
2.5	Examples of images from each sample studied by cryo-TEM: A) P0, B) P50, C) P100, D) S0, E) S50, F) S100. . . . .	52
2.6	Average bilayer thickness measured on cryo-TEM images as a function of POPC and SOPC hydroperoxidation degree. Error bars represent the standard deviation. . . . .	54
2.7	Cooling scans of POPC containing 0, 5, 10, 15 and 20 mol % of POPC-OOH. Scans are acquired with 0.25 °C/min speed and are stopped when the water starts to freeze. . . . .	54
2.8	Heating scan of POPC. The scan is acquired with 0.25 °C/min speed. The "bouncing" artifact is visible at the beginning of the scan (at lower temperatures). . . . .	55
2.9	Cooling scans of SOPC containing 0, 25, 50, 70 and 100 mol % of SOPC-OOH. Scans are acquired with 0.25°C/min speed and are cut when the water starts to freeze. . . . .	56
2.10	Cooling scans of SOPC containing 30, 39, 44, 47, 48, and 53 mol % of SOPC-OOH. Scans are acquired with 0.25°C/min speed and are stopped when the water starts to freeze. . . . .	56
2.11	Evolution of the phase transition temperature of POPC and SOPC containing an increasing amount of their hydroperoxidized forms. Error bars represent the standard deviation. . . . .	57
2.12	Evolution of generalized polarization (GP) of SOPC-OOH/SOPC mixtures as a function of the temperature. . . . .	58
2.13	Evolution of the phase transition enthalpy of POPC and SOPC containing an increasing amount of their hydroperoxidized forms. Error bars represent the standard deviation. . . . .	59
3.1	Scheme of the gel-assisted method used to grow GUVs in sucrose. . . .	65
3.2	The free-standing lipid bilayer anchored on a Meca 4 recording chip. (A) is the representation of the Meca 4 chip. (B) shows a vertical cut of one of the wells with a painted bilayer. The lipid bilayer spans a large but not full fraction of the well top, separating a bottom from a top electrolyte solution. In (C) is depicted for illustration purposes the hypothetical geometry of bilayers anchored along the aperture rim. . . . .	66

- 3.3 Scheme of the air bubble technique used to paint free-standing lipid bilayer on top of the Meca 4 well. . . . . 67
- 3.4 Voltage protocol  $U(t)$  used for current intensity recordings. Voltages are increased by steps of 25 mV and kept constant for 6 seconds. For each step, negative and positive voltages are applied, all separated by intermediate steps at 0 mV. . . . . 67
- 3.5 Intensity  $I(t)$  (top) and concomitant voltage  $U(t)$  (bottom) recording as a function of time evidencing (a POPC) membrane rupture. . . . . 68
- 3.6 Scheme of the *threshold* detection method to detect opening time ( $t_o$ ), closing time ( $t_c$ ), and intensity  $I_p$  for two isolated pores. Only pores above the detection threshold are considered.  $s$  represent the maximal intensity of a pore, and  $r$  the first point after pore closure. . . . . 71
- 3.7 Example of detection of time isolated pores using the *threshold method* showing 6 short lifetime pores and one long lifetime pore. . . . . 72
- 3.8 Example of signal filtering for long lifetime pore detection using the *square gating method*. . . . . 72
- 3.9 (A) POPC and (B) POPC-OOH GUV radially averaged gray level evolution over 30 min after KCl addition in the outer media. . . . . 73
- 3.10 Capacitance values  $C_m$  of the investigated bilayers depending on the hydroperoxidation amount in membranes ( $X_{OOH}$ ). The box plot represents the distribution of membrane capacitance based on the first quartile, the median, the mean (filled square symbol), the third quartile, and with whiskers showing standard deviation. The dashed lines correspond to 6 and 13.5 pF, the usual range of membrane capacitance. 74
- 3.11 Microscopy image of a Meca 4 chip cavity on which lipid bilayers are formed. As the image shows, the aperture edge displays small irregularities, which are different from well to well, contributing to the variations in the quality of the anchored bilayers and corresponding signals. . . . . 75
- 3.12 Examples of current traces obtained under voltage-clamp conditions for POPC membranes containing 0 %, 50 %, or 100 % of POPC-OOH under applied voltages of  $\pm 50$  mV,  $\pm 100$  mV and  $\pm 150$  mV. Expanded traces are shown in the right panels. . . . . 76
- 3.13 Current traces and associated membrane geometry. (A) Identifiable sections of the current intensity traces  $I(t)$  along with (B) their schematic representation and (C) their presumed membrane conformation. Under no (i) or small (ii) applied voltages, the current fluctuates smoothly about a small ( $\sim$  pA) average current. Charge accumulation on both sides of the membrane acts as a capacitor, and a small number of ions cross the membrane. Under larger applied voltages, the opening of short lifetime pores (iii) and long lifetime pores (iv) can be detected by the sudden rise of the current corresponding to angstrom-size pores. Pores can accommodate lipid heads along the pore rim, in a conformation referred to as hydrophilic pores. When a small amount of pores is opened they can still be individually detected in the current traces (v). . . . . 77

- 3.14 Typical  $I(t)$  traces observed during electroporation, all intensities are presented as positive. (A) shows the clustering of pore formations in time (POPC under -225 mV). (B) shows the intensity - size - relaxation of a long lifetime pore (POPC under -225 mV). (C) shows the opening of long lifetime pores of specific sizes (POPC containing 70 mol % of POPC-OOH under 100 mV). (D) Example of two types of heterogeneous noise (POPC containing 70 mol % of POPC-OOH under 125 mV). (E) shows complex signals eventually going back to a more stable state (POPC under -300 mV). (F) Example of a periodic baseline oscillation (POPC containing 70 mol % of POPC-OOH under -150 mV). . . . . 80
- 3.15 Probability of the membrane survival as a function of the applied voltage (during 6 seconds) and hydroperoxidation degree of POPC membranes. Symbols represent the calculated probability from at least 50 membranes. Solid lines are a visual guide to the eyes. . . . . 81
- 3.16 Shape of the  $i_c(U)$  curves depending on the membrane potential shape.  $\Delta E_m$  is the membrane potential barrier,  $b$  the hydrophobic thickness of the bilayer and  $d$  the total thickness. . . . . 82
- 3.17 Intrinsic membrane electropermeability. (A)  $i_c(u)$  is the average current flowing through a pore-free membrane. The left axis measures current density  $i_c$  while the scale on the right axis expresses current  $I_c$  across a patch of 42  $\mu\text{m}$  diameter. The bottom axis displays normalized voltage units  $u = eU/(k_B T)$  while applied voltage  $U$  is shown at the top horizontal axis. The solid line represents the cubic fit of the data, dashed lines show when the fit starts to be less relevant. (B) Permeability  $P_m$  of POPC membranes as a function of  $X_{\text{OOH}}$ , the molar fraction of hydroperoxidized lipids. For both panels, error bars represent the standard deviation. . . . . 83
- 3.18 Probability for membranes to be free of pores during 6 seconds as a function of the voltage and the hydroperoxidation degree of POPC membranes. Symbols represent the calculated probability, solid lines are visual guides to the eyes. The dashed line represents the half probability of pore opening. . . . . 84
- 3.19 The validity range of the trapezoidal representation of the membrane potential  $U_{\text{cubic}}$  correlates to a high enough voltage that corresponds to the probability of opening at least one pore in 6 s close to 0.9,  $U_{90}$ .  $X_{\text{OOH}}$  values are given for each corresponding data point. . . . . 85
- 3.20 Membrane probability to open (A) short, (B) long lifetime pore or (C) exhibiting complex behavior at different voltages and lipid hydroperoxidation degree. Symbols are the experimental probabilities, solid lines are visual guides for relevant probabilities and dashed lines are visual guides for biased data due to membrane rupture. . . . . 86
- 3.21 Mean current intensity  $\bar{I}$  as a function of the applied voltage for the different lipid membrane compositions. Solid lines represent visual guide to the eyes and error bars the standard deviation. . . . . 87
- 3.22 Comparison between the pore-free intrinsic current  $I_c$  and the total average current  $\bar{I}$  taken at +150 mV, as a function of hydroperoxydation. 87

- 3.23 Pore lifetime distribution (bins=0.8 ms) normalized for 1000 pores. The solid line represents a guide for the eyes of the distribution decay. The figure in caption shows the independence of the pore lifetime median evolution with the applied voltage, justifying to group all lifetimes regardless of the voltage. . . . . 88
- 3.24 Average pore diameter  $D_p$  of short lifetime pores for different hydroperoxidation degrees  $X_{OOH}$ . The filled square represents the average, the middle line the median, the edges of the box the first and third quartile, and the whiskers the standard deviation. . . . . 89
- 3.25 (A) Average number of short lifetime pores opening per second  $N_s$  as a function of the voltage for the different hydroperoxidation degrees in POPC membranes. Error bars represent standard deviation. Solid lines represent exponential fit. (B) The master curve is obtained by normalizing  $N_s$  over  $f_p(X_{OOH})/f_p(0)$ . . . . . 90
- 3.26 Pore opening attempt rate for positive  $f_p^+$  and negative  $f_p^-$  voltages for the different hydroperoxydation degree of membranes  $X_{OOH}$  (normalized by  $f_p^+(0)$  and  $f_p^-(0)$  respectively). . . . . 91
- 3.27 Average pore diameter  $D_p$  of long lifetime pores over the different voltages for different hydroperoxidation degree  $X_{OOH}$ . The filled squares represent the average, the middle line the median, the edges of the box the first and third quartile and the whiskers the standard deviation. . . . . 92
- 3.28 Pore lifetime distribution (bins = 100 ms) for long lifetime pores detected with the squared signal idealization technique (Normalized to 100 pores). The solid line correspond to visual guide for the eyes. . . . . 93
- 4.1 Evolution of the viscosity as a function of POPC hydroperoxidation, (A) using the BC10 probe in pre-made mixtures, (B) using BC6++ in pre-made mixtures and (C) using BC10 in in-situ hydroperoxidation (red curve) and no oxidation (blue curve). Error bars represent the standard deviation. . . . . 98
- 4.2 (A to C) FLIM images of POPC-OOH/POPC (0/100, 50/50 and 100/0) GUVs stained with BC6++ (scale bar: 20  $\mu\text{m}$ ) with (D) the associated viscosity distribution for the three different compositions. . . . . 99
- 4.3 (A) Laurdan fluorescent spectra depending on the lipid membrane composition (at 22.5  $^\circ\text{C}$ ). (B) GP evolution calculated from (A) as a function of the amount of POPC-OOH using equation 2.1. . . . . 99
- 4.4 Evolution of the GP as a function of the temperature for vesicles made of POPC containing 0, 50 and 100 mol % of POPC-OOH. Error bard represent the standard deviation. . . . . 100
- 4.5 X-Ray scattering intensity profiles for POPC-OOH/POPC mixtures. (A) SAXS profiles and (B) WAXS profiles. . . . . 101
- 4.6 Average lipid order parameter  $S_{cd}$  as a function of the carbon position for (A) POPC, (B) a mixed POPC-OOH/POPC 50/50 mol % and (C) the two POPC-OOH isomers. Dashed lines correspond to the saturated chain (16:0) while solid lines to the (18:1) chain. POPC-OOH<sub>*n*</sub> correspond to POPC-OOH with the peroxide group on the *n*<sup>th</sup> carbon. 101

- 5.1 Hydroperoxydation effect on structural organization of lipid membranes. Hydroperoxydation increases the area per lipid and creates interactions between water and the peroxide group that facilitate water defects in the hydrophobic core. In addition, the conical shape of hydroperoxydized lipid facilitates the hydrophilic pore stabilisation. . . 105
- 6.1 Hydroperoxydation d'un lipide monoinsaturé. Repositionnement du groupe peroxyde à la surface de la bicouche pour interagir avec la tête polaire et les molécules d'eau dans le cas d'un assemblage en bicouche. 110
- 6.2 Images de cryo-TEM de SUV de POPC. Des structures bosselées sont visibles sur les bicouches de POPC. . . . . 112
- 6.3 Variation de l'épaisseur de bicouches de POPC et SOPC en fonction de leur degré d'hydroperoxydation (en % molaire). Note : l'épaisseur réelle n'est pas mesurée ici, mais une projection des bicouches de vésicules 3D sur un plan 2D. . . . . 112
- 6.4 (A) Température de transition entre la phase gel et fluide de vésicules de POPC et SOPC contenant différentes proportions de leur version hydroperoxydée (B) Enthalpie de transition entre la phase gel et fluide de vésicules de POPC et SOPC contenant différentes proportions de leur version hydroperoxydée. . . . . 113
- 6.5 Augmentation de la viscosité dans les membranes de POPC contenant une quantité de POPC-OOH croissante obtenues à partir des temps de vie du fluorophore (A) BC10 et (B) BC6++ . . . . . 114
- 6.6 (A) SAXS et (B) WAXS montrant un élargissement des pics de diffraction obtenus avec l'augmentation du degré d'hydroperoxydation dans les membranes. . . . . 115
- 6.7 Paramètre d'ordre de chaque carbone des chaînes lipidiques saturées et insaturées du (A) POPC, (B) POPC-OOH/POPC 50/50 %mol et (C) POPC-OOH. . . . . 115
- 6.8 (A) Intensité de la ligne de base (correspondant aux ions passant sans former de pores) normalisée par la surface des membranes en fonction du voltage appliqué et du degré d'hydroperoxydation des membranes de POPC. (B) Perméabilité calculée des membranes de POPC par rapport aux ions  $K^+$ ,  $Cl^-$  en fonction du degré d'hydroperoxydation. 116
- 6.9 (A) Nombre de pores ouverts par seconde en fonction du voltage et du degré d'hydroperoxydation des membranes de POPC. (B) Probabilité de former au moins un pore pour chaque application de voltage (6 s) pour différentes membranes de POPC contenant différents degrés d'hydroperoxydation. . . . . 117
- 6.10 Effet de l'hydroperoxydation sur l'organisation structurale des membranes. Les membranes hydroperoxydées ont une plus grande aire par lipide et peuvent plus facilement accueillir des molécules d'eau de part l'espace entre les lipides et d'autre part par les interactions du groupe peroxyde avec l'eau. La forme plus conique des lipides hydroperoxydés apporte une plus grande courbure au membrane, facilitant la stabilisation des pores. . . . . 118

- A.1 Equivalent electric circuit of a free-standing bilayer.  $R_s$  is the instrument resistance, which also includes the electrolyte,  $C_m$  is the membrane capacitance, and  $R_c$  is the intrinsic membrane resistance in absence of pores through which flows a current  $I_c$ . When a pore opens, an added current  $I_p$  flows through the pore resistance  $R_p$ . The instrument works in a voltage clamp mode where the potential difference  $U$  is always kept constant. . . . . 121
- A.2 Capacitance peak followed by completely and partially developed pore signals. The black solid line corresponds to ideal intensity measurements using our filtering conditions (bandwidth 0.6 kHz,  $\tau \sim 2.8$  ms), while the gray dash line shows the current that instantaneously ( $\sim$  nanosecond [135]) flow across the pore. The capacitance peak corresponds to ions charging the membranes, other current fluctuations correspond to pore opening or closing. When pores are closed, the current crossing the membrane is called  $I_c$ , when a pore opens ( $t_o$ ) the intensity value increases by  $I(\tau_p)$ . The intensity value can increase up to a stationary intensity  $I_p$  if the pore is long-lived enough ( $\tau_p > \tau$ ). After pore closure ( $t_c$ ) the current goes back to its initial  $I_c$  value. . . . . 123



# List of Tables

1	List of parameters used in equation 10 to compute Figure 20. . . . .	21
1.1	Singlet dioxygen lifetime in different solvent taken from Ross Table [151].	33
2.1	Indicative sonication time to prepare SUVs of each different lipid mixture for cryo-TEM analysis. The first sonication is performed before extrusion and the second sonication (when required) is always performed after extrusion. . . . .	45
2.2	DSC scans protocol. . . . .	49

# Eulalie LAFARGE

## Pore Formation in Oxidized Lipid Membranes

### Résumé

Les membranes biologiques sont principalement composées de lipides s'assemblant en bicouches imperméables empêchant le transport de différentes molécules à l'intérieur de la cellule. L'électroporation est une technique récemment développée, utilisée en thérapie pour insérer des principes actifs ou des gènes à l'intérieur des cellules afin d'augmenter l'efficacité du traitement et réduire les effets secondaires. En appliquant un stress électrique aux membranes, des pores se forment, augmentant considérablement la perméabilité des membranes. L'électroporation est utilisée pour soigner de nombreuses maladies, souvent liées à la présence de lipides oxydés, compromettant les propriétés structurales et mécaniques des membranes, entraînant le mauvais fonctionnement de mécanismes biologiques essentiels.

Il est pertinent d'étudier les membranes hydroperoxydées, afin d'avoir une meilleure caractérisation de leur propriétés mécaniques et structurales et de l'influence de l'hydroperoxydation sur la perméabilité des membranes et leur capacité à former des pores. Nous avons mis en évidence un amincissement de la membrane accompagné d'une fluidité et élasticité modifiées. Ces changements induisent une augmentation de la perméabilité et de la formation de pores obtenus durant l'électroporation de membranes suspendues.

Mots-clés : Membranes biologiques, Phospholipides, Hydroperoxydation, Perméabilité, Electroporation, Propriété mécaniques et structurales

### Résumé en anglais

Biological cell membranes are mainly composed of lipids assembling into impermeable bilayer preventing the translocation of numerous molecules inside of the cell. Electroporation is a recently developed technic used in therapy to insert drugs or gene inside a cell in order to increase treatment efficiency and decrease side effects. By applying an electric stress to the membrane, pores are able to open, increasing considerably the membrane permeability. Electroporation can be used in the treatment of numerous diseases often linked to the presence of oxidized lipid, compromising the membrane structural and mechanical properties leading to the non-functioning of essential biological mechanisms.

It is relevant to study hydroperoxidized membranes, to get a better characterisation of their mechanical and structural properties and study the hydroperoxidation impact on the membrane permeability and ability to form pores. Especially, we showed how hydroperoxidation thinner the membrane and modify its fluidity and elasticity. The modified properties of such membrane induce increased permeability and enhance pore formation during electroporation of free-standing bilayers.

Keywords: Biological membranes, Phospholipids, Hydroperoxidation, Permeability, Electroporation, Mechanical and structural properties.